Paul Rademeyer

Pembroke College

Supervised by

Professor Eleanor Stride

A New Technique for Microbubble Characterisation and the Implications to Contrast Enhanced Ultrasound

A thesis submitted for the degree of Doctor of Philosophy

Michaelmas 2015

Abstract

The utility of microbubble agents in a variety of diagnostic and therapeutic ultrasound techniques has been widely demonstrated, most notably in Contrast Enhanced Ultrasound (CEUS) imaging. Unfortunately, the underlying mechanisms of their response to ultrasound excitation are poorly understood, restricting the development of promising techniques, such as quantitative perfusion imaging. A significant reason for this is that current microbubble characterisation techniques suffer from one or more of the following limitations: i) large experimental uncertainties, ii) physical restrictions on microbubble response and iii) failure to provide large data sets suitable for statistical analysis. This thesis presents a new technique to overcome these limitations. A co-axial microfluidic device is used to hydrodynamically confine microbubbles through the focal region of a laser and ultrasound field. The magnitude of light scattered by isolated microbubbles during ultrasound excitation is converted to radius using Mie Scattering theory. This technique is capable of obtaining large samples (>10^3/min) of microbubbles to be efficiently characterised.

The response of a commercial contrast agent, SonoVue®, is first investigated for a range of ultrasound exposure parameters; frequency (2 MHz – 4.5 MHz), peak negative pressure (6 kPa - 400 kPa) and pulse length (3 cycles – 8 cycles). Second the device is used to investigate the effect of composition and fabrication on microbubble response to similar ultrasound conditions. The results demonstrate a very large variability in microbubble response independent of initial size, indicating a significant lack of uniformity of coating properties. This is further supported by quantitative fluorescence imaging and quasi-static pressure chamber measurements.

The implications of the findings for CEUS imaging and the development of microbubble contrast agents are discussed, as well as the limitations and suggested improvements of the characterisation technique.

Statement of Originality

I hereby declare that this submission is my own work and to the best of my knowledge it contains no materials previously published or written by another person, or substantial proportions of material which have been accepted for the award of any other degree or diploma at the University of Oxford or any other educational institution, except where due acknowledgement is made in the thesis.

Any contribution made to the research by others, with whom I have worked at the University of Oxford or elsewhere, is explicitly acknowledged in the thesis. I also declare that the intellectual content of this thesis is the product of my own work, except to the extent that assistance from others in the project's design and conception or in style, presentation and linguistic expression is acknowledged.

Paul Rademeyer

December 18th, 2015.

Acknowledgements

First and foremost I offer my sincere and heartfelt gratitude for the support, teaching and guidance I received from my supervisor, Professor Eleanor Stride. I thank her for going well beyond the duties of a supervisor to ensure I was on track, while seamlessly giving me the space to find my own way. I hope that this thesis (and my reluctance to stray from the engineering principles she taught me during my undergraduate) is representative of her investment in time and effort.

I also extend my appreciation to all those, past and present, in the BUBBL lab who have encouraged my work and made it such a pleasant working environment. In particular I would like to thank Prof. Robin Cleveland, Dr. Ming-Wei Chang, Dr. Joshua Owen, Dr. Dario Carugo and Dr. Richard Browning. I would like to thank Miles Aron and Dr Lester Barnsley for their enthusiasm and much appreciated positive criticism. External to the group I also would like to express my gratitude to Prof. Glynn Holt for his time to discuss Mie Scattering theory and the application of it when I was just getting to grips with the subject.

This thesis would not have been possible without the expertise and patience of James Fisk and David Salisbury in the BUBBL workshop. Thank you for the invaluable advice and good humour in the building of the experimental set up. I would also like to thank Kevin Doyle from GPE Scientific for advice when designing the glass microfluidic device and their engineers for building it to such a high quality.

I express my gratitude to the RCUK Digital Economy Programme, EPRSC, for funding my DPhil and all of those who I have had a pleasure to work with at the Oxford Centre for Doctoral Training in Healthcare Innovation.

On a more personal note, it is with great pleasure that I can thank my family and friends for the unlimited support and patience while I've been working on this thesis. My thanks to Ben Wentworth and KiJoo Pahk for their comradeship throughout our undergraduate and the many long nights spent finishing reports together. It turned out to be essential preparation for writing my thesis!

I must express my gratitude for all of those I have had the pleasure of getting to know in Oxford over the last few years and making me feel at home. In particular, for the support and shared adventures I thank Nicholas and Andy O'Brien, Ali Avery, Stefania Giordano, Lauren Spiceley and Patrick Gabo. Most importantly I would like to express my thanks to the lovely Oda Almas, for her continued support and giving me perspective during the most difficult times.

Finally, I cannot begin to express how grateful I am to my parents, Elizabeth and David Rademeyer, and siblings, Alison Henderson and Jon Rademeyer, for their unlimited support and love. I would like to dedicate this work to my niece and nephew, Esther and Joel Henderson, for reminding me to stay curious.

Dissemination

Peer Reviewed Publications

Rademeyer, P., Carugo, D., Owen, J., and Stride, E., *Behaviour of SonoVue® Microbubbles: Size matters,* In preparation

Rademeyer, P., Carugo, D., Lee, J.Y. and Stride, E., *Microfluidic system for high throughput characterisation of echogenic particles,* Lab on a Chip, 2015,15, 417-428

Owen, J., **Rademeyer, P**., Chung, D., Cheng, Q., Holroyd, D., Coussios, C. and Stride, E. *Magnetic targeting of microbubbles against physiologically relevant flow conditions*. Interface Focus, 2015, 5(5), 20150001.

Owen, J., Grove, P., **Rademeyer, P**. and Stride, E. *The influence of blood on targeted microbubbles*. Journal of the Royal Society Interface, 2014, 11(100), 20140622.

Neveen A. H., Graciela M., **Rademeyer, P**., Owen, J., Wu, Y., Tang, M., Eckersley, R., Stride, E. and Kuimova, M*., Mapping microbubble viscosity using fluorescence lifetime imaging of molecular rotor.* Proceedings of the National Academy of Science (PNAS), May 2013 (front cover)*;* doi:10.1073/pnas.1301479110

Owen, J., **Rademeyer, P.** and Stride, E., *Magnetic targeting of microbubbles at physiologically relevant flow rates.* J. Acoust. Soc. Am., 2013, 134(3992); doi:10.1121/1.4830560

Conference Presentations

Rademeyer, P., Carugo, D., Browning, R., Owen, J., Teo, B. and Stride, E., *High Throughput Acoustic and Optical Characterisation of Microbubbles for Optimised Contrast Ultrasound Imaging,* 170th Meeting of the Acoustical Society of America in Jacksonville, 2015

Rademeyer, P., Carugo, D., Sezgin, E., Serna, J., Zhang, C., Owen, J. and Stride, E., *A multi-technique Investigation of the Effect of Coating Composition on Microbubble Behaviour*, 21st European Symposium on Ultrasound Contrast Imaging 2015, Rotterdam, Netherlands.

Rademeyer, P., Owen, J., Chang, M. and Stride, E.*, A High Throughput Device for Measuring Single Microbubble Response to Ultrasound Excitation.* The 19th European Symposium on Ultrasound Contrast Imaging 2013, Rotterdam, Netherlands.

Contents

List of Figures

Acronyms

CEQUS	Contrast Enhanced Quantitative Ultrasound
CEUS	Contrast Enhanced Ultrasound
CT	Computer Tomography
CTR	Contrast to Tissue Ratio
DPBS	Dulbecco's Phosphate-Buffered Saline
DPPC	1,2-dihexadecanoyl-sn-glycero-3-phosphocholine
DSPC	1,2-distearoyl-sn-glycero-3-phosphocholine
DPSG	1,2-dioctadecanoyl-sn-glycero-3-phospho-(1'-rac-glycerol)
FLIM	Fluorescence Lifetime Imaging
GP	Generalised Polarisation
LD	Laser Diffraction
MRI	Magnetic Resonance Imaging
OM	Optical Microscopy
PEG40S (PEG)	Polyoxyethylene glycol 40 stearate.
PMT	Photo-Multiplier Tube
RMS	Root Mean Square
SNR	Signal to Noise Ratio
SPOS	Single Particle Optical Sizing
TEM	Transmission Electron Microscopy
TIC	Time Intensity Curves
UCA	Ultrasound Contrast Agent

List of Symbols

r	Instantaneous microbubble radius
R	Distance from a central point
d	Diameter
f_0	Fundamental ultrasound driving frequency
ρ	Density
c	Speed of sound
P	Pressure
μ	Dynamic viscosity
κ	Kinematic Viscosity
G	Elastic Modulus
T	time
NA	Numerical Aperture
λ	Wavelength
Re	Reynolds Number
Q	Fluid flow rate
V	Fluid velocity
Σ	Surface tension
d_s	Thickness of a microbubble's coating
a	Distance from centre of microbubble

	Subscripts
i	Initial state
S	At the surface interface
L	Surrounding liquid medium
∞	Infinite or far field

"We are continually faced with great opportunities which are brilliantly disguised as unsolvable problems."

— Margaret Mead

Background, Motivation and Overview

Ultrasound Imaging is a non-invasive, real time and cost effective diagnostic tool. Microbubble agents, injected intravenously, during ultrasound imaging are able to significantly improve the contrast between blood vessels and surrounding tissue using techniques that exploit their nonlinear behaviour. The maximum contrast to tissue ratio and spatial resolution, however, are still inferior to those of more resource intensive and potentially damaging modalities such as Magnetic Resonance or X-Ray imaging. One reason for this is the incomplete understanding of the relationship between microbubble response and ultrasound excitation parameters. Previous characterisation methods have been limited by small sample numbers, high uncertainties and physical boundaries restricting a microbubble's response. This chapter describes the previous methods and provides the context for the work presented in this thesis.

1.1. Ultrasound Imaging: A Brief History

By far the most sophisticated use of sound waves was already in place an estimated 1 million years ago [1] . This is, of course, the echolocation technique used by bats to navigate their surroundings and locate insects in the dark, successfully filling an evolutionary niche in nature. It wasn't until the early 20th century that humans found a similar use for sound waves, provoked by two tragic events. After the sinking of the Titanic, physicist Paul Langevin developed the first hydrophone coupled with a low frequency sound source that could detect rogue ice bergs up to 2 miles away [1]. This technology was then further developed during World War 1 for the detection of submarines and became known as SONAR (*So*und, *na*vigation and *r*anging) [2]. No more than 40 years after this Karl Dussik was investigating the use of high frequency sound waves above 20 kHz, termed ultrasound, as a medical diagnostic tool [3]. In even less time this technique developed into what is known today as ultrasound imaging, the use of sound waves to construct an image of an internal environment that is not otherwise visible. Since the 1950's ultrasound imaging has been steadily increasing in its use for medical imaging and diagnostics, in 2014 ultrasound imaging accounted for over a quarter of all clinical imaging procedures [4].

The reason for ultrasound's increasing popularity is its low cost, system portability, low risk, patient acceptability and real time imaging capabilities [5] unrivalled by other imaging modalities. Unfortunately these benefits are often outweighed by the lower resolution and contrast of conventional ultrasound

imaging (B-Mode) when compared to imaging modalities such as Magnetic Resonance Imaging (MRI) and X-Ray imaging, both planar and Computed Tomography (CT). For example, in cancer diagnosis, the ultrasound contrast to tissue ratio (CTR) between healthy tissue and early stage tumours is greatly inferior to that achievable with MRI or CT [6]. These high contrast and resolution imaging techniques, however, have disadvantages not only associated with much higher costs (initial and operational) but also ionising radiation, increased scan times, lower availability, and increased sensitivity to movement artefacts. This means that the diagnostic use of these techniques is frequently confined to patients deemed high risk and already symptomatic.

Research into a potential solution was set into motion in 1968 when Gramiak *et al.* [7] reported increased ultrasound contrast at the tip of a catheter during a routine ultrasound scan. The increase in contrast was caused by microbubbles forming at the exit of the catheter as a saline solution was injected. This finding helped to fuel a growing research field into Contrast Enhanced Ultrasound (CEUS) by exploiting the echogenicity of microbubbles, often referred to as Ultrasound Contrast Agents (UCA).

1.2. Microbubbles as Contrast Agents

For this work a microbubble will be defined as a gas or vapour cavity in a liquid medium that has a diameter of less than 1 millimetre, typically 1 – 10 micrometres in diameter for medical applications. In the context of biomedical

ultrasound, microbubbles are typically gas filled and fabricated using sonication [8], or more recently techniques such as microfluidics [9] or co-axial electro-hydrodynamic atomisation [10]. Due to the combination of gas concentration gradient and surface tension (Laplace pressure), the effect of which is inversely proportional to the bubble size, the gas inside a microbubble will tend to dissolve into the surrounding liquid [11]. In the case of an air bubble of a few micrometres in size in water this will occur very rapidly (<< 1 second). Stability can be significantly increased, however, by utilising relatively insoluble higher molecular weight gases (e.g. perfluorocarbons) and encapsulating the microbubbles with a protein, surfactant, lipid or polymer shell [12]. In addition to inhibiting gas diffusion, the coating enables the engineering of desirable mechanical/acoustic properties [13], [14] and can also be loaded with therapeutic agents and/or a large variety of nanoparticles for targeting, such as magnetic nanoparticles [15]. Table 1.1: lists the currently approved ultrasound contrast agents available for clinical use in the USA and Europe.

Agent	Manufacturer	Gas	Coating	Approval
SonoVue®	Bracco Imaging	Sulphur hexafluoride	Phospolipid	EMEA
Optison®	GE Healthcare	Perfluoropropane	Albumin	FDA/EMEA
Definity®	Lantheus Medical Imaging	Perfluoropropane	Phospolipid	FDA/EMEA

Table 1.1: Clinically available microbubbles for use as Ultrasound Contrast Agents [16]

Microbubbles are the ideal Ultrasound Contrast Agents due to their high compressibility and hence impedance contrast compared to particles of a similar

size, for example red blood cells. The high compressibility of a microbubble leads to large volume expansions during ultrasound excitation that produces significant back scattered pressures. The response is further enhanced by resonant effects for which microbubbles are predicted to exhibit in the range of typical diagnostic ultrasound frequencies.

1.2.1. Methods for improved ultrasound contrast

The high echogenicity of UCAs improves contrast in standard B-Mode imaging, however, it is their nonlinear behaviour that makes it possible to achieve contrast comparable to MRI and CT imaging [17]. When driven at an ultrasound frequency of f_0, microbubbles respond producing a signal containing sub-harmonics and harmonics at $n*f_0$ where n = 0.5, 2, 4, 6…. These frequencies can be used to discern signals produced by microbubbles in the vasculature from the surrounding tissue, known as standard harmonic imaging [18]. The challenge, however, has been that there is a compromise between the signal to noise ratio (SNR) and contrast to tissue ratio (CTR) [19] for such conventional techniques [20]. By increasing the driving ultrasound pressure the SNR is increased due to increased backscattering, however the CTR decreases since the nonlinear propagation of ultrasound through tissue is proportional to ultrasound pressure. Thus the back scattered signal from tissue may also contain harmonic components. In addition the likelihood of microbubble destruction increases. Improvements in low noise transducers and amplifiers for ultrasound platforms [21] have enabled low pressure CEUS that reduces these problems, however a trade-off is typically made for a decrease in the receiving bandwidth [22]

resulting in lower spatial resolution and a reduction in the sensitivity to higher order harmonics.

1.2.2. Extended CEUS imaging techniques

There are, however, promising techniques that are able to overcome the SNR and CTR compromise by further exploiting the nonlinear behaviour of microbubbles. Amplitude modulation and pulse inversion imaging [18], for example, exploit the nonlinear scaling of a microbubble's response compared to the more linear scaling of a tissue's response. Pulse inversion imaging combines the received responses after sending two identical pulses that are 180 degrees out of phase, shown in Figure 1.1 below. This process results in a nonlinear residual for signals originating from microbubbles, but not for tissue, thus increasing the CTR. Both techniques, however, require the transmission of multiple ultrasound pulses reducing the temporal resolution [23].

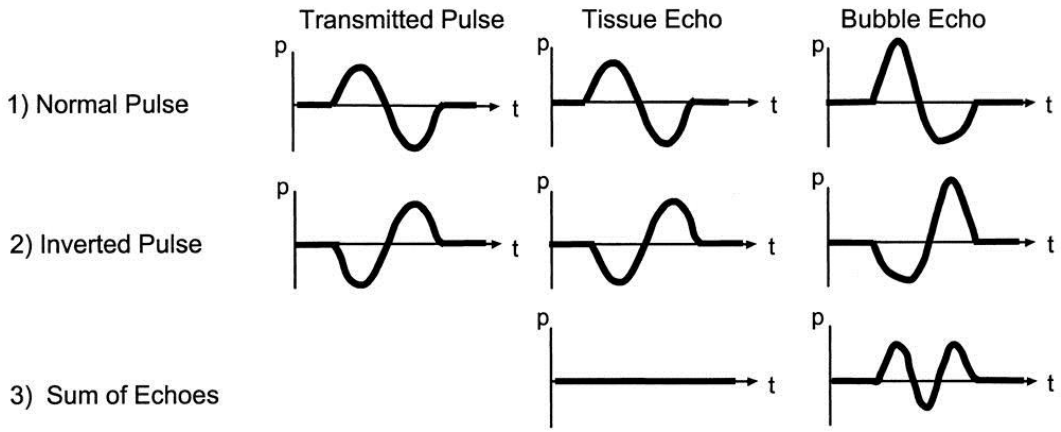

Figure 1.1: Principle of Pulse Inversion Imaging: The sum of the inverted responses cancel out for linear scatters, such as tissue, however for microbubbles there is a nonlinear residual that can be used to improve the CTR. Figure and caption adapted from [24]

A further technique, known as Coded Excitation [25], has been explored to increase the magnitude of a microbubble's response at lower pressures while minimising the nonlinear propagation of ultrasound. Coded excitation pulses, such as linear chirp signals, have been shown to significantly improve the SNR by up to 20 dB, allowing greater depth penetration while achieving the same lateral resolution when carefully designed to minimise side-lobes [25]. Borsboom *et al.* [19] have shown in simulations that an extended pulse increases the amplitude of a microbubble's oscillation as well as the generation of harmonic emissions without requiring an increase in the driving ultrasound pressure. This they suggest is caused by the microbubble undergoing a stable rather than transient response at longer pulse lengths. It has also been shown to be possible to combine pulse inversion or amplitude modulation imaging with coded pulses to get the advantages of both techniques for CEUS imaging, i.e. increased CTR and SNR [26]. However, these techniques are still developing and are an active field of research due to the challenge of optimising the pulses such that the axial resolution is not reduced.

1.2.3. Contrast enhanced quantitative ultrasound imaging

Recent advances in microbubble fabrication and nonlinear signal processing have demonstrated the potential for obtaining quantitative information; termed Contrast Enhanced Quantitative Ultrasound (CEQUS) [27] [28]. CEQUS imaging is a non-invasive technique to measure physiological parameters including tissue perfusion, flow velocity, vascular volume and hydrostatic pressure. It is desirable for clinicians to be able to measure these

parameters to identify local regions of abnormal blood flow, e.g. in the presence of tumours or cardiovascular disease [29]. Further, absolute metrics enable the comparison of patients, better monitoring of a treatment and, importantly, personalised guidelines for diagnosis and therapy. Unfortunately there are many challenges to overcome before the potential of CEQUS imaging can be fully realised [27]. Significant amongst these challenges, is the poor understanding of the response of microbubbles *in vivo* to ultrasound excitation. Factors that influence this interaction include; microbubble size distribution and coating properties, biological interactions and nonlinear ultrasound propagation through tissue [27]. Microbubble characterisation is therefore crucial to improving our understanding of a microbubble's response to ultrasound excitation and to the development of CEQUS imaging.

Promising CEQUS applications include the estimation of tissue perfusion based on Time Intensity Curves (TICs) and hydrostatic pressure using Sub-harmonic Aided Pressure Estimation (SHAPE): TICs are measured by destroying microbubbles with a high pressure pulse and then monitoring their replenishment with lower pressure ultrasound [30],[31]. This technique has been employed successfully *in vitro* to measure flow velocity [32] and with promising results *in vivo* assessing patient response to anti-inflammatory medication [33], however, larger studies are still required. SHAPE exploits the sub-harmonic response of microbubbles as an indicator of hydrostatic pressure *in vivo* [34]. Studies again have been with very limited sample sizes and only shown

significant results *in vitro* [35]. Reports on both methods have highlighted the need for better characterisation of microbubbles.

1.3. Techniques for the Characterisation of Microbubble Properties

Encapsulated microbubbles are commonly defined by their resting radius and coating's physical properties. This section details methods for directly measuring these, as well as techniques for estimating properties by fitting theoretical models to experimental measurements.

1.3.1. Microbubble sizing

As will be discussed in this thesis, size is an important factor in determining how a microbubble will respond to ultrasound excitation. The clinical contrast agent SonoVue® is reported to have a mean diameter of 2.5 µm, with 90% of the sample under 8 µm [36]. There are many different methods for measuring microbubble size and a population's distribution. A recent review by Sennoga, *et al.* [37] compared three methods: electro-impedance volumetric zone sensing (ES), optical microscopy (OM) and low-angle laser diffraction (LD). They concluded that both OM and ES produced reproducible size distributions with errors below 5% when estimating a population's mean diameter, whereas LD had too large uncertainties to be recommended as a suitable method. Two further techniques have been investigated in separate works that are able to indirectly estimate microbubble size based on the scatter of plane wave light or

high frequency ultrasound. Light scattering has been successfully applied to the sizing of individual microbubbles [38] and theoretically achieves a higher resolution than OM [39]. It does, however, require very accurate calibration of the optical components. Sizing using high frequency ultrasound aims to exploit the linear back scattering of microbubbles when excited much above their resonant frequency. However, the technique is limited by the inherent uncertainty in transducer calibration (see Section 2.5.3) and difficulty in accurately locating the microbubble in a focussed ultrasound field. A study by Maresca *et al.* [40] produced mean errors of 26 % (n = 86) when investigating the acoustic sizing of Definity® microbubbles at 25 MHz.

1.3.2. Direct measurement of coating properties

As mentioned previously, a microbubble's coating imparts mechanical properties that alter its response to ultrasound excitation. As will be discussed in Section 3.1.2, the physical properties, relevant to this study, of an encapsulated microbubble are commonly modelled as an elastic modulus, G, and viscosity, μ [41]. However, these properties are of theoretical convenience, and at best can only approximate the effects of the rheological properties of phospholipid coatings (discussed further in Section 3.1.2). There are two quantitative fluorescence techniques that are particularly interesting for understanding the physical properties of phospholipid membranes and can be applied to microbubble coatings. They have been used to support the findings of this work and are described in greater detail in Section 2.4.2. Briefly, Fluorescence Lifetime Imaging Microscopy (FLIM) uses a special type of fluorescent probe (molecular

rotors) that is able to measure an effective viscosity of the lipid membrane and has already been applied to the study of microbubble composition, Hosny *et al.* [42]. More recently, a technique known as Spectral Lambda imaging [43] has been applied to microbubble coatings to measure the packing density of phospholipids, where the packing density is proportional to the interfacial tension of a microbubble's coating and hence effective visco-elastic properties.

In other fields of research, the mechanical properties of lipid mono-layers are measured using a Langmuir Trough; however the experiment involves compressing large samples between two plates and so neither the effect of curvature or high frequency motion can be evaluated. To the best of the author's knowledge, the quantitative fluorescence techniques described briefly above are the only two methods currently in use to directly measure physical properties of the phospholipid coating. There are, however, indirect methods as described in the next section.

1.3.3. Indirect measurement of coating properties

The effective elastic modulus (assuming the coating acts as a visco-elastic material) can be measured by fitting Hooke's law to measurements of a microbubble's diameter while undergoing quasi-static changes in hydrostatic pressure. Hydrostatic pressure chambers are commonly used for pressure studies on biological samples [44] but can be adapted for microbubble studies. Zhushma, *et al.* [45], for example, built a pressure chamber for the study of microbubbles for high pressure (27 MPa) oil exploration. However, their design is

not suitable for observing microbubble behaviour at clinically relevant pressures due to thick windows restricting optical resolution. This limitation has been addressed by the design of a custom hydrostatic pressure chamber, described in Section 3.4.1.

A common characterisation approach has been to determine the elastic modulus and viscosity by fitting a theoretical model[1] to experimentally measured microbubble responses. To determine these properties the error between the modelled and empirical response is minimised by adjusting the unknown parameters, for example Eq.1.1. The models do not have analytical solutions and therefore must be solved numerically. Figure 1.2 shows the best fits for three different models solved numerically compared to light scattering data[2] from a study by Matula *et al.* [46].

$$minimise: f(r_0, G_s, \mu_s) = \sum_{t=0}^{\infty} [r_{empirical}(t) - r_{theoretical}(t, r_0, G_s, \mu_s)]^2 \quad (1.1)$$

[1] Such as the Modified Rayleigh-Plesset equation or derivations of it. See Section 3.1.2
[2] The method used to obtained these data is discussed further in Section 1.4.3

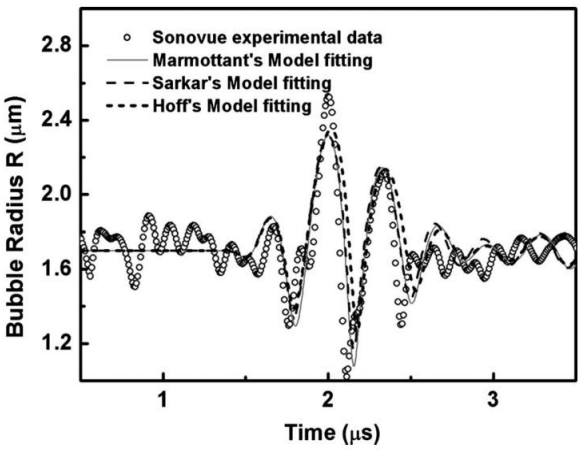

Figure 1.2: Comparison of simulated models fitted for the parameters of viscosity and elasticity to a light scattering measurement of a microbubble oscillation. Figure taken from Matula et al. [46].

However, in order to derive parameters using this method the models should be i) validated, ii) assessed for their sensitivity to experimental uncertainties and iii) assessed for the uniqueness of solving for the various unknown parameters. To the author's knowledge, neither has been done or attempted in this context. Further, as will be discussed in Section 3.1.2, the assumption of the coating behaving as a visco-elastic material is an over simplification. As new phenomena are discovered, models are becoming more complicated with an increasing number of parameters, further reducing the certainty with which properties can be derived from conventional experiments. Phenomena that have been identified that are not accounted for in the conventional models include lipid shedding [13], time dependent dissolution [47] and non-spherical oscillations [48]. Further, it has been observed in this study and by several previous works (for example Faez *et al.* [49], Sprague *et al.* [50]

and Postema *et al.* [51]) that there is inconsistent behaviour between microbubbles of identical initial size.

In addition to the challenges relating to the models themselves, there are significant limitations in the current techniques for measuring a microbubble's response under ultrasound excitation. The following section reviews the current state of the art and identifies the key limitations that will be addressed in this thesis.

1.4. Measuring a Microbubble's Response to Ultrasound

To better understand the behaviour of microbubbles under ultrasound excitation it is desirable to be able to observe individual microbubbles in an "infinite" medium, i.e. away from any boundaries/objects that might affect the response. This is important for fitting data to theoretical models. The experimental methods and consequences of microbubble isolation are discussed in Section 2.1.1. It will be discussed that previous techniques, namely high speed imaging, have been limited by not being able to fully isolate single microbubbles. This section summarises the common methods used to measure their response.

1.4.1. Acoustic scattering

The scattered pressure produced by a stably oscillating microbubble can be detected by an ultrasound transducer [52] [53] and the SNR will be maximised

if the bubble is located at the transducer's focal point. Single element ultrasound transducers have a relatively narrow bandwidth, requiring multiple transducers of varying centre frequencies to detect harmonics; although medical ultrasound probes have been used to attain higher bandwidths [54] [55].

Studies [56] [57] are generally conducted at excitation frequencies between 1 – 10 MHz which covers the range over which microbubbles are theoretically resonant. Higher frequency studies have been performed to exploit the more linear behaviour of microbubbles when excited off resonance [58] [59] [60]. However with higher frequencies the ultrasound -6 dB beam width, Eq. 1.2 decreases [61] and the uncertainty of the excitation pressure at the microbubble location increases.

$$BD(-6dB) = \frac{1.02Fc}{fD} \tag{1.2}$$

Where *F* is the focal length, *c* is the speed of sound, *f* is the frequency and *D* the element diameter.

As mentioned before, the acoustic response of a microbubble can be used to derive its physical properties by comparing the measurements to theoretical models. However, the simulated response is in terms of radial displacement and must be converted to the scattered pressure. This is achieved, assuming spherical oscillations, using potential flow theory [62], and is discussed further in Section 3.1.3.

The majority of acoustic studies [52], [57], [63] isolate microbubbles in a capillary tube and obtain the initial microbubble radius by imaging with a microscope objective. This reduces the number of unknown parameters to solve for, improving the accuracy of the fitting. However, there are two significant problems with this method, i) the presence of the microscope objective (typically 1 - 3 mm working distance) and the capillary tube interfere with the ultrasound field and ii) the effect of buoyancy pushes microbubbles against the surface of the capillary tube which results in asymmetric oscillations, not comparable to the symmetrical models. This is also a challenge for high speed imaging studies, described in the next section, which rely on the microbubbles being stationary.

1.4.2. High speed imaging

High speed imaging has arguably provided the greatest insights into microbubble behaviour and response to ultrasound excitation. Some of the significant phenomena observed include non-spherical behaviour and surface modes [48] (shown in Figure 1.3), compression-only behaviour [64], sub-harmonic thresholds and lipid shedding [65]. It does, however, require a camera capable of capturing millions of frames per second to temporally resolve microbubble oscillations. To meet such demanding specifications, it is necessary to relay a projected image onto an array of CCD (or CMOS) sensors. This may be done electronically or mechanically. In the case of the latter, the image is usually relayed using a mirror prism rotated at high speeds by a helium powered turbine. These cameras are very expensive; require a large supply of helium and physical space. Solid state cameras are more convenient to use but current models can

only capture a very limited number of frames (typically 8). Several groups in the Netherlands, United Kingdom and United States of America [66],[67],[68],[69] have used high speed imaging to observe individual microbubbles during ultrasound excitation.

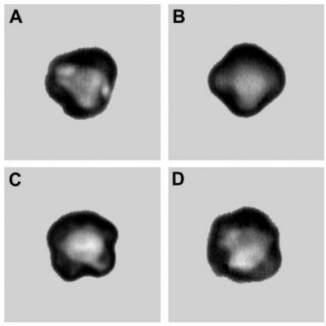

Figure 1.3: Surface modes of microbubbles as imaged with the Brandaris 128 camera. A – B are basic modes whereas C-D are mixing modes. Image taken from [48]

High speed imaging of microbubbles has been pioneered by research groups in the Netherlands who developed the Brandaris camera 128 [69], and optimised for microbubble imaging. The camera is capable of recording up to 25 Mfps, 6 sequences of 128 frames with 80 ms between each sequence (up to 125 sequences for reduced ROI), isolation of microbubbles using optical tweezers and fluorescence imaging up to 2 Mfps [70]. A good example of the camera's functionality is using a segmented mode to capture 12-24 sequences of a microbubble's oscillation over a range of frequencies in a single experiment, dubbed microbubble spectroscopy [71].

High speed imaging is fundamentally limited by the frame rate and the resolution of the optical system. The theoretical spatial resolution limit is

determined by the Numerical Aperture (NA) and the wave length of light (λ), as given by the Rayleigh Criterion [51]:

$$r_{theoretical} = 1.22\frac{\lambda}{NA} \tag{1.3}$$

The Rayleigh Criterion gives an estimate of the smallest resolvable distance between two point scatterers and does not necessarily account for the diffraction of light due to the spherical microbubbles which may allow improved resolution when sizing. However, more significant than these limitations is that i) large sample analysis (more than 100 samples in a day) is not possible due to the time required to position and prepare microbubbles in a typical experiment, ii) microbubbles may, and have been shown to, change size or collapse over the duration of experiments and iii) the images obtained represent only a single 2-dimensional plane of each microbubble's response.

1.4.3. Light scattering

Measurements can also be obtained from oscillating microbubbles by detecting the light scattered as microbubbles pass through a focussed laser beam with sensitive photo-multiplier tubes (PMT) [72]. The scattering of light from small spheres can be predicted using Mie theory and has been adapted for coated microbubbles [73], this is discussed further in Section 3.1.4. For microbubbles considered in this study investigated in the visible light spectrum, simulations show an R^2 dependence between scattered intensity and microbubble size [72]. Unlike high speed imaging, light scattering does not provide any direct information about shape oscillations or microbubble

destruction; however it does provide a non-invasive method for microbubble sizing and is better suited for high throughput measurements.

Laser scattering measurements of microbubbles undergoing ultrasound excitation have been made by Matula *et al.* [46] using off-the-shelf components to obtain high SNR measurements. The SNR was then further improved by the same group by adapting a flow cytometer [38]. The adaption enabled the location of the microbubble to be known more precisely, but, unfortunately restricted the control of ultrasound excitation and imposing a solid boundary that may restrict a microbubble's expansion.

1.4.4. Combined characterisation

The feasibility of simultaneously obtaining images and acoustic measurements has been demonstrated by Dayton *et al.* [74]. A 600 Hz camera combined with a 1 μs flash to image microbubble oscillations driven at 500 kHz while detecting the scattered acoustic pressure with a second transducer. Sijl *et al.* [53] applied this concept using the Brandaris camera. In the work simultaneous high speed images and the scattered pressure from a single microbubble constrained in a capillary tube were captured and compared. It was found that the uncertainty in transducer measurements led to large (up to a factor of 3) variations in radial amplitude predictions when compared to the high speed images, and that the acoustic measurements achieved better sensitivity at the harmonics when compared to optical due to the restricted spatial resolution (0.2 μm/pixel) and camera frame rate.

1.5. Objectives

The objectives of this thesis are to:

i) Develop an experimental apparatus that overcomes the limitations associated with the current microbubble characterisation techniques
ii) Utilise this technique to investigate an existing clinical microbubble contrast agent and
iii) Investigate microbubble composition and fabrication with a view to optimised performance as contrast agents.

Previous characterisation techniques have suffered from one or more of the following limitations:

- experimental uncertainty translating into large uncertainties in fitted parameters;
- failure of existing set ups to provide data that can be directly compared with models (e.g. due to boundary interactions);
- failure of existing methods to provide large data sets suitable for statistical analysis;

Although previous characterisation methods have allowed for a much greater understanding of microbubble behaviour, due to these limitations it has not been possible to apply the insights to the optimisation of their application as contrast or therapeutic agents.

1.6. Thesis Overview

The content of each chapter is summarised in the table below. For convenience and ease of reading, the relevant background literature is reviewed in individual chapters rather than in a single chapter.

Chapter	Title	Summary
1	*Background, Motivation and Overview*	
2	*Rig Design and Calibration*	*An experimental rig is developed and calibrated for the characterisation of single microbubbles at high throughput rates.*
3	*Theory, Data Analysis Protocol and Methods*	*An overview of the theory relating to the light scattering from isolated microbubbles and a protocol for data analysis.*
4	*Behaviour of a Clinical Ultrasound Contrast Agent*	*Investigation of the response of SonoVue® microbubbles under varying environmental and ultrasound condition*
5	*Comparison of Microbubble Composition and Fabrication Techniques*	*Investigation comparing in-house microbubble composition (lipid, emulsifier:lipid ratio, nanoparticles) and fabrication techniques (sonication, microfluidic)*
6	*Conclusions and Future Work*	*A summary of the work, highlighting the implications to CUES imaging and the development of microbubble contrast agents. Limitations of the thesis and suggested improvements are discussed.*

Table 1.1. Overview of thesis chapters

“Lack of experience diminishes our power of taking a comprehensive view of the admitted facts. Hence those who dwell in intimate association with nature and its phenomena grow more and more able to formulate, as the foundations of their theories, principles such as to admit of a wide and coherent development: while those whom devotion to abstract discussions has rendered unobservant of the facts are too ready to dogmatize on the basis of a few observations.”

Aristotle

CHAPTER 2

Rig Design and Calibration

This chapter describes the design, construction and calibration of an experimental rig to measure the radial response of single microbubbles under ultrasound excitation to better understand and characterise their behaviour. The design overcomes several limitations of previous methods and is shown to meet the design criteria. This work has been published in modified form by the author [75].

As described in Chapter 1, existing methods for the characterisation of individual microbubbles suffer from a number of disadvantages that has limited their ability to improve understanding of microbubble behaviour and the potential optimisation of their clinical applications. Previous techniques, such as high speed imaging and acoustic studies, have suffered from one or more of the following limitations: i) large experimental uncertainties, ii) the need to

physically constrain microbubbles leading to a change in acoustic response and iii) low sample numbers unsuitable for statistical analysis. In this chapter a microfluidic system is presented that addresses these limitations enabling high throughput characterisation of the unconstrained response of echogenic particles to ultrasound excitation. The following sections describe the underlying principles of the system, its design, construction and calibration.

2.1. Design Requirements

The design is based on three main criteria to address previous limitations of single microbubble characterisation:

1. Isolation of single microbubbles unconstrained from physical boundaries
2. High throughput for statistical analysis
3. Accurate measurement of microbubble size and radial response to ultrasound excitation

2.1.1. Microbubble isolation

A key aspect of characterising the acoustic response of individual microbubbles is achieving sufficient isolation, i.e. observing a response in the absence of physical boundaries and/or neighbouring microbubbles that may alter its behaviour. Commonly, isolation from other microbubbles/particles is achieved by pumping a highly diluted solution of particles through an optically and acoustically transparent cellulose tube (typically 100-200 μm internal diameter) [52], [63]. The tube aids in the alignment of optical and acoustic

instruments, however the tube wall has been shown to affect the behaviour of microbubbles, reducing its radial response by up to 50% [76], [77].

In order to eliminate physical interactions with boundaries two methods have been successfully employed: optical tweezers and hydrodynamically focussed flows. Optical tweezers can be used to counter a microbubble's buoyancy and push it away from the top surface of a capillary tube; this has been utilised in several high speed camera studies [78]. However, a tube is still required that may affect the ultrasound field and the time required to isolate a single microbubble makes large sample analysis unfeasible [79]. Hydrodynamic focussing [80], [81] is less restrictive in this sense. The method was pioneered for ultrasonic particle analysis in the late 80's by Roos [82] and further developed by Apfel [83] and Roy [81]. A similar set up was also used by Everbach to measure the size distribution of a population of single microbubbles [84]. A hydrodynamically focussed flow is produced by two concentric needles each with independently controllable flow rates. The outer flow (sheath flow) causes the inner flow (particle flow) to taper along a well-defined path from the exit of the needles. This approach allows for a very high throughput of particles and accurate control of their spatial location as shown by Roy and Apfel [83].

With the advent of microfluidic technologies, a range of devices have been developed to achieve two- or three-dimensional hydrodynamic focussing of micro-scale objects [85]. Three-dimensional hydrodynamic focussing can be achieved by different means, e.g. by using co-axially aligned microchannels [86]; by exploiting the inertial forces resulting from particle

confinement at Reynolds numbers, Re > 1 (also known as inertial focussing) [87]; by combining inertial focussing with lateral particle drift generated by secondary flows in curved microchannels [88]; or by designing for specific microstructures (e.g. chevrons) which deflect a particle's trajectory towards a desired location [89]. The main features of co-axial focussing architectures which make them suitable for this application include: i) the need for controlling two inlet flow lines only, ii) the physical separation between the focussed stream and the inner surfaces of the device, iii) the ease of priming, cleaning and operation.

2.1.2. Sample numbers

Previous individual microbubble studies have suffered from low sample numbers that are not necessarily representative of a population's response. Further, due to the time and effort required to isolate and locate individual microbubbles, a bias is introduced by only observing a sub-set of the population that are likely to be the most stable. Typical high speed imaging studies contain the analysis of around 100 individual microbubbles, studied over the course of several days or weeks [70]. The particle isolation technique discussed above, however, enables a much higher throughput and measurement of microbubble responses. Not only does this provide a better representation of a population in terms of numbers, but also the microbubbles can be measured under the same conditions within an hour of each other for a typical experiment of n > 100,000. The throughput rate is limited only by the collection rate of the oscilloscope, often referred to as the 'dead' time, i.e. the time taken to save each sample to a hard drive.

2.1.3. Accurate measurement of microbubble size and response

As discussed in Sections 1.3.1 and 1.4, simultaneous measurements of a microbubble's size and response can be obtained either optically or acoustically. Ultrasonic scattering measurements are easier to perform and provide data that are directly relevant to imaging applications. Unfortunately, acoustic particle sizing is relatively imprecise [90] and there is a trade-off between transducer sensitivity and bandwidth that results in a significantly lower SNR when compared to optical measurements.

Light scattering offers many advantages over both optical microscopy (high speed imaging studies) and ultrasound scattering measurements. The theory of plane wave light scattering from spherical particles is well established, and has been successfully employed in the sizing of microbubbles [91] and for measuring their radial response, Holt [92]. Previous work by Matula *et al.*[38], [72] has demonstrated the potential of light scattering as a powerful microbubble characterisation technique by adapting a flow cytometry device to include a piezoelectric transducer. An example of the type of data obtained is shown in Figure 2.1. High SNR was achieved, although the flow cell used in this case imposed a physical boundary making it difficult to characterise the acoustic pressure field and eliminate boundary interactions.

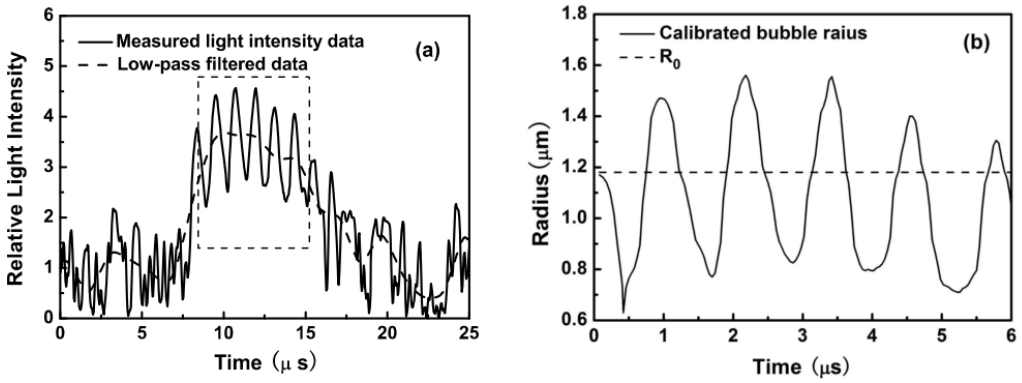

Figure 2.1: Example of light scattering data (a) and the calibrated radius (b) from measurements of single microbubble response by Matula et al. using an adapted flow cytometer with a piezoelectric element driven at 1 MHz. Figure taken from Matula et al. [38]

2.2. Experimental Set Up and Design

A schematic of the experimental set up is shown in Figure 2.2. The key components are the co-axial microfluidic flow focussing device, ultrasound transducer(s), laser diode and a PMT. The system is submerged in a water tank to enable efficient acoustic coupling and temperature control. Manual positioning stages (model 443, Newport), secured to an external frame, allow precise alignment of the laser, microscope objective, microfluidic device and ultrasound transducer. The system has been designed to enable substitution of different ultrasonic and optical components, e.g. to be able to vary the frequency of ultrasound excitation or the laser source.

Measurements are performed as follows: i) particles are isolated and streamed into the focal zone of the laser, microscope objective and ultrasound transducer, ii) as a particle passes through the laser beam, light is scattered and detected by a PMT, iii) this triggers ultrasound excitation while the particle is still

in the laser beam and the resulting particle response can be recorded from the scattered light.

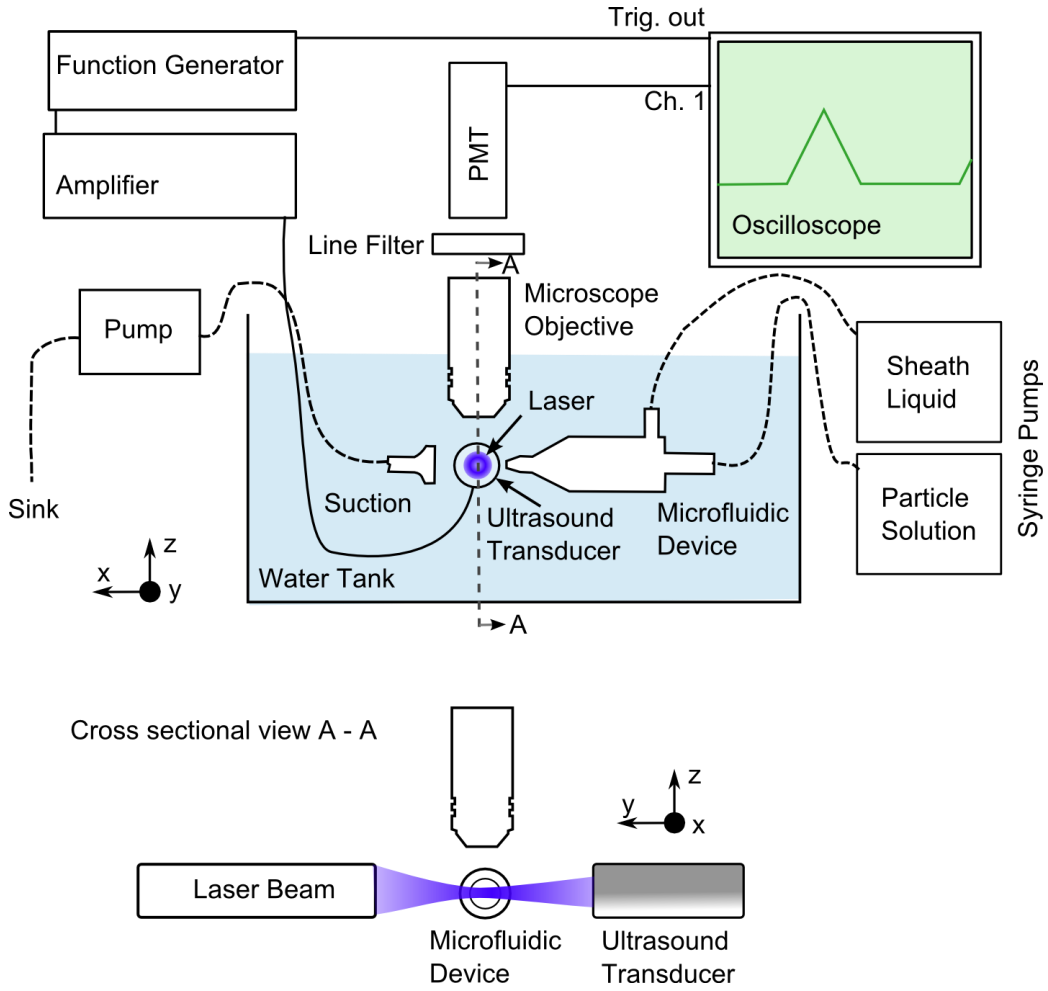

Figure 2.2: Schematic diagram (not in scale) for the characterisation of single microbubbles using light scattering. The co-axial device and suction element are shown in greater detail in Figure 2.4. Dotted lines indicate fluid flows.

It was found experimentally that the SNR, defined as the smallest change in microbubble radius detectable over the root mean square (RMS) of background signal, was acceptable given the following components: i) a 4.5 mW laser diode (405 nm, Thorlabs) focussed using a single plano-convex lens (f = 30 mm, #69-339, Edmund Optics) built into a water tight casing, ii) a 0.8 NA water immersible microscope objective (3 mm working distance, LUMPLFLN 40XW

Olympus) and iii) a 405 nm laser line filter (FB405-10, Thorlabs) to filter out unwanted sources of light. For the detection of scattered light a PMT with an inbuilt DC - 8 MHz low pass amplifier (H10493-003, Hamamatsu) was employed. PMTs provide a higher sensitivity in low light conditions with lower dark and gain noise than avalanche diodes, although care must be taken not to exceed the saturation limit above which point the relationship between light intensity and voltage is no longer linear.

Alignment of the laser, microscope objective and particle stream was achieved by maximising the PMT output on an oscilloscope (Waverunner 64Xi, Lecroy). Scattering of the laser beam from impurities in the water allows the focal plane of the microscope objective to be aligned with that of the laser, from which the maximum scattered light signal will be detected by the PMT. Size standard polystyrene microspheres were then added to the particle flow of the microfluidic device (see below) and the light scattering amplitude maximised by adjusting the position of the microfluidic device.

For the ultrasound excitation both focussed and unfocussed transducers can be used. At the scale of a single microbubble, unfocussed transducers produce an approximately plane wave, such that the pressure within the laser beam can be assumed to be uniform. Focussed transducers are required to achieve higher pressures (on the order of MPa) where the pressure field follows a Gaussian distribution, the width of which can be estimated from Eq. 1.2. The ultrasound beam -6 dB width must be sufficiently large, such that the variation in particle location in the focussed flow does not significantly alter the acoustic

pressure experienced by the microbubble. Provided this condition is met, however, the system offers considerable advantages over other techniques in which particle location and hence excitation pressure may be poorly defined [80]. Here, because the laser is used to trigger the ultrasound excitation, the location of the microbubble with respect to the optical and ultrasound foci is the same for each microbubble that is observed.

Microbubbles travelling through the laser beam are detected using a threshold on the oscilloscope. The threshold triggers when the gradient of the scattered light signal goes above an empirically chosen value. The dynamic range and threshold value on the oscilloscope can be manually adjusted during an experiment to capture differently sized particles. Once a particle is detected, the oscilloscope sends a trigger signal to the function generator (Agilent, model 33220A, Berkshire, UK) which in turn sends the desired driving wave form, amplified by 50dB (Electric and Innovation, model 325LA, Rochester, NY), to the ultrasound transducer. Since the speed of sound is significantly smaller than the speed of light, the acoustic wave will only reach the particle 10 – 30 µs later, for example Figure 2.3, depending on the transducer focal length. It is also important that microbubbles that have already been excited in the focal region of the ultrasound are excluded from subsequent measurements. This is achieved by setting a 'hold off' time on the oscilloscope to allow time for those microbubbles to pass, given a flow velocity of an estimated 0.2 m/s and a beam diameter of 10 mm, the hold-off time was set to 50ms, given a maximum throughput rate of 20 samples per second.

For calibration of the acoustic field a fibre-optic hydrophone (90 degree acceptance, Precision Acoustics, Dorset) can replace the microscope objective, and the acoustic field experienced by the microbubbles is measured by moving the tip of the fibre into the focus of the laser beam.

A further inherent advantage of this system is the ease with which unwanted particles, such as dust motes introduced from the water tank, can be excluded from analysis based on the time taken to pass through the laser beam. Since the flow velocity profile will be approximately parabolic, the time of travel can be used to determine where in the flow the particle is. Particles of interest will be travelling the fastest at the centre of the flow and take the least time to travel through the laser beam.

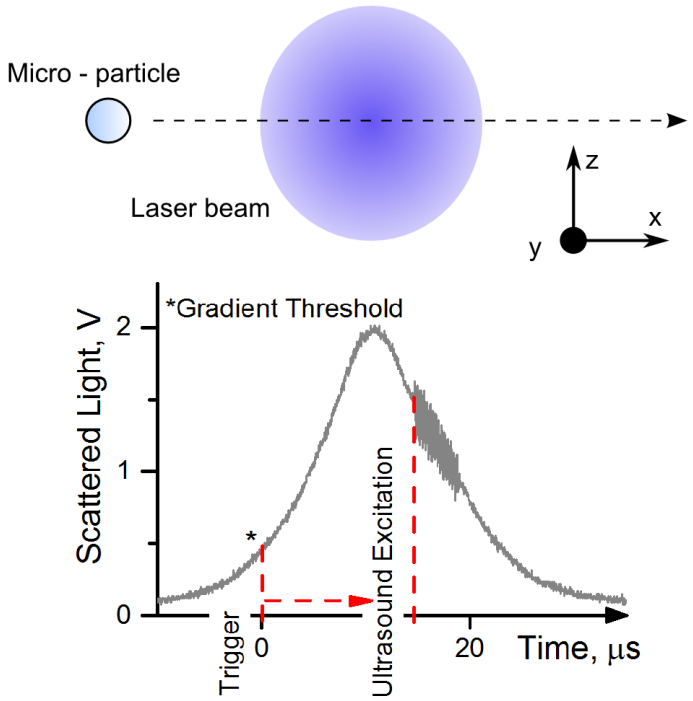

Figure 2.3: Illustration of particle detection and ultrasound excitation. Ultrasound excitation is triggered from a gradient threshold (in the scattered light signal) as the particle enters the laser beam. After a short delay the ultrasound wave reaches the particle while it is still traversing the laser beam and the resulting volume oscillation is recorded. Data shown is of a SonoVue® microbubble.

2.2.1. Co-axial microfluidic device for microbubble isolation

As discussed previously, isolation of microbubbles away from physical boundaries and each other is achieved using a hydrodynamically focussed flow [81], [83], [84]. To enable this, a custom microfluidic co-axial focussing device was designed, Figure 2.4. An all glass device (fabricated by GPE Scientific) was selected to ensure concentricity of the nozzles, ease of cleaning and because it would allow for visualisation of the flow and detection of unwanted gas pockets.

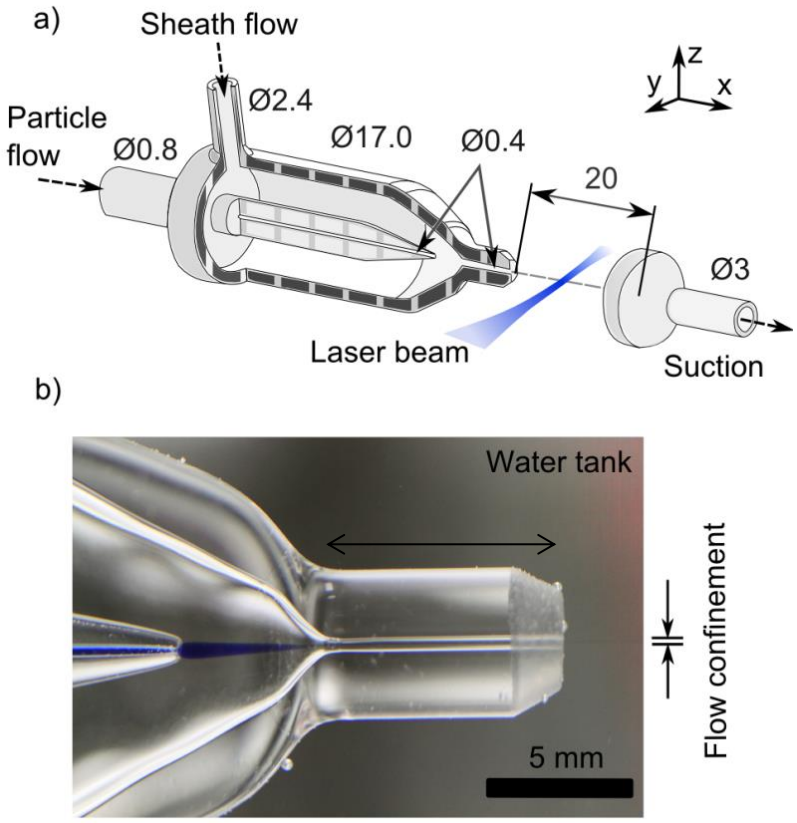

Figure 2.4: A microfluidic hydrodynamic focussing device for the isolation of echogenic particles in free space: a) Design of device with a suction element 20 mm away from the nozzle exit. All dimensions are given in mm and material is glass, surfaces are grounded and polished. b) Photograph of device to demonstrate focussing of inner flow stream (blue ink). Glass enables flow visualisation and checking for unwanted gas pockets that may otherwise disturb the flow.

The inner and outer diameters for the various elements were selected based on i) industry standard sizes to reduce cost, and ii) requirements for laminar flow. In particular, the length of the nozzle (indicated on Figure 2.4.b), was chosen to ensure a fully developed laminar flow by consideration of the entrance length, that is the distance required for the velocity profile to become constant [93]. Given a typical flow rate of 5 ml/min, and a nozzle diameter of 400 µm, the tube length had to be larger than 6.4 mm. For the operation of the microfluidic device, microbubbles are diluted to a concentration of the order of

10^5 particles per ml with filtered (0.2 µm) deionised water and placed in a syringe connected to the particle flow channel of the microfluidic device. Both the particle and sheath (filtered deionised water, degassed for sheath flow) flows are driven by syringe pumps (World Precision Instruments, model AL-1000, Sarasota, Florida).

Due to the nature of microbubbles, care must be taken during handling and loading into the microfluidic device. Air traps need to be added to the syringes to reduce flow pulsations and pressure waves that may arise from changing of flow rates or connecting tubing. During operation of the device the back pressure, ΔP, generated from a liquid with a kinematic viscosity, ν, and flow rate, Q, in tubing of length L is inversely proportional to the fourth power of tubing diameter *d*:

$$\Delta P \propto \left(\frac{QL\nu}{d^4}\right) \tag{2.1}$$

For the setup presented in this paper, not considering tubing connections, the maximum generated back pressure is of the order of a few Pascals. This is insignificant when compared to clinical ultrasound pressures and the physiological variation in human blood pressure of up to 120 mmHg (~16 kPa) [94].

2.2.2. Computational fluid dynamic simulations[3]

A three-dimensional numerical model was developed as a design tool to predict and characterise the fluid dynamic field and the trajectories of

[3] Method and description of computational simulations by Dr Dario Carugo

microbubbles exiting the microfluidic device. This proved to be particularly useful to verify if the microbubble's flow behaviour (i.e., position in the focussed stream and velocity) was compatible with the system's requirements for microbubble detection/excitation, under a range of different operational conditions (i.e., inlet flow rates and particle's physical properties). The model geometry was constructed and meshed using ICEM CFD 14.5 (Ansys Inc., USA). The geometry consisted of two components: i) the co-axial flow focussing device and ii) the suction element. A truncated cone was designed to join the two components, so as to model the outer fluid surrounding the focussed stream within the water tank (Appendix A1).

The geometry was meshed using tetrahedral elements (total number of elements = 4,914,892). A boundary-layer meshing strategy was adopted, with mesh element size reducing from the outer surfaces towards the focussed fluid stream. The transition in mesh element size was controlled by generating interior surfaces coaxially with the focussed stream (Figure A1.1b). The equations for mass conservation (Eq. 2.2) and momentum conservation (Eq. 2.3) were solved over the computational flow domain, using Ansys Fluent (version 14.5, Ansys Inc., USA):

$$\nabla \cdot (\mathrm{v}) = 0 \tag{2.2}$$

$$\rho \frac{\partial \mathrm{v}}{\partial t} + \rho \mathrm{v} \cdot \nabla \mathrm{v} = -\nabla \mathrm{P} + \mu \nabla^2 \mathrm{v} \tag{2.3}$$

where v, ρ, μ and P are fluid velocity, density, dynamic viscosity and pressure, respectively. The working fluid was assumed to be incompressible and

Newtonian, with a density of 1000 kg m^{-3} and a dynamic viscosity of 0.001 Pa s. The flow was assumed to be steady and laminar. The Semi-Implicit Method for Pressure-Linked Equations (SIMPLE) algorithm was employed for solving the governing equations. A second order upwind discretisation scheme was adopted to discretise the momentum equations, and a second order scheme was adopted for pressure interpolation. Mass flow boundary conditions were applied at the inlets of the microfluidic device. An outflow boundary condition was applied at the suction element (flow rate weighting = 1). In order to reproduce the effect of fluid suctioning generated by the vacuum pump, a mass flow inlet boundary condition was applied at the surface of the truncated cone joining the microfluidic device with the suction element. This flow rate was set equal to the difference between the total flow entering the microfluidic device and the flow exiting the suction element (which was experimentally defined). Walls were assumed to be rigid, with a no slip flow boundary condition.

A simplified, one-way discrete phase model was adopted to predict the microbubbles' flow behaviour. The model included the contribution of Saffman lift force. A suspension of microbubbles was injected from the central inlet of the microfluidic device. Microbubbles' diameter followed a Rosin-Rammler distribution [95], with minimum diameter = 1 µm, maximum diameter = 15 µm, mean diameter = 3.5 µm, and spread parameter = 0.8. A custom built MATLAB (R2012a, The Math Works Inc.) script was used to process the numerical data and determine the radial position and velocity of microbubbles exiting the microfluidic device.

2.3. Calibration Procedures

2.3.1. Flow and particle confinement

Calibrations were performed to investigate the effect of sheath and particle flow rates on the upstream microbubble confinement. Standard pen ink was added to the particle flow solution and the resulting ink flow diameter 6 mm downstream from the exit of the microfluidic device was measured optically. Images were captured by replacing the PMT with a USB camera (DCU224M, Thorlabs) in line with the 40X microscope objective (see Figure 2.2). Images were then processed using ImageJ (NIH, USA) [96] to measure the width of the ink flow, Figure 2.5. Since a particle's trajectory may differ from the fluid path lines due to differences in densities and the effect of lift forces, SonoVue® (Bracco Diagnostics) microbubbles were then added to the particle flow and their trajectories filmed at 50,000 frames per second (fps) using a high speed camera (Memrecam HX-4, NAC), in place of the USB camera. Snapshots from the video are shown in Figure 2.6. The video was processed offline using ImageJ, where the microbubbles were tracked using the MosaicSuite (MOSAIC Group, Dresden) plugin for ImageJ.

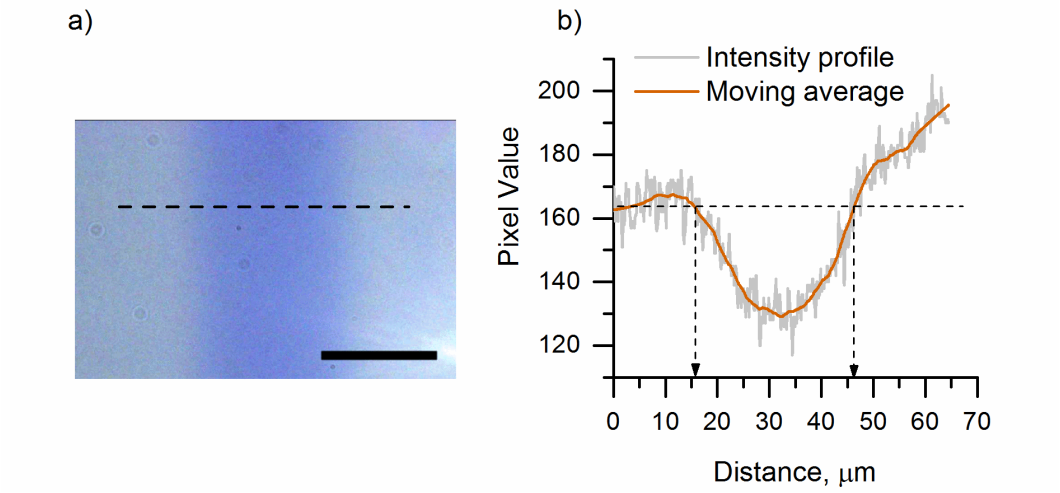

Figure 2.5: Example measurement of the confinement width of ink added to the particle flow. a) shows the raw image, where the scale bar represents 25 µm. b) shows the processing method to estimate the confinement width based on the moving average of the signal. Note glare artefact on bottom right of image due to poor lighting conditions meant that a threshold was set only based on the average values to the left of the ink.

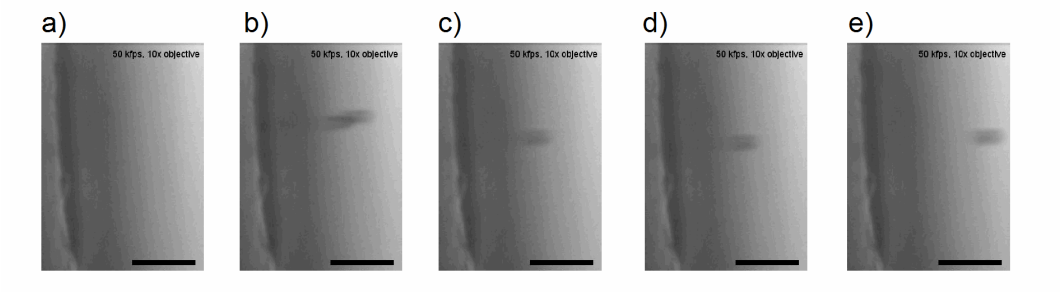

Figure 2.6: Snapshots from high speed imaging of SonoVue® microbubbles flowing through the microfluidic device, the exit of which can be seen on the left of the images. (a- e) are images of different microbubbles. Scale bar represents 40 µm.

2.3.2. Sizing sensitivity

To assess the sensitivity and accuracy of the optical set up, samples of three different size standard polystyrene microspheres (Polysciences, Int.) with mean diameters of 0.9, 4.52 and 11 µm, were diluted and added separately to

the particle flow. To prevent inter-particle clustering, 0.1 ml of Tween 20 (Sigma Aldrich) was added to the microsphere solutions (3 ml). Sheath and particle flow rates were set to 5 ml/min and 30 µl/min, respectively, for all runs. The dynamic range of the oscilloscope was set for each different size such that the light scattering intensity was at least three quarters of the available range. As described previously, scattering events were recorded on the oscilloscope once a manually set gradient threshold was reached. Data were then transferred to a PC and the maximum voltage of each trace measured using a custom written MATLAB (R2012a, The Math Works Inc.) script. Mie Scattering simulations were performed for comparison to experimental results, using refractive indices of 1 and 1.6 for water and polystyrene respectively, a laser wavelength of 405 nm and an aperture of 80^{o} perpendicular to the laser beam (corresponding to the 0.8 NA of the objective used).

2.4. Calibration Results

2.4.1. Hydrodynamically focussed flow confinement

The confinement of ink downstream of the co-axial microfluidic device was assessed to optimise the sheath and particle flow rates. The focussed flow was observed to be stable in the open water tank between the microfluidic device and suction element approximately 20 mm away. Ink was first added to the particle flow and the downstream flow confinement was measured for particle flow rates from 10 to 60 µl/min and sheath flow rates of 3 to 9 ml/min,

Figure 2.7. The smallest confinement in the y axis (optical imaging limited to 2D) of the ink was 12 µm (particle and sheath flow rates of 10 µl/min and 9 ml/min respectively) with control up to 57 µm. Fluid streamlines were also determined computationally, and good agreement with the experimental results was observed (solid lines) validating the use of the computational model to investigate the confinement of particles.

Further, the jet was observed to be stable in videos captured during the measurement of ink confinement. An investigation was also performed to check jet stability in the presence of ultrasound and microbubbles, for which the jet remained stable at peak negative pressures of around 400 kPa, (5 cycles, and 3.5 MHz and pulse repetition rate of 1 kHz).

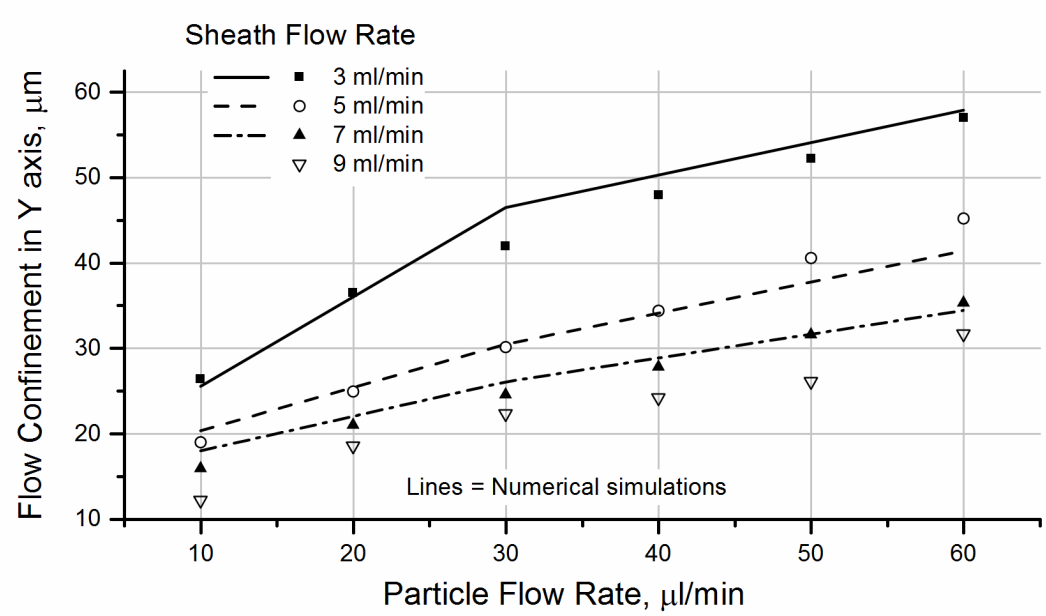

Figure 2.7: Effect of sheath and particle flow rates on the hydrodynamic flow confinement 6 mm downstream from the exit of the microfluidic device. Numerical simulations (lines) are reported together with the experimental points (symbols).

2.4.2. Hydrodynamically focussed microbubble confinement

High speed imaging was used to observe a variation in particle position along the y axis of 33.3 µm using SonoVue® microbubbles 6 mm downstream from the microfluidic device (particle and sheath flow rates of 20 µl/min and 3 ml/min respectively). Figure 2.8b shows the superimposed paths of individual bubbles from multiple runs. Diluted polystyrene microparticles were also observed at the exit of the device to verify that the particles were isolated from each other. Numerical simulations were then performed to predict particle trajectories and velocities under a wider range of experimental conditions, providing a useful tool to fully characterise the system's performance. Simulations of the particle's confinement (Figure 2.8c) agreed well with the high speed camera observations and demonstrated that the particles were more tightly confined along the z axis (Figure 2.8a), possibly an effect due to gravity. The z axis confinement is more important for assessing the sensitivity to variation in a particle's location; along the y axis the laser beam intensity varies with the focussing of the laser beam, this is however far more gradual than the variation due to the Gaussian beam as seen along the z axis (Figure 2.3). Computational simulations showed that the mean particle velocity varies linearly with sheath flow rate (from 0.23 to 0.68 m/s at sheath flow rates of 3 and 7 ml/min) and it is not significantly affected by the particle flow rate. Particle velocity determines the time taken to pass through the laser beam and can therefore be used to estimate the laser beam diameter at the intersection with the particle's trajectory.

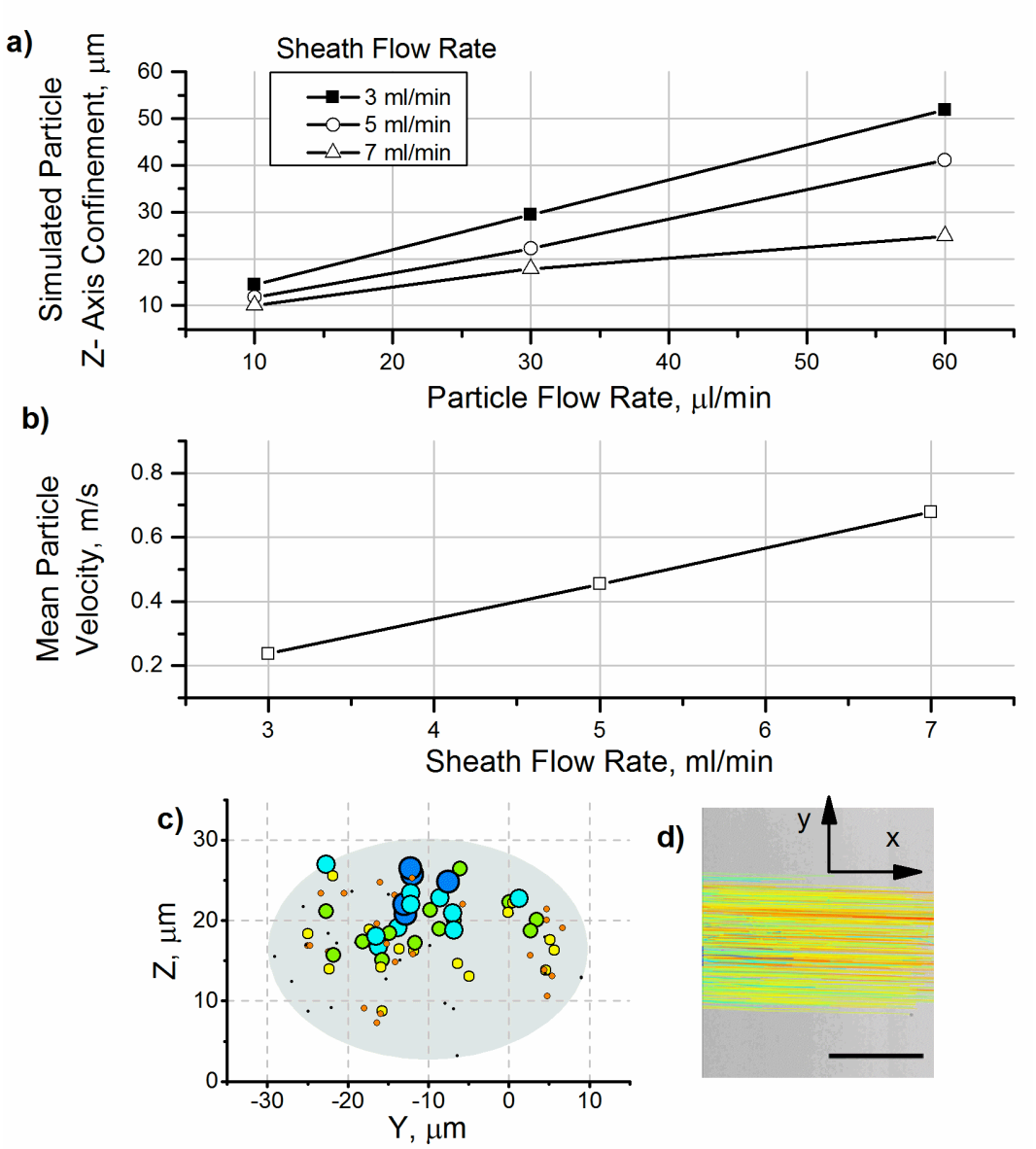

Figure 2.8: *Simulations from particle tracking (density 1.331 kg/m^3, radii between 1 to 15 µm with a mean radius of 3.5 µm).* ***a)*** *Confinement of particles in z axis, where confinement is the largest distance between two particles* ***b)*** *Particle velocities as a function of outer flow rate.* ***c)*** *Example of particle spatial spread (n = 93) upstream, 6 mm away from the nozzle exit, particle radius is represented by the marker size, larger microbubbles tend towards the top of the distribution due to the likely combined effect of buoyancy and lift forces. Outer flow rate = 3 ml/min, inner flow rate = 20 µl/min.* ***d)*** *Experimental data of SonoVue® microbubbles at same flow conditions at c, recorded using a high speed camera at 50 kfps, each line represents the path of a single bubble which could be compared with the simulated trajectories. Scale bar = 20 µm.*

Notably, the numerical results show that under a range of different operational conditions and particle dimensions: i) particle confinement can be restricted down to 10 µm for accurate sizing within the laser beam, ii) particle velocity enables ultrasound excitation while the particle is still traversing the laser beam, and iii) it is possible to adjust the particles' confinement by finely controlling the flow rate ratio between the two inlet lines, at high throughput total flow rates.

2.4.3. Sizing calibration

Measurements from size standard microparticles were compared with Mie Scattering simulations to assess the sizing sensitivity and accuracy of the apparatus (Figure 2.9). Light scattering from the microparticles was found to agree well with Mie theory predictions and the standard deviation in light scattering (vertical bars) was also in agreement with the standard deviation in microparticle size (horizontal bars). This provided the means of calibrating the system for sizing of gas cavities and to assess the accuracy of the technique.

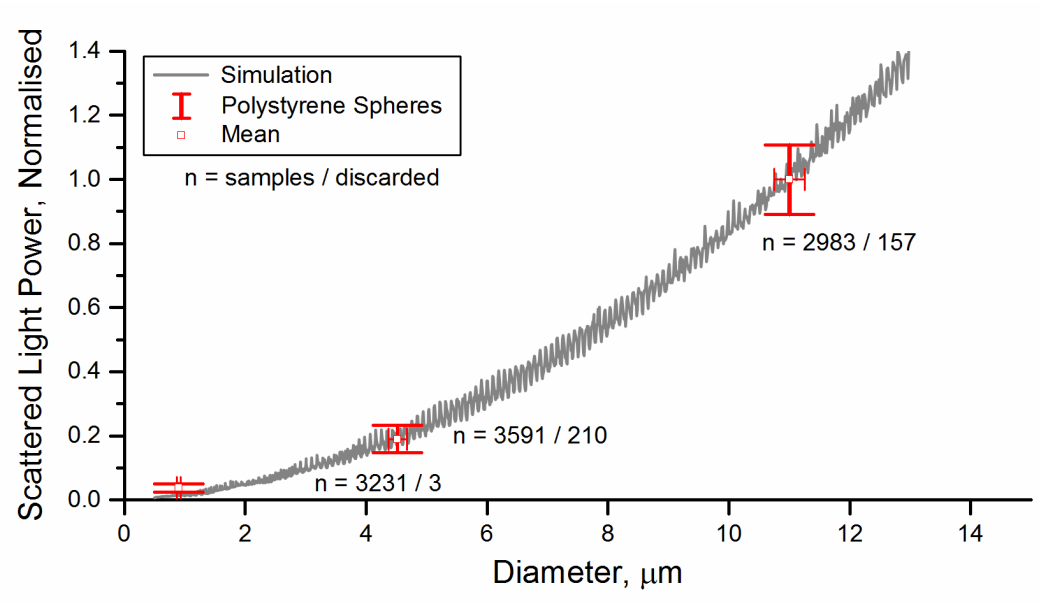

Figure 2.9: Sizing and sensitivity calibration using size standard polystyrene microparticles. Light scattering results (vertical red bars represent ± standard deviation in light scattering intensity, horizontal red bars represent standard deviation in microparticle size from manufacturer's specification) are compared to Mie Scattering simulations of the polystyrene microparticles (refractive indices of water = 1 and microparticles = 1.6, unpolarised light at 405 nm, 80^{o} aperture). Discarded samples refer to particles outside of the normal transit time through the laser beam. The scattered light intensity is normalised with respect to the Mie Scattering estimation for an 11 μm microsphere.

2.5. Uncertainty Analysis

2.5.1. ADC quantisation

Quantisation of the analogue light intensity signal from the PMT will introduce an error proportional to the 8-bit oscilloscope's (256 levels) dynamic range. This presents an inconvenience for the detection of oscillations that are significantly larger than the size of the microbubble. Assuming a linear relationship between scattered light intensity and microbubble size, the theoretical uncertainty, assuming a dynamic range such that light scatter due to

the microbubble size fills 50% of the available range gives an error of 0.78% of particle radius.

2.5.2. Spatial sensitivity

Spatial sensitivity refers to the error generated due to variation in a particle's location in the laser beam. Referring to Figure 2.4, a microbubble travelling parallel to the x axis could experience displacement in either the y or z planes that would cause uncertainty in the measurements. Assuming the laser intensity is a Gaussian distribution, the variation in laser intensity along the y axis can be estimated by calculating the focal depth of field which is the distance between which the Gaussian beam width (ω_0) increases by $\sqrt{2}$ [97]:

$$DOF = \left(\frac{8\lambda}{\pi}\right)\left(\frac{F}{D}\right)^2 \tag{2.4}$$

Given the optical components used for this study (Focal length, $F = 30mm * Refractive\ index \cong 40mm$ and collimated beam diameter, $D = 2\,mm$) the DOF is approximately 400 µm, i.e. ± 200 µm from the minimum beam waist. Therefore, given that the intensity along the beam axis is proportional to the beam width, the variation in laser intensity as a function of the distance from the focal point, y, can be approximated by:

$$\Delta I_y = 1 - \left(\frac{1}{1 + \left(\frac{2y}{DOF}\right)^2}\right) \tag{2.5}$$

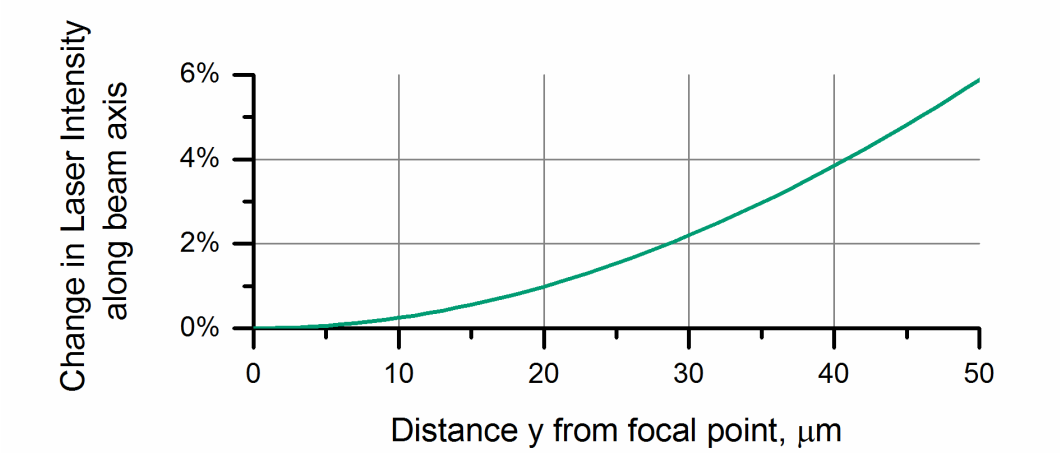

Figure 2.10: Estimation of change in laser intensity with distance along beam from focal point, or point of minimum beam width. Calculated from Eq. 2.5 where DOF is equal to 400 μm.

The variation in laser intensity along the beams direction (y-axis) shown in figure 2.10, shows that for a microbubble confinement of 20 μm, the variation in laser intensity would be approximately only 1%. Along the y-axis, displacement will also occur due to i) radiation forces due to the ultrasound excitation and ii) a microbubble's dipole response. Given the relatively small contribution of the dipole response as modelled by Allen, *et. al.* [98] and the translation due to radiation force experimentally observed to be on the order of microns by Dayton *et. al.* [99] at similar ultrasound conditions to this study, although much higher pulse repetition rates of 1 kHz, the spatial variation along the y axis can be assumed to be negligible.

However, in the z-axis the variation in laser intensity is of much greater significance. Given a variation of *z* μm and assuming that the laser intensity is a Gaussian distribution, where ω_0 is the Gaussian beam radius. The variation in laser intensity, *I*, can be estimated as

$$\Delta I_z = 1 - \exp\left[-\frac{2z^2}{{\omega_0}^2}\right] \tag{2.6}$$

The uncertainty in laser intensity, for estimating the gas cavity size, can be reduced therefore by increasing the laser beam width to reduce the effect of a particle's spatial variation. A larger beam also provides more time to interrogate a particle as it travels through, however the maximum intensity and hence the SNR will be reduced.

Variation in a particle's confinement in the z axis will lead to uncertainty in the laser intensity and subsequently the estimated microbubble's radius. Using Mie theory the uncertainty has been estimated for varying laser beam width and microbubble confinement, Figure 2.11. The typical operating conditions for experimental work given the set up described in this chapter are shown by the dotted orange box. To achieve a suitable SNR, the -6 dB width of the laser beam used in this apparatus was measured to be around 100 µm giving an estimated uncertainty of 5% - 15% for a flow confinement under 20 µm. The noise floor, given as the maximum RMS noise measured from the SonoVue® samples, was approximately 100 nm when converted to radius using Mie Scattering theory.

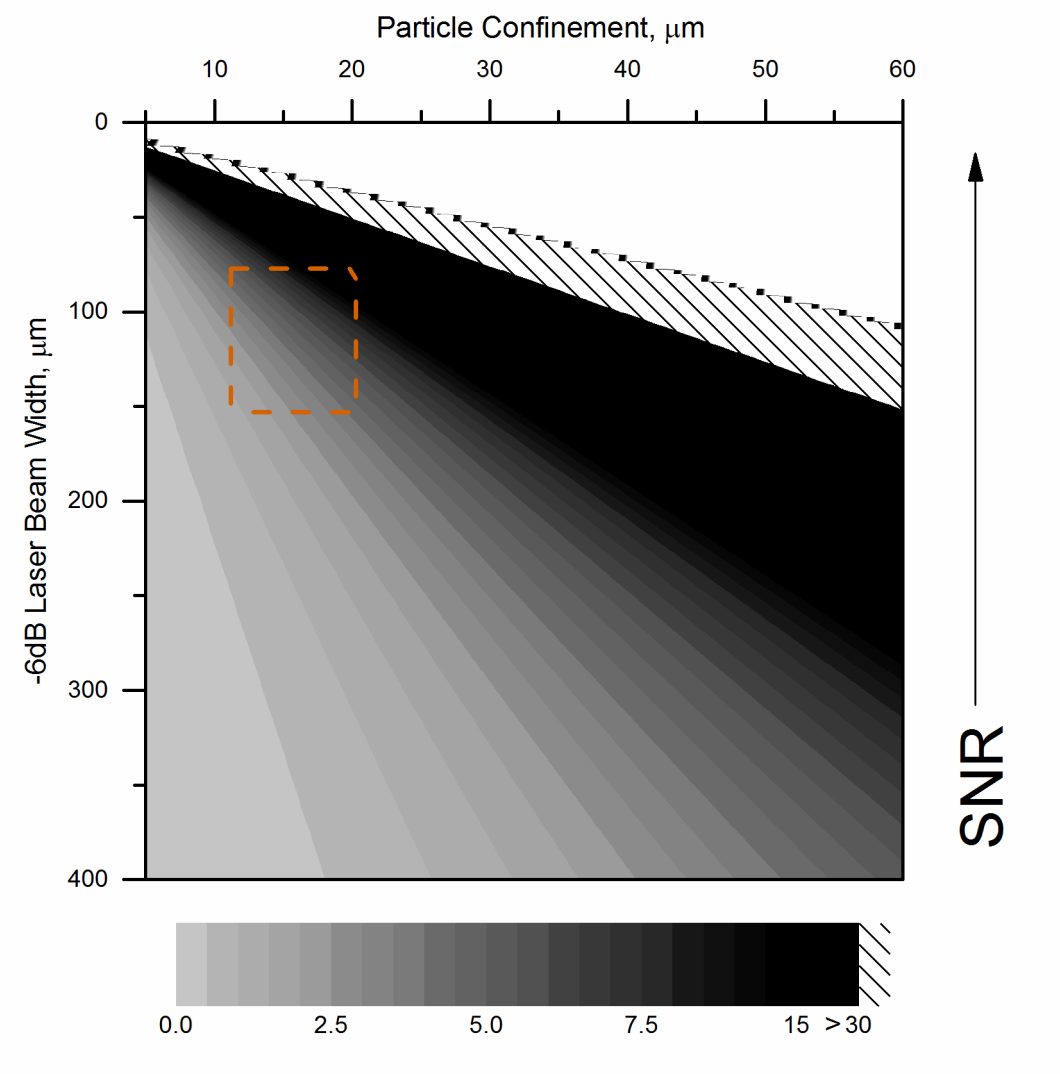

Figure 2.11: Theoretical uncertainty in microbubble radius estimation due to the variation in a particle's confinement while travelling through a Gaussian laser beam. Conditions are shown for varying laser beam width and particle confinement.

2.5.3. Measurement of ultrasound field

As mentioned previously, the focussed laser beam allows for accurate positioning of the hydrophone to measure the acoustic field at the interrogation site. The error in acoustic calibration due to spatial location is therefore assumed to be negligible provided that the acoustic beam width is significantly larger than the laser beam width. The largest uncertainty is unfortunately inherent in the

hydrophone calibrations which come with a standard ± 10 – 15% uncertainty. For the experimental results shown in this work the same hydrophone (Precision Acoustics 500 µm Needle Hydrophone) has been used throughout when calibrating ultrasound pressure. To ensure the accuracy of the Precision Acoustics® hydrophone, it was compared to a recently purchased Onda® hydrophone (HNP, 500 µm aperture diameter) that had been calibrated within the previous month. The absolute error between the two hydrophones are within approximately 20% of each other for the range of frequencies investigated, Figure 2.12.

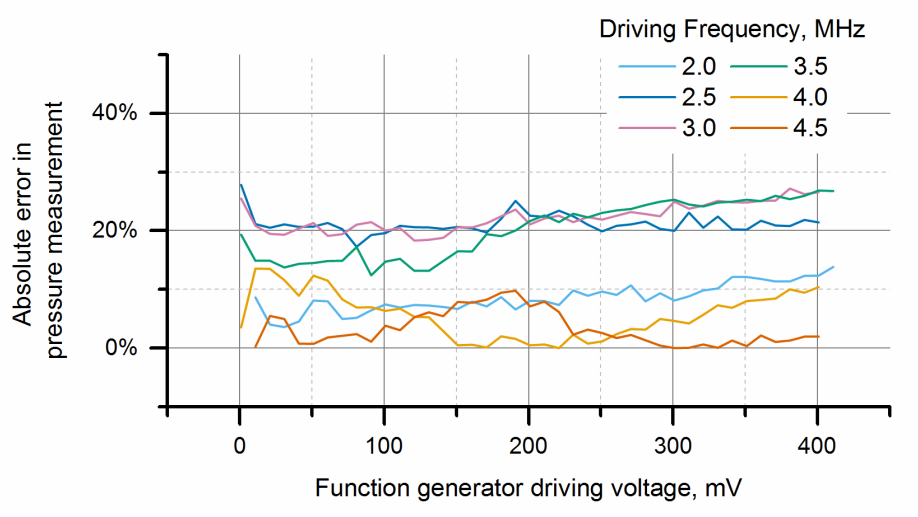

Figure 2.12: Absolute error in the measurement of peak negative pressure as a function of the driving voltage between the hydrophone used in this study and a second reference hydrophone.

2.6. Design Evaluation

The aim in developing the rig described in the preceding sections was to satisfy the design criteria, set out in Section 2.1, specifically:

1. Microbubble isolation: Use of the hydrodynamic focussed flow technique, by design and construction of a glass microfluidic device (Figure 2.4), has shown to achieve excellent upstream microbubble isolation from physical boundaries and from each other (Figure 2.6).

2. High throughput: By virtue of the technique used individual microbubbles can be measured at high throughput rates, limited only by the data collection rate of the oscilloscope. From typical experiments, the number of suitable samples obtained in an hour is around n > 10,000.

3. Low uncertainty: The isolation technique has been shown to be able to confine microbubbles to within 10 – 20 µm. Demonstrated both experimentally (Figure 2.7) and using numerical simulations (Figure 2.8). This has potential for very low uncertainties of around 1 – 3 % error in the radius estimation (Figure 2.9). Unfortunately, for the laser power used a suitable SNR could only be achieved at small laser beam widths, resulting in an increase in the sizing uncertainty of up to 15 % for a microbubble confinement of 20 µm.

The novelty of this design is primarily the custom designed and calibrated glass microfluidic device for streaming of single microbubbles through the laser and ultrasound beams.

Theory, Data Analysis Protocol and Methods

This chapter presents an overview of the theories describing a microbubble's interaction with ultrasound and plane wave light. This leads to the development of a robust protocol for the analysis of the light scattering data obtained using the device in Chapter 2. Finally, supplementary methods are presented to support the findings from the light scattering data, including a custom built microscopy hydrostatic pressure chamber and quantitative fluorescence microscopy techniques.

As described in Chapter 2, the microfluidic device is capable of obtaining the light scattered from individual microbubbles during ultrasound excitation at up to 20 samples per second. Typical experiments lasting a few hours produce over 100,000 samples to analyse, for which a robust protocol is required to efficiently sort and from which to obtain useful metrics. However before analysis, the light scattering intensity data must be converted to radius and for that an understanding of the underlying theory is required. This chapter is split into three sections that describe the i) theory of microbubble interaction with

ultrasound and light, ii) protocol for analysis of light scattering data obtained from the device and iii) supplementary and complimentary methods of microbubble characterisation.

3.1. Theory

3.1.1. Modelling the nonlinear response of an uncoated microbubble

A model for an uncoated bubble undergoing spherical oscillations was first derived by Lord Rayleigh [100] and later adapted, to include the effect of surface tension and the surrounding liquid's properties, by various contributors to become the Rayleigh Plesset Noltingk Neppiras Poritsky (RPNNP) equation [101] :

$$\rho_L\left(r\ddot{r}+\frac{3}{2}\dot{r}^2\right)=P_g\left(\frac{r_0}{r}\right)^{3\kappa}+P_v-P_{stat}-\frac{4\mu_L}{r}\dot{r}-\frac{2\sigma}{r}-P_\infty(t) \tag{3.1}$$

$$\text{Where } P_g=\frac{2\sigma}{r_0}+P_{stat}-P_v$$

Here the dot notation represents the time derivative, where P_v and P_{stat} are the vapour and hydrostatic pressures respectively. $P_\infty(t)$ is the externally applied time varying pressure field, ρ_L and μ_L are the surrounding liquid density and dynamic viscosity, respectively; r is the instantaneous bubble radius and σ is the surface tension.

The RPNNP equation is subject to the following assumptions:

- The bubble remains spherical

- There is negligible heat or mass transfer across the bubble-liquid interface
- The surrounding liquid is incompressible
- Internal gas is ideal and polytrophic
- The wave length of the incident ultrasound field in the surrounding liquid is sufficiently large compared to the size of the bubble at all times that the pressure can be considered uniform

These assumptions may hold for small amplitude oscillations, however, at larger amplitudes the compressibility of the surrounding liquid must be considered to take into account energy lost through radiation damping [102]. Models such as the Trilling [103] and Keller-Misksis [104] incorporate linear compressibility of the surrounding liquid with a finite speed of sound and are commonly used for the study of the violent inertially driven collapse of microbubbles.

3.1.2. Modelling the response of coated microbubbles

As discussed in Section 1.2, microbubbles can be encapsulated with a coating (such as polymers or lipids) that makes them stable enough to be used as Ultrasound Contrast Agents. However, the coating also modifies the surface tension and viscosity at the gas-liquid interface and thus alters a microbubble's response to ultrasound excitation when compared to the equivalent sized uncoated microbubble.

There is evidence that the properties of a microbubble's coating are in-homogenous and in a constant state of flux. For example, Borden *et al.* [105], used fluorescence microscopy to visualise the coating structure of phospholipid

(PEG : DSPC) microbubbles (Figure 3.1), and found it to be highly dependent on the cooling rate and lipid composition. Further, several studies have observed the discharge of lipids, termed lipid shedding, during ultrasound excitation [65] and with increasing temperature [106] suggesting that there is constant rearrangement of the lipids within the coating.

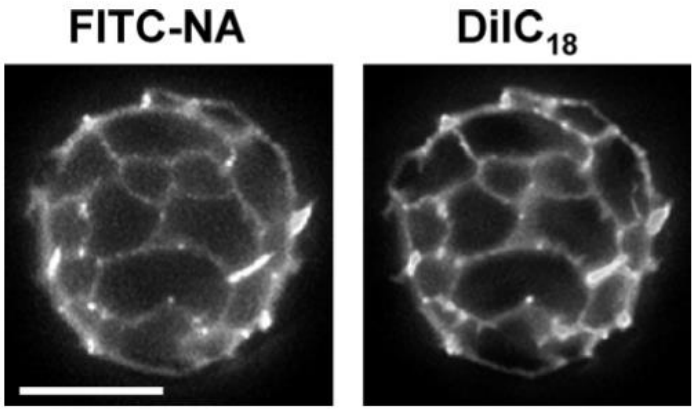

Figure 3.1: Evidence of phase separation of phospholipid microbubbles not accounted for in current theoretical models. Scale bar equals 10 µm. Figure and caption adapted from Borden et al. [105]

The most widely used models for encapsulated microbubbles are modified versions of the Rayleigh-Plesset equation such as those derived by de Jong *et al.* [107], Church [11], Hoff *et al.* [56], and Sarkar *et al.* [108]. The microbubble coating is treated as an incompressible thin visco-elastic spherical shell characterised by a viscosity (μ_s) and shear modulus (G_s). This approach may be more suitable to describe the behaviour of polymer and protein coatings, however it cannot account for phenomena observed in high speed studies of phospholipid microbubbles, such as threshold behaviour and compression dominated responses (discussed in Section 1.4.2). Marmottant *et al.* [109]

proposed a model that could account for both of these phenomena by taking into account a relationship between surface tension and the phospholipid surface concentration (originally proposed by Glazman [110]). In this model, compression dominated responses occur due to an asymmetry of the surface tension during compression and expansion. During compression the coating buckles and the surface tension reduces, however during the expansion phase the surface tension rises rapidly as the coating becomes elastic again. Likewise, for expansion dominated behaviour, once the coating has ruptured the surface tension decreases on expansion and subsequently increases during compression. The model features three behaviour regimes; buckled, elastic and ruptured as shown in comparison to microbubble surface area and surface tension in Figure 3.2 below.

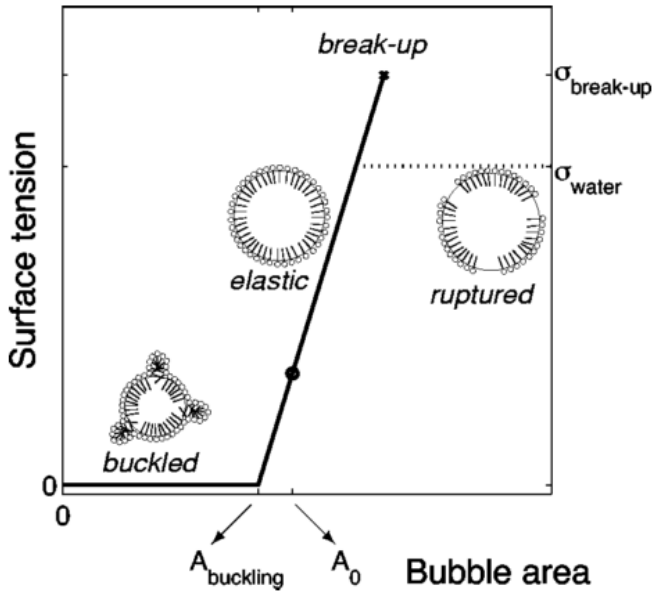

Figure 3.2: Behaviour regimes of phospholipid microbubbles as modelled by Marmottant et al. A relationship exists between the surface tension and surface concentration. Figure taken from [109]

Further, models have been proposed that treat the coating as a continuum with more realistic rheological properties, avoiding the need for defined regimes as in the Marmottant model. One such model by Stride [111], considered the effect of surface concentration on not only the coating's elasticity but also the viscosity. Significantly, Stride derived the coating's interfacial tension based on insoluble molecular films rather than mechanical constitutive laws. As with the Marmottant model, Stride's model predicts similar compression dominated behaviour and increased non-linearity at low ultrasound driving pressures. The effect of a coating on a microbubble's predicted resonance frequency is clearly shown from Stride's model, Figure 3.3.

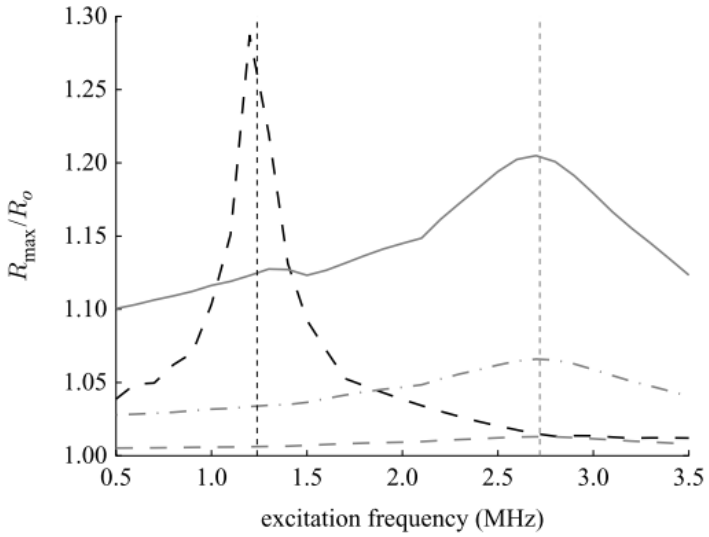

Figure 3.3: Resonance curves predicted by Stride's model for a 2.5 µm microbubble shows that uncoated microbubbles (black dashed line) have a much more pronounced resonance at a lower frequency compared to coated microbubbles (grey solid and dashed lines, ranging from driving peak negative pressures of 10 kPa, 50kPa and 150 kPa). Figure and caption adapted from Stride [111].

Stride, however, also identifies that there are no suitable empirical measurements to validate or inform the models. It is apparent that the development of theoretical models has been driven largely to account for observations from high speed imaging studies. However, as discussed in Chapter 1, there are several limitations in the high speed imaging studies that are not being accounted for in the theoretical models (such as boundary interaction and variability of response due to small sample numbers). The device presented in Chapter 2 overcomes these challenges and the results can hopefully be used, in conjunction with previous observations, to better inform theoretical models. As mentioned in Chapter 1, the prediction of a microbubble's response to ultrasound is one of the key challenges for the optimisation of CEUS imaging.

3.1.3. Conversion from radial response to scattered pressure

For ultrasound imaging it is not the radial response of a microbubble that is of interest but rather the resulting scattered pressure that will be detected by a receiving transducer. The scattered pressure produced by a spherically oscillating microbubble can be predicted from potential flow theory, as in the derivation by Hilgenfeldt *et al.* [112]:

$$P_{Scatter}(r,t) = \rho_L \left(\frac{r}{R} (r^2 \ddot{r} + 2r\dot{r}^2) \right) \tag{3.2}$$

This equation represents the *active* far field contribution to the scattered pressure caused by a change in volume of the microbubble. There is also a *passive* contribution caused by the impedance mismatch presented by the microbubble, however the latter is insignificant when compared to the *active*

contribution and can be ignored for the purposes of ultrasound imaging [112]. Interestingly, the scattered pressure is a function of the microbubble wall velocity and acceleration and therefore it cannot be assumed that the radial response is representative of the scattered pressure. For example, Figure 3.4 shows a comparison between the respective power spectra of the radial and scattered pressure responses. Here it can be seen that as the oscillation amplitude increases, the nonlinear frequency components are under-estimated if only observing the radial power spectra (orange lines).

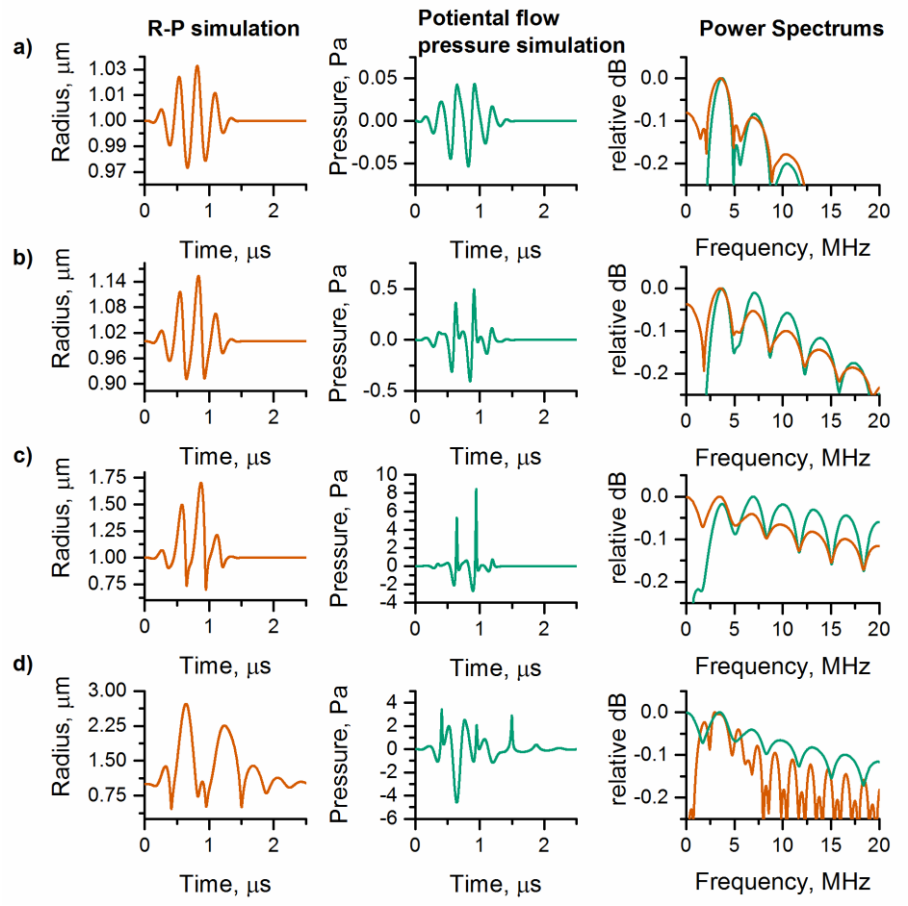

Figure 3.4: Predicted radius- time curves using the Modified Rayleigh-Plesset equation, scattered pressure and respective power spectra at varying peak negative driving pressures and coating thickness (a: 0.1 MPa, b: 0.4 MPa, c: 1 MPa and d: 1 MPa with λ = 10nm). Unless stated otherwise coating parameters are: Elasticity= 50 MPa, viscosity: 1 Pa.s and coating thickness = 20nm)

3.1.4. Scattering of light from microbubbles

As discussed in Chapter 2, the magnitude of the scattered light can be used to estimate a microbubble's radius before, during and after ultrasound excitation. Given the set up described in Chapter 2, incident photons scattered onto the PMT are converted to an electrical current by a process known as the photoelectric effect. The PMT consists of a series of dynodes that increase in positive potential, causing photo electrons generated at the photocathode to accelerate between dynodes and on impact 4 or 5 more electrons are emitted for each initial electron. This cascading effect is able to produce gains of up to 10^8 times at the anode, controllable by adjusting the bias voltage applied to the dynode chain. The gain for an incident electron is given as:

$$G = \delta^n \tag{3.3}$$

Where δ is the secondary emission ratio and n is the number of dynodes.

Thus the scattered light intensity, I_{Scat}, is converted to a voltage that, for the experimental set up in Chapter 2, is given by:

$$V_o = \Omega \cdot \mathrm{G} \cdot E(\lambda) \int_{\theta_{min}}^{\theta_{max}} I_{Scat}(\lambda, r, \theta)\ d\theta \tag{3.4}$$

Where G and $E(\lambda)$ are the PMT gain and radiant sensitivity [mA/W] respectively. The light collected over an angle of θ is converted to a current which multiplied by the system's resistance, Ω, gives the voltage as measured on the oscilloscope, V_o.

3.1.5. Mie Scattering

The scattering of plane wave light from dielectric spherical particles of radius, r, can be described by Mie Scattering theory. At particle sizes approximately 1/10th of the incident wavelength the simpler Rayleigh Scattering can be used, where the Rayleigh criteria is given by the size parameter $\alpha \ll 1$ where $\alpha = \frac{2\pi r}{\lambda}$. For the scatter of visible light from a microbubble the size parameter is much larger than 1 and requires Mie Scattering theory to predict the scattered light intensity.

A brief overview of Mie Scattering is given here, for a more detailed description see [113]. The scattered light intensity, $I_{Scat}\ [W/m^2]$, at the angle θ to the direction of incident light is equal to a fraction of the initial intensity, I_0, multiplied by the differential scattering cross section, σ'_{Scat}, of the particle.

$$I_{Scat}(\theta) = I_0 \frac{1}{R^2} \sigma'_{Scat}(\lambda, r, \theta) \tag{3.5}$$

The scattered light intensity thus reduces by the square of the distance from the particle, *R*, however this can be compensated for by increasing the aperture, i.e. integrating over θ. The scattering cross section, σ'_{Scat}, for unpolarised light is given as the average of the two angular intensity functions, i:

$$\sigma'_{Scat} = \frac{\lambda^2}{8\pi^2}(i_1 + i_2) \tag{3.6}$$

The intensity functions describe the scattered light at the scattering angle, θ:

$$i_1 = \left| \sum_{n=1}^{\infty} \frac{2n+1}{n(n+1)} [a_n \pi_n(cos\,\theta) + b_n \tau_n(cos\theta)] \right|^2 \quad (3.7)$$

$$i_2 = \left| \sum_{n=1}^{\infty} \frac{2n+1}{n(n+1)} [a_n \tau_n(cos\,\theta) + b_n \pi_n(cos\theta)] \right|^2$$

Where π_n and τ_n are the angular dependent functions expressed as Legendre polynomials. The parameters a_n and b_n are functions of the size parameter,α.

If the entire cross section of the particle is considered over all angles then the scattering cross section is given as:

$$\sigma_{Scat} = \frac{\lambda^2}{2\pi} \sum_{n=0}^{\infty} (2n+1)(|a_n|^2 + |b_n|^2) \quad (3.8)$$

However, in the set up presented, it is only possible to collect over a finite angle range of less than ± 90 degrees. If the aperture is too small then a highly nonlinear response with respect to light scattering intensity and particle size is produced. By increasing the aperture from 1 degree to 80 degrees (approximately the acceptance angle for the objective used in this study), a monotonic curve is obtained that can then be used for accurate sizing as shown in Figure 3.5.

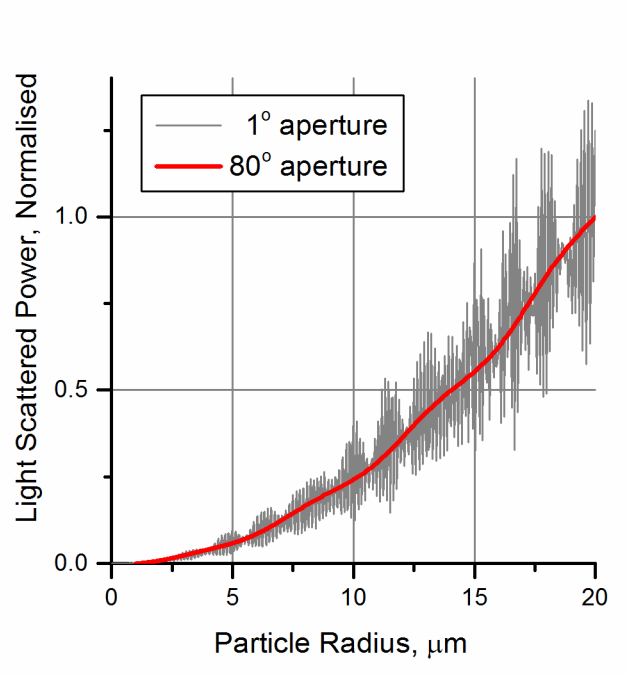

Figure 3.5: Mie Scattering simulations of the scattered light power (normalised to the scatter from a 20 μm sphere) vs. microcavity radius (in μm) and light collection aperture. Increasing the aperture provides a monotonic relationship suitable for experimentally estimating a microbubble's radius. Freely available software, Mie Plot by Phillip Laven [114]*, was used to create this figure.*

2.1.5.1. Mie Scattering considerations

Mie Scattering theory does not include the effect of a particle's coating on the light scattering, however previous work by Marston [73] has suggested that in the case of surfactant stabilised bubbles the coating effect is negligible since its thickness (10 – 20 nm) is much smaller than the light wavelength.

The sizing of nanoparticles, i.e. particles much smaller than the optical wavelength, using light scattering is feasible [115] and less complex using Rayleigh Scattering. However, due to the sixth power dependency on the particle size it is limited to higher power optical equipment and is not possible with the system described in this study. The device presented in Chapter 2 is however

able to measure the micrometre sized gas bubbles that may be intentionally produced by nanoparticle cavitation nuclei.

3.2. Data Analysis Protocol

The following section describes the analysis protocol for the light scattering data obtained from the microfluidic device. An overview of the protocol is given for reference in Table 3.1. The protocol is executed using custom MATLAB scripts and has been written to be robust to variation in experimental conditions, for example changing laser profile shape. For the complete processing of the output from a typical experiment (~100,000 samples) the script takes roughly 5 - 6 hours (3.30 GHz processor, 16 GB RAM running windows 7), the code, except for file handling procedures, is included in Appendix A2.

Step	**Description**
3.2.1. Sample selection	Criteria are imposed to filter out samples not suitable for analysis
3.2.2. Sizing	The light scatter intensity of suitable samples is converted to radius based on a Gaussian fit and a transfer function calculated in step 3.2.1.
3.3.1. Categorisation of response to ultrasound excitation	Each radial response is categorised based on the magnitudes of its expansion and compression phases, as well as initial and final radius.
3.3.2. Quantitative Measurements	Measurements are made of the expansion ratios and estimation of the scattered pressure

Table 3.1. Overview of analysis protocol for light scattering data

It was observed during experiments that adjusting the oscilloscope's dynamic range to capture smaller microbubbles resulted in some measurements exceeding the dynamic range of the oscilloscope. These samples were discarded, while only accounting for at most 30% of the entire population at the highest pressures tested; an attempt to interpolate the clipped data is discussed in Appendix A3. Fortunately, the clipped samples do not represent a population that cannot be measured, as the same sized microbubbles and expansions can be measured when the dynamic range is increased.

3.2.1. Sample selection

As described previously, scattered light is measured from single microbubbles travelling through the focus of a laser beam. The laser beam typically has a Gaussian intensity profile, and as a consequence any particle travelling through the beam will recreate this profile in the light scattering intensity. Figure 3.6, below shows a typical trace obtained from a microbubble passing through the laser beam and then excited by ultrasound (grey line). A Gaussian curve is fitted to the light scattering data up to the point of ultrasound excitation, which gives an estimation of the scattered light intensity had the microbubble not been excited by ultrasound (orange line) and can be used for the selection of suitable samples based on three criteria:

i) Microbubbles are isolated and produce a Gaussian profile close to that of the size standard beads. The test for this is an R^2 error less than 0.97 (empirically determined) between the fitted profile (discussed below) and the light scattering data up to the ultrasound scattering event.

ii) Microbubbles are travelling along the centre-line of the flow. To test for this the -6dB width of the Gaussian profile must be within the standard deviation calculated for the size standard beads

iii) Ultrasound excitation occurs after the microbubble passes the peak laser intensity (centre of laser beam) and before it leaves the laser beam. This is tested by measuring the position of the ultrasound excitation as a portion of the time between the peak laser intensity and the -6dB point, the ultrasound excitation must occur within 3% - 120%. This criterion ensures that there is enough data to accurately fit the Gaussian profile and that the scattering event occurs while still traveling in the laser beam.

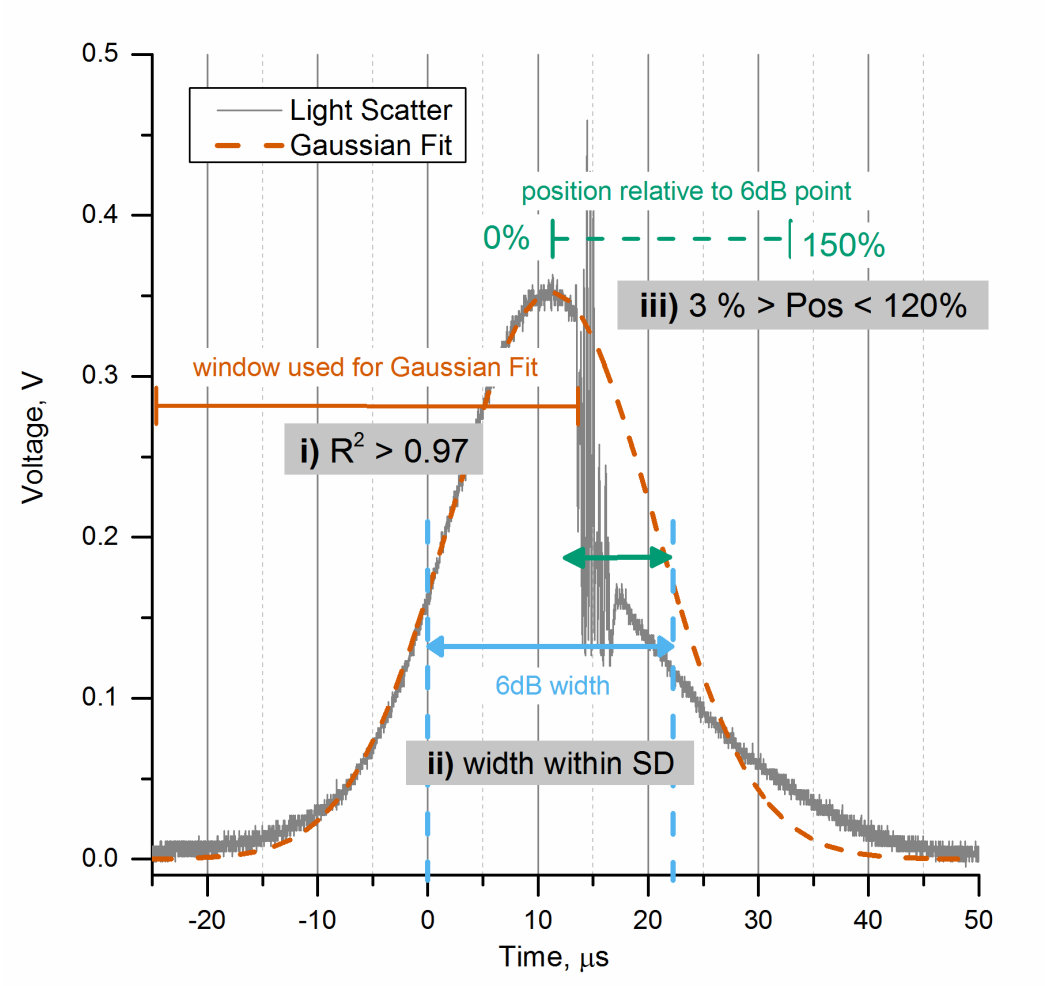

Figure 3.6: Selection criteria for filtering out samples that are not suitable for processing or have too large uncertainty. The criteria are i) the light scatter follows a Gaussian profile (r^2 value > 0.97), ii) the -6dB width of the Gaussian profile is within the standard deviation of all samples processed and iii) the scattering event occurs after the peak laser intensity and before the SNR is too low (empirically estimated). Samples that fit all of these criteria are then deemed suitable to be analysed. The change of slope after ultrasound excitation suggests that for this case (not typical) the microbubble continued to expand from its resting size.*

For the fitting of the Gaussian curve, it was found that the most robust fit could be achieved using a second order model, Eq. 3.9. This is able to account for a skewed Gaussian profile that occurs if the laser's elliptical axis is slightly off perpendicular to the travel of the microbubbles. The model is fitted using

MATLAB's *'fit'* function that solves for the constants $a_{1,2}, b_{1,2}\ and\ c_{1,2}$ using a least squares error method:

$$f(a_{1,2}, b_{1,2}, c_{1,2}, x) = a_1\, e^{-(\frac{x-b_1}{c_1})^2} + a_2\, e^{-(\frac{x-b_2}{c_2})^2} \tag{3.9}$$

However, there are two challenges: i) a second order model is prone to 'overfitting' and ii) only the light scattering data up to the point of ultrasound excitation can be fitted to, as it cannot be assumed a microbubble will stay the same size after ultrasound excitation. Therefore, to further ensure an accurate and realistic fit, limits are placed on the constants $a_{1,2}, b_{1,2}\ and\ c_{1,2}$. To estimate the limits, Eq. 3.9 is first fitted to the entire trace of each size standard particle going through the laser beam. This is usually around 1000 samples, for which a distribution of the fitting parameters is obtained. This distribution then represents the possible range of constants that produce suitable fits to the laser beam profile. The 25th and 75th percentile values for each constant are then used as upper and lower limits imposed when fitting the microbubble traces. Examples of fitted Gaussian profiles using this method are shown in Figure 3.7.

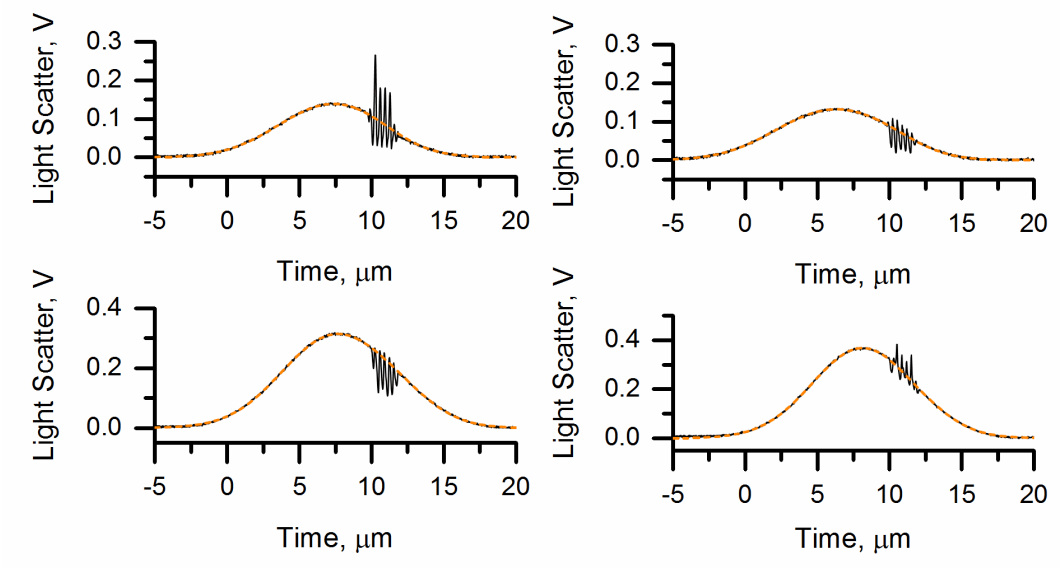

Figure 3.7: Examples of Gaussian model (dotted orange line) fitted to experimental light scattering data (black line). A second order model is used with constants constrained by estimations obtained from the light scattering intensity produce by size standard beads passing through the laser.

3.2.2. Sizing calibration

As discussed in Section 2.3, size standard beads can be used to calibrate the system based on the Mie Scattering theory described previously. The calibration proceeds as follows:

i) The mean maximum light scattering intensity from size standard beads of a given radius, *r*, is experimentally measured: $V_{SS}|_r$

ii) This value is compared to the simulated light scattered intensity that is calculated from Mie theory as a function of the radius, *r*, and index of refraction, η : $I_{Mie}(\eta)|_r$

$$k = \frac{I_{Mie}(\eta)|_r}{V_{SS}|_r} = \frac{1}{[V]} \tag{3.10}$$

iii) The simulated radius- light scatter intensity curve can now be divided by this factor to obtain a calibrated voltage – radius curve, Figure 3.8 below.

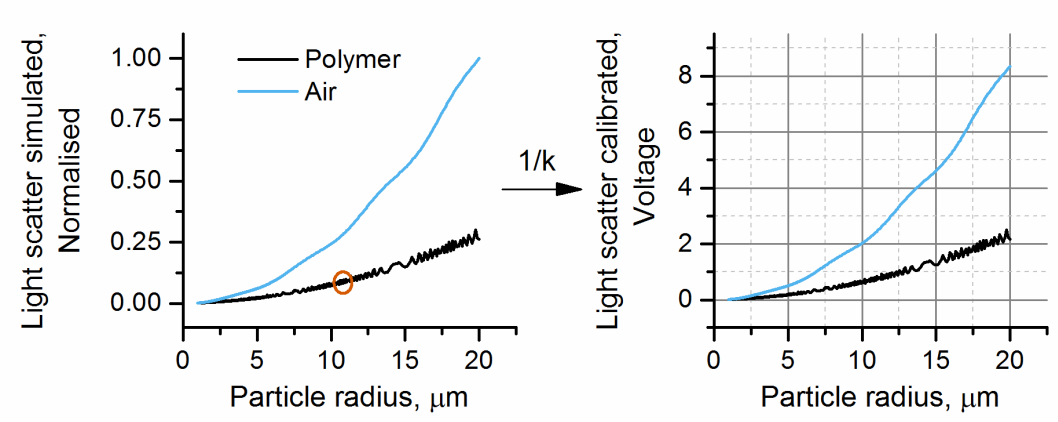

Figure 3.8: Calculation of the voltage to radius transfer function where k is given as the simulated light scatter divided by the mean voltage measured from the size standard particle with respect to the radius, see Eq. 3.10.

However, this curve is only calibrated for the peak intensity, i.e. when the microbubble is in the centre of the laser beam. Since the laser intensity is changing as the microbubble passes through, a further transfer function is required to account for this. Fortunately this has already been calculated, as the Gaussian profile fitted previously, Eq. 3.9, can be used to size the microbubble during any point in its passage through the laser, including during ultrasound excitation. However, it should be noted that the maximum SNR is achieved at the peak intensity of the laser and therefore it is desirable to time the ultrasound excitation such that it reaches the microbubble just after it passes through the point at which this this occurs.

3.3. Metrics

Once the samples have been filtered and calibrated from scattered light intensity to radius it is possible to perform analysis on each microbubble's response to ultrasound excitation. This is achieved by i) categorising each response based on its asymmetry, and ii) calculating the magnitude of the radial response and the corresponding scattered acoustic power. Both of these are important aspects in the understanding of how microbubbles respond to ultrasound and their application to CEUS imaging. As discussed previously, for all CEUS imaging techniques it is desirable to increase both the magnitude of the scattered pressure and the non-linearity of a microbubble's response.

3.3.1. Response categorisation

The method for assessing a microbubble's response asymmetry is as follows and demonstrated in Figure 3.9:

i) Detect minima of the expansion and compression phases (x)

ii) Compute the mean amplitudes (solid lines)

iii) Compute the ratio of expansion/compression using the following equation:

$$Asymmetry = \left(0.5 - \frac{\Delta r_{initial}}{\Delta r_{during}}\right) \times 100\% \quad (3.11)$$

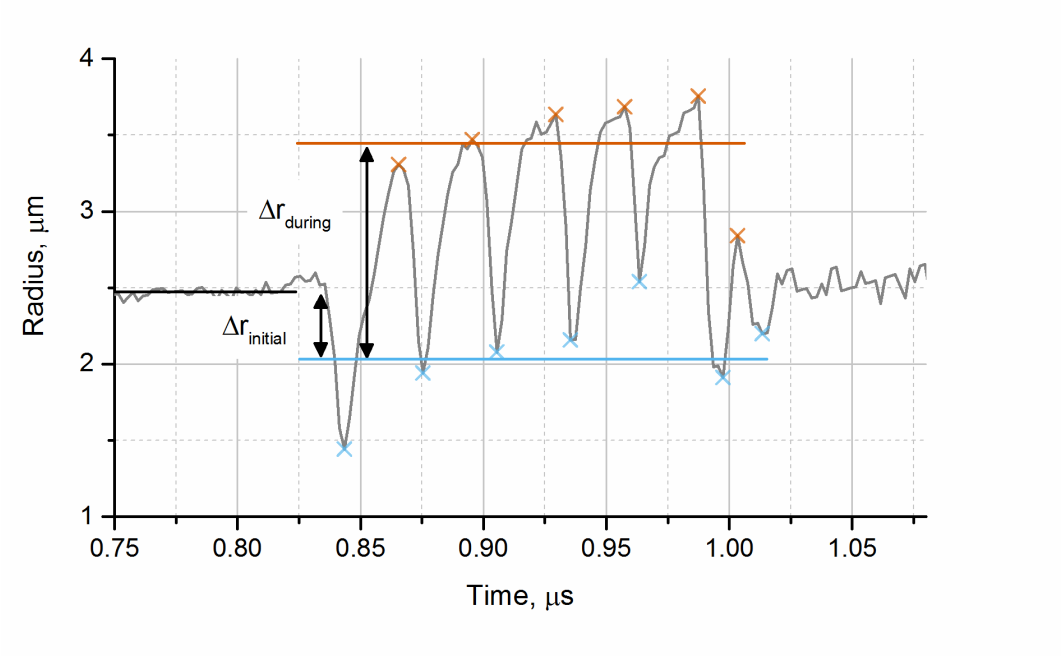

Figure 3.9: Metrics used for the classification of microbubble response to ultrasound excitation. Peak and trough detection (x) is used to estimate the mean amplitude of expansion and compression (solid lines). The ratio given above is then used to classify the response into, expansion/compression or symmetrically dominated classes.

For example, 0% represents a perfectly symmetrical radial response, > 0% is expansion dominated and less than 0% is compression dominated response. To account for noise, errors in the peak detection and the difficulty in accounting for change in the initial microbubble size after ultrasound excitation, thresholds were empirically set to categorise compression and expansion dominated behaviour at –25% and 25% respectively. The following figures show examples with the corresponding asymmetry values.

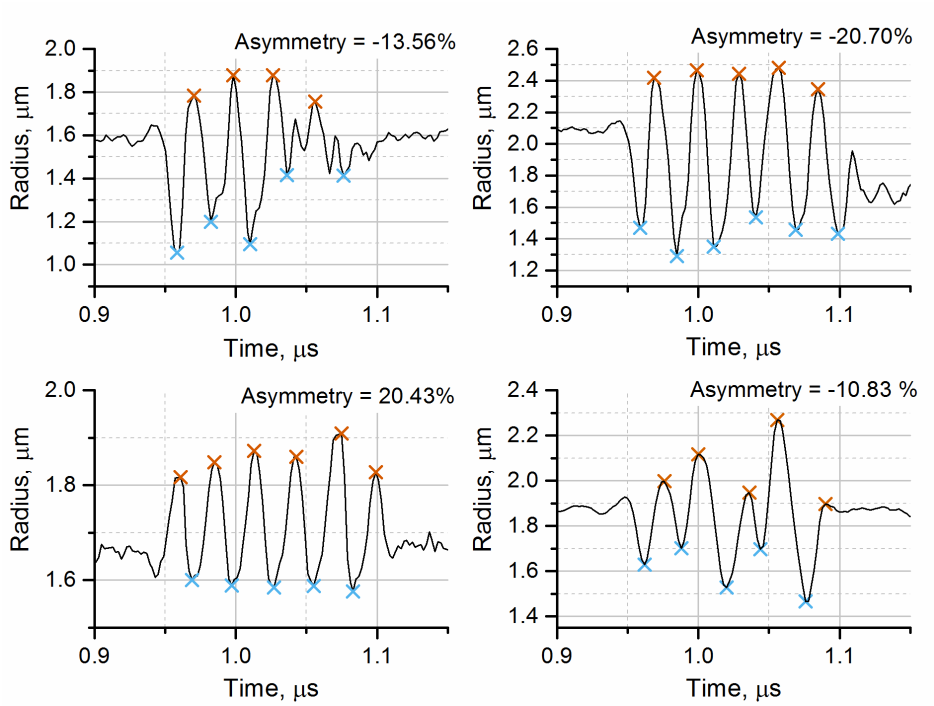

Figure 3.10: *Typical examples of symmetrical behaviour, based on asymmetry between -25% and +25%.*

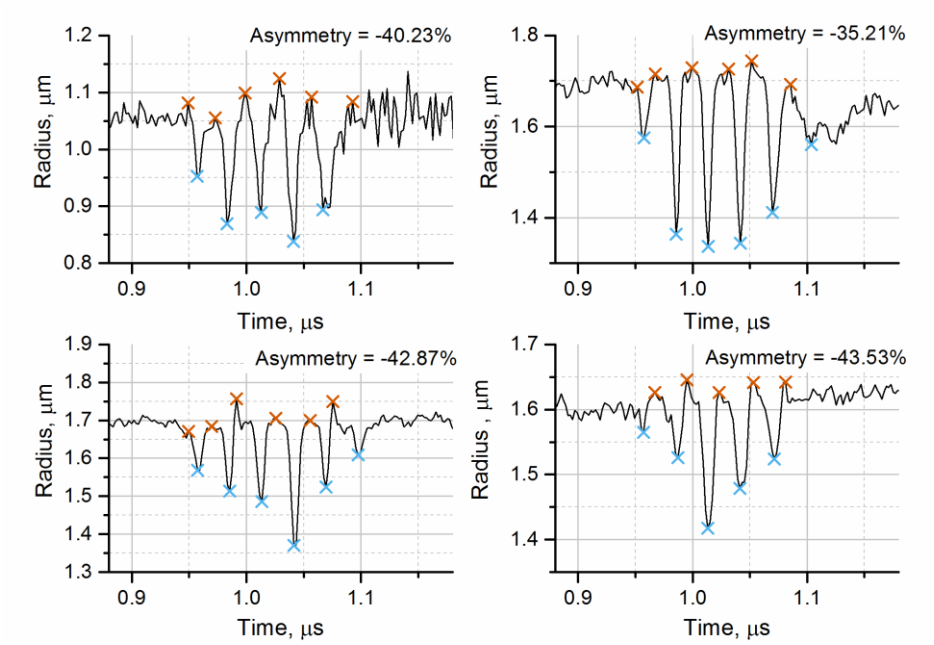

Figure 3.11: *Typical examples of compression dominated behaviour, based on asymmetry below -25%*

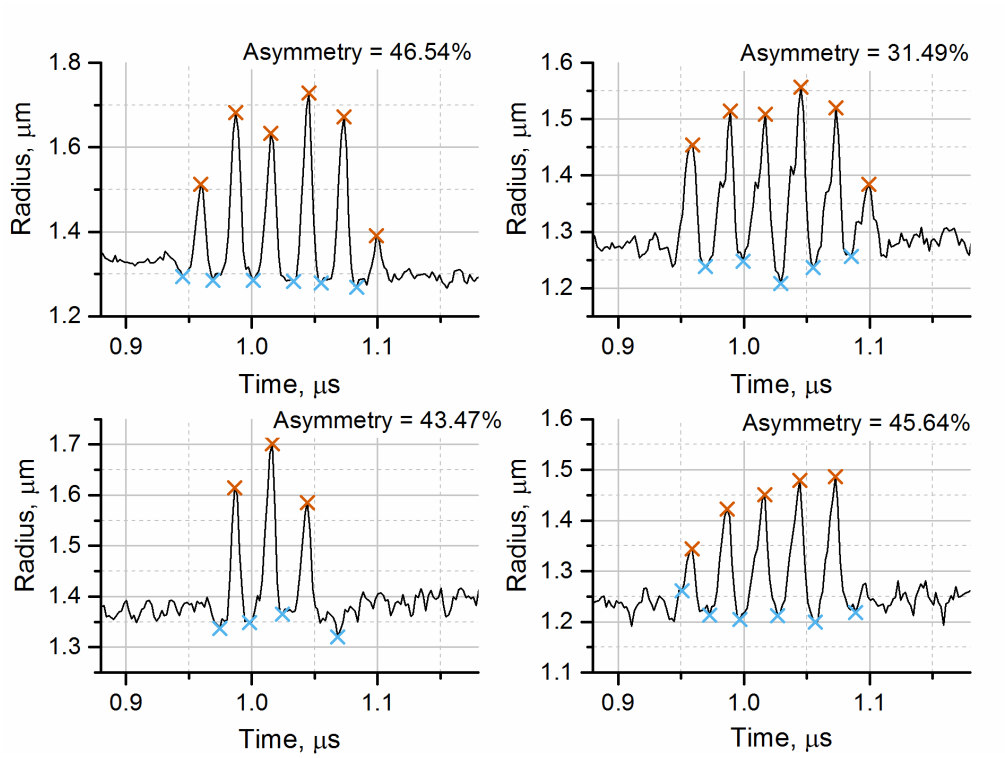

Figure 3.12: Typical examples of expansion dominated behaviour, based on asymmetry above +25%

Microbubbles also have the tendency to change size after ultrasound excitation. This makes the response categorisation more difficult. However, the approach given in Eq. 3.11, is fairly robust as it uses the initial radius of the microbubble. A further metric can be obtained based on the percentage change in radius over the course of the oscillations, Eq. 3.12, examples for which are shown in Figure 3.13.

$$\Delta r = \left(\frac{r_f}{r_i} - 1\right) \times 100\% \tag{3.12}$$

Where the subscripts i and f are the initial and final radii respectively.

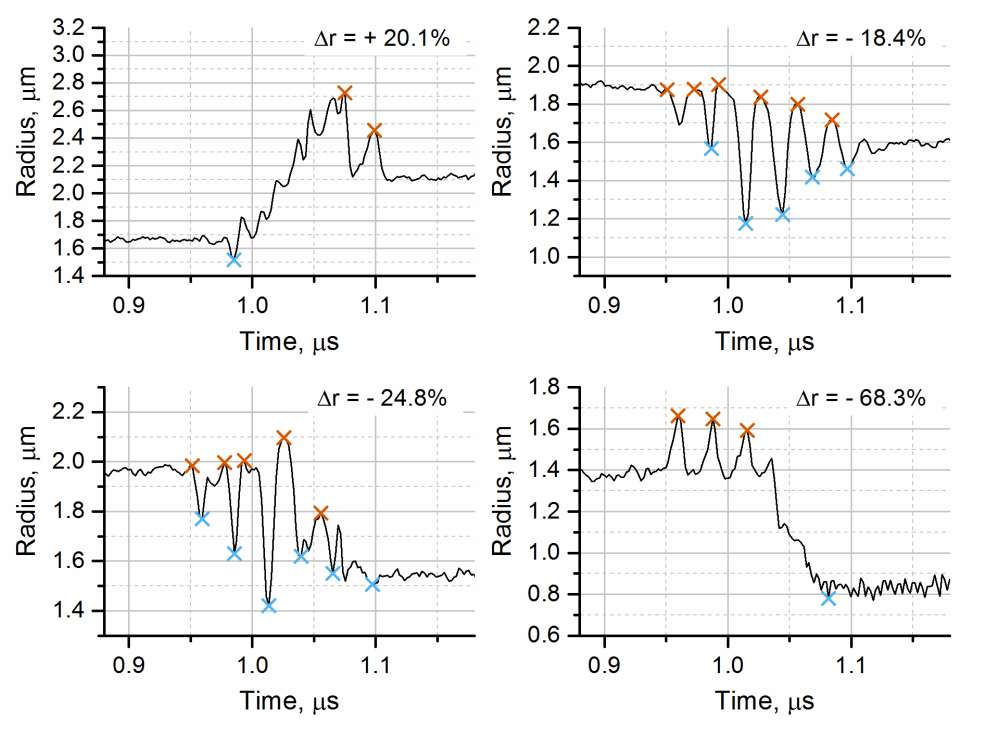

Figure 3.13: Examples of changes in resting radius, at higher pressures it is common to observe significant numbers of samples decreasing in size. Increases in size however only account for at most 1 – 3 % of the total responses.

3.3.2. Scattered pressure / echogenicity

The categorisation of individual microbubble responses provides useful information regarding what proportion of microbubbles in a population are undergoing a certain behaviour at a given frequency and pressure. It is also of interest to quantify the scattered pressure from each microbubble using Eq. 3.2 discussed previously in Section 3.1.3. Figure 3.14 shows examples of the conversion from radial response to scattered pressure and the corresponding power spectra using this method. Empirical measurements of the scattered pressure from single microbubbles was attempted, however, the sensitivity of the available hydrophones was not great enough and the poor SNR made it

difficult if not impossible to discern any signals originating from the microbubbles.

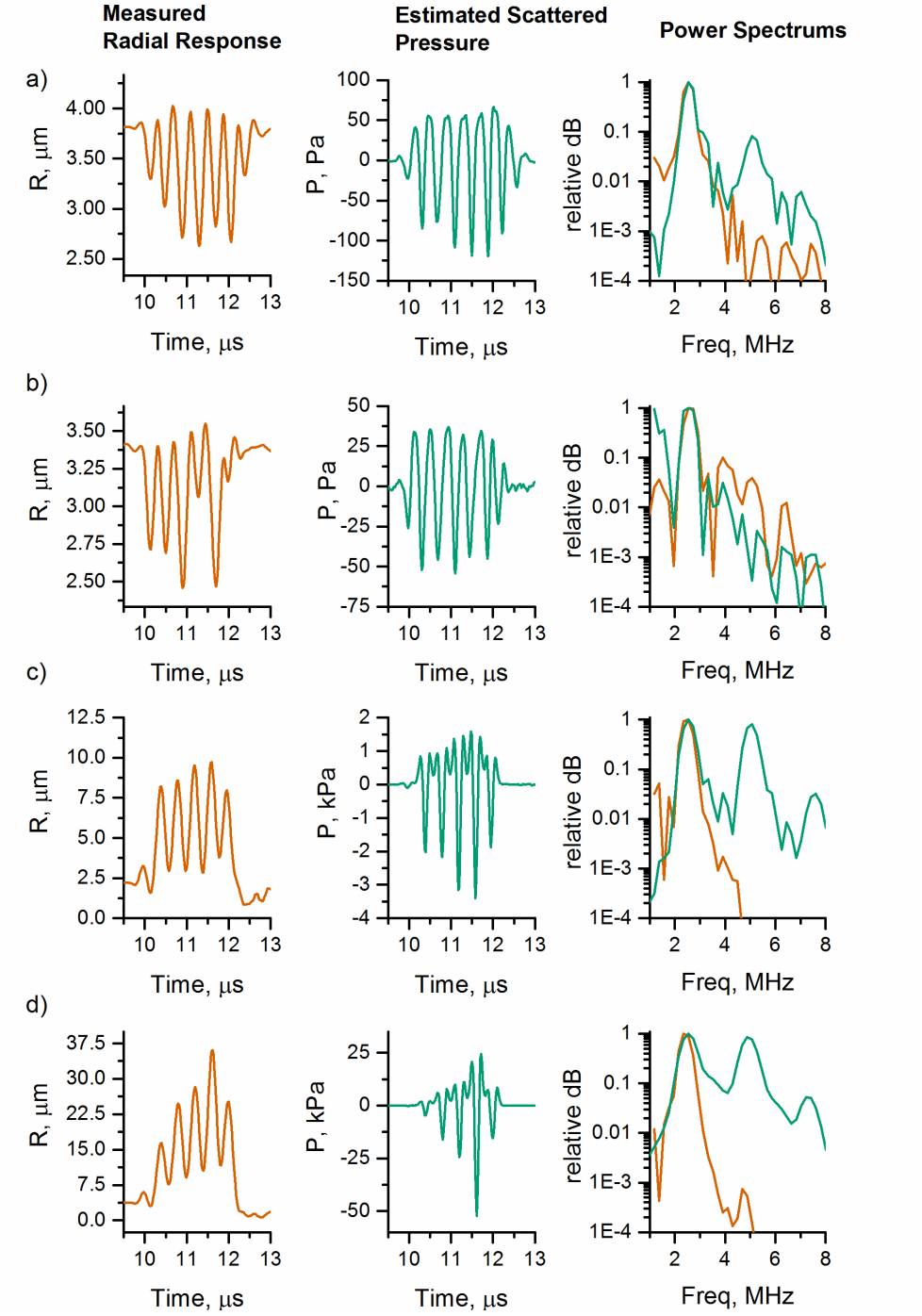

Figure 3.14: Examples of estimation of scattered pressure from measured radial time curves and the corresponding power spectra varying peak negative driving pressure: a and b) 40 kPa, c and d) 180 kPa. All responses are at a driving frequency of 2.5 MHz and the scattered pressure is estimated at a distance of 75 mm using Eq. 3.2.

3.3.3. Presentation of results and statistical analysis

As will be shown there is considerable variability in microbubble behaviour that makes it difficult to clearly and accurately present the distribution of responses. For this reason, the responses of individual microbubbles from a sample are presented either as:

i) Percentiles of the response distribution (5^{th},25^{th},50^{th},75^{th} and 95^{th}), to clearly represent variability
ii) Or only the median response, for clarity when comparing multiple parameters such as the ultrasound driving pressure.

Importantly, since this study is concerned with the behaviour of individual microbubbles in a given population, the median value and percentiles have been chosen over the more conventional mean and standard deviation/ confidence intervals. The confidence intervals that arise from experimental uncertainties are not shown since they are negligible when compared to the variability in microbubble response. The uncertainty and limitations of the results in this thesis are discussed in Section 6.1.

When investigating the effect of initial radius on a population's response, size categories are automatically calculated such that there is the maximum number of size bins with at least 100 microbubbles at each.

2.3.3.1. Statistical significance

Due to the unknown functional relationships of the many variables involved in the fabrication and behaviour of microbubbles (Figure 3.15), it would

be disingenuous to apply conventional statistical tests such as multivariate paired tests.

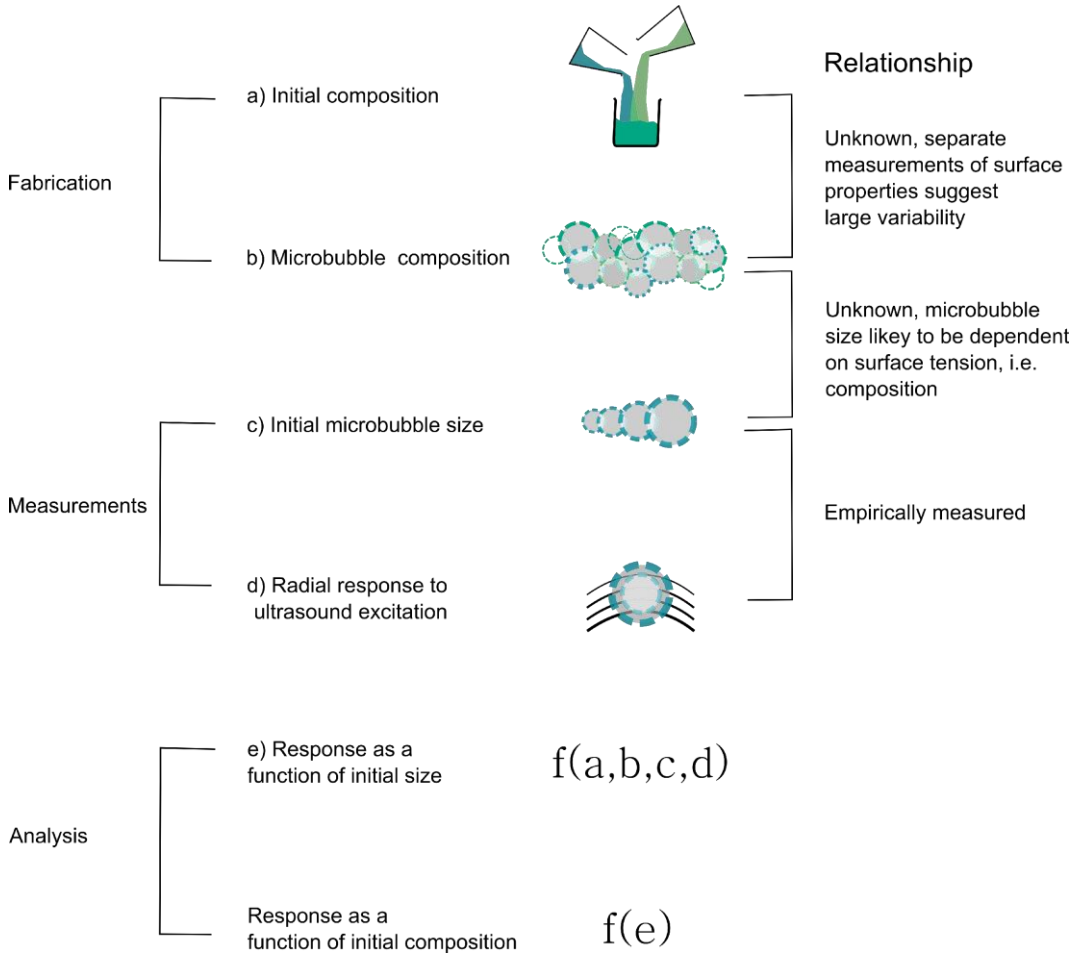

Figure 3.15: Schematic illustration of the unknown functional relationships between factors that influence microbubble response.

For assessing whether or not there is a significant difference between the responses of two microbubble populations therefore, reference is made to the degree of over lapping in the response distribution percentiles. A significant difference between two populations is defined as when less than 5% of responses in either population overlap.

2.3.3.2. Size distributions

It is important to note that the size distributions shown in this thesis do not represent the size distribution of the microbubble sample being tested, but rather the distribution of sizes measured during an experiment. The difference arises due to two factors: i) larger microbubble will tend to get stuck in the tubing, which is likely to be representative of the microbubble distribution after administration for CEUS imaging, and ii) the size of microbubbles measured is dependent on the threshold set on the oscilloscope which is manually varied during an experiment to account for the full range of microbubble sizes.

3.4. Supporting Methods

The following sections present the design and/or description of experimental methods used in this thesis to, alongside previous works, help to substantiate the findings from light scattering measurements obtained using the device in Chapter 2. The two methods utilised are i) a custom built quasi-static pressure chamber and ii) quantitative fluorescence microscopy.

3.4.1. Quasi-static pressure chamber design

A hydrostatic pressure chamber was built for this work as a further method of microbubble characterisation. Observing microbubbles under quasi-static conditions of changing hydrostatic pressure is able to give insight into the elasticity of a microbubble's coating, as well as to observe the variability between similar microbubbles under well controlled experimental conditions.

Although microscopy pressure chambers are common in biomedical research, there were no suitable 'off-the-shelf' options that met the requirements. To observe the effects of changing hydrostatic pressure on a microbubble's structure the following design criteria needed to be met:

i) Accurate measurement of a microbubble's radius from 1 – 20 µm
ii) Isolation from physical boundaries to prevent asymmetrical forces
iii) Accurate control of hydrostatic pressure from -100 kPa to 1 MPa (gauge)
iv) Regulation of internal temperature

This section details the design and calibration of a microscopy pressure chamber built specifically for the bright field and fluorescence imaging of microbubbles isolated from physical constraints in a hydrogel.

2.4.1.1. Design considerations

One of the most important aspects is the resolution obtainable by the optical system, allowing for detailed observations and measurements. In bright field imaging microbubbles are unfortunately at the limit of conventional microscopy due to the wavelength of light (~400 – 700 nm) being close to that of the smallest bubbles radius (500 nm). The resolving power of an optical system is given by [116]:

$$d_{min} = \frac{1.22\lambda}{NA_{obj} + NA_{cond}}\Bigg|_{NA_{cond} \leq NA_{obj}} \tag{3.13}$$

Where $NA_i = n_i \sin\theta$ and d_{min} is smallest distance resolvable between two point scatterers (where i is subscript for either the objective, obj , or

condenser, $cond$). Although this is not necessarily applicable to microbubble imaging due to the diffraction of light, it is desirable to improve the resolving power of the point scatterers for any imaging application by maximising the NA (bearing in mind that increasing the condenser's NA above the objectives has no added benefit, eq. 3.13). The implication is to design for the largest possible pressure vessel window diameter and minimum thickness.

Sapphire crystal was selected as the window material, similar to previous works [44], [117], [118], due to its high tensile strength, second only to diamond, and linear transmission of visible light, allowing for both bright field and fluorescence imaging at reduced window thickness. The thickness of the window will determine the imaging quality as it will restrict the working distance of an objective. Assuming small deflections and that it is evenly but freely supported, the minimum thickness allowable is calculated from thick plate theory [119].

$$t_{min} = D\sqrt{\frac{0.302P \cdot SF}{\sigma_U}} \tag{3.14}$$

Where D is the unsupported diameter of the window, P is the pressure, SF is the safety factor and σ_U is ultimate tensile strength of the glass. For brittle materials it is common to use a safety factor of 10, giving a design stress limit ($\frac{\sigma_U}{SF}$) for Sapphire of 40 MPa depending on its crystal arrangement.

To ensure that the application of hydrostatic pressure is uniform the microbubbles must be suspended away from physical boundaries and each other. Through experimentation it was found that microbubbles can be

suspended in a hydrogel that is then syringed onto the chamber window. To achieve a suitable viscosity of the hydrogel, 10g of non-alcoholic ultrasound gel is diluted with 10ml of deionised/filtered water and then mixed thoroughly with a vortex mixer.

Accurate control of the hydrostatic pressure can be achieved by using a high accuracy electronic regulator (QPV1, ProportionAir), fed by a pressurised air gas cylinder (10 bar) at the inlet and a vacuum pump (VacuuBrand, ME 8 NT) on the exhaust outlet. Using feedback from an internal pressure transducer, the electronic regulator uses a closed loop control to maintain the pressure, primarily compensating for convection within the pressure chamber and the gas line. Control of the hydrostatic pressure is performed automatically through custom built LabView software with data acquisition and control signals using a NI – USB DAQ device.

The temperature within the chamber will vary with pressure, assuming the volume is constant the ideal gas law can be written as:

$$T\big|_{\frac{dV}{dt}=0} \propto \frac{P}{n} \tag{3.15}$$

The system, however, is not closed, and the sides of the chamber will conduct heat. A copper plug can be used to help regulate the internal temperature by allowing efficient convection (thermal conductance of copper is 401 W/mK compared to 16 W/mK for stainless steel). To maximise convection the surface area of the copper plug was increased by machining cut outs. The temperature

was measured close to the centre of the chamber with an internal thermocouple (K type, TC ltd.) secured with a compression fitting.

2.4.1.2. Chamber design

Figure 3.16 shows a cross section of the design with dimensions and Figure 3.17 shows an illustration of the final design. The features based on this design are summarised in Table 3.2 below. Due to the specification of the electronic regulator, the internal volume had to be larger than 16 ml to negate pressure waves in the closed loop control, this made the chamber slightly too large for standard glass slide microscopes but suitable for most larger inverted microscopes. There are three ports on the main chamber body. All are NPT tapered threads to fit the gas line, pressure transducer and temperature probe.

Specification	**Value**	**Units**
Gauge pressure range	-0.1 to 1.0	MPa
Pressure accuracy[+]	± 2.0	kPa
Internal volume	24.0	ml
Max. NA	0.87	-
Dimensions (w, t, h)	60, 60,42	mm
Top window dimensions (thickness, diameter)	1.00, 12.75	mm
Bottom window dimensions (thickness, diameter)	2.00, 25.40	mm
Design safety factor	10	-

Table 3.2. Design specifications for pressure chamber. [+]taken from equipment specifications

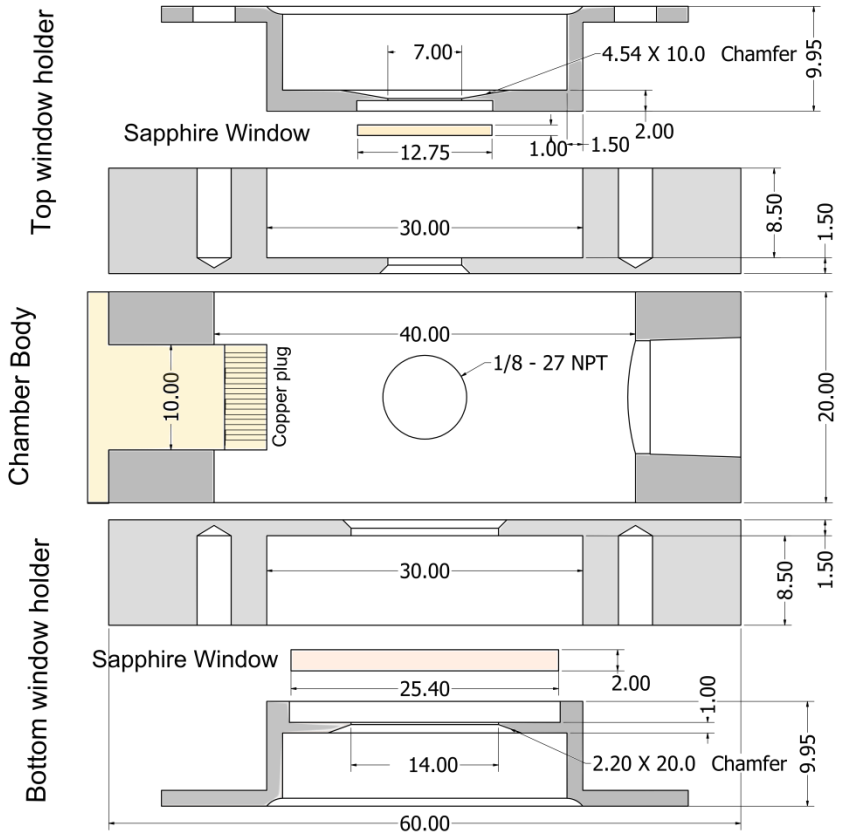

Figure 3.16: Cross section view of a microscopy pressure chamber design, for the quasi-static measurement of microbubbles under varying hydrostatic pressure. Dimensions shown are all in mm.

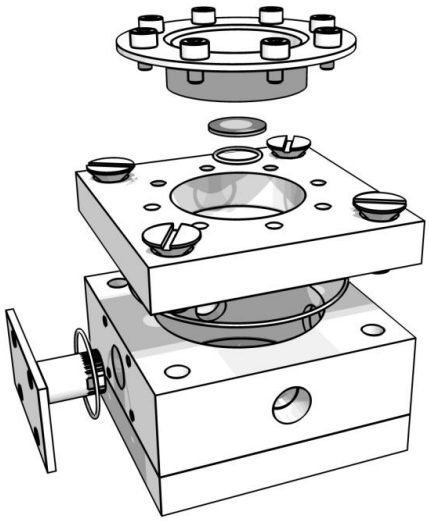

Figure 3.17: Illustration of microscopy pressure chamber. Samples are loaded below the top window plate and an air tight seal is created with o-rings when secured with screws.

2.4.1.3. Calibration experiments

Calibrations were performed to assess the optical resolution and pressure-temperature curves. To estimate the optical resolution, a calibration grid (G204, Athene) was placed in the chamber, resting in the gel, and imaged using a 40x objective (Nikon microscope Ti). The maximum theoretical resolution is 350 nm (Eq. 3.13 given a NA of 0.87 at an imaging wavelength of 500 nm) Multiple measurements of the calibration grid (n = 10), Figure 3.18, were found to be within 0.5 µm of each other when estimating the square width. The change in temperature due to varying rates of pressurisation was measured to find acceptable operating conditions. Figure 3.19 shows the minimum and maximum variation in temperature for both decompression and compression experiments (denoting the initial pressurisation rate).

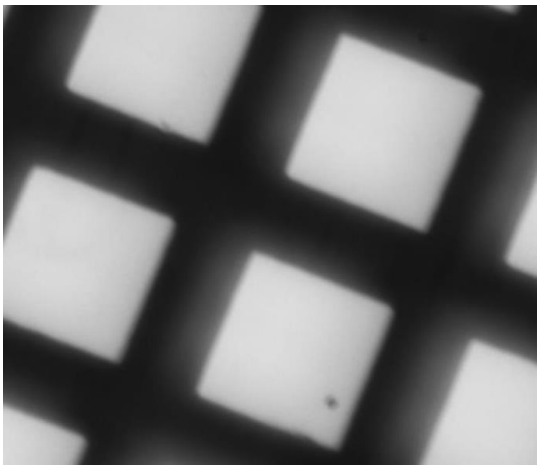

Figure 3.18: Image of calibration grid used to estimate pixel resolution. Square size is 45 µm.

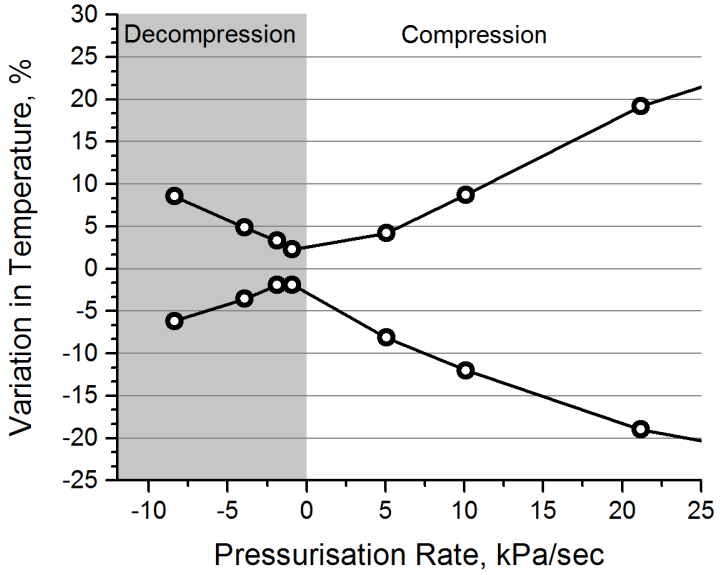

Figure 3.19: Calibration of temperature change due to varying pressurisation rate. Chamber ambient temperature between calibrations was approximately 26 degrees.

2.4.2. Quantitative fluorescence microscopy

This section describes two quantitative fluorescence imaging techniques used in this work to support the findings of the light scattering data. The techniques, Fluorescence Lifetime Imaging and Spectral Lambda Imaging, have only recently been applied to better understand the properties and structure of a microbubble's phospholipid coating. The measurements of viscosity and lipid packing using the respective techniques are used to support the finding of large variability between identically sized microbubbles and to give support to more realistic models of the coatings behaviour. As discussed in Section 3.1.2, treating the coating as a homogenous visco-elastic solid material could not account for the nonlinear responses observed in high speed imaging studies.

These techniques have been performed and are described, unless otherwise referenced, by Dr. Dario Carugo and Dr. Richard Browning.

2.4.2.1. Fluorescence lifetime imaging

The method for Fluorescence lifetime Imaging (FLIM) has been published (Hosny *et al.*[120]) and is referenced directly here. FLIM exploits the viscosity-sensitive photophysical properties of a "molecular rotor," the mesosubstituted 4,4-difluoro-4-bora-3a,4a-diaza-s-indacene (BODIPY-C10). As the molecule rotates, the nonradiative decay pathways are activated, leading to a reduction in the fluorescence quantum yield and the lifetime of the rotor compared with that in a viscous environment. Unlike fluorescence intensity, which changes as a function of the dye concentration, the fluorescence lifetime can provide a viscosity measure that is not affected by inhomogeneous distribution of the rotor in a given region of the bubble coating. The relationship between the fluorescence lifetime and viscosity for BODIPY-C10 for a wide range of viscosities [0.6–1140 centipoise (CP)] was determined empirically, Figure 3.20. This provided the means to produce a calibration graph for converting lifetime into a quantitative measure of viscosity. FLIM can detect individual lifetimes with the spatial resolution of a multiphoton microscope (ca. 200 nm). Thus, FLIM of the molecular rotor BODIPY-C10 provides a minimally invasive technique that can directly quantify and image viscosity at a macro- or microscopic resolution from lipid membranes of individual microbubbles. Importantly, the rate of intramolecular rotation in BODIPY-C10 also corresponds to bubble oscillations at ultrasonic frequencies.

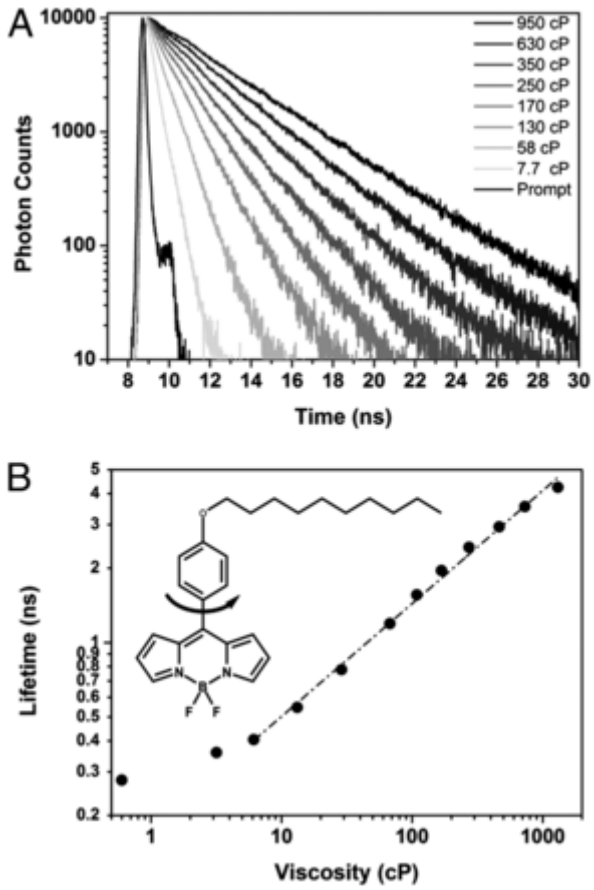

Figure 3.20: BODIPY-C10 fluorescence lifetime calibration vs. viscosity. (A) Selected fluorescence decay traces recorded in methanol/glycerol mixtures (30–95% glycerol) of different viscosity. (B) The logarithmic calibration plot of measured lifetimes vs. viscosity plotted according to the Förster–Hoffmann equation, which was fitted with a linear fit (dash-dot line) and found to be linear between 7.7 and 1,140 cP. Chemical structure of BODIPY-C10 is also shown. Figure and caption taken from published work [120]

2.4.2.2. Spectral lambda imaging

Spectral lambda imaging can be used to estimate the lipid packing of a microbubble's coating. This is useful because the density of lipid on the surface of a microbubble gives an indication of the local surface tension. The surface tension is inversely proportional to packing density and contributes significantly to the stability and response of coated microbubbles. To examine the lipid packing of the microbubble shell, microbubbles were stained with C-Laurdan, a

lipophilic, polarity sensitive dye. C-Laurdan is a derivative of Laurdan, modified to decrease bleaching over longer laser exposures. Laurdan is sensitive to the polarity of the surrounding environment, with the wavelength of maximum emission red-shifting from approximately 440 nm to 490 nm as the polarity increases. The hydrophobic portion of the dye ensures that it preferentially stains lipid regions, resulting in a dye that can give quantifiable information of the packing density of a lipid monolayer or bilayer. Ordered, gel-phase lipid layers have closer packing with greater exclusion of a polar solvent, reducing the polarity of the environment and resulting in a blue-shifted emission from Laurdan. Conversely, in disordered, liquid-phase lipid layers, a greater amount of the solvent is in the environment around Laurdan, red-shifting the emission.

Microbubble lipid packing density was examined by C-Laurdan staining and general polarisation analysis. To reduce potential fluorescence background from unincorporated lipids in the suspension, microbubbles were washed once by centrifugation. Approximately 3 mL of freshly prepared microbubbles were loaded into a disposable 10 mL Luer-Lok syringe (BD, COUNTRY) adapted to fit upright within a 50 mL centrifuge tube (Corning, COUNTRY) and spun at 1000g relative centrifugal force at 10^{o}C for 10 minutes in a swing bucket rotor (Heraeus Labofuge 400R, Thermo Scientific, PLACE, USA) to form a bubble cake against the plunger. The subnatant was discarded and the bubbles re-suspended within the syringe using 2 mL of Dulbecco's phosphate-buffered saline (DPBS). This was then transferred to a glass vial for future use. To stain with C-Laurdan, 1.5 to 5 µL of C-Laurdan (CONC) was added to 30 µL of washed microbubbles diluted in 70

µL of Milli-Q water (total volume 100 µL) and left to incubate for up to 30 minutes at 4^{o}C before use.

All Generalised Polarisation (GP) imaging was performed on a LSM 780 Inverted Confocal Microscope (Carl Zeiss Microscopy GmbH, Jena, Germany) using a previously reported methodology (REF). Briefly, 10 µL of stained microbubbles was loaded onto a 170 µm-thick glass cover slide and covered with a cover slip. Individual microbubbles were then located and imaged using the 63x objective. C-Laurdan dye was excited using the 405 nm laser and spectral images from 410 to 680 nm were captured on the spectral sensor (XXX check name) using the Zen Black software (Carl Zeiss Microscopy GmbH, Jena, Germany). This resulted in a single stacked image, with each stack corresponding to the intensity image at a single wavelength (n=30). Approximately 20 images were taken per formulation and each formulation was repeated three times using a freshly prepared microbubble suspension created from a new lipid film.

Fluorescence microscopy images were processed using a custom script in MATLAB (The Mathworks Inc.). Images were first opened using the BioFormats for MATLAB scripts (BIOFORMATS INFO). Microbubbles were identified by a semi-automated implementation of the *imfindcircles()* function and the background and internal volume of the bubble removed by cropping, leaving only the pixels of the stained bubble shell. GP values were calculated per pixel using intensity data from the 440 nm and 490 nm wavelength stacks by the following equation.

$$GP = \frac{I_{440} - I_{490}}{I_{440} + I_{490}} \tag{3.16}$$

Whole microbubble GP values were calculated from the average of the GP per pixel values. Standard deviations, medians and histogram plots were also taken from this data. Bubbles with saturation (pixel intensity of 255) in any wavelength were discarded. For spectral analysis, average intensity values of the shell per wavelength were calculated from pixel intensity values.

3.5. Summary

This chapter has presented an overview of the theory of the interaction of ultrasound and plane wave incident light with isolated microbubbles. Understanding of the theory led to the development of a robust analysis protocol, implemented in MATLAB, for the light scattering measurements obtained using the device presented in Chapter 2. In particular, the use of Mie Scattering theory to estimate a microbubble's radius from the magnitude of scattered light (Section 3.1.4) and the resulting scattered acoustic pressure given its radial response (Eq.3.2). The novelty of this design and set up over existing techniques is the ability to measure single microbubble radial responses to ultrasound excitation at high throughput rates without physical restrictions on the microbubble's response.

Supplementary methods, that are used to support the findings of the light scattering measurements, are presented that include a custom built hydrostatic

pressure chamber (Section 3.4.1) and quantitative flourescence imaging techniques (Section 2.4.2).

CHAPTER 4

Behaviour of a Clinical Ultrasound Contrast Agent

In this Chapter the response of a clinical ultrasound contrast agent to ultrasound excitation is investigated through multiple experiments using the device presented in Chapter 2 and the analysis techniques described in Chapter 3. Study is made of the effect of ultrasound parameters (peak negative pressure, frequency and number of cycles), initial microbubble size and environmental conditions. Supplementary methods, described in Section 3.4, are used to support the findings. The analysis is primarily focussed on the application and optimisation of Contrast Enhanced Ultrasound imaging which is discussed at the end of the chapter.

This chapter investigates the response of individual SonoVue® microbubbles to ultrasound excitation using the microfluidic device presented in

Chapter 2 with supporting observations from previous works and the techniques described in Chapter 3, including the quasi-static pressure chamber and quantitative fluorescence microscopy. SonoVue® microbubbles are of particular interest due to their current wide spread clinical use for multiple indications with CEUS imaging. However, as discussed in Chapter 1, there are limited data available regarding their response under different ultrasound and environmental conditions. Better understanding and predictability of their response could be used to optimise CEUS imaging, discussed later in this chapter, as well as give insight into the fabrication of the next generation of microbubbles, discussed in Chapter 5.

The results, supported by the supplementary methods, have yielded some interesting observations; in particular that initial size is not the main determinant of microbubble response. This has significant implications for theoretical frameworks and the understanding of the results. Therefore the significance of initial size and variability in coating properties is first discussed, providing context for the following analysis into optimising CEUS imaging using SonoVue® microbubbles. The desirable characteristics, as discussed in Section 1.2.1, for improved contrast using current CEUS imaging techniques are:

- Increased Echogenicity
- Nonlinear behaviour
- Stability

4.1. Significance of Initial Radius

It has been not only theorised but also observed that a microbubble's initial size plays an important role in its response to different ultrasound parameters, as observed for example in the high speed imaging spectroscopy studies [71], [121]. A microbubble will exhibit resonant behaviour that is a function of its physical and environmental properties. For uncoated microbubbles this phenomenon is well characterised and, given initial size, the resonant frequency can be accurately predicted. For coated microbubbles, however, both resonance frequency and resting radius is a function of physical properties imparted by the coating, see Section 3.1.2. Therefore, these properties as well as initial size need to be known in order to predict a microbubble's response. This section demonstrates that there is significant variation in the response of similarly sized microbubbles and therefore the coating properties.

4.1.1. Supporting observations of response variability

Previous works have demonstrated a large variability in microbubble response independent of size, for example the estimation of shell viscosity from the impulse response of 106 microbubbles [122] and the amplitude of radial expansions of 78 microbubbles in a capillary tube [123]. However, as discussed in Chapter 1, the associated experimental techniques are limited by low sample numbers, high uncertainties and physical restrictions on each microbubble's response. The quasi-static pressure chamber, presented in Section 3.4.1,

provides a controlled environment and high accuracy method of observing microbubbles under varying hydrostatic pressure. Figure 4.1, shows a typical photo series obtained from a decompression experiment (36 kPa below atmospheric over 30 seconds). There are two bubbles that appear to be the same size, microbubble B behaves as would be expected, expanding as the hydrostatic pressure is reduced; microbubble A, however, does not show any response under the same conditions. The variability in response is even better shown over the range of SonoVue® microbubbles investigated (Figure 4.2). Here it can be seen that there is a large variability (up to 1.5 times) in the expansion of similarly sized microbubbles. On subsequent decompressions the response is less predictable, some show an increase in size and others significantly decreasing, suggesting rearrangement of or loss from the lipid coating. Data for Figure 4.2 were selected from several hours of experiments and there are about the same number of samples that did not respond or collapsed soon after the onset of decompression.

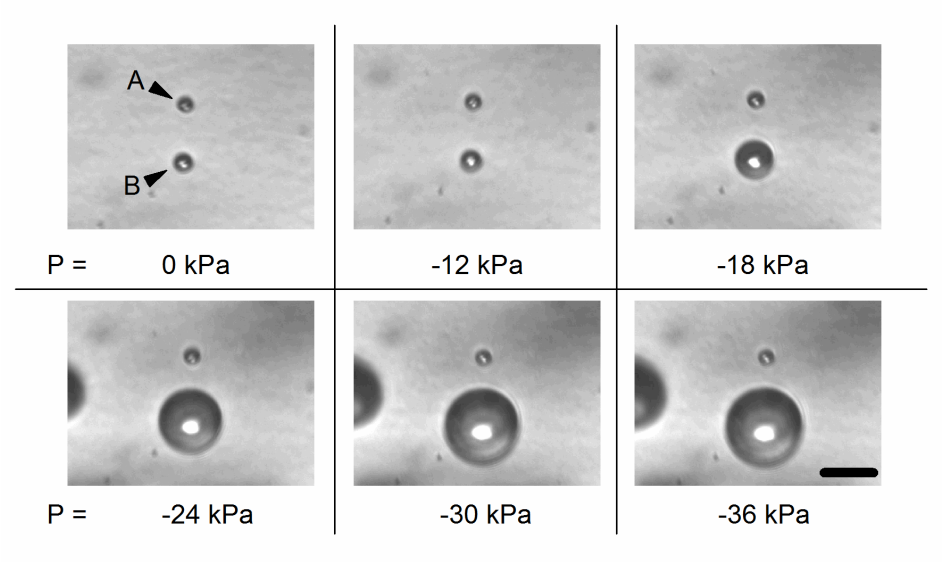

Figure 4.1: Example series of photos obtained during decompression of two similar sized SonoVue® microbubbles. The lower microbubble, B, expands as would be expected as the pressure is decreased, however the top microbubble, A, shows no response. Scale bar = 45 microns, P is gauge pressure.

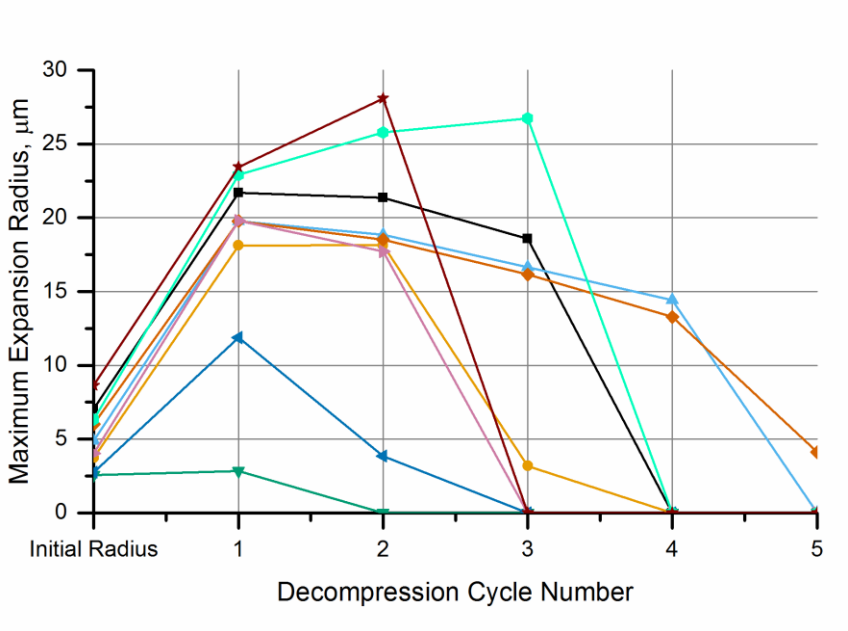

Figure 4.2: Maximum Expansion ratio as a function of initial radius and decompression cycle number demonstrates variability in SonoVue® response under varying hydrostatic pressure. An expansion radius of 0 indicates that the microbubble has collapsed. Decompression protocol was 36 kPa over 30 seconds. N = 14.

Unfortunately the pressure chamber experiment and current methods of individual microbubble characterisation such as the fluorescence microscopy and high speed imaging (discussed in Section 1.4) are time consuming and can only generate data with small sample numbers not particularly suitable for statistical analysis. Further, due to the experimenters individual selection of microbubbles a bias may be introduced according to preferential responses and microbubbles that are the most stable. These methods have and will continue to bring better understanding of microbubble behaviour and their complex phenomena, but they are unfortunately not suitable for representing a population's response and the observations are challenging to compare to theoretical models due to the restriction of a physical boundary on a microbubble's response. Insight into a microbubble population's response requires much larger sample sizes, which is made possible with the microfluidic device developed for this work. For example, in Figure 4.3, the volume expansion ratios (maximum expansion volume / initial volume) as a function of initial radius of 3164 SonoVue® microbubbles are plotted for a range of driving frequencies of 2 MHz to 3.5 MHz at around a peak negative pressure of 120 kPa. The percentile lines are used to show more clearly the large distribution in microbubble responses of similar radius. For all frequencies there is at least a variation of 10 times in the volume expansion ratio independent of initial radius. Compared with previous studies, such as the high speed imaging spectroscopy [71] and theoretical predictions (Section 3.1.2, Figure 3.3), the results here show much less pronounced resonance effects. This is likely due to the large variability in coating properties discussed in the

following section. The frequency content of the ultrasound pulses, Figure 4.4, show larger bandwidths at higher frequencies, however without much overlap at the -6dB width.

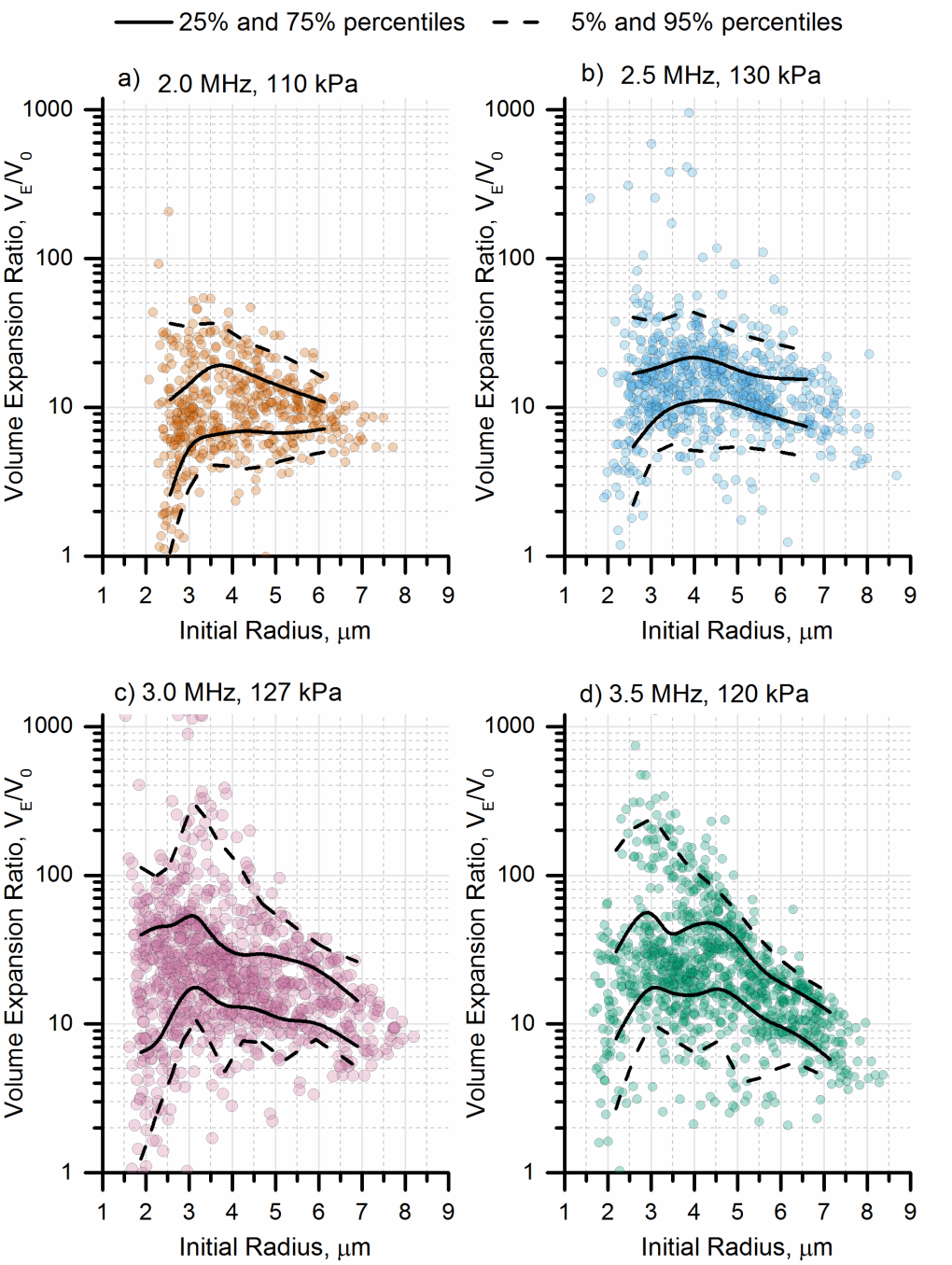

Figure 4.3: Volume expansion ratio against initial radius shows significant variability in response. Solid lines represent the 25th and 75th percentiles and dashed lines represent the 5th and 95th percentiles. Ultrasound parameters shown above figures, pulse length is 5 cycles. Number of samples for each graph is as follows: a) 493, b) 699, c) 941 and d) 1031

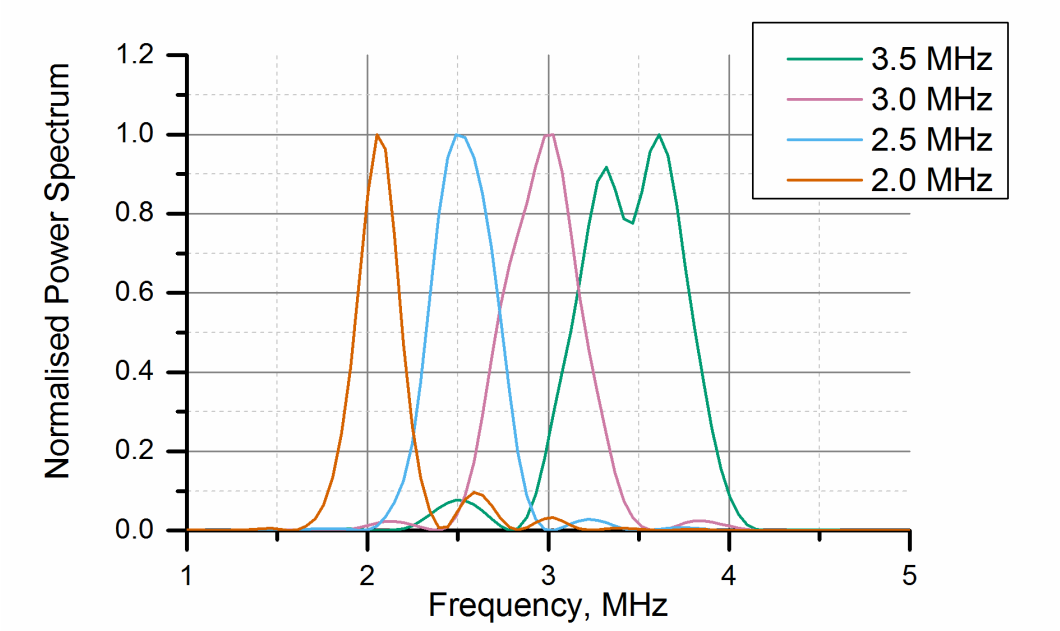

Figure 4.4: Ultrasound frequency content for ultrasound pulses used in figure 4.3 above.

These observations of response variability support the argument that large sample numbers are required to better represent the variability of microbubble behaviour; it is suggested that the reason for this is due to variation in the initial coating properties and this is investigated in the following section.

4.1.2. Variation in coating properties

As demonstrated in the pressure chamber experiments (Figure 4.2), each time a SonoVue® microbubble was decompressed its equilibrium radius either decreased or increased. This behaviour has been suggested to arise from the rearrangement and shedding of the lipid coating [106] and has been repeatedly observed in the high speed imaging studies in both fluorescence imaging [124] and the observation of microbubbles decreasing in size after ultrasound

excitation [109]. To better understand the processes involved, it is possible to measure the lipid packing density of a microbubble's coating using a technique known as Spectral Lambda Imaging, described in Section 2.4.2.2. This quantitative fluorescence microscopy technique provides a relative measure, termed GP, for how tightly packed the lipids are on a microbubble's coating, intuitively this gives an indication of the surface tension (packing density is inversely proportional to surface tension, as described in Section 2.4.2.2), and can be used to demonstrate the variation in coating properties. The GP measurements of SonoVue® microbubbles, Figure 4.5, show that there is: i) considerable variation in the mean lipid packing density across the population investigated independent of size and ii) a possible inversely proportional trend with microbubble size and lipid packing density. This variation in coating properties has also been observed for other lipid composite microbubbles using FLIM (see Section 2.4.2.1) to estimate the coating's viscosity, Figure 4.6. The mean viscosity within the samples of each microbubble composition investigated can be seen to vary by at least 300 cP. Further, preliminary experiments were performed that combined Spectral Lambda Imaging with the hydrostatic pressure chamber, Figure 4.7. Here phase separation of the lipid coating was observed as the hydrostatic pressure was decreased. The variability in the properties could be used to explain the large variability observed in microbubble response to ultrasound excitation (Figure 4.3). Suggesting that coating properties have an equal, if not larger, effect on a microbubble's response compared to its initial size. It could also be argued that a microbubble's size is also a function of

its coating's phospholipid surface concentration, such that the initial radius must be considered as a function of the coating properties.

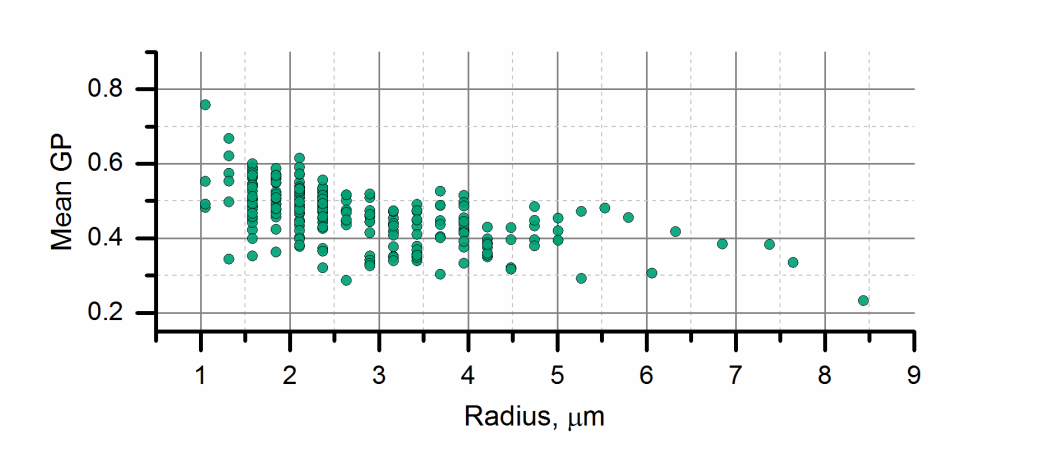

Figure 4.5: Variability in the coating properties of SonoVue® microbubbles. Mean GP gives an estimation of the lipid packing that ranges from 1 (tightly packed) to -1 (loosely packed). Experiment performed by Dr Dario Carugo and Dr Richard Browning.

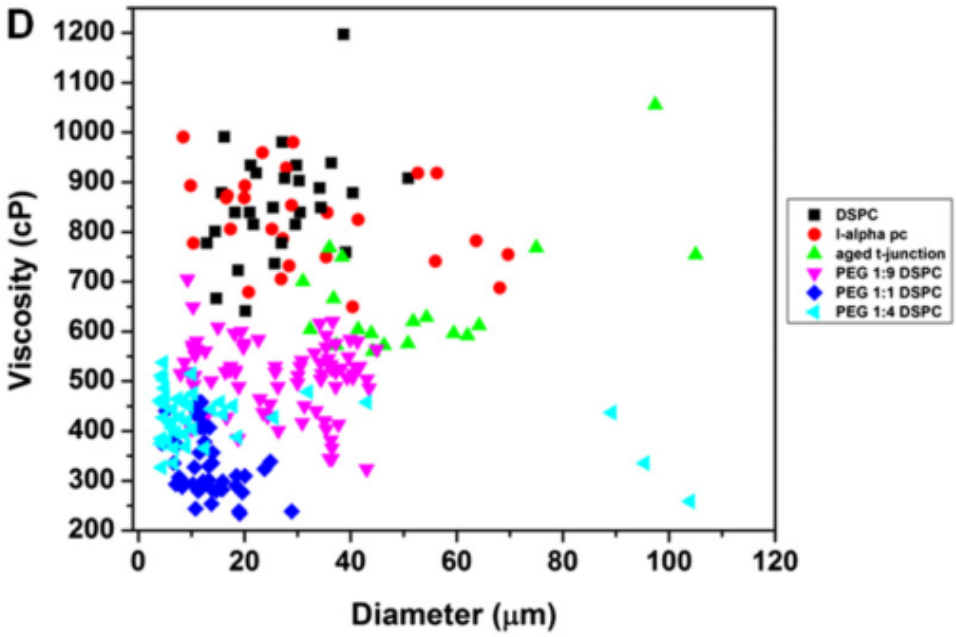

Figure 4.6: Estimation of coating viscosity as a function of microbubble initial diameter using FLIM for a variety of microbubble compositions. Figure taken from [120]

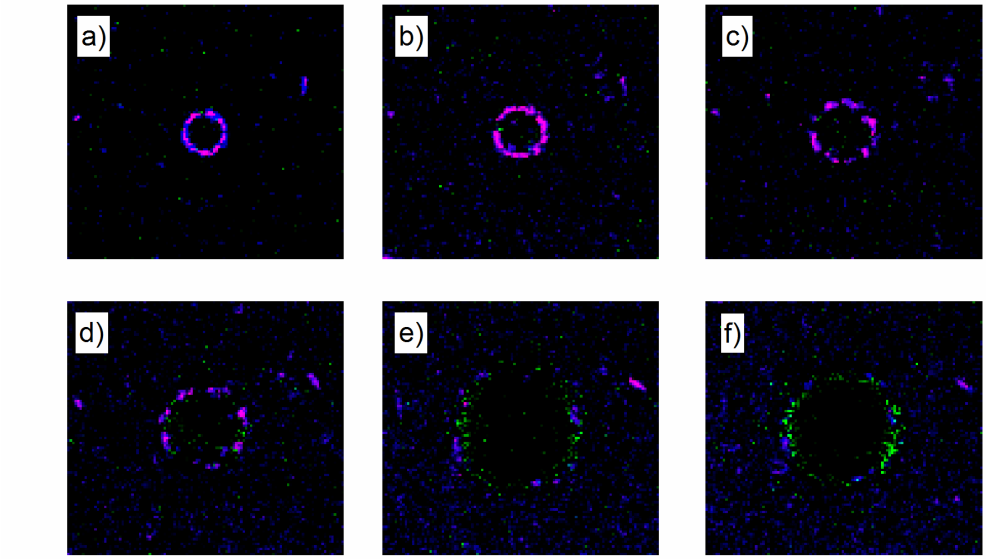

Figure 4.7: Measurement of lipid packing of a DSPC:PEG microbubble using Spectra Lambda fluorescence imaging during decompression using the hydrostatic pressure chamber. Hydrostatic pressure decreases from atmospheric to – 35 kPa (gauge) over the course of the images. Separation of the lipid can be seen in figures c and d.

4.1.3. Dependence of microbubble behaviour on initial radius

It has been shown that there is significant variation in the radial response of individual SonoVue® microbubbles with respect to initial radius. There are, however, population trends evident when observing the behaviour of sufficiently large samples. The response categorisation, Section 3.3.1, is a useful method for observing trends representative of a population. In Figure 4.8 this categorisation is shown for ultrasound driving frequencies of 3 MHz and 4 MHz and split into three size categories of initial radius, < 2.5 µm, < 4.5 µm and > 4.5 µm. There are several consistent size dependent trends that can be seen in Figure 4.8:

i) At a driving pressure of 50 kPa for both frequencies, microbubbles larger than 4.5 µm show less compression dominated responses compared to those smaller than 2.5 µm

ii) The response rate, microbubbles exhibiting an expansion greater than 20% of its initial radius, for microbubbles smaller than 4.5 µm is higher at pressures below 25 kPa at 3 MHz compared to 4 MHz.

iii) At pressures above 100 kPa the median expansion ratio is inversely proportional to microbubble initial radius. Most significantly, at both 3 MHz and 4 MHz microbubbles above 4.5 µm show about a factor of 2 less median expansion compared to microbubbles below 4.5 µm

iv) A higher proportion of microbubbles above 4.5 µm decrease in size at pressures above 100 kPa

Observation (i) is particularly interesting for its implications for CEUS. There is a clear transition from compression to expansion dominated behaviour that occurs around a peak negative pressure of 50 kPa for both frequencies and microbubble sizes. Larger microbubbles ($r > 4.5$ µm), however, appear to exhibit a transition that is dominated by symmetrical response (75%) compared to microbubbles below 2.5 µm that are still predominantly showing compression dominated behaviour at 50 kPa. For demonstration, Figure 4.9 shows examples of typical radial time curves at these pressures and radii of above 4.5 µm. This could potentially be exploited in amplitude modulation imaging by maximising the nonlinear residual, discussed in Section 1.2.1, where it is desirable to subtract a linear signal from a nonlinear signal at the lowest pressure possible.

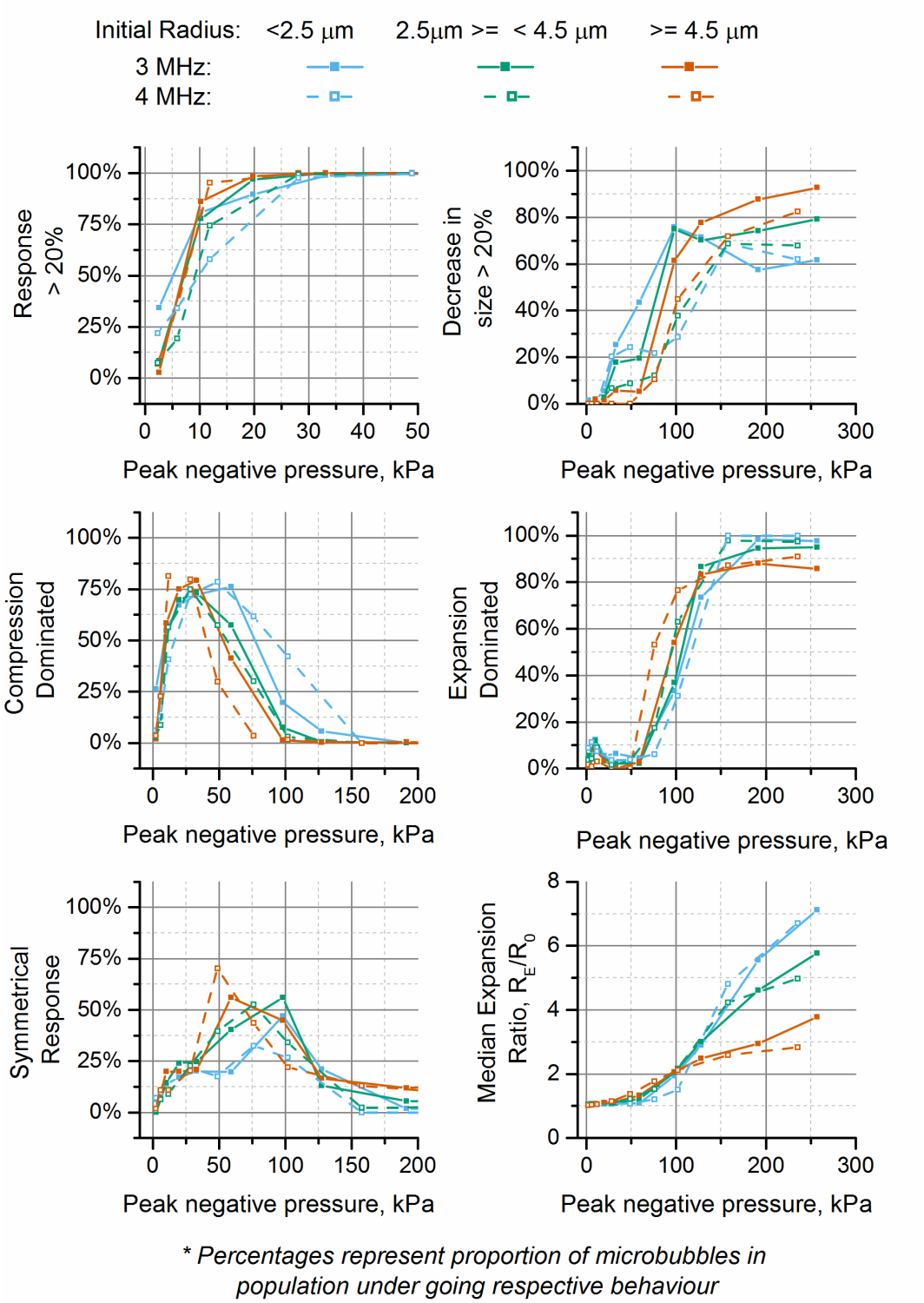

Figure 4.8: Size separated SonoVue® response categorisation as a function of peak negative pressure. Samples are compared for 3 MHz solid lines (< 2.5 µm n = 4352, 2.5 µm >= < 4.5 µm n = 3169 and > 4.5 µm n = 4090) and 4 MHz dotted lines(< 2.5 µm n = 3328, 2.5µm >= < 4.5 µm n = 2103 and > 4.5 µm n = 2502).

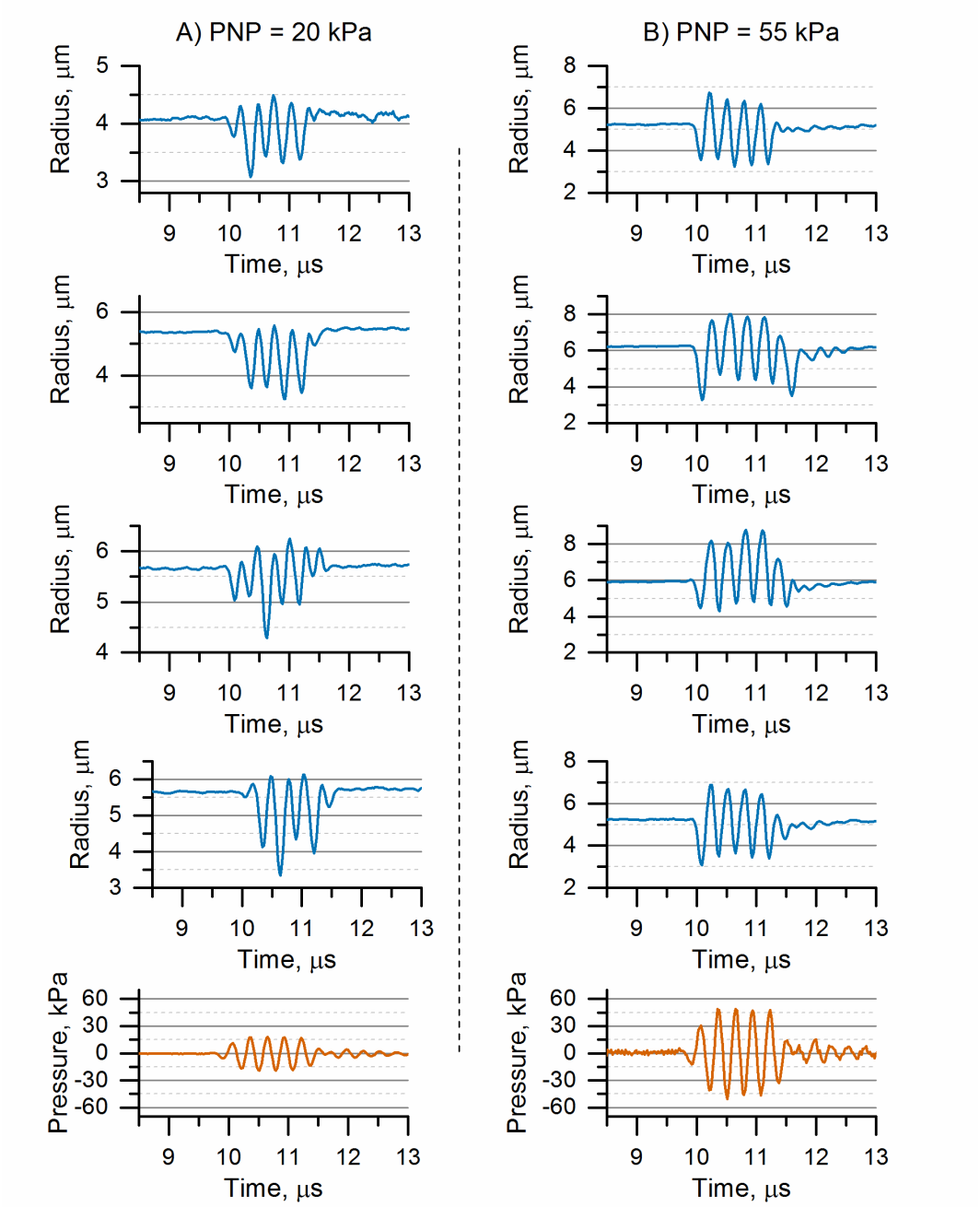

Figure 4.9: Example of typical radial time curves show compression dominated responses at peak negative pressure of 20 kPa, column A, and symmetric responses at higher pressure of 55 kPa, column B. Pressure traces recorded with hydrophone are displayed in orange for reference.

These results are in contrast to previous observations of the dependence of microbubble response on initial size, for example in the high speed imaging spectroscopy studies [125]. It is argued that by analysing a larger number of samples a better representation of a microbubble response to ultrasound and its variability is obtained. Despite the variability there are still size dependent trends that have been observed and they will be investigated further in the following sections with respect to the desirable characteristics for CEUS imaging.

4.2. Overview of Radial Response

This section attempts to provide an overview of SonoVue® microbubble behaviour as a function of the ultrasound parameters and initial radius.

4.2.1. Pressure and frequency dependence

As expected there is a proportional relationship between ultrasound driving pressure and the magnitude of a microbubble's radial response. Figure 4.10 shows the percentiles (5^{th}, 50^{th} and 95^{th}) of the expansion and compression ratios for SonoVue® microbubbles as a function of driving pressure at a driving frequency of 3.5 MHz. The relationship, however, is not linear due to the transition between compression and expansion dominated behaviour regimes discussed briefly in section 4.1.3. it can be seen that up to a pressure of 50 kPa the median compression ratio is larger than the expansion ratio, 1.64 compared to 1.13 respectively at a driving pressure of 40.1 kPa. However, as the pressure increases up to 100 kPa the expansion ratio shows a stepped increase while the

compression ratio appears to level off. This effect is evidence of the transition between compression dominated and expansion dominated behaviour at around 50 kPa discussed previously. The transition from compression to expansion dominated behaviour is more clearly shown in Figure 4.11. Here the median values have been plotted for different driving frequencies and at lower pressures to visualise the behaviour below 50 kPa. There are two interesting observations: i) at the frequencies tested, except for 2.5 MHz and 2 MHz, the intersection between the compression and expansion ratios occurs close to 100 kPa and ii) at 50 kPa the compression ratio starts to level off and then starts to increase again at around 100 kPa. The increase in the median compression ratio above 100 kPa can be explained by a large proportion of the microbubbles collapsing to or below the optical resolution of the system, as indicated by the sudden increase in the 95th percentile.

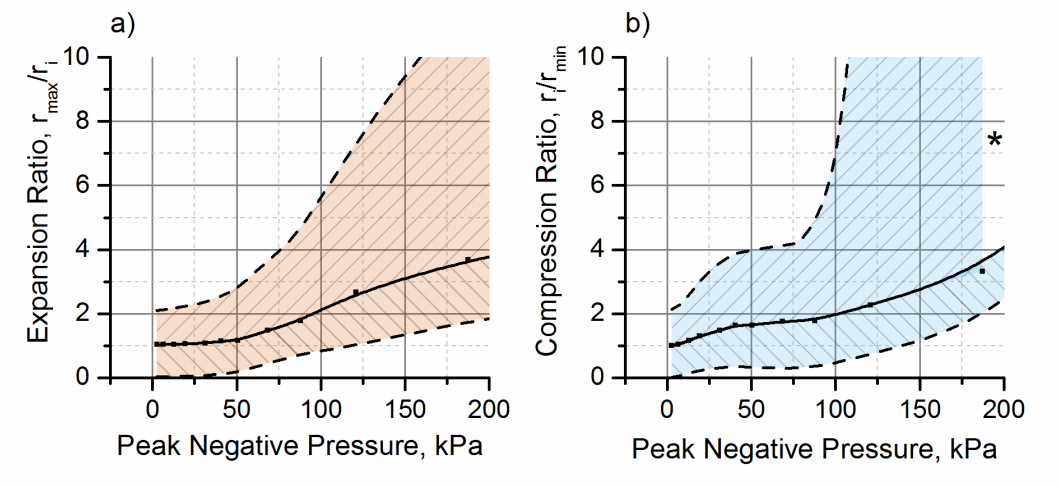

Figure 4.10: Expansion (a) and compression (b) ratios of individual SonoVue® microbubbles as a function of peak negative pressure. Dotted lines represent 5th and 95th percentiles, solid lines represent the median responses. Ultrasound driving frequency of 3.5 MHz of 5 cycles. N = 10938 samples across all points displayed (squares), each point represents the median across the full distribution of sizes

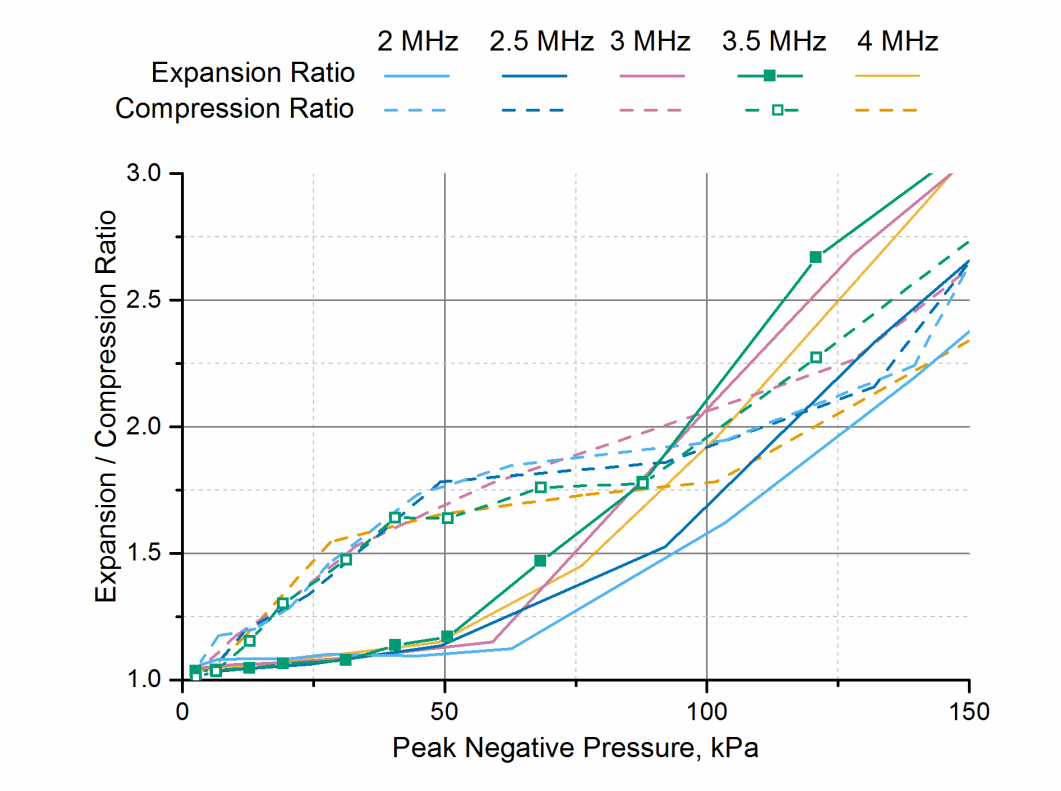

Figure 4.11: Direct comparison of expansion (solid lines) and compression (dashed lines) ratios as a function of peak negative pressure, plotted for different driving frequencies. For clarity, sample points that the lines are fitted to have not been show except for those at 3.5 MHz .Note that all lines are within the 20% pressure calibration error, see Section 2.5.3.

4.2.2. Initial size dependence

As discussed previously, the radial expansion ratio appears to show dependence on the initial microbubble radius. This can be better demonstrated by plotting the expansion/compression ratios as a function of initial radius for different driving pressures, Figure 4.12. Here it can be seen that at peak negative pressures below 120 kPa, the expansion ratio (Figure 4.12.a,c), increases proportionally with initial microbubble radius, however above this pressure the trend appears to reverse. Interestingly, this is not the case for the compression

ratio (Figure 4.12.b,d), where for all peak negative driving pressures the compression ratio increases with initial radius.

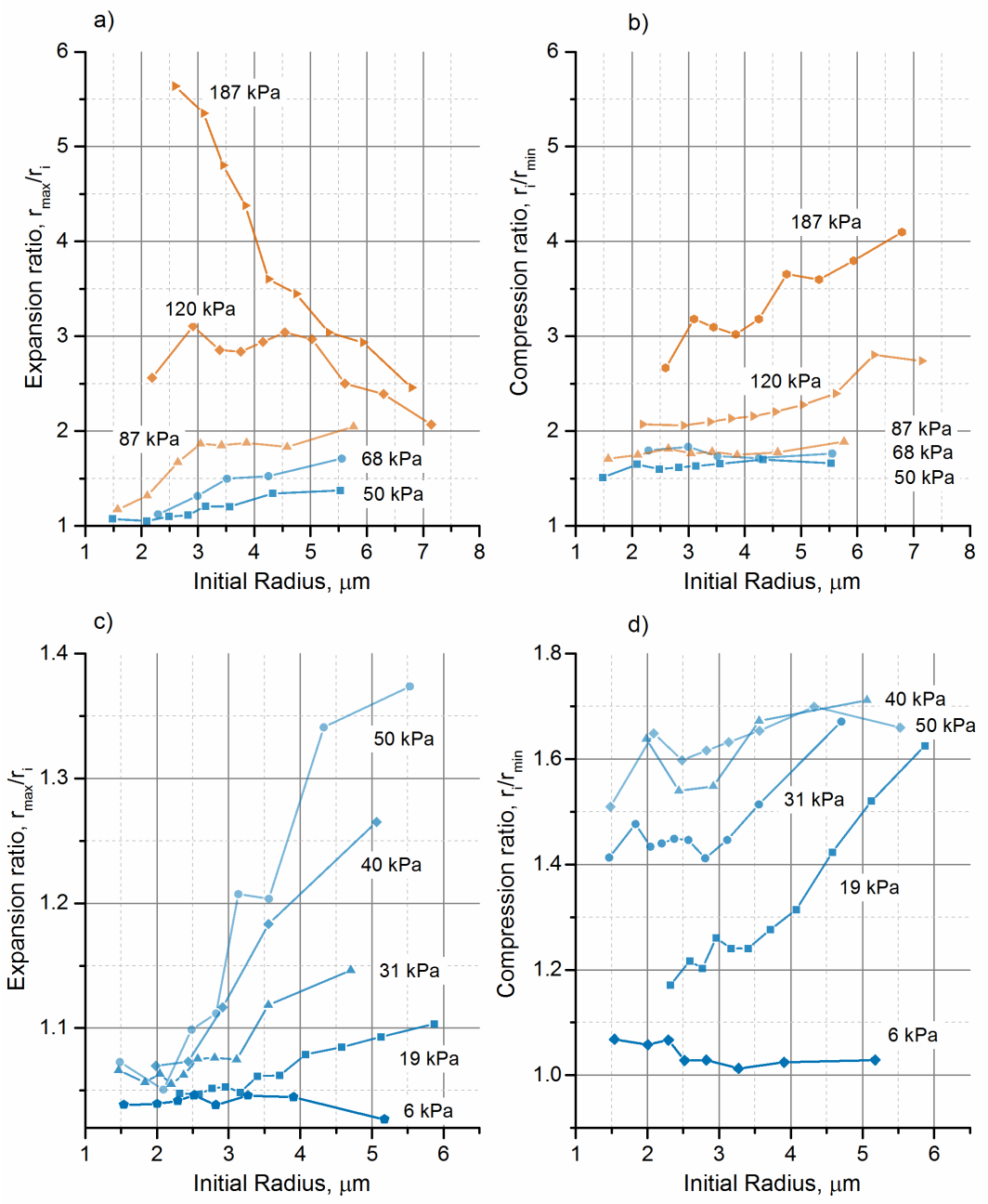

Figure 4.12: Median expansion (a,c) and compression (b,d) ratios as a function of initial radius and peak negative driving pressures from 50 kPa to 187 kPa(a, b) and lower pressures from 6 kPa to 50 kPa (c,d). Ultrasound frequency is 3.5 MHz and pulse length of 5 cycles. Each point represents the median expansion or compression ratio of at least 100 individual SonoVue® microbubbles. For clarity the 25th and 75th percentiles are not shown.

This trend observed for the expansion ratio is consistent with observations from a high speed imaging study [126] shown in Figure 4.13 below. Here it can be seen that the excursion ratio (difference between maximum and minimum diameters divided by the initial diameter) of the largest microbubbles tend towards an asymptote as the driving pressure increases, while the smallest microbubbles show exponential expansion. The change in behaviour appears to occur around a radius between 4 µm – 5 µm. Interestingly, the excursion ratios are much smaller than that observed in this thesis, for comparison the data from Figure 4.12 are replotted as the excursion ratio, Figure 4.14. The ultrasound parameters are of the same order of magnitude in both experiments and yet in the high speed imaging study at a driving pressure of 200 kPa the excursion rate does not exceed 0.6, whereas in this study the median excursion rate was up to 4.5. It is suggested that this difference could arise from i) the physical boundary imposed by the tube on the microbubbles in the high speed imaging studies (which is known to reduce the observed amplitude of oscillation but was not accounted for in the study) ii) the large variability in response only observed over large sample numbers or, iii) calibration errors of the ultrasound field.

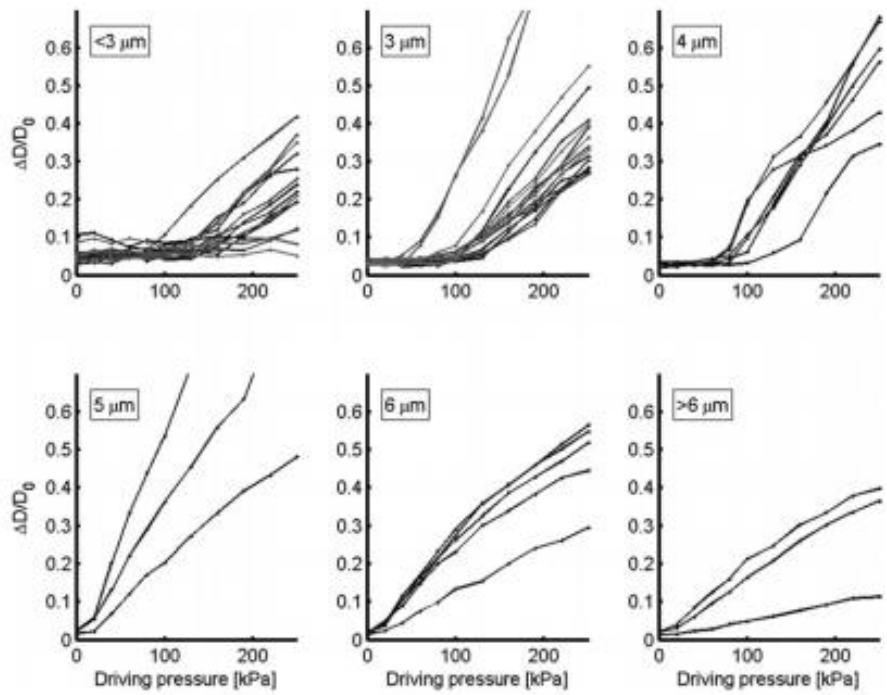

Figure 4.13: Excursion ratio of SonoVue® microbubbles from high speed camera experiments, results categorised by microbubble size. Figure taken from [126]*. The ultrasound driving centre frequency was 1.7 MHz and pulse length 6 cycles, N =~ 51*

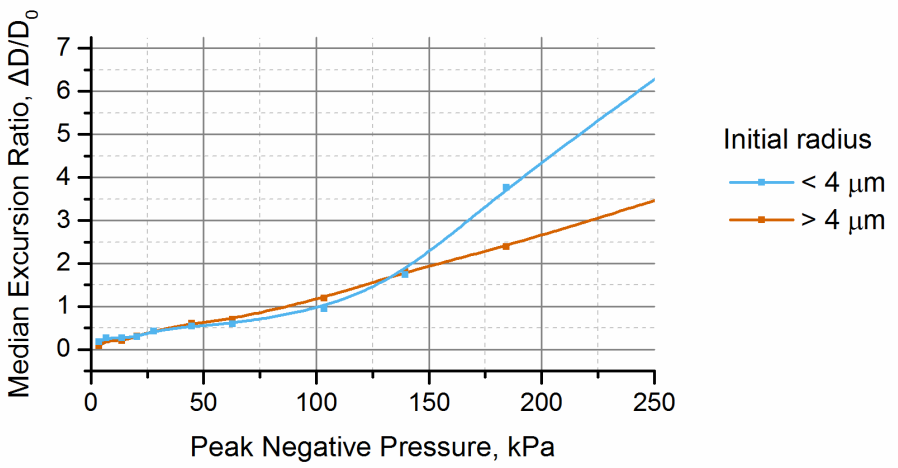

Figure 4.14: Median excursion ratio from light scattering experiments as a function of peak negative pressure, plotted for microbubbles of initial radius above and below 4 µm. The data in this figure have been presented for direct comparison to the previous figure. The ultrasound driving centre frequency was 2 MHz and pulse length 5 cycles. N = 371 microbubbles.

4.2.3. Asymmetric response

In agreement with previous studies, nonlinear behaviour, as observed through compression or expansion dominated responses or increased harmonics in the acoustic power spectrum, is observed to occur at peak negative driving pressures as low as 6 kPa (reference studies: 6kPa [127], 13 kPa [128] and 12.5 kPa [129]). Figure 4.15, shows examples of typical SonoVue® radial responses when driven at a driving frequency of 3.5 MHz and peak negative pressure of 6 kPa. In fact, at pressures below 40 kPa the majority of responses (> 50%) are asymmetric; this was clearly shown in the compression dominated behaviour in Figure 4.8 previously.

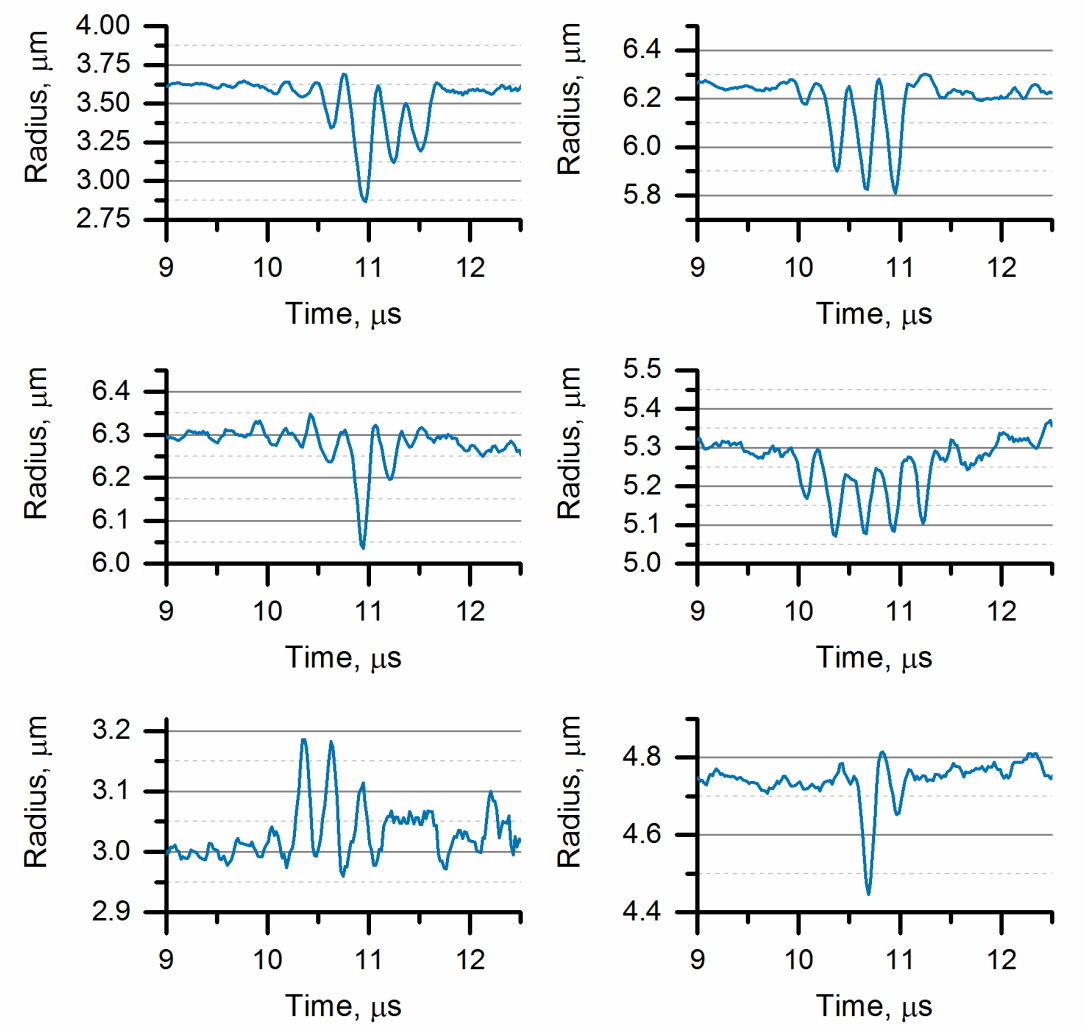

Figure 4.15: Examples of the nonlinear radial time curves of SonoVue® microbubbles driven at a peak negative pressure of 6 kPa. Ultrasound driving frequency is 3.5 MHz at 5 cycles.

For statistical analysis the nonlinear response can be shown by estimating the asymmetry of each microbubble's response, the method for which is described in Section 3.3.1. The asymmetry value is given from -50% to 50%, where 0% represents a perfectly symmetric response, > 25% is defined as expansion dominated behaviour and less than -25% is described as compression dominated behaviour. The asymmetry, Figure 4.16, shows that the transition from compression dominated behaviour to expansion dominated behaviour occurs gradually between 50 kPa and 100 kPa and that only at pressures above

150 kPa are 95% of the microbubbles showing a response which is expansion dominated. This result is consistent with the prediction by Marmottant's model (discussed in Section 3.1.2), Figure 4.17. For similar ultrasound conditions there is a clear transition from compression to expansion dominated behaviour, however in their model this occurs at a much higher driving peak negative pressure of around 280 kPa.

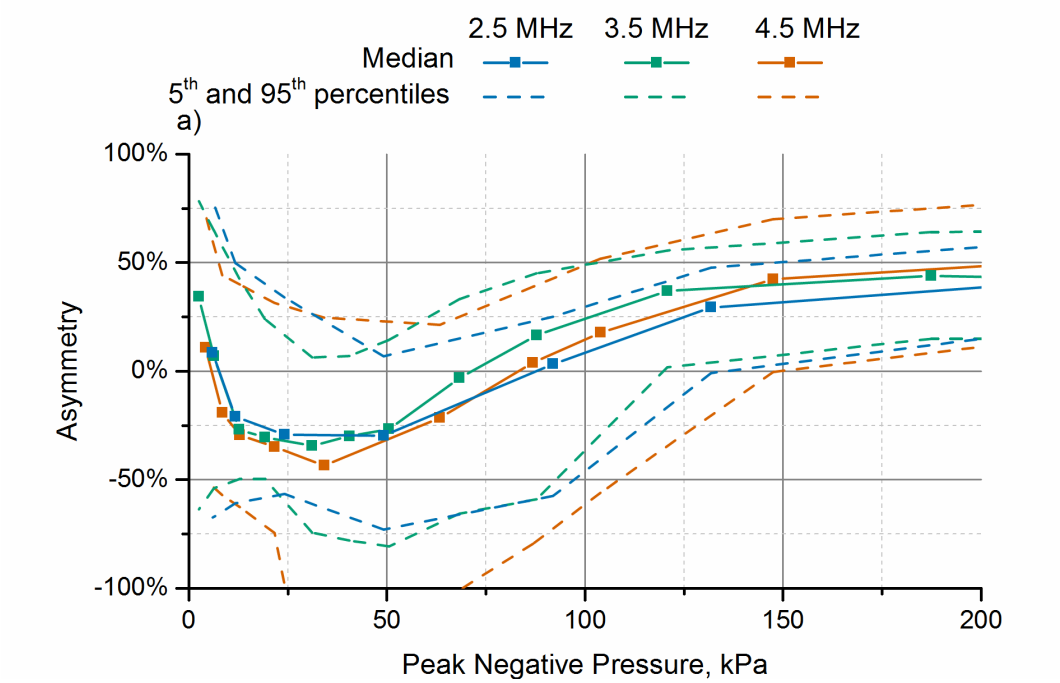

Figure 4.16: Asymmetry of SonoVue microbubble responses, plotted for driving frequencies of 2.5 MHz, 3.5 MHz and 4.5 MHz. Each point represents the analysis of at least 100 individual microbubbles.

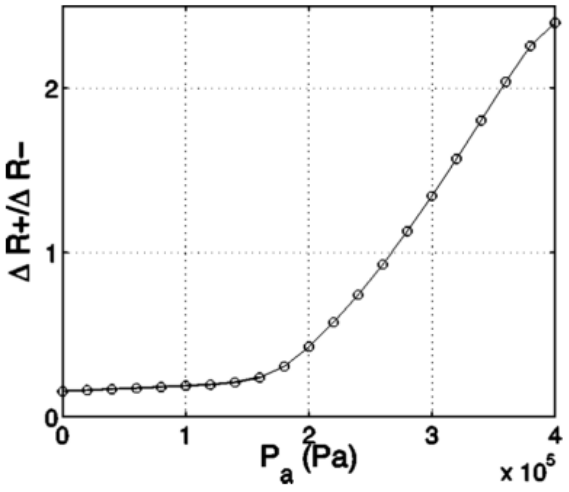

Figure 4.17: Effect of an increasing acoustic pressure on the asymmetry of a microbubble's response (initial radius = 0.8 µm, ultrasound pulse length of 5 cycles at 2MHz). Compression behaviour occurs when $\Delta R+/\Delta R- < 1$ *. Figure and caption from Marmottant* [109]

The dependence of the asymmetry on the observed microbubble's initial radius is investigated in Figure 4.18 below. Here it can be seen that for peak negative pressures above 20 kPa and below 120 kPa larger microbubbles are more likely to exhibit a compression dominated response than smaller microbubbles at the same driving pressure. An interesting observation is that at the transition between the two behaviours, for example at 68 kPa and driving frequency of 3.5 MHz (Figure 4.18.a) there is a transition within the microbubble population as well. Microbubbles with an initial radius greater than approximately 3.6 µm show a median expansion dominated behaviour and those smaller show a median compression dominated response. As the peak negative pressure increases to 87 kPa, this 'transition' radius decreases to approximately 2.5 µm. As discussed in Section 3.1.2, the asymmetry of a microbubble's response can be attributed to physical properties imparted by the coating. Given

the size dependent asymmetry observed in Figure 4.18, it is suggested that the coating properties are size dependent. Further due to the change in the asymmetry behaviour with respect to driving ultrasound pressure, it could be suggested that the effects of the coating properties are both size and pressure dependent.

Interestingly, at peak negative pressures above 120 kPa, the proportional trend disappears and there appears to be a 'resonant' initial microbubble size for the expansion asymmetry that occurs around radii of 4 – 5 µm. This peak will be further discussed with regard to a phenomenon that occurs as a microbubble expands to roughly twice its initial radius (Section 4.5).

Figure 4.18: Median microbubble response asymmetry as a function of initial radius plotted for varying peak negative driving pressure and frequencies 3.5 MHz (a) and 4.5 MHz (b). Each point represents the median value of at least 100 microbubbles.

4.3. Echogenicity

For this work echogenicity is defined as the magnitude of the overall scattered power from a microbubble. It follows that the larger the scattered pressure the more detectable a microbubble's signal is during ultrasound imaging at the transducer's receive frequency. As discussed in Section 1.2.1, the increased scattering from microbubbles increases the CTR ratio in both conventional B-Mode imaging and CEUS. The former relies on the overall increase in scattered power where as CEUS achieves higher contrast by exploiting the increase in nonlinear scattered power. This chapter investigates both of these features.

The first graph below (Figure 4.19) shows the total scattered power as a function of initial radius and plotted for increasing peak negative driving pressure, from 19 kPa up to 120 kPa. It is interesting to observe the directly proportional relationship with initial size and the scattered power at peak negative pressures below 50 kPa (Figure 4.19.a and .b), and the fact that there does not appear to be any resonance. The variation in microbuble response with respect to initial size appears to increase with driving pressure, for example at 19 kPa there is a variaiton in response for a 5 µm of approxametly 10 times, compared to almost 100 times at 50 kPa. At higher pressures above 87 kPa, there is a much larger variation in response of the smaller microbubbles (initial radius < 5 µm), and it appears as the pressure increases up to 120 kPa that the smaller microbubbles show larger scattered pressures (Figure 4.19.d) in the 95th percentile (up to 6

times higher scattered pressure for microbubbles of initial radius 3 – 4 µm compared to 8 µm). However, the median scattered pressure is still dominated by microbubbles with initial radius > 4.5 µm. Figure 4.20 shows the median estimated scattered power across the entire size distribution for a range of driving frequencies as a function of peak negative pressure. There does not appear to be any specific trends related to frequency dependence on the scattered power as they are within the 20% error estimated for the pressure calibrations, see Section 2.5.3. As expected, the median back scattered power increases with driving pressure. The magnitude of the scattered pressure can be calculated as the square root of the power, i.e. at driving pressures of 150 kPa the median scattered pressure is around 0.1 to 1 kPa at a distance of 75 mm.

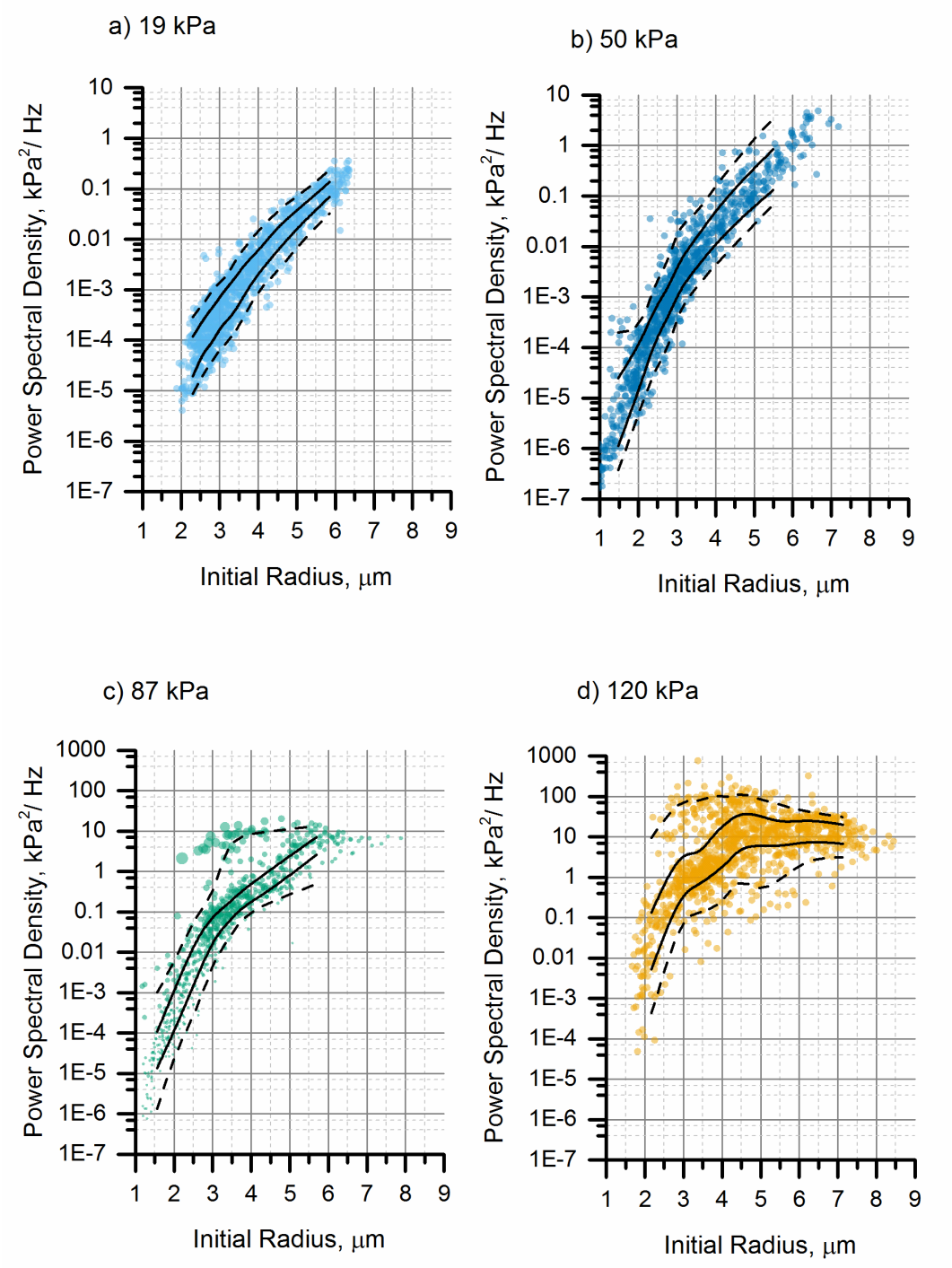

Figure 4.19: Total scattered power plotted for each microbubble as a function of initial radius, plotted for peak negative driving pressures of a) 19 kPa, b) 50 kPa, c) 87 kPa and d) 120 kPa. Ultrasound driving frequency is 3.5 MHz at 5 cycles. Dotted lines represent the 5th and 95th percentiles, solid lines represent the 25th and 75th percentiles.

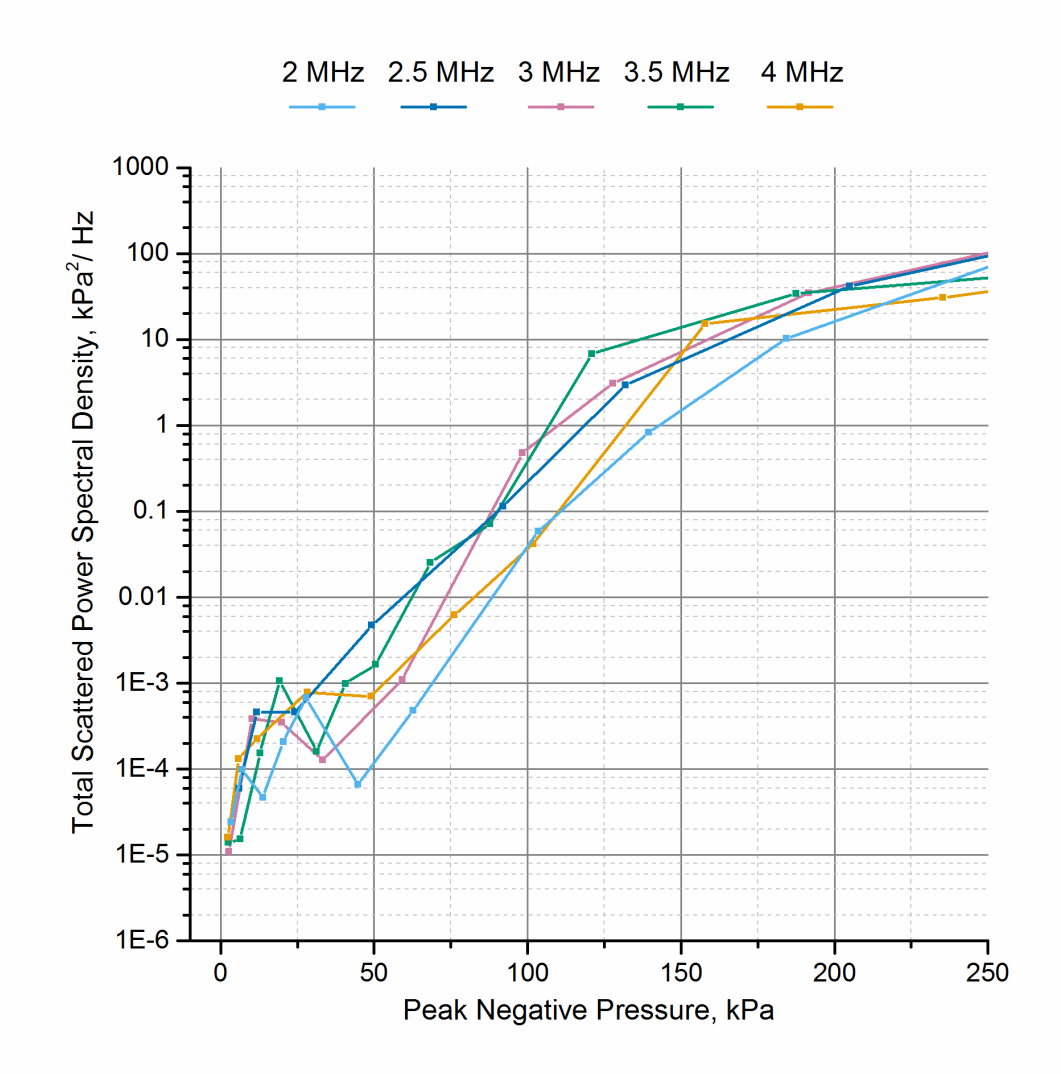

Figure 4.20: Median total scattered power of SonoVue® responses as a function of peak negative pressure, plotted for driving frequency.

4.3.1. Fundamental scattered power

The fundamental scattered power is measured as the sum of the power spectrum at the driving frequency between 0.75 and 1.5 over the frequency range, Figure 4.21. Here the same trend can be seen as before, however at lower values compared to the total scattering power, the difference in scattering powering is due to the sub-harmonic and harmonic components.

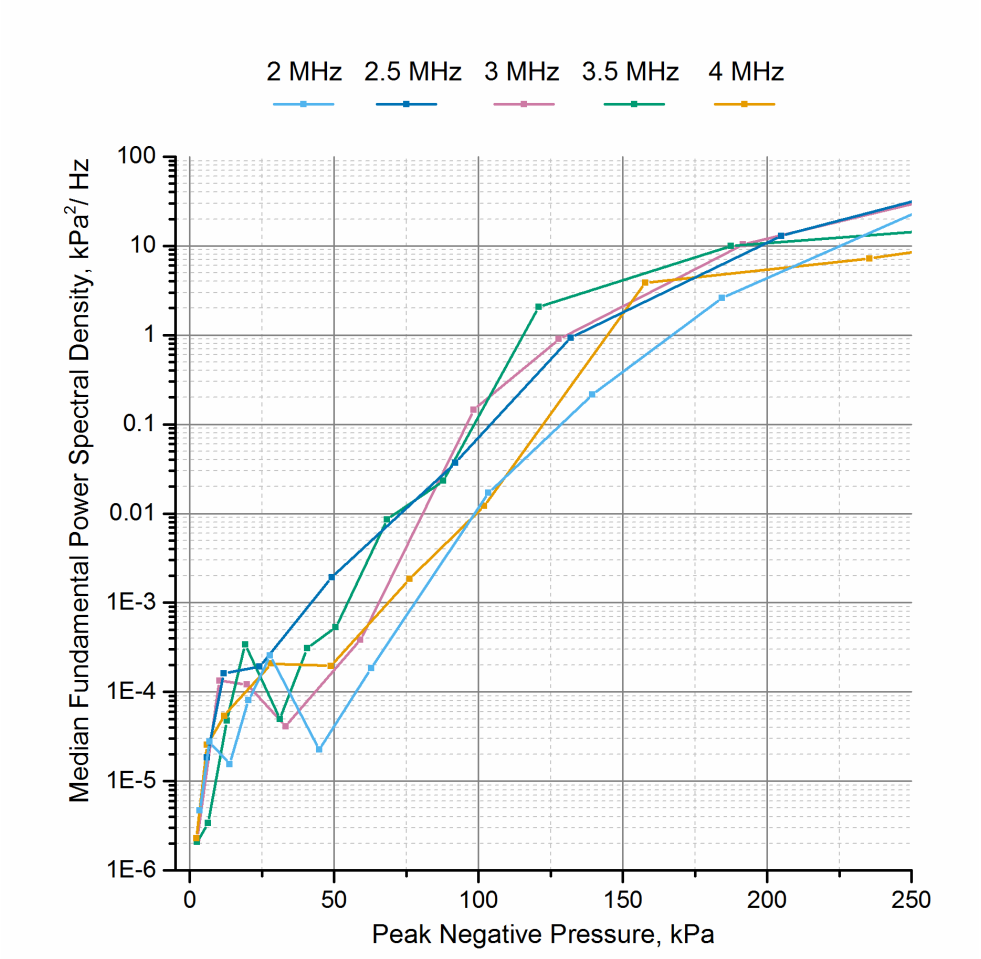

Figure 4.21: Median fundamental scattered pressure power as a function of peak negative pressure and plotted for driving frequency.

The size dependence on the fundamental scattered pressure is shown in Figure 4.22. Here it can be seen that up to a peak negative pressure of around 120 – 130 kPa the scattering power increases proportionally with size. This is in agreement with the expansion ratios (Figure 4.12) and the total scattered pressure (Figure 4.21) that showed the same trend. At higher pressures the largest expansions were dominated by the smallest microbubbles, interestingly; however this does not manifest in the fundamental scattered pressure where there is less clear dependency on initial radius.

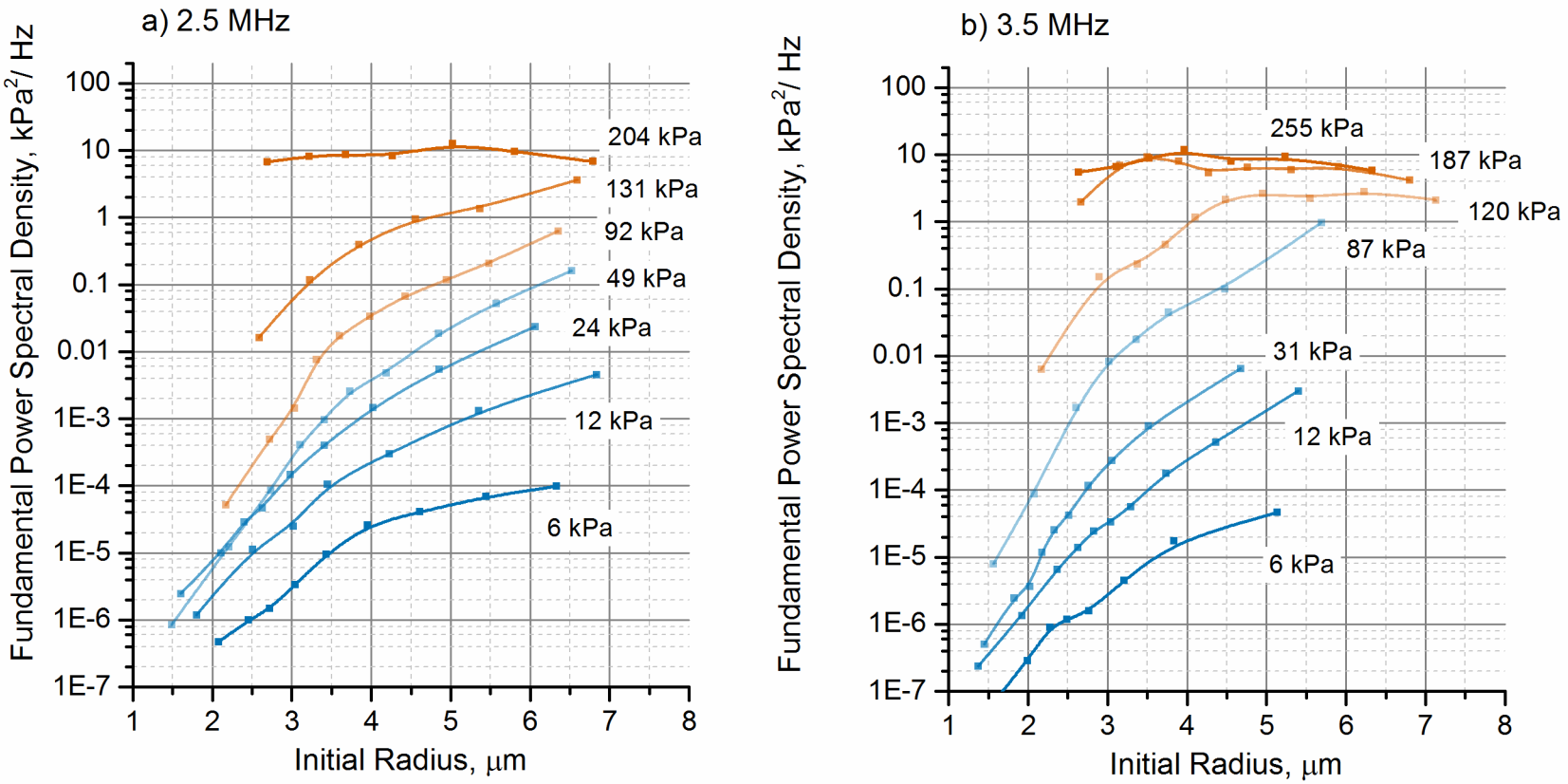

Figure 4.22: Median fundamental scattered power as a function of initial radius plotted for driving peak negative pressure and frequencies, a) 2.5 MHz and b) 3.5 MHz. Each point represents at least 100 individual microbubble responses.

4.3.2. Nonlinear scattered pressure

As discussed in Section 1.2.1, CEUS imaging exploits a microbubble's large scattering cross-section and nonlinear response to distinguish microbubble signals from those due to the surrounding tissue – specifically to sub-harmonic, harmonic, and fractional harmonics in the scattered pressure. The nonlinear response is investigated through the following three graphs. Here Sub-harmonic refers to any frequency components below $0.75f_0$ and harmonic refers to components above $1.5f_0$, as in Figure 4.23 that shows the respective scattered powers. Here it can be seen that both the sub-harmonic and harmonic power components follow the same trend as the fundamental power component (Figure 4.21) as the peak negative driving pressure increases. Interestingly, a similar discontinuity is observed for all driving frequencies at around a peak negative driving pressure of 25 kPa for both the sub-harmonic and harmonic components. The cause of this is not known, however, unlikely to be an artefact of measurement uncertainty giving that it is observed at all driving frequencies (on new samples from the same microbubble population). The size dependence for the sub-harmonic and harmonic components, Figure 4.24, again shows a similar trend to that of the fundamental scattered power with respect to initial radius (Figure 4.22), where the scattered power is proportional to initial radius up to higher pressures of around 120 kPa – 187 kPa. This relationship is of considerable interest to the application of CEUS imaging. For example at a peak negative pressure of 50 kPa, the scattered harmonic power is ~100,000 times greater for a microbubble with an initial radius of 5 μm compared to 2 μm.

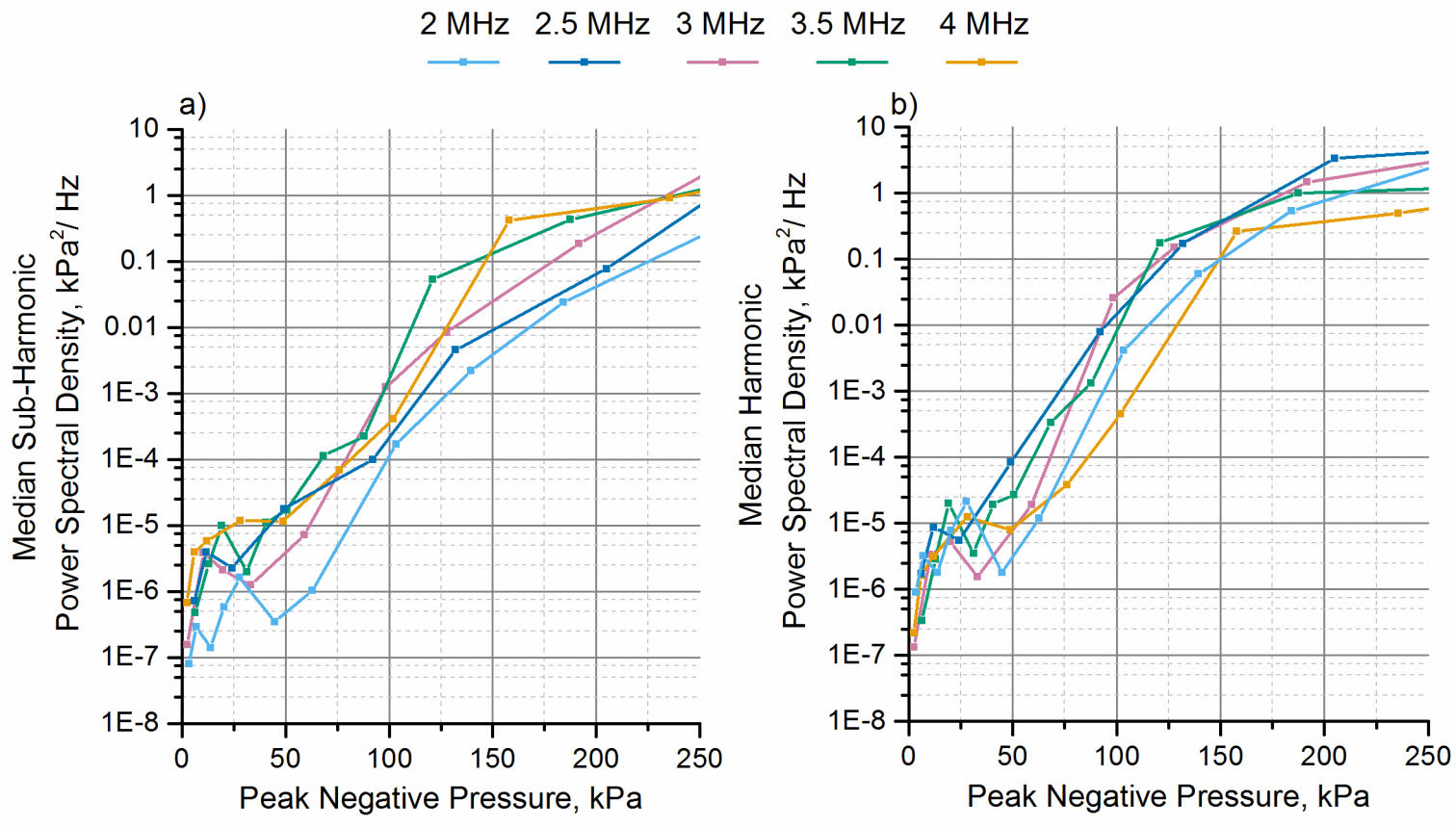

Figure 4.23: Median Sub-harmonic (a) and harmonic (b) scattered power as a function of driving peak negative pressure. For comparison the pressure magnitude of the ultrasound excitation pulses for both subharmonic and harmonic frequencies is given in Appendix A4.

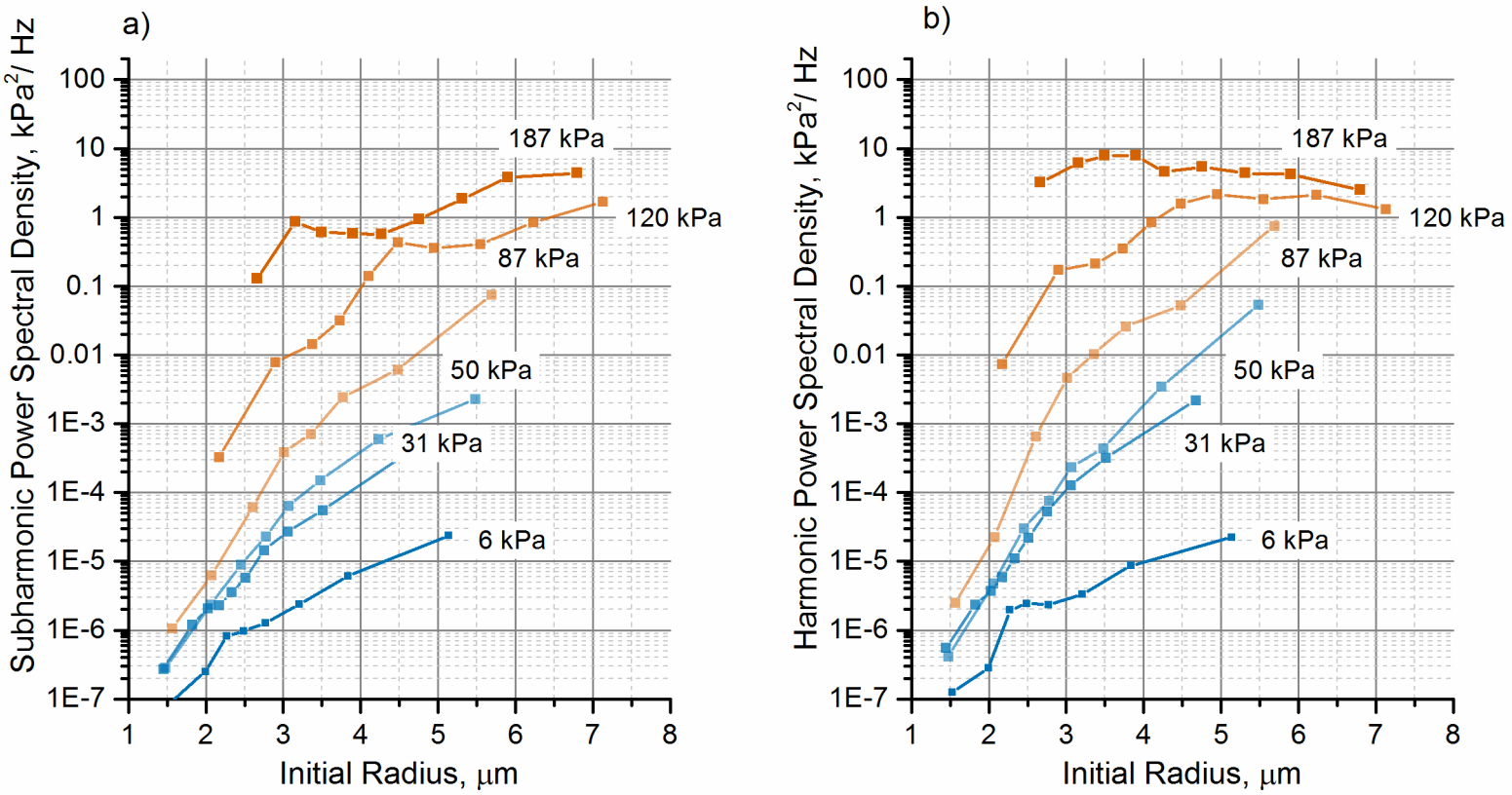

Figure 4.24: Median Sub-harmonic (a) and harmonic (b) scattered power as a function of initial microbubble radius, plotted for driving peak negative pressure at a frequency of 3.5 MHz. Each point represents a minimum of 100 samples.

4.4. Stability

Microbubble stability refers to the ability of a microbubble to remain in its initial state after ultrasound excitation, as well as over time. It is an important characteristic for three reasons, i) the predictability of a microbubble's behaviour is assumed to be related to its stability, ii) the efficiency of low power CEUS imaging relies on microbubbles surviving multiple excitations and iii) in the context of microbubble mediated therapy, for drug delivery it is desirable to understand how a microbubble will break down during ultrasound excitation and under which ultrasound conditions.

As described in Section 3.2, the microfluidic device not only measures the microbubble size before and during ultrasound excitation but also afterwards. The resting radius after ultrasound excitation can give an indication to the microbubble's initial stability and, as discussed in Section 4.1.2, an indication of the loss of lipid from its coating, termed lipid shedding. Lipid shedding has been observed in several studies, an example below is shown from a high speed fluorescence imaging study by Luan *et al.* [124]

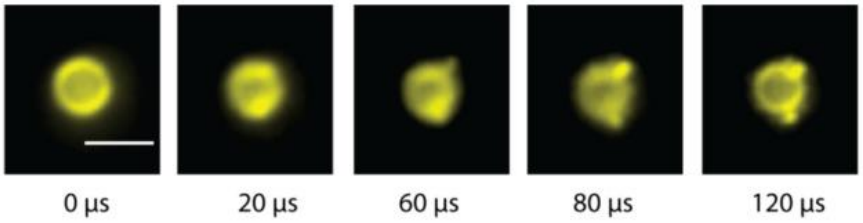

Figure 4.25: High Speed fluorescent images of a phospholipid microbubble driven at a acoustic pressure of 255 kPa and pulse length 100 cycles. During and after ultrasound excitation 'budding' can be observed, suggested to be due to the shedding/rearrangement of lipid. Image taken from Luan et al. [124]

Previous studies have shown that the same microbubble will respond differently on repeated excitations, similar to what was demonstrated in the pressure chamber experiments (Figure 4.1). Unfortunately, with the microfluidic device as set up in Chapter 2, there is not enough time for repeated ultrasound excitations of the same microbubble before it leaves the focussed laser beam. However, it is common for the microbubbles to change in size after single excitations of 5 cycles. Examples of the typical responses that have shown a decrease in radius after ultrasound excitation are shown in Figure 4.26. From these examples it can be seen that it is difficult, if not impossible, to assess if the change in size is gradual over the course of the excitation or occurring at a specific expansion/compression.

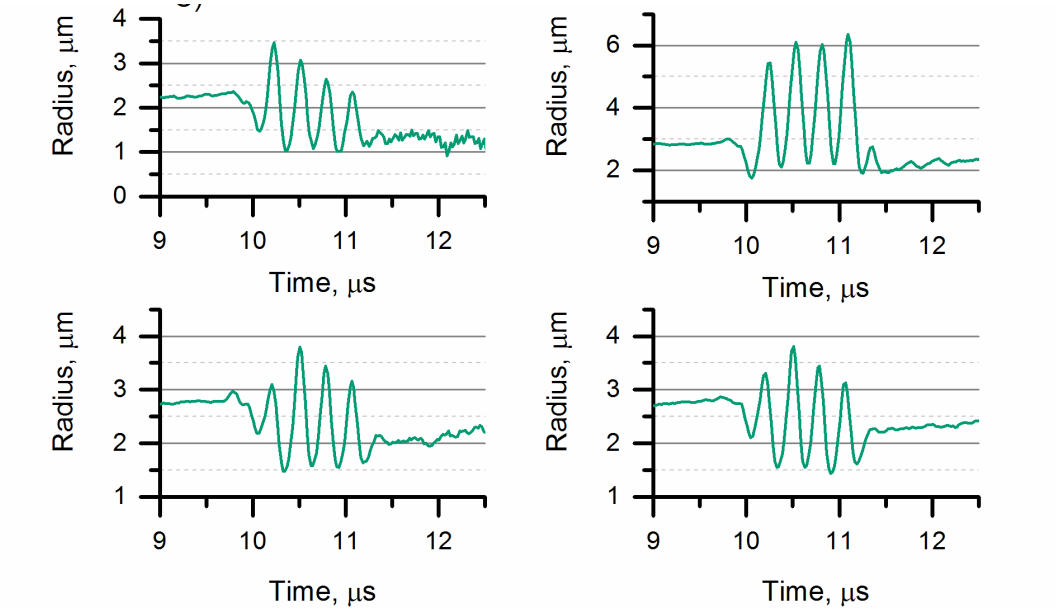

Figure 4.26: Examples of SonoVue® responses that show a significant decrease in size after or during ultrasound excitation.

Figure 4.27 shows that there is a large variation in the change in microbubble size as observed at peak negative pressures of 50 kPa and 120 kPa at 3.5 MHz. As the pressure is increased the distribution shows a much larger decreases in size, particularly for microbubbles of an initial radius > 3.5 µm. At the lower pressure of 50 kPa it appears that the smaller microbubbles show the largest decrease in size. For both, it can be seen that there are samples that appear to increase in size, although they are not within the 95th percentile. Two examples are shown in Figure 4.28 below; the author is unaware of this being reported in any previous works, although this phenomenon was observed in two cases in the pressure chamber experiments shown in Figure 4.2. This finding agrees with the idea of a rearrangement of the lipid coating and suggests that the microbubbles may have been oversaturated with lipid which, during the ultrasound expansion, was able to rearrange to cover a larger surface area.

Throughout all experiments an increase in size was only ever observed for less than 3 % of the samples and therefore the effect to CEUS imaging is assumed to be negligible.

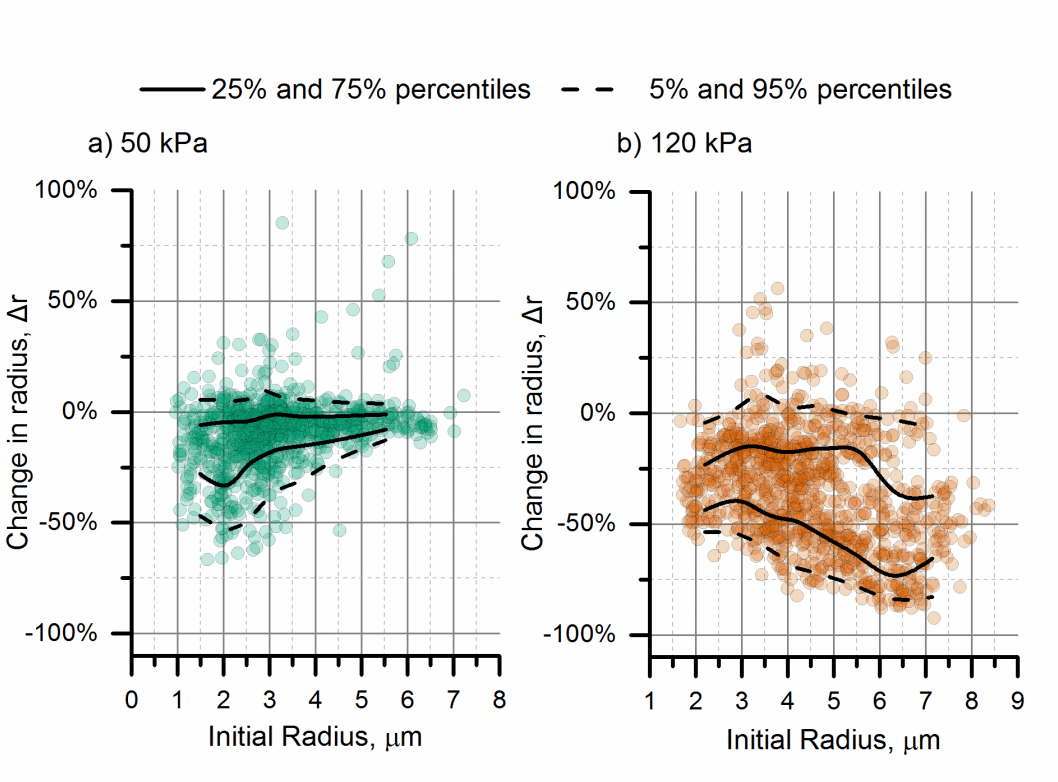

Figure 4.27: Change in individual microbubble radius' after ultrasound excitation as a function of initial microbubble radius at peak negative pressures of a) 50 kPa and b) 120 kPa. Ultrasound driving frequency is 3.5 MHz. Solid lines show 25th and 75th percentiles and dashed lines show 5th and 95th percentiles.

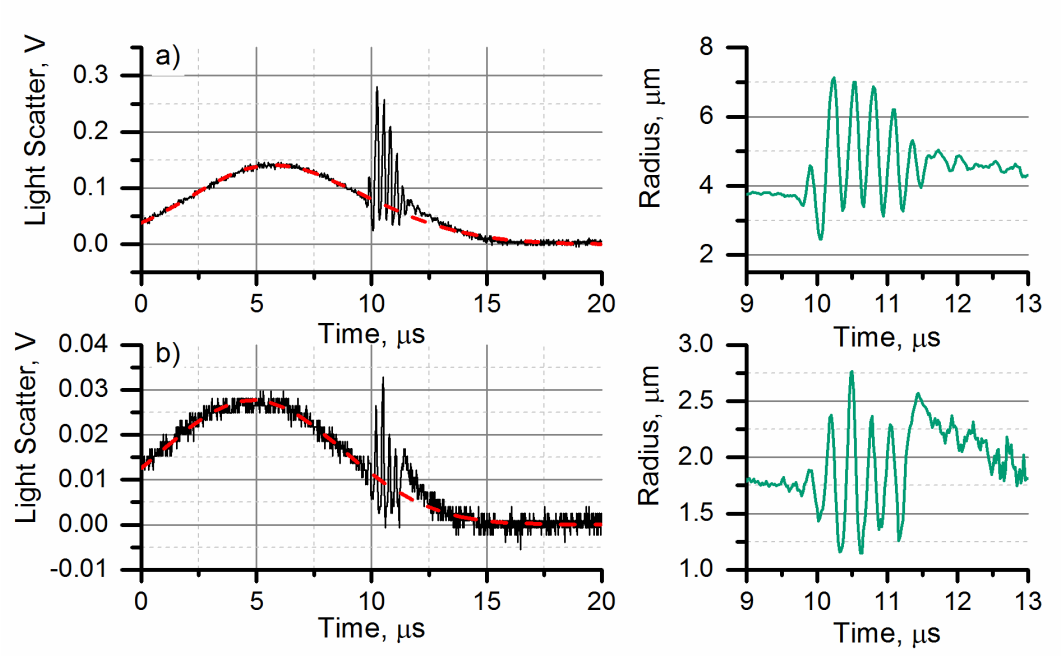

Figure 4.28: Examples of microbubbles appearing to increase in size after ultrasound excitation, both examples are at a peak negative driving pressure of 50 kPa, frequency of 3.5 MHz and 5 cycles. Figures on the left hand column show the raw light scattering data and the fitted curve used for size estimation (red dashed line), figures on the right show the same examples but calibrated to µm.

4.4.1. Pressure and frequency dependence

The effect of driving pressure and frequency on the median change in size is shown in Figure 4.29. As would be expected there is a fairly monotonic and linear relationship with the decrease in size and increasing pressure. The percentiles (dashed lines) show that there is a large variation in the populations which overlap for driving frequencies of 2.5 MHz and 3.5 MHz. A 200 kPa, 5 cycle pulse will reduce the majority of microbubbles by 50% of their original size, which equates to a change in surface area of 4 times. This may have significant implications for the delivery of drugs that are can be attached to the lipid coating of a microbubble.

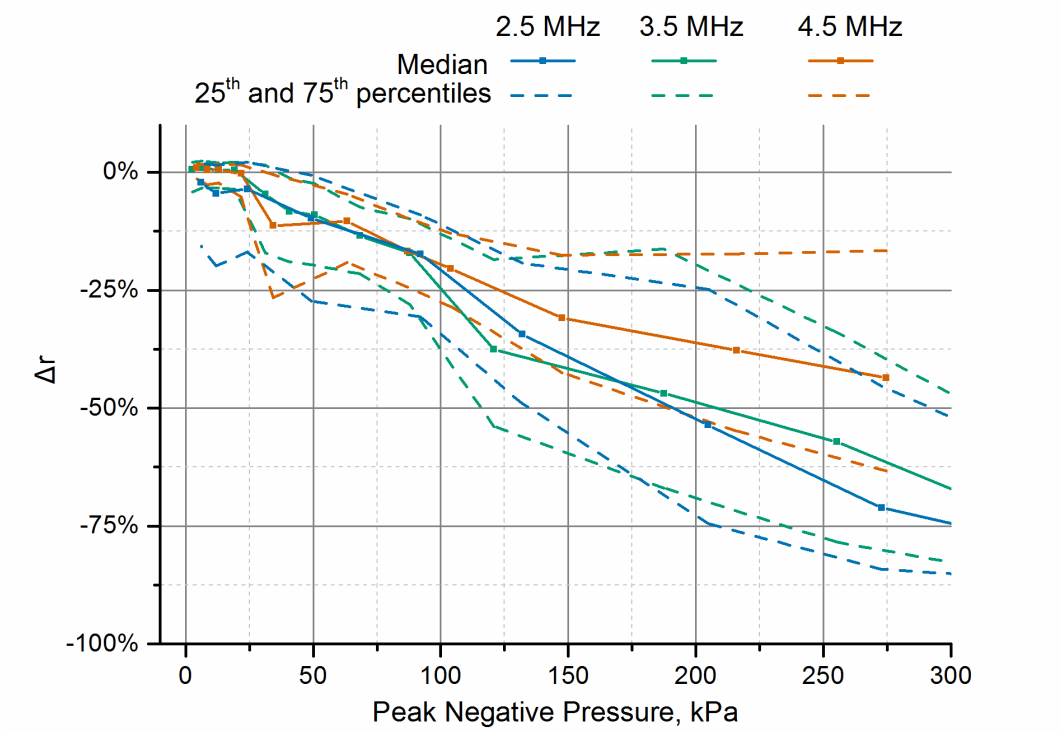

Figure 4.29: Median change in microbubble radius after ultrasound excitation as a function of peak negative driving pressure plotted for varying driving frequencies. Dashed lines represent 25th and 75th percentiles and Solid lines represent the median. Each point represents at least 100 microbubbles.

4.4.2. Initial size dependence

The effect of initial size on the microbubble's stability is investigated in Figure 4.30. It was seen previously that size plays an important role in the magnitudes of a microbubble's radial expansion and scattered pressure. The results in Figure 4.30 suggest that at pressures above 120 kPa the larger the microbubble the greater its change in size after ultrasound excitation. Below 87 kPa it appears to be fairly constant for all microbubble sizes. Interestingly this trend correlates with the compression ratios shown in Figure 4.12.b. However, it is difficult to assess the cause of this phenomenon and the fact that the smaller microbubbles appear to decrease less in size as the pressure increases above 187

kPa. At these pressures it is the smallest microbubbles that show the largest expansions, which appears to be contrary to the findings here. This might suggest that the initial state of larger microbubbles makes them less stable and more likely to shed/loss lipid and form smaller microbubbles after excitation.

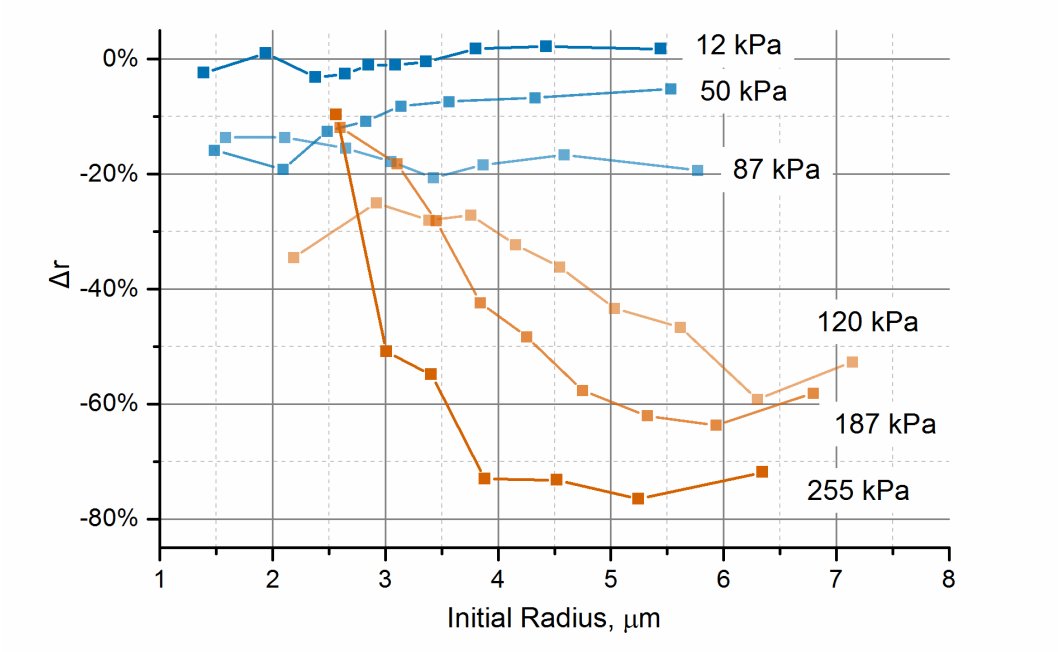

Figure 4.30: Median change in microbubble radius after ultrasound excitation as a function of initial radius plotted for varying driving peak negative pressures from 12 kPa up to 255 kPa. Ultrasound driving frequency is 3.5 MHz at 5 cycles. Each point represents at least 100 microbubbles.

4.4.3. Effect of number of cycles

As well as varying the driving frequency and pressure, the number of ultrasound cycles in each pulse has also been varied. The only difference observed was a reduction in the change in microbubble radius after 3 cycles when compared to 5 or 8 cycles at driving pressures above 50 kPa, Figure 4.31.

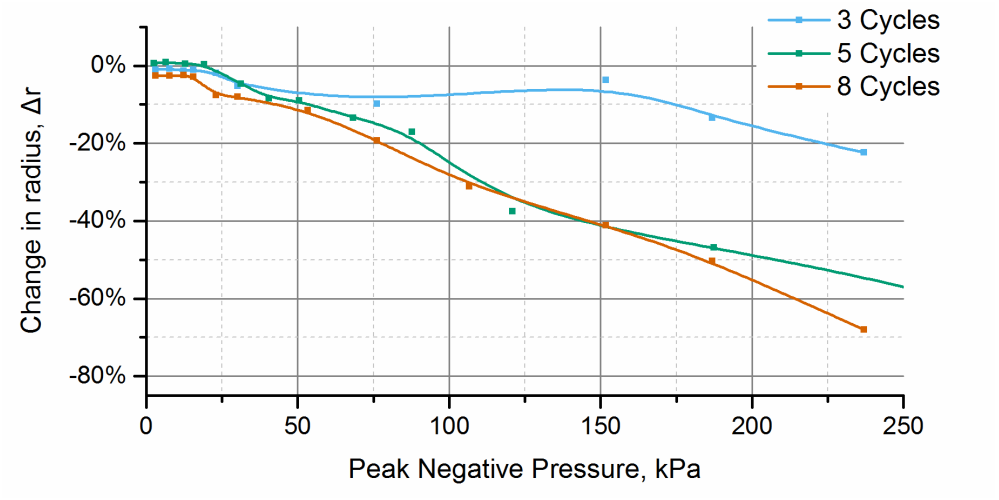

Figure 4.31: Change in radius after ultrasound excitation as a function of peak negative driving pressure, plotted for varying number of ultrasound cycles. Driving frequency is 3.5 MHz.

This trend is intuitive; however, it also correlates with a decrease in the amplitude of radial response for a 3 cycle pulse length at peak negative pressures above 186 kPa, Figure 4.32. Here it can be seen that for peak negative pressures below 76 kPa there is little difference between the expansion ratio and the number of cycles, however at higher pressures a proportional difference becomes clearer. These findings suggest that at peak negative pressures below 100 kPa that the length of the ultrasound pulse (varying from 3 – 8 cycles) has minimal effect on the radial response and stability. However, at higher pressures the median response amplitude appears to be proportional to the length of the pulse.

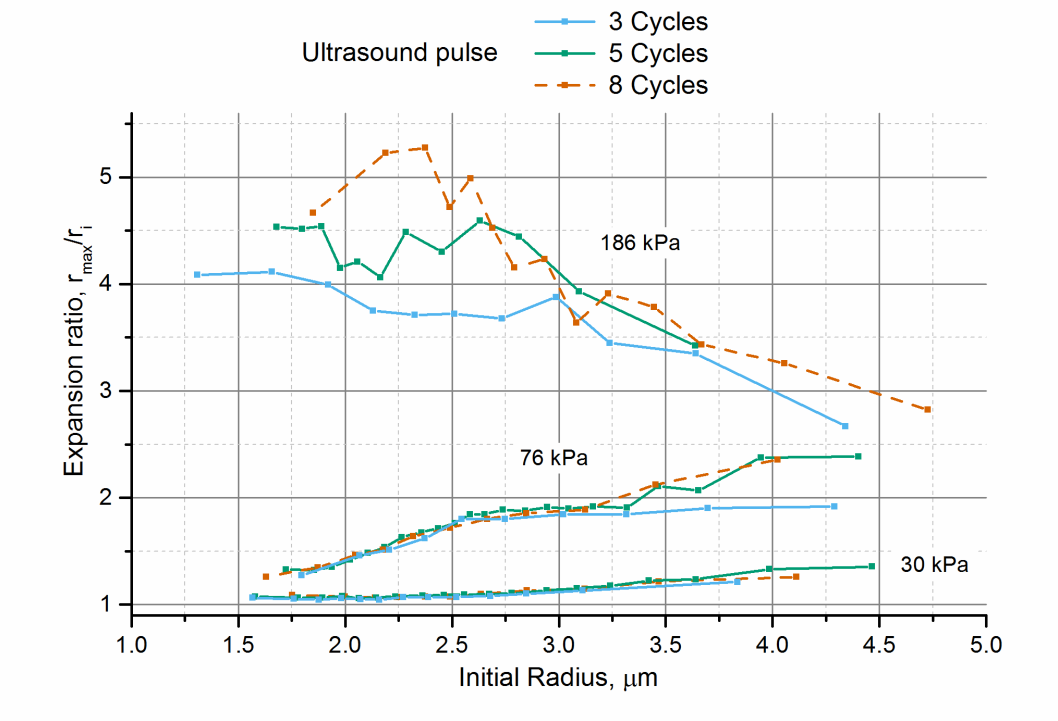

Figure 4.32: Expansion ratio of SonoVue® as a function of initial radius, plotted for varying length of cycles in ultrasound pulse at increasing driving pressures. Ultrasound driving frequency is 3.5 MHz.

4.5. Threshold Behaviour at Twice the Initial Radius

From the results presented so far there is a trend so prevalent that it deserves its own section. The trend is that at around a pressure of 100 kPa there seems to be a significant shift in behaviour of the majority of microbubbles in a population. At around a peak negative pressure of 100 kPa for all the driving frequencies investigated (2 MHz – 4.5 MHz) the following significant behaviours have been observed: i) The majority of microbubbles show expansion dominated behaviour, ii) The expansion ratio intercepts with the compression ratio, iii) The expansion ratio becomes inversely proportional to microbubble initial radius iv)

and the estimated scattered power shows a similar trend and, v) there is a sudden size dependency on the decrease in size after ultrasound excitation.

On closer inspection it can be seen that between a peak negative pressure of 100 kPa and 150 kPa, the majority of microbubbles are showing an expansion ratio of twice their original size, Figure 4.33. At this point there appears to be a significant change in the expansion ratio with respect to initial radius: Microbubbles smaller than 4.5 µm start to show larger expansions than microbubbles greater than 4.5 µm, which is the opposite trend at expansions below this threshold. Practical implications aside, this finding agrees and provides evidence for the theoretical work developed by Flynn [130], [131]. Flynn predicted that there is a transition expansion radius, R_t, that occurs at around expansions ratios of $2r_0$ for a microbubble with an initial radius of 5 µm, Figure 4.34. Flynn states that above this transitional expansion radius *'the inertial forces in the liquid supply an ever- increasing amount of kinetic energy to the cavity and an ever-decreasing fraction of this energy will be lost through dissipative mechanisms'* [131] and suggests this to be a threshold for inertial cavitation, or the observation of bio effects commonly attributed to cavitation; erosion, chemical reactions and sonoluminescence. The theory shows that there is a significant size dependence of the transition radius where the lowest transition occurs at 5 µm and increases either side of it. This minimum is caused by the intersection between the expansion ratios that relate to the maximum fraction of dissipated energy, R_d, and the equilibrium of inertial and pressure forces, R_c.

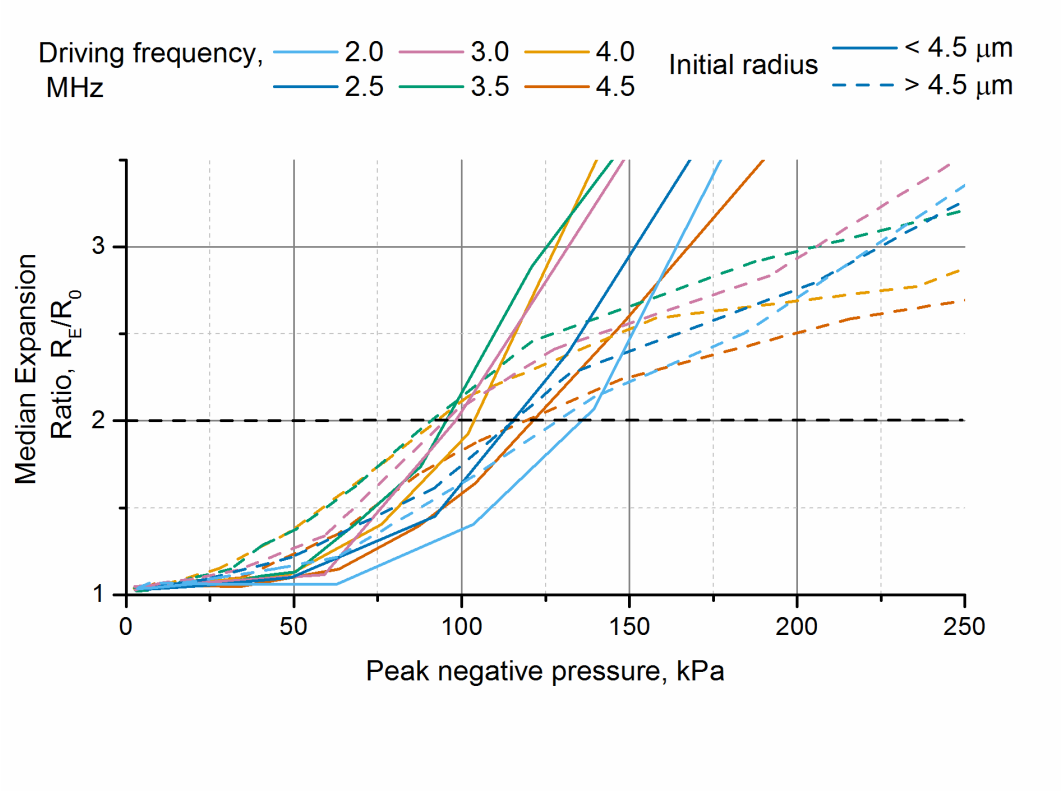

Figure 4.33: Median expansion ratio as a function of peak negative pressure at varying driving frequency. Samples are separated into two size categories: < 4.5 µm (solid lines) and > 4.5 µm (dashed lines). It can be seen that there is a transition that occurs around an expansion ratio of 2 and peak negative pressure of 100 kPa.

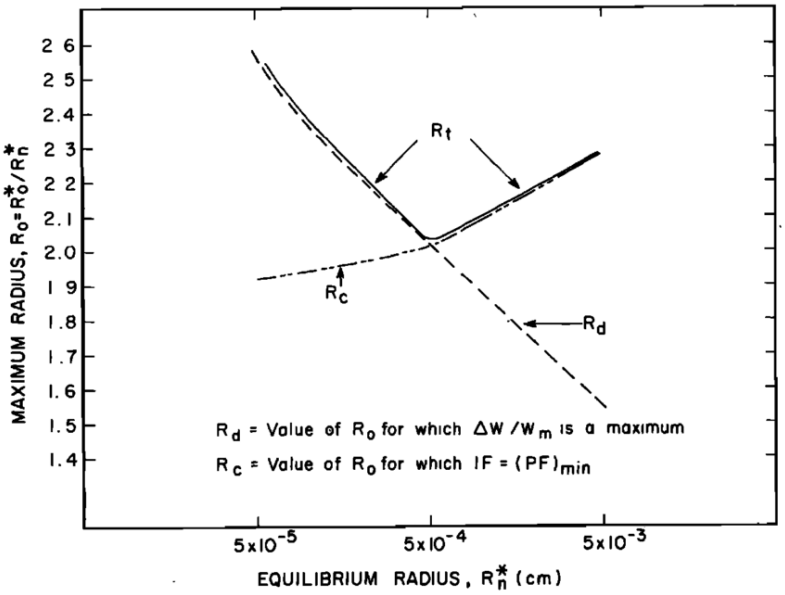

Figure 4.34: Radius thresholds as a function of the initial radius, R_n^*. Maximum radius is the expansion ratio with respect to the initial radius. R_c is the maximum radius at which the pressure and inertial forces due to acceleration intersect, R_d is the maximum radius at which the fraction of dissipated energy is greatest and R_t represents the maximum radius that is always greater than both of the former, this is suggested the point at which the effects of cavitation are observed. Figure taken from [131]

It may come as a surprising result that 'inertial cavitation' by Flynn's maximum radius definition is being observed in this work at pressures as low as 100 kPa. Apfel and Holland [132] calculated the minimum cavitation threshold, based on the internal temperature of a microbubble exceeding 5000 K which is derived from Flynn's definition [133], and showed that the threshold is frequency dependent, at a frequency of 3.5 MHz the cavitation threshold is estimated to be around 0.6 MPa for a range of nuclei sizes, Figure 4.35. However, Church later investigated the effect of microbubble radius on the cavitation threshold based on both of the above criteria and found that there is a size dependence with

thresholds as low as 100 kPa for a 1 µm air bubble when driven at 3 MHz for 4 – 10 cycles [133].

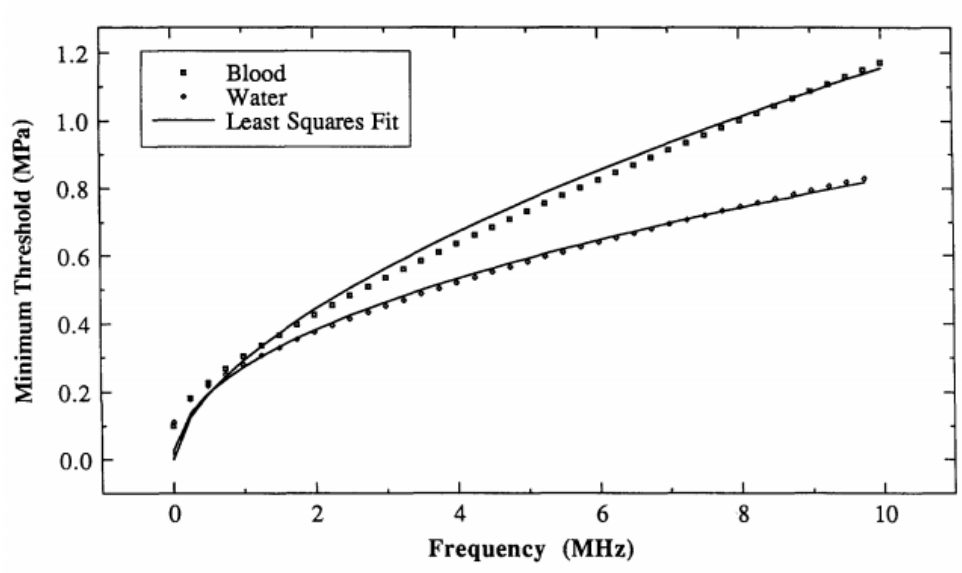

Figure 4.35: Minimum cavitation threshold modelled for blood and water as a function of driving frequency. The threshold is based on the internal temperature of the microbubble exceeding 5000 K. Figure taken from [132].

Experimental observations of cavitation are usually assessed based on the detection of increased broadband noise. A recent study by Tung *et al.* [134] observed sudden appearance of increased broadband noise at 0.45 MPa when imaging at 100 cycles, at 1.525 MHz. This approach is, however, limited by the sensitivity of the receiving ultrasound transducer. The implications of these findings are discussed in more detail in the concluding remarks of this chapter.

4.6. Summary of Findings

This chapter investigated the behaviour of SonoVue® microbubbles with respect to ultrasound exposure parameters (driving frequency, peak negative pressure and number of cycles) and initial microbubble radius. The main findings are as follows:

i. There is significant variation in microbubble radial response that is independent of initial radius (Figure 4.3). This is supported by direct measurements of coating properties (Figures 4.5 and 4.6) and observations of behaviour under controlled hydrostatic pressure (Figure 4.2).
ii. Size dependent trends are however evident when observing large sample numbers (Figure 4.8).
iii. There is a transition from compression to expansion dominated behaviour as the peak negative driving pressure increases from 50 kPa up to 100 kPa (Figure 4.16).
iv. Up to peak negative pressures of 100 kPa the expansion ratio is proportional to initial microbubble radius, above this pressure this trend becomes inversely proportional (Figure 4.12).
v. Nonlinear responses are observed as compression and expansion dominated behaviours at pressures as low as 6 kPa (Figure 4.15)
vi. The estimated fundamental scattering acoustic power shows a proportional relationship with peak negative pressure up to around 20

kPa; from 20 kPa to 40 kPa there appears to be less or no gain in the scattered pressure, however above 50 kPa the proportional relationship resumes, there is no evidence of resonance effects (Figure 4.19)

vii. Nonlinear radial and estimated acoustic responses were observed at peak negative driving pressures as low as 6 kPa. The nonlinear and fundamental acoustic emissions follow a similar trend (Figure 4.24)

viii. Evidence of lipid shedding by the change in size of microbubbles after ultrasound excitation is presented (Figure 4.26) and it is shown that there is a linear relationship with pressure and decrease in size (Figure 4.29) and this effect increases with the number of cycles in an ultrasound pulse (Figure 4.31)

ix. 'Inertial Cavitation' defined as a microbubble expanding twice its initial radius is shown to occur between 100 kPa and 150 kPa for the majority of microbubbles in a population at all frequencies tested (Figure 4.33)

x. Above this threshold, microbubbles smaller than 4.5 µm show higher expansion ratios than those larger than 4.5 µm which is the opposite trend to below this pressure (Figure 4.33). This agrees well with the theoretical predictions (Figure 4.34)

4.7. Implications of Findings

Given these findings can the behaviour of SonoVue® microbubbles be further exploited to optimise current CEUS imaging techniques?

4.7.1. Scattered pressure - stability trade-off

As discussed there are three microbubble characteristics that are desirable to maximise for the optimisation of current CEUS imaging techniques: i) echogenicity, ii) nonlinear response and iii) stability. Figure 4.36 demonstrates an important trade-off that exists with microbubble response and change in size after ultrasound excitation. With increasing, nonlinear and linear, back scattered pressure response from SonoVue® there is a significant decrease in microbubble stability, such that it is desirable to image at as low peak negative pressures as possible. This work found no evidence of a nonlinear behaviour pressure threshold, suggesting that current CEUS techniques are partly limited by the receiving sensitivity, bandwidth and SNR of the ultrasound hardware. However, there is a trade-off with SonoVue® stability and its acoustic response. As in the figure below, at a driving frequency 3.5 MHz, the majority of SonoVue® microbubbles were observed to show a decrease in size greater than 50% at driving peak negative pressures of 200 kPa and above.

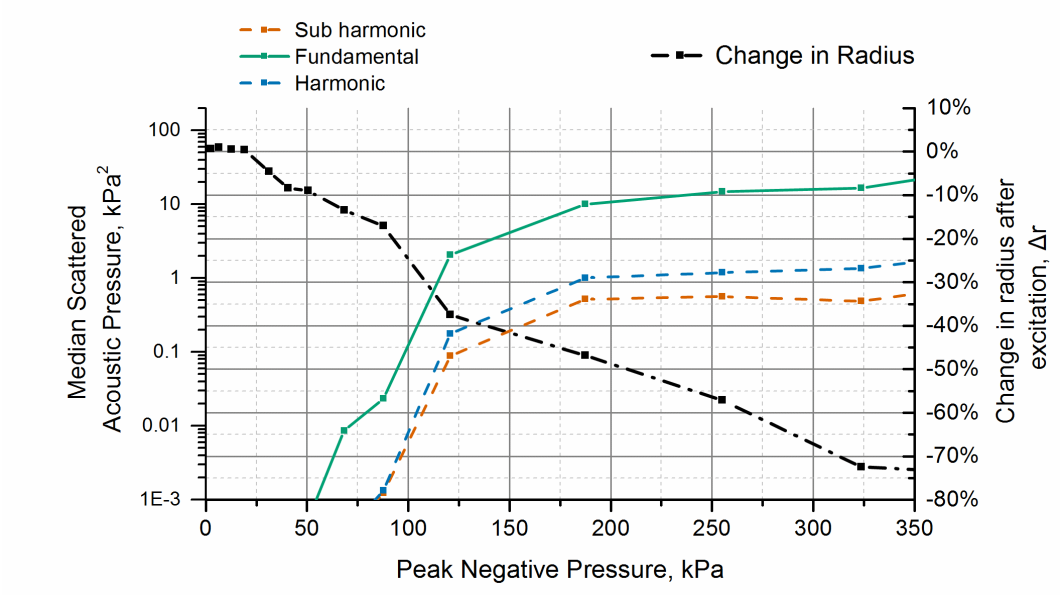

Figure 4.36: Median scattered pressure (fundamental – solid line, and nonlinear – dashed lines) estimated from the radial response of over 3000 individual SonoVue microbubbles as a function of the peak negative pressure (ultrasound parameters: 3.5 MHz, 5 cycles pulse length). On the second axes the median change in microbubble size is plotted for comparison.

4.7.2. Significance of microbubble size distribution

It is commonly assumed that the initial size of a microbubble determines its resonant behaviour, such that it is desirable to match the ultrasound imaging frequency to a population's mean resonant frequency. However, the findings from this thesis have found little evidence of resonant effects as a function of initial microbubble size and, that, any significance of apparent resonant responses appear to be further reduced when considering the estimated back scattered pressure (Section 4.3). It was found that there is a proportional relationship between the scattered pressure and microbubble size at pressures below 100 kPa, such that the SNR and CTR for CEUS imaging would be enhanced by microbubble populations that have a larger mean size. However, at higher

peak negative pressures above 100 kPa, typical for CEUS imaging, the initial size of the microbubble has less effect on the back scattered pressure since larger expansions compensate for the smaller scattering cross sections.

4.7.3. Length of ultrasound pulse

As discussed in Section 1.2.2, a new CEUS technique termed 'Coded Excitation' is being developed that exploits larger microbubble oscillations that occur when increasing the ultrasound pulse length. The results in this thesis have shown that this effect occurs at higher ultrasound pressures above 100 kPa when comparing ultrasound excitation lengths of 3 cycles to 8 cycles. However, the longer cycle lengths also resulted in decreased microbubble stability, which should be considered if that is a requirement for efficient imaging. Therefore, at peak negative pressures below 100 kPa, a pulse length of 3 cycles improves the microbubble lifetimes (based on stability) while obtaining the same magnitude of back scattered pressure when compared to pulse lengths of 5 or 8 cycles.

4.7.4. Implications towards other clinical applications

The findings have also raised two interesting observations for which the implications should be further discussed. They are that i) 'inertial cavitation', defined as a microbubble expansion of twice its initial size, occurs at pressures as low as 100 kPa and ii) the large variability of SonoVue microbubble response makes them unsuitable for the prospect of CEQUS, i.e. quantitative ultrasound imaging that was discussed in Section 1.2.3

Briefly, it has been demonstrated that the presence of microbubbles under ultrasound excitation are able to enhance several therapeutic applications, such as the breakdown of thrombus, drug/gene delivery and thermal ablation of tissue using High Intensity Focussed Ultrasound (HiFu) [135]. These applications typically use lower driving frequencies around 0.5 MHz and much higher pressures than have been investigated in this study. One possible mechanism for the enhancement is commonly attributed to the violent and sudden collapse of microbubbles. However, this is an active field of research for which the mechanisms are poorly understood, it is also not known if Flynn's inertial cavitation threshold necessarily relates to the bioeffects observed in these studies. However, the results in this thesis have shown large microbubble expansions at lower pressures than have been observed previously. It is therefore suggested that therapeutic studies should consider investigating these effects at lower pressures (at least for driving frequencies between 2 MHz and 4.5 MHz) of around 100 kPa. The findings have shown that the majority of SonoVue® microbubbles are undergoing 'inertial cavitation' at this pressure without significant loss of size, which may make this 'low' pressure approach more efficient. The collapse of microbubbles could be further investigated using a higher bandwidth PMT amplifier in order to observe the sudden collapse characteristic of microbubble inertial cavitation, the experimental requirements for which are discussed further in Section 6.3.1. Examples of the radial responses observed with a bandwidth of 8 MHz are shown below in Figure 4.37.

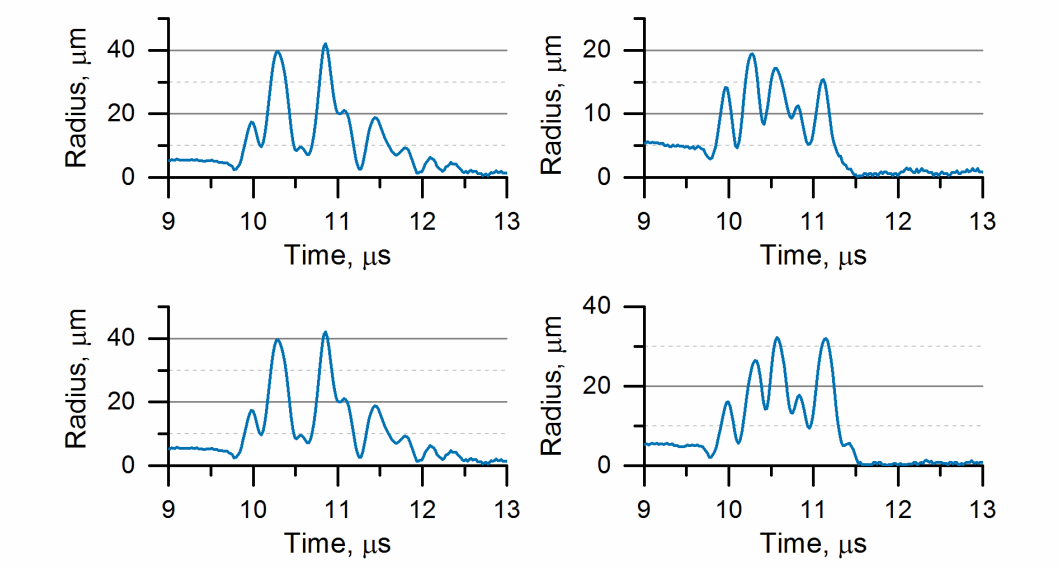

Figure 4.37: Examples of SonoVue radial response when driven at a peak negative pressure of 0.69 MPa, driving frequency of 3.5 MHz and pulse length of 5 cycles.

As for CEQUS (quantitative ultrasound imaging), it is suggested that more stable and predictable microbubbles are required than SonoVue®. The effect of fabrication and composition on microbubble response is investigated in the following Chapter 5. For such sensitive measurements, the response of microbubbles *in vivo* must also be considered, as will be discussed, *in vivo* conditions are likely to affect a microbubble's acoustic response.

4.8. Relevance to *in vivo* Conditions

A key feature of the design in Chapter 2 is the ability to measure the response of single microbubbles isolated from each other and physical boundaries. This is useful for a fundamental understanding of their behaviour and to allow comparisons to the theoretical models that make these simplifying assumptions. Unfortunately, however, the environmental conditions that

microbubbles experience *in vivo* during CEUS imaging are significantly different to those corresponding to the data presented in this thesis. *In vivo*, microbubbles are not only flowing in the confinement of each other, vessel walls and blood cells but they will also pass through regions of changing hydrostatic pressure and ambient temperature. Even before microbubbles reach the vasculature, the preparation and injection of them has been shown to alter their size distribution [136]. Therefore to place these findings into context, it is important to consider the effect of *in vivo* conditions on a microbubble's response.

4.8.1. Population response

It has been observed in multiple studies that the attenuation and backscattered pressure of ultrasound increases proportionally to microbubble concentration [137]–[139]. However, it is difficult to assess the local concentration of microbubbles *in vivo* as it is largely dependent upon the injection duration, initial concentration and the location of imaging [137]. From the vial, SonoVue® microbubble concentrations are to the order of 10^7 to 10^8 per ml and volumes of up to 4 ml can be injected during routine CEUS imaging [36]. The ability to estimate the *in vivo* concentration based on the backscattered intensity would allow quantitative measurements of flow perfusion. The estimation of the backscattered pressure from SonoVue® microbubbles has shown that below driving pressures of 100 kPa the backscattered acoustic pressure is proportional to microbubble size. Although there is large variation in microbubble response, the mean or median response remains monotonic. Significantly, this work found no evidence of resonant effects that would disturb

this relationship. Therefore, it is suggested that if the microbubble size distribution were known, it would be possible to estimate concentration based on the backscattering amplitude. However, this makes two assumptions, i) *in vivo* environmental conditions do not change the properties of the microbubbles (i.e. size distribution, stability, magnitude of response) and ii) that a population's response is the sum of the individual microbubble responses. These two assumptions will be shown to not be justified in the following discussion.

The effect of microbubble proximity has been investigated by several authors. High speed imaging studies have observed that microbubble oscillations are reduced in the presence of another oscillating microbubble 8 µm away [140]. A theoretical model developed by Wiedemair *et al.* [141] predicted similar behaviour as well as increased non-spherical oscillations and a decrease in resonance frequency. Simulations using microbubble concentrations as would be expected *in vivo* by Stride *et al.* [138] showed that the effects of a microbubble's scattered pressure on neighbouring microbubbles during ultrasound excitation could be observed, is size dependent and proportional to the driving pressure of the ultrasound. The resulting effect was an increase in the ultrasound attenuation that agreed with experimental observations. However, it was not possible to quantifiably compare the theoretical models and the experimental results without knowing the microbubble coating properties.

4.8.2. Interactions with whole blood

Microbubbles *in vivo* are situated in blood plasma and are likely to be in close proximity to blood cells of comparable size. Since blood plasma is approximately 97% by volume water it can be assumed that there is negligible change in response from the experiments reported here due to the surrounding medium. An investigation into the effect of red blood cells in close proximity on microbubble behaviour by Stride *et al.* [142] found that due to the low backscattering from red blood cells and their relatively low elasticity that the predicted change in microbubble behaviour would be minimal. Again this agreed with their experimental investigation, showing only a marginal increase in attenuation when red blood cells were added to the solution *in vitro.* Other studies, however, have found significant effects*: A*t higher driving pressures Deng *et. al.* [143] observed a significant increase in the cavitation threshold in blood compared to water and Owen *et. al.* demonstrated significantly reduced targeting efficiency of biotinylated microbubbles in the presence of blood cells [144].

4.8.3. Effect of ambient temperature

In vivo the ambient temperature for a healthy patient is maintained at around 37 ^{o}C, however the results presented so far and the majority that have been reported in the literature are performed at room temperature. Experiments performed by Guiot, *et al.* [145] investigated the potential of microbubbles to be used to quantify hypothermia. In their experiments,

conducted over 15 - 90 minutes, they found that the microbubble size distribution was largest at 40 ^{o}C and then decreased again as the temperature approached the lipid's phase transition temperature. A more detailed investigation was performed by Mulvana *et al.* [146] with experiments over the course of 2 – 10 minutes. They found that the increase in the ambient temperature of SonoVue® decreased its stability over time, increased ultrasound attenuation at 3.5 MHz and decreased the mean back scattered pressure over a period of 10 minutes. Optical imaging also showed evidence of buckling and shape deformations of SonoVue® microbubbles that were kept at 40 ^{o}C for 10 minutes. The paper concluded by stating that 'measurements made at room temperature require careful interpretation before conclusions can be drawn regarding contrast agent behaviour *in vivo'*. This is certainly true and is an area that requires better understanding.

Experiments were performed for this work that investigated the effect of *in vivo* temperature on the response of individual SonoVue® microbubbles using the device described in Chapter 2. The experimental procedure followed as before except that the water tank and sheath flow were heated to 37 ^{o}C. To simulate clinical conditions, a vial of SonoVue® was prepared at room temperature following the manufacturer's instructions and diluted with deionised water at room temperature. This was then placed into the syringe (outside of tank at ambient room temperature) connected to the microfluidic device. The tubing to the microfluidic device and the device itself is in the heated tank such that the microbubbles will heat up as they travel through the tubing

and mix with the sheath flow. This set up means that although the measurements of individual microbubbles are obtained over the course of an hour, each microbubble experiences the same amount of heating. Given the flow rate of the syringe pump (20 µl/min), diameter of the tubing (400 µm) and the length of tubing in the tank (~ 20 cm) each microbubble is in the 37 ^{o}C environment (from exit of microfluidic device to ultrasound excitation) for an estimated 75 seconds. The results from Mulvana's study showed that the changes due to temperature were time dependent over the course of 5 – 10 minutes and found no measurable differences at 2 minutes. For a typical CEUS scan, depending on the location, imaging can take place within 30 seconds to 1 minute of injecting the microbubbles given that blood circulates the body roughly once every minute [147]. But the duration of the scan can last for several more minutes. Therefore the following results are a better representation of the initial scans within the first minute of injection. The size distribution of the samples analysed, Figure 4.38, appears to show no difference between microbubbles at 37^{o}C and 26^{o}C. Although, it must be noted that the size distribution is of microbubbles that are measured during the experiment and is also dependent on the threshold set on the oscilloscope during the experiment. Here it can be seen that the size distributions are comparable and the response categorisation is shown in Figure 4.39.

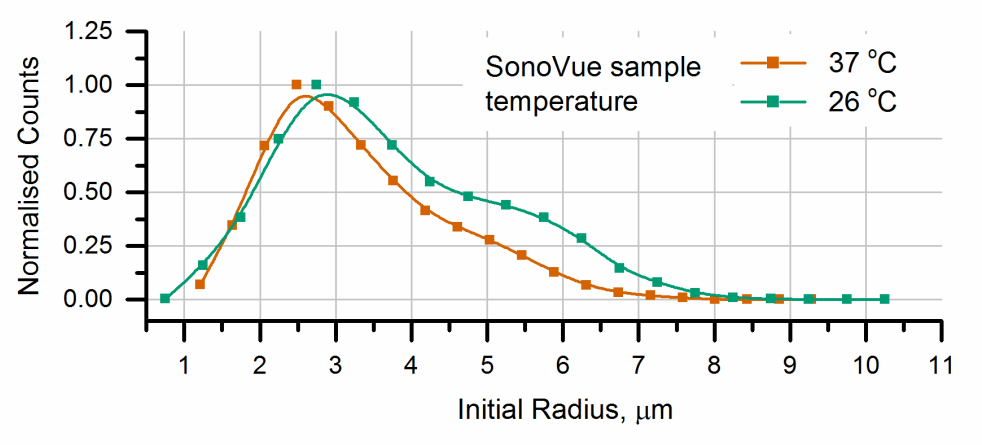

Figure 4.38: Size distribution of SonoVue® microbubbles analysed at room temperature (n = 12,266) compared to in vivo temperature of 37 °C (n = 19,179).

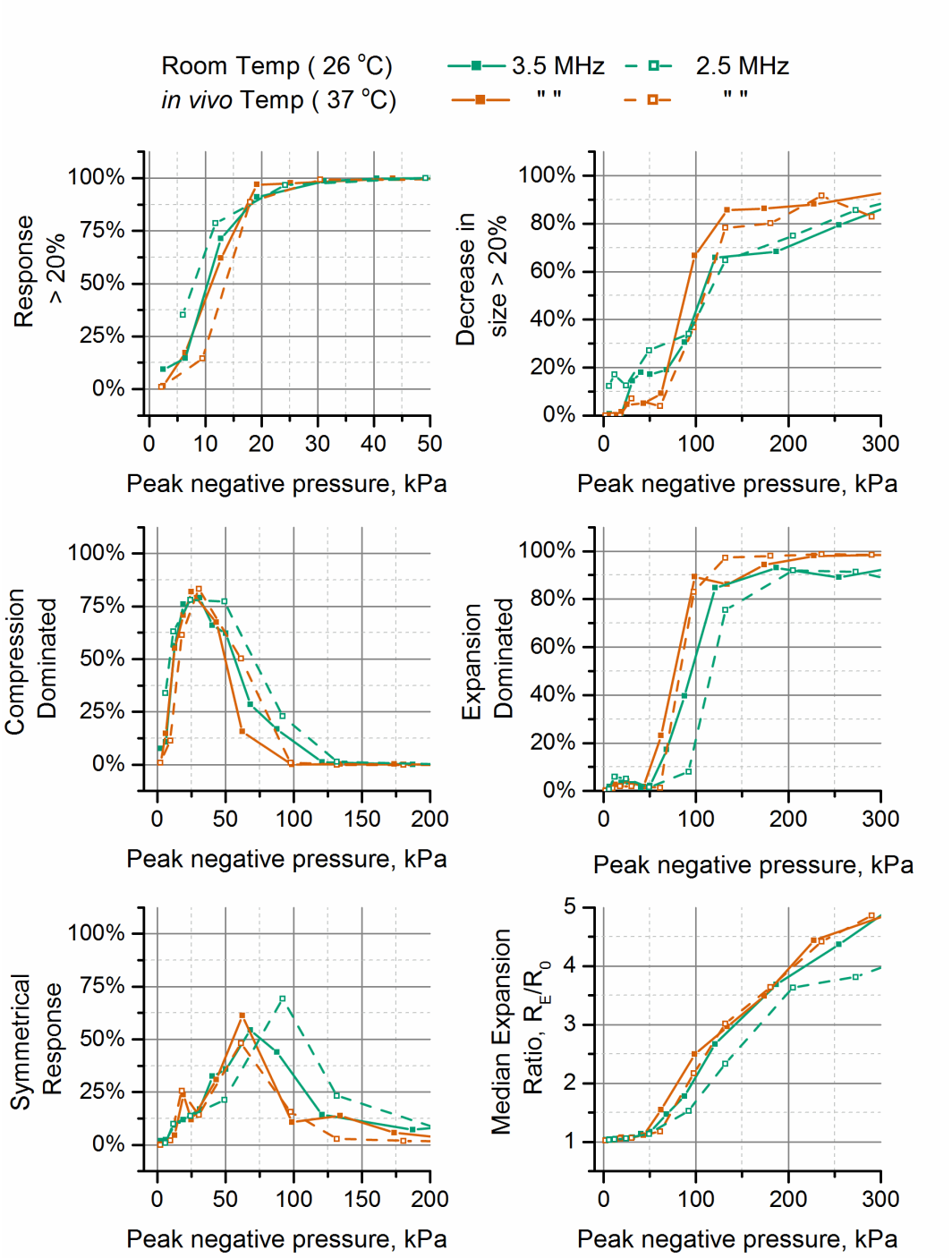

Figure 4.39: Response categorisation as a function of peak negative pressure comparing SonoVue® microbubbles at room temperature (26 °C) and in vivo temperature (37 °C for approximately 1 minute). The response are compared at two driving ultrasound frequencies of 3.5 MHz (solid lines) and 2.5 MHz (dashed lines)

The response categorisation (Figure 4.39) does not appear to show any significant differences between the microbubble responses at room temperature and *in vivo* temperature. There are two findings that are observed for both frequencies tested for the microbubbles at 37 ^{o}C; i) at peak negative pressures tested above 50 kPa there is an average of 16% more microbubbles undergoing expansion dominated behaviour ii) and above 100 kPa, there is an average of 15% more microbubbles decreasing in size by more than 20%.

Again, the categorisation gives a more qualitative representation of the microbubble's response. The two findings above are compared quantitatively in the following figures. Figure 4.40 shows the distribution of the change in radius as a function of peak negative pressure. Here it can be seen that the median change in size after ultrasound excitation is greater for microbubbles at 37 ^{o}C and that the response distribution (dotted lines indicate the 25th and 75th percentiles) is narrower suggesting that there is less variability in response. This could be explained by an increase in coating homogeneity due to an increased ability for the lipids to rearrange. However, this narrowing of the response distribution was not seen when investigating the amplitude of individual microbubble responses. At driving pressures below 150 kPa it can be seen that the median expansion ratio for the heated microbubbles is approximately 10 – 20 % greater, Figure 4.41. The characteristic size dependent expansion ratio (as discussed previously in Section 4.5) is again observed. However, it was found that the threshold of 2 times the initial radius occurred at a transition radius of around 3 µm for the heated microbubbles, compared to 4.5 µm for microbubbles

at room temperature. The implication and cause of this is unknown, however, may be of interest in future theoretical studies of this phenomena.

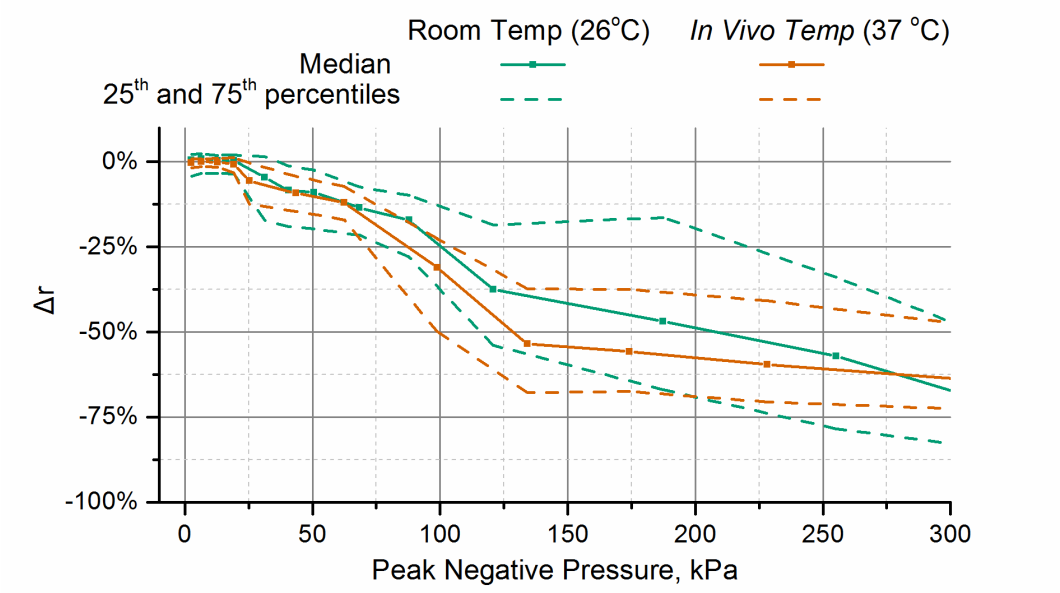

Figure 4.40: Change in radius after ultrasound excitation as a function of peak negative driving pressure comparing microbubbles at room temperature and at in vivo temperature (37 °C). Ultrasound driving frequency is 3.5 MHz and each pulse contains 5 cycles.

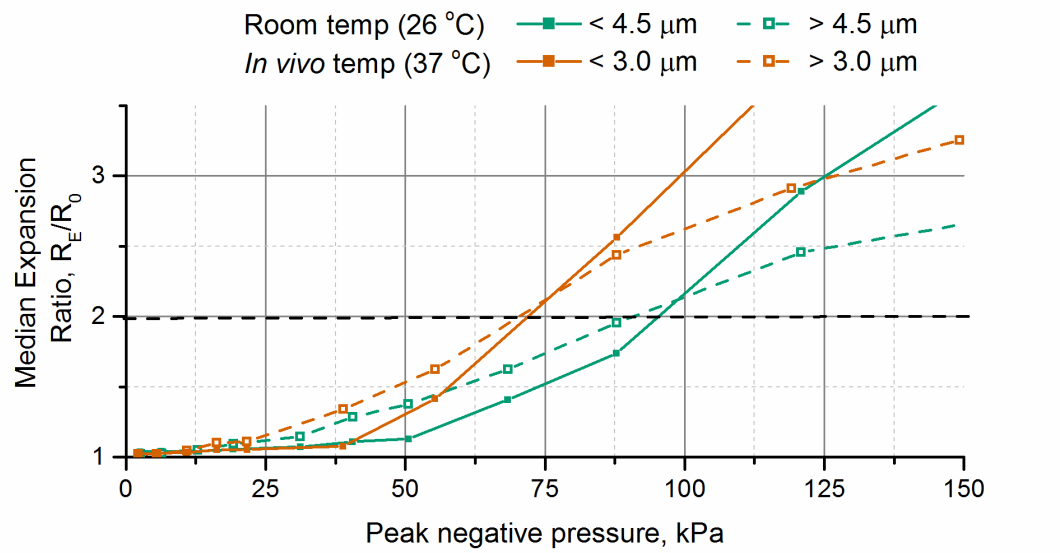

Figure 4.41: Median expansion ratios separated by initial microbubble radius (solid lines are the smaller microbubbles and dashed lines are the larger microbubbles, the exact radius used is given in figure legend) as a function of peak negative driving pressure comparing microbubbles at room temperature and at in vivo temperature (37 °C). Ultrasound driving frequency is 3.5 MHz and each pulse contains 5 cycles.

Although the effects of temperature should not be disregarded, the observations here suggest that there is little effect given an equivalent amount of heating that microbubbles may receive in the first minute of ultrasound scanning *in vivo*.

4.8.4. Hydrostatic pressure

The hydrostatic blood pressure for a healthy patient varies every second or less from 16 kPa during the systolic phase and 10 kPa during diastolic phase [94]. As observed in the pressure chamber experiments (Figure 4.1) a decrease in pressure of 18 kPa was able to cause a significant change in microbubble size. There have been a number of investigations into the effect of physiologically

relevant hydrostatic pressures on microbubble acoustic response. Brayman *et al.* [148] found that the attenuation through a sample of Albumin microbubbles significantly decreased with increasing hydrostatic pressure and suggested that this was due to irreversible destabilisation of the microbubbles. Similar measurements on Sonozoid® microbubbles by Hoff [56] agreed with Brayman's attenuation results, however showed that the effect was reversible when the hydrostatic pressure was returned to atmospheric pressure after 30 seconds at 16 kPa (120 mmHg), Figure 4.42. These two observations suggest that the increased hydrostatic pressure reduces the overall response of the microbubbles, resulting in less energy from the ultrasound being reflected or absorbed. This effect, however, also appears to influence the nonlinear behaviour: As discussed regarding the quantitative Contrast Enhanced Ultrasound imaging in Section 1.3.2, Dave *et al.* [149] observed an increase in the magnitude of the sub-harmonic response from Sonozoid® microbubbles with increasing hydrostatic pressure in both *in vitro* and *in vivo* experiments. These experiments suggest that the conditions *in vitro* with increased hydrostatic pressure are comparable, at least for a microbubble's sub-harmonic response, to *in vivo* conditions.

Given these observations by previous authors, it can be said that the *in vivo* increase in hydrostatic pressure needs to be taken into account when considering the relevance of observations made at ambient hydrostatic pressure, such as in this thesis. This is an area that requires more research; however, it can be argued that the effect of hydrostatic pressure on a microbubble's response

may be more predictable given a better understanding of a microbubble's response to ultrasound and improved theoretical models.

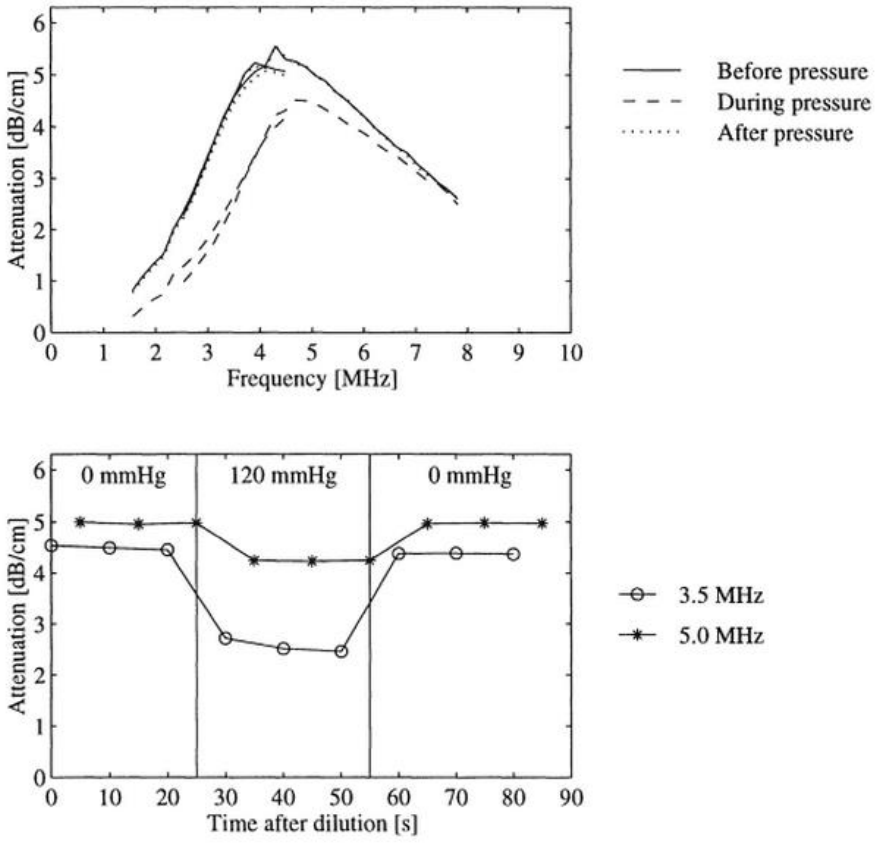

Figure 4.42: Ultrasound attenuation of population of Sonozoid® microbubbles as a function of the top) applied hydrostatic pressure and bottom) time of pressurisation, figure taken from Hoff [56]*. Where 120 mm Hg is equal to change in pressure of 16 kPa.*

CHAPTER 5

Comparison of Microbubble Composition and Fabrication Techniques

In this chapter the effect of microbubble coating composition and fabrication technique on radial response is investigated using the device presented in Chapter 2. The findings suggest that neither the molecular weight of the phospholipid nor the ratio of lipid to emulsifier has any observable difference on microbubble radial response; but the addition of nanoparticles does. The response of microbubbles produced using a microfluidic device was also investigated and were found to show comparable but much lower responses to that of microbubbles produced by sonication. The implications of the findings for contrast enhanced imaging are discussed.

As discussed previously, the properties of a microbubble's coating have a significant effect on its response to ultrasound excitation. Since the coating

properties and structure is determined by its composition and fabrication, it is of interest to investigate how these two factors influence a microbubble's response. A limiting step in the development of new microbubble formulations and fabrication methods is the lack of suitable characterisation techniques that can efficiently compare large samples. The device developed for this work is able to overcome previous characterisation limitations, namely the ability to characterise large sample numbers, as demonstrated in the analysis of SonoVue® microbubbles (Chapter 4). This chapter investigates the effect of the composition and fabrication process on the stability and radial response of phospholipid coated microbubbles. In particular, the effects of phospholipid chain length, phospholipid: emulsifier ratio, the addition of solid nanoparticles and whether the microbubbles were prepared by sonication or in a microfluidic device are examined. The results are discussed in the context of improving the next generation of microbubbles for diagnostic and therapeutic techniques. First, the composition and fabrication methods used to prepare the bubbles described in this chapter are summarised.

5.1. In-house Microbubble Preparation

5.1.1. Phospholipid microbubbles[4]

The lipids 1,2-dipalmitoyl-sn-glycero-3-phosphocholine (DPPC, 850355), 1,2-distearoyl-sn-glycero-3-ethylphosphocholine (DSEPC, 890703) and 1,2-distearoyl-sn-glycero-3-phosphocholine (DSPC, 850365) were purchased as 25

[4] Method and description by Dr Joshua Owen

mg/mL solutions in chloroform from Avanti Polar Lipids, Inc., Alabaster, AL, USA. Unless otherwise stated, all other chemicals were purchased from Sigma Aldrich (St. Louis, MO, USA).

DSPC or DPPC (25 mg/mL in chloroform) and polyoxyethylene (40) stearate (PEG-40S, 10 mg/mL in chloroform) were mixed in a glass vial to form a chloroform solution containing 20 mg total of lipid constituents at a molar ratio of 9:1 respectively. For charged bubbles, DSPC, DSEPC (25 mg/mL in chloroform) and PEG-40S were mixed in a glass vial to a 20 mg total of lipid constituents at a molar ratio of 19.4:9:1 respectively. Chloroform solutions were covered with perforated Parafilm (Bemis Company, Inc., Neenah, WI, USA) and allowed to evaporate to form a homogenous lipid film. Lipid films were then used immediately or stored at -20^{o}C under a headspace of nitrogen (BOC, UK).

Lipid films were then re-suspended in 5 mL DPBS (Life Technologies, Paisley, UK) and stirred at 100^{o}C on a magnetic stirrer hotplate for a minimum of 30 minutes. The lipids were then homogenously dispersed within the solution by sonication for approximately 2.5 minutes using a micro-sonicator tip fully immersed in the solution at a power setting of 3 (Microson XL 2000, QSonica, Newtown, CT, USA). The sonicator tip was then moved to the air-liquid interface and the headspace in the vial filled with sulphur hexafluoride. The solution was again sonicated under constant sulphur hexafluoride flow for 30 seconds at a power setting of 14 to form a cloudy suspension of microbubbles. The suspension was immediately placed in ice to cool and then capped.

5.1.2. Magnetic iron-oxide coated microbubbles[5]

Magnetic microbubbles were prepared as described in the publication by Owen, et .al [150] which is directly quoted below: "1,2-Distearoyl-sn-glycero-3-phosphocholine (DSPC) was purchased from Avanti Polar Lipids Inc. (Alabaster, AL, USA). A ferrofluid suspension of 10 nm spherical magnetite nanoparticles in isoparaffin (10% volume fraction) was purchased from Liquids Research Ltd. (Bangor, UK). DSPC (15 mg) was weighed into a vial previously rinsed with surgical spirit (BP Unichem, Surrey, UK). Filtered deionised water (15 ml) was then added to the vial and the mixture sonicated using an ultrasonic cell disruptor (XL2000, probe diameter 3 mm; Misonix Inc., Farmingdale, NY, USA) at power setting 4 (15 s) followed by sonication at the air water interface (15 s). 15 µL of the 10 nm magnetite nanoparticle suspension was added followed by sonication (15 s in the liquid and 15 s at the air water interface) at power setting 4. The solution was then manually shaken for 30 s to produce magnetic microbubbles."

5.1.3. Gold nanoparticle coated microbubbles[6]

Two sizes of gold nanoparticles were prepared. For particles of 2 nm, aqueous HAuCl4 solution (5 mL, 10 mM, 37 °C) was added to BSA solution (5 mL, 50 mg/mL, 37 °C) under vigorous stirring. NaOH solution (0.5 mL, 1 M) was then introduced 2 min later, and the reaction was allowed to proceed under vigorous stirring at 37 °C. The same process is followed for 50 nm particles without the

[5] Method and description by Dr Joshua Owen
[6] Method and description by Dr Boon Teo

addition of NaOH and longer stirring until there was no change in the measured UV absorption.

5.1.4. Microfluidic microbubbles[7]

In addition to the sonication method described above, a microfluidic device consisting of a T-junction with an integrated low frequency ultrasound transducer was used to prepare phospholipid coated microbubbles. A suspension of 1,2-distearoyl-sn-glycero-3-phosphocholine (DSPC) and polyoxyethylene (40) stearate (PEG40 Stearate) in a 9:1 molar ratio with a total lipid concentration of 2 mg/mL in distilled water, was flown through the microfluidic device by syringe pump. At the T-junction, nitrogen gas was introduced to form large bubbles of ~200 µm in diameter, which then passed through the acoustic field of the transducer. Under acoustic insonation, the larger bubbles break up into microbubbles ranging in size from 0.5-10 µm according to the acoustic pressure, pulse repetition frequency and duty cycle. To avoid bubbles being destroyed as a result of pressure changes induced by syringe loading (Chapter 2), the outlet of the microfluidic device was coupled directly to the inlet of the characterisation system.

[7] Method and description by Dr Dario Carugo and Dr Richard Browning

5.2. Effect of Lipid Properties

5.2.1. Lipid composition

For this study the radial responses of lipid:PEG microbubbles with the following lipid compositions were investigated: DSPC (C_{18}), DPPC (C_{16}) and DSPC-DSEPC. The protocol for the fabrication of these microbubbles was as described in section 5.1. DSPC and DPPC have different chain lengths and DSPC-DSEPC is positively charged. As before, the radial responses measured using the device presented in Chapter 2 were analysed using the methods described in Chapter 3. The results showed no significant differences between the radial responses of the different types of lipid microbubbles and were found to be comparable to those of SonoVue microbubbles.

There have been several studies investigating the effect of lipid type on a microbubble's properties and acoustic response. A high speed imaging study [151] found there to be no significant differences in the radial response of sonicated lipid: PEG microbubbles when they varied the lipid chain length (based on the carbon chain lengths C16, C18, C20 and C22). They also found no difference in the magnitude of radial response between microbubbles prepared in-house and SonoVue®. Measurements of GP value (Section 2.4.2.2) for the various microbubble compositions found no significant differences between the samples and, as before, a large variability was observed within samples, Figure 5.1.

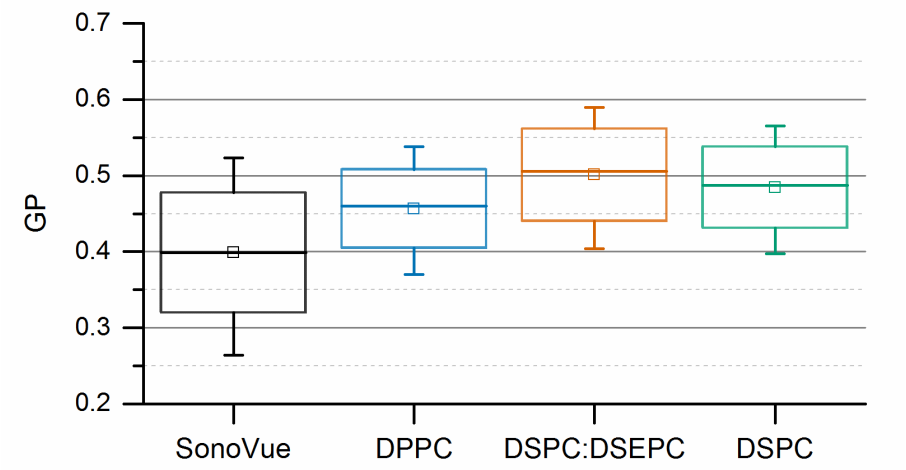

Figure 5.1: Distribution of measured GP values for SonoVue, DPPC, DSPC:DSEPC and DSPC. The 'GP' values give an estimation of the lipid packing that ranges from 1 (tightly packed) to -1 (loosely packed). Experiment performed and data provided by Dr Dario Carugo and Dr Richard Browning.

Figure 5.2a shows the median expansion ratio as a function of initial radius. For clarity the results have been coloured by peak negative driving pressure rather than lipid composition. It can be seen that the median expansion ratios are similar at all of the three peak negative pressures shown in the figure. Again, the responses are also comparable to that of SonoVue, Figure 5.2b and also in agreement with the findings of Emmer [151].

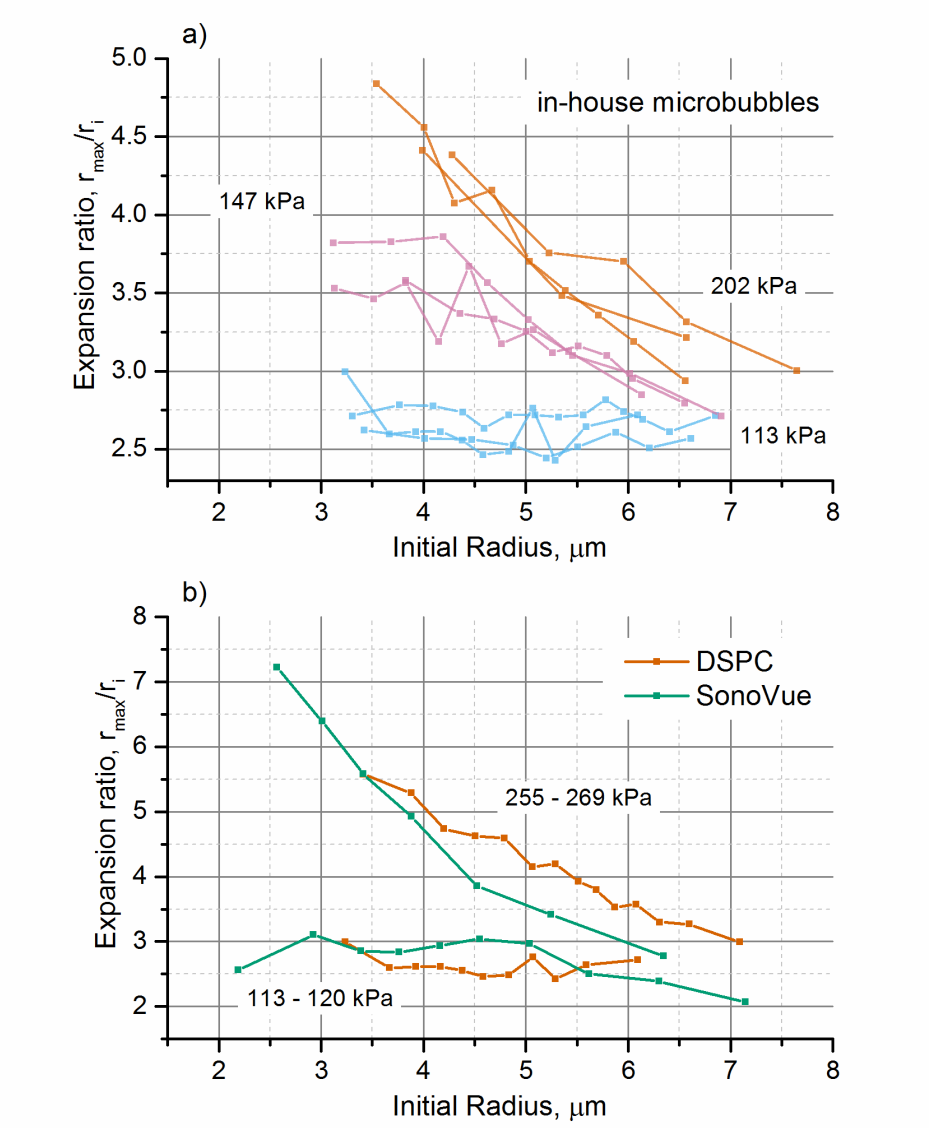

Figure 5.2: Expansion ratio as a function of initial radius for a) in-house lipid microbubbles (DSPC, DPPC and DSPC-DSEPC), For clarity the data have been coloured by peak negative driving pressure rather than lipid composition, and b) a comparison between DSPC and SonoVue® microbubbles. Each point represents the median of at least 100 microbubbles. Ultrasound parameters: 3.5 MHz driving frequency with pulse length of 5 cycles.

Investigations by Borden *et al.* [13] into the acoustic stability of lipid coated microbubbles at a driving frequency of 2.25MHz, observed that longer chain lengths decreased the rate of acoustic dissolution (change in microbubble

size after multiple ultrasound pulses) and the probability of fragmentation or lipid shedding. This suggests a proportional relationship between stability and chain length; however, their study was limited by small sample numbers ($n < 100$ for all types of microbubbles considered) and under quite different ultrasound conditions when compared to this thesis (peak negative pressures of 400 kPa, of multiple one-cycle ultrasound pulses, i.e. 40 repeated ultrasound pulses with a length of 1 cycle). Figure 5.3 shows the median, 25^{th} and 75^{th} percentiles of the change in microbubble radius after ultrasound excitation (3.5 MHz, 5 cycles) for the three different lipid compositions considered in this study. Here it can be seen that there is no significant difference in the microbubble stability as the distributions clearly overlap. To demonstrate that the initial microbubble size does not influence this finding, the change in radius is plotted as a function of initial radius below in Figure 5.4.

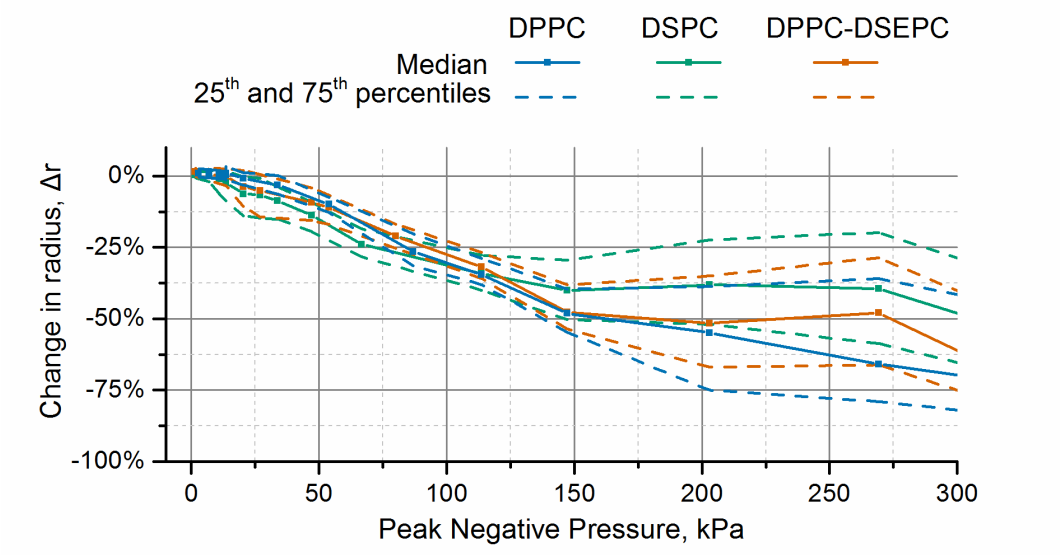

Figure 5.3: Change in microbubble radius after ultrasound excitation as a function of peak negative driving pressure plotted for varying lipid compositions: DPPC (dark blue), DSPC (green) and DSPC-DSEPC (orange). Dashed lines represent 25th and 75th percentiles and solid lines represent the median. Each point represents at least 100 microbubbles. Ultrasound parameters: 3.5 MHz driving frequency with pulse length of 5 cycles.

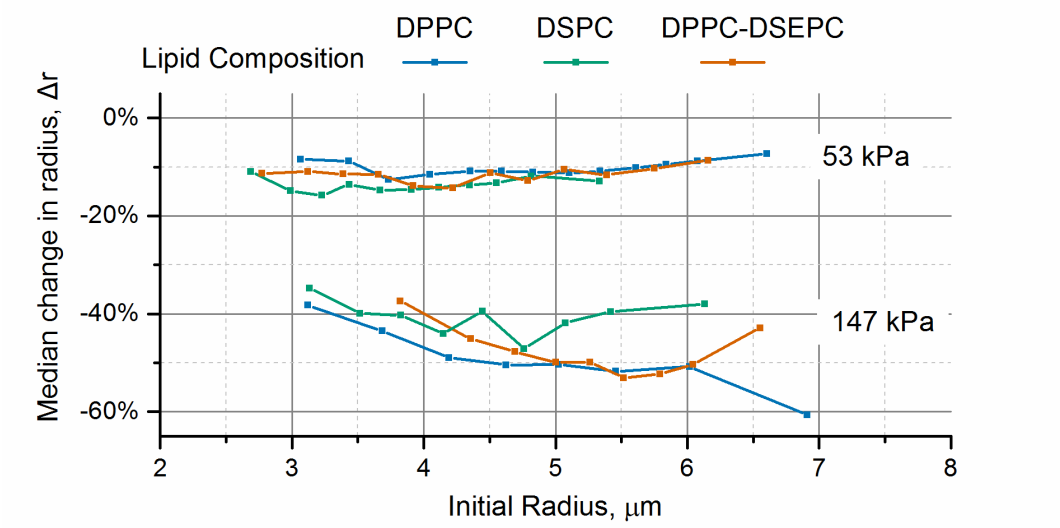

Figure 5.4: Median change in radius as a function of initial radius and peak negative pressures (53 kPa and 147kPa), plotted for lipid compositions: DPPC (dark blue), DSPC (green) and DSPC-DSEPC (orange). Ultrasound parameters: 3.5 MHz driving frequency with pulse length of 5 cycles.

5.2.2. Emulsifier: lipid ratio

There have been only a few investigations into the effect of the ratio of emulsifier: lipid on microbubble behaviour. Borden *et al.* [105] demonstrated that increasing the percentage of PEG changed the microstructure of the coating, generally resulting in larger domains visible on the surface and greater phase separation of the lipid and PEG constituents, although there was large variation between individual microbubbles. Wang *et al.* [152] demonstrated that a microbubble sample's size distribution could be varied by the ratios between DPPC:DSPG:PEG40S. To the best of the author's knowledge, the only study on the effect of the emulsifier:lipid ratio on microbubble acoustic response was performed early in the development of the microfluidic device presented in Chapter 2. In this experiment microbubbles coated with different ratios of PEG40S to DSPC (1:9, 1:4 and 1:1) were tested for their acoustic response and coating viscosity (see FLIM Section 2.4.2.1) [120]. The results shown in Figure 5.5 below indicate that changing the ratio produced a measureable difference in microbubble surface viscosity and also in scattered acoustic power (Figure 5.5.d). However, the acoustic measurements were limited in terms of sample numbers ($n < 46$ for all samples) and the size distributions were unknown so could not be accounted for.

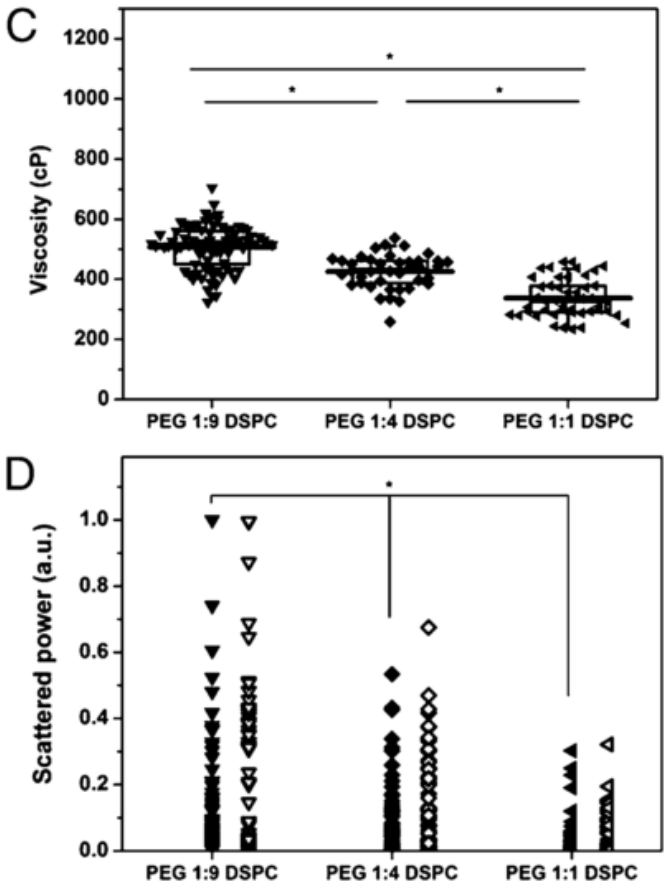

Figure 5.5: Estimation of c) coating viscosity for microbubbles of varying PEG : DSPC ratio (1: 9 ,1: 4 and 1:1) and d) corresponding acoustic scattered power experimental measurements (closed symbols) and simulations (open symbols). Figure taken from Naveen et al. [120]

Hydrostatic pressure chamber experiments (see Section 3.4.1), performed as part of an MSc project by Cen Zhang, found no observable difference between the different microbubble compositions in terms of the expansion ratio (Figure 5.6). However, the results were again limited by low sample numbers (n < 50 in total) and, although the method provides the ability to estimate the elastic modulus of the coating, the behaviour of lipid coatings under quasi-static conditions may not be comparable to that under ultrasound excitation.

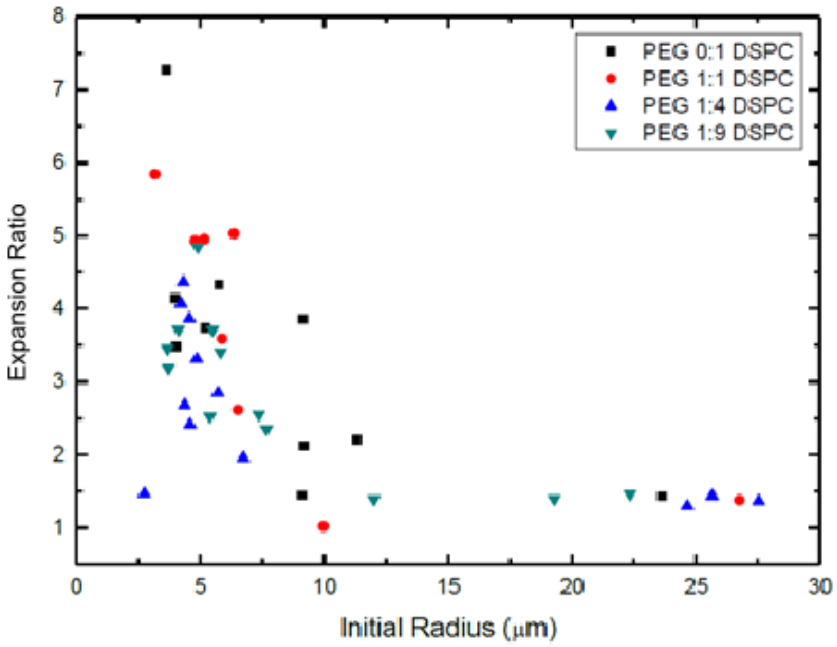

Figure 5.6: Expansion ratio as a function of initial radius for microbubbles of varying lipid : PEG ratios during decompression experiments using hydrostatic pressure chamber. Figure taken from work by Cen Zhang during MSc project [153]

For this study, PEG:DSPC microbubbles with ratios 1:1, 1:4 and 1:9 were prepared as described in Section 5.1. As with the analysis of the lipid type, the results showed no significant difference between the radial responses of the various PEG:DSPC ratio microbubbles. Figure 5.7 demonstrates that both the response rate and median expansion ratio for the samples were comparable to each other and to the response of SonoVue microbubbles. The asymmetry of the microbubble responses were also found to show no significant differences between the median responses for varying PEG:DSPC ratio, Figure 5.8.

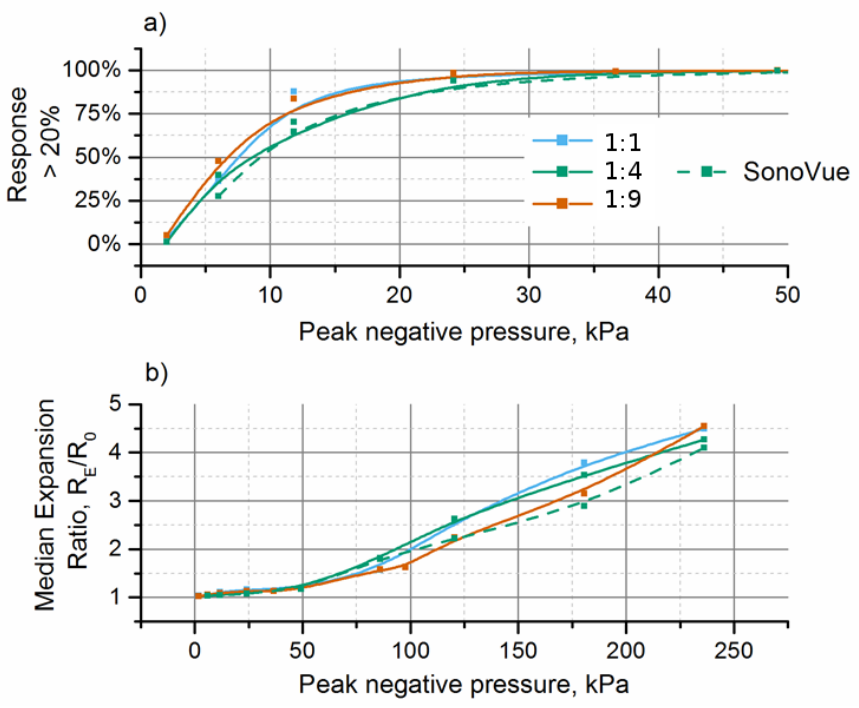

Figure 5.7: Comparison of PEG:DSPC microbubbles, 1:1 (light blue), 1:4(green) and 1:9(orange) and SonoVue (dashed green).a) percentage of microbubbles expanding to greater than 20% of their initial radius as a function of peak negative driving pressure. b) Median expansion ratio as a function of peak negative driving pressure.

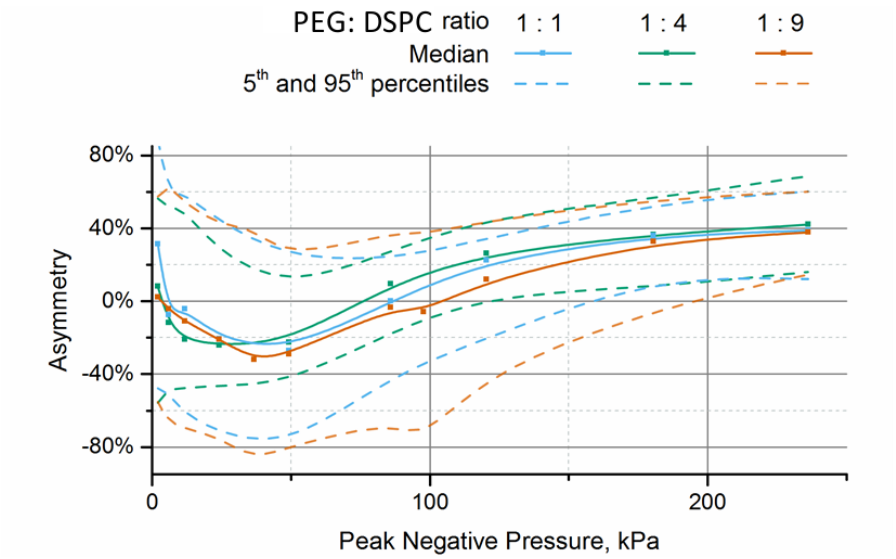

Figure 5.8: Asymmetry of microbubble response as a function of peak negative driving pressure, plotted for varying PEG:DSPC ratio microbubble compositions: 1:1 (light blue), 1:4 (green) and 1:9 (orange). Ultrasound parameters are 3.5 MHz driving frequency at pulse lengths of 5 cycles.

These findings suggest that neither the lipid composition (DSPC, DPPC or DSPC-DSEPC) nor the ratio of emulsifier to lipid (1:1, 1:4 and 1:9) have any observable effect on the radial response of coated microbubbles under ultrasound conditions of 3.5 MHz of pulse length of 5 cycles. This is in agreement with measurements of lipid packing, as shown for lipid composition (Figure 5.1). Together with the findings from Chapter 4, it is suggested that similar results would be seen for ultrasound frequencies from 2 to 4.5 MHz and for pulse lengths of 3 to 8 cycles.

5.3. Effect of Surface Nanoparticles

Nanoparticle coated microbubbles have many promising clinical applications including drug delivery [154], combined MRI contrast [155] and site specific targeting, for example using magnetic fields [156]. Studies have also hypothesised and shown preliminary results of enhanced nonlinear acoustic response [157], [158]. Stride *et al.* [157] modelled the response and showed that the addition of nanoparticles could lead to increased packing on a microbubble's surface, restricting compression and increasing a microbubble's nonlinear behaviour. As the results show, the addition of surface nanoparticles has a considerable effect on a microbubble's radial response when compared to SonoVue®, or any of the in-house microbubbles described above.

5.3.1. Gold nanoparticles

Gold nanoparticles below 50 nm are a plasmonic system [159], meaning that incident electromagnetic radiation (e.g. a laser beam) is efficiently converted to heat. It has been shown that this effect can be exploited to nucleate cavitation and subsequently generate a shockwave that can be used for photoacoustic imaging [160]–[162] and to enhance thermal ablation therapies [163]. Here two different sizes of gold nanoparticles were investigated; 2 nm and 50 nm, the preparation for the gold coated microbubbles is as described in section 5.1.3. Figure 5.9 below shows a transmission electron microscopy (TEM) image, using a technique developed by Owen *et al.* [164], of two 50 nm gold nanoparticle coated microbubbles next to each other. From the set of images obtained it is clear that there is significant variation in the quantity and distribution of gold nanoparticles on the microbubbles. The image shows two microbubbles from the same solution; however, only one appears to be coated with gold nanoparticles indicating a large variability in the fabrication process.

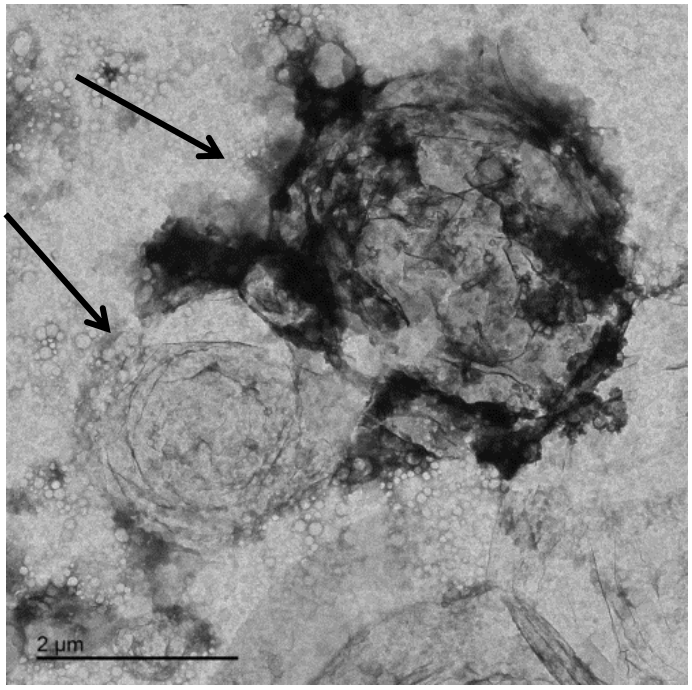

Figure 5.9: TEM image of 50 nm gold particles on the surface of microbubbles, dark regions indicate the presence of gold nanoparticles. Two microbubbles are indicated by the arrows. Sample preparation and image by Dr. Joshua Owen, technique as described in Owen et al. [164].

4.3.1.1. Reduction in radial response

Figure 5.10, shows the median expansion ratios measured over two separate experiments with freshly prepared microbubble batches, in total the graph below represents the analysis of n = 68,187 microbubbles. As can be seen, both the gold coated microbubbles and the control (DSPC: PEG 1:9 without gold particles) showed similar size distributions and reasonable consistency of the median expansion ratio between the two experiments. Another data set was excluded due to significant differences in the size distributions. These results demonstrate that the addition of gold- nanoparticles during microbubble fabrication can significantly reduce a population's median expansion ratio. Further, it appears that the larger 50 nm gold particles reduce the expansion

ratio more than 2 nm gold particles. There are several possible explanations for this effect, including: i) increased density, viscosity and/or 'stiffness' of the coating leading to smaller amplitude oscillations, ii) changes in the coating structure/composition due to the presence of gold nanoparticles similarly leading to a change in effective surface properties and iii) a decrease in microbubble stability leading to fragmentation. The mechanisms for the above observations are unknown and would be of interest for further study.

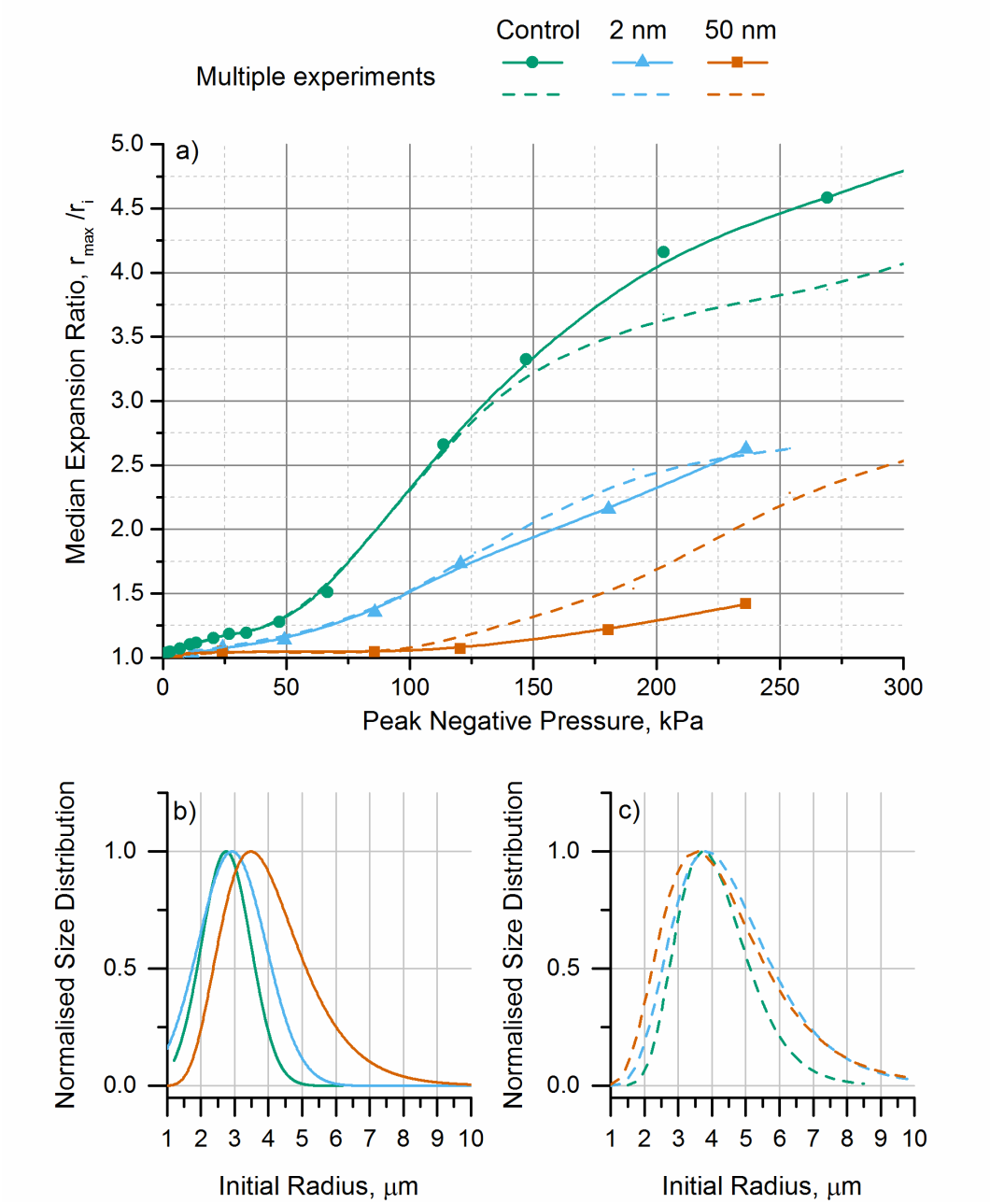

Figure 5.10: Investigating the expansion ratio of microbubbles with and without gold nanoparticles*. a) Expansion ratio as a function of peak negative pressure, plotted for gold nanoparticle coated microbubbles of 2nm (blue) and 50 nm (orange) and compared to the control without* nanoparticles*, PEG:DSPC 1:9 (green) Dashed lines represent data from experiments on different days and with freshly prepared samples. For clarity data markers have only been included for the 1st set of experimental results (solid lines).Normalised size distributions for the respective experiments are shown in b) and c).*

Figure 5.11 shows the median expansion ratio as before, however, the samples have been split by initial radius above and below 4.5 µm. Here it can be seen that dependency of the expansion ratio on the initial radius, discussed for SonoVue® in Section 4.5, occurs at radial expansions of ~$2r_o$. Interestingly, however, the pressure threshold for this phenomenon has been significantly increased by the inclusion of gold nanoparticles. This finding is significant as it demonstrates, in agreement with Flynn [131], that this behaviour occurs at a threshold of expansion rather than driving pressure. It is therefore, also observed that the addition of gold nanoparticles increases the threshold for 'inertial cavitation' by Flynn's definition.

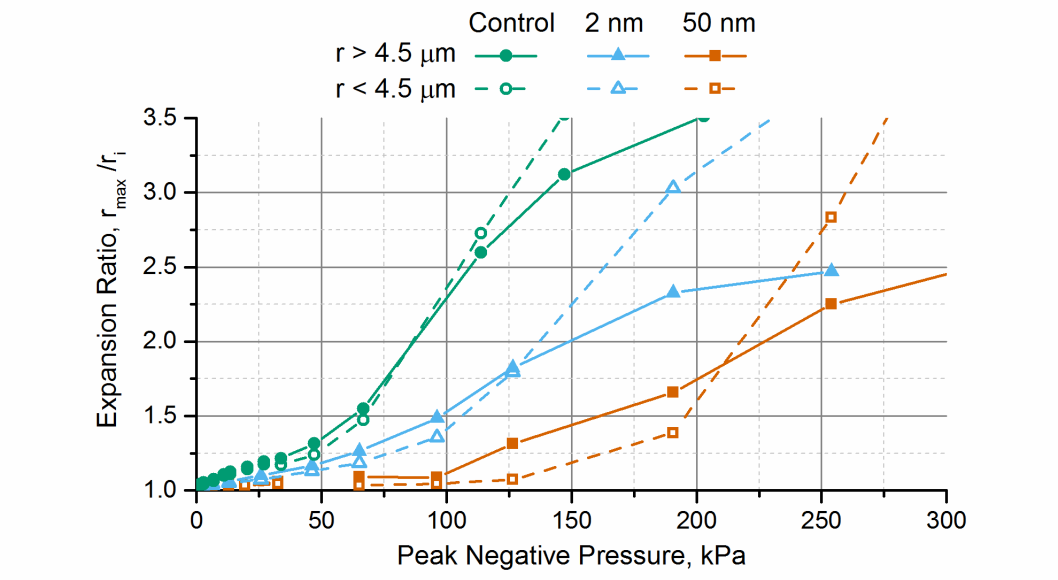

Figure 5.11: Expansion ratio for Gold nanoparticle coated microbubbles and control as a function of peak negative pressure split by initial size of microbubble above and below 4.5 µm.

4.3.1.2. Change in response asymmetry

The addition of gold nanoparticles was observed to change the response asymmetry of the microbubbles, Figure 5.12. For clarity, only one set of results are shown, however the same trend was observed in both experiments. Here it can be seen that both the 2 nm and 50 nm gold coated microbubbles showed a slight decrease in the median compression asymmetry at peak negative driving pressures from 6 kPa up to 50 kPa. The 5^{th} and 95^{th} percentiles show that a larger proportion of the responses exhibit expansion dominated behaviour at these pressures. This is in agreement with Stride's [157] model that suggests a reduction in compression due to the close packing of surface nanoparticles. The large variability in compression and expansion dominated behaviour could be explained again by the variability in coating properties. Based on the TEM images obtained (for example Figure 5.9), it is likely that not all microbubbles are coated with gold nanoparticles.

At pressures above 100 kPa the control sample showed typical expansion behaviour as observed for SonoVue® over a range of conditions. However, unlike SonoVue and the control sample, both the 2 nm and, particularly, the 50 nm gold coated microbubbles continue to exhibit compression dominated behaviour up to peak negative pressures of 200 – 300 kPa. For visual comparison, example radial responses for the 50 nm gold coated and PEG:DSPC 1:9 microbubbles are shown in Figure 5.13 at a driving peak negative pressure of around 125 kPa. Here it can be clearly seen that the gold coated microbubbles shown a much lower

magnitude of response, as well as less typical expansion dominated behaviour observed for the PEG:DSPC microbubbles.

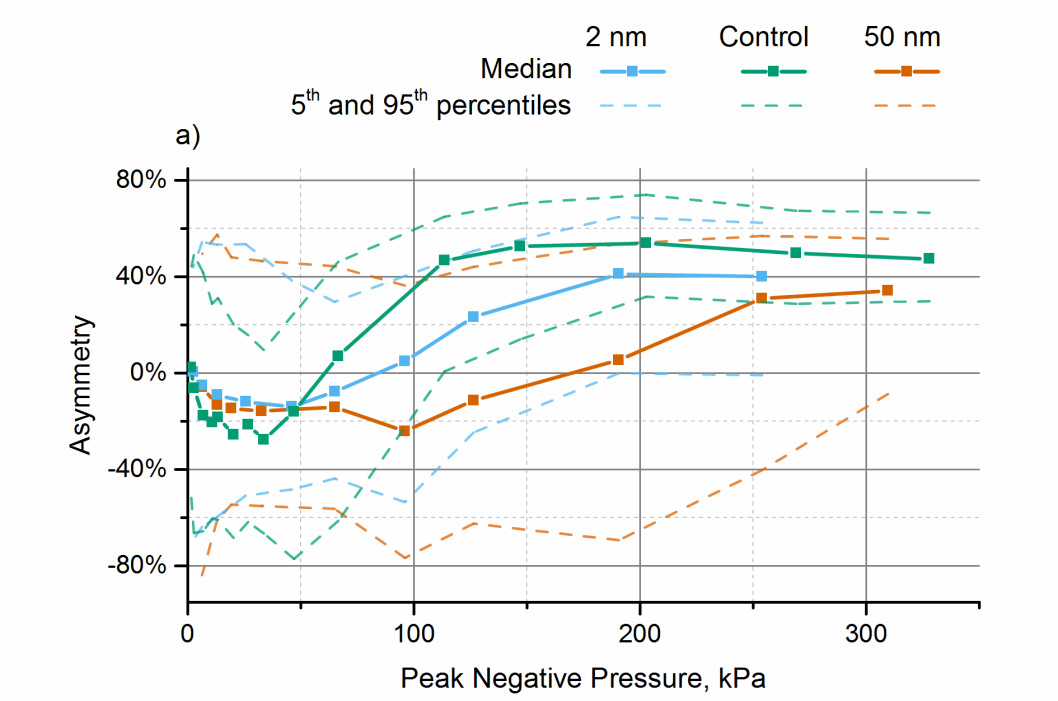

Figure 5.12: Asymmetry as a function of peak negative driving pressure for the comparison of 2 nm and 50 nm gold nanoparticle coated microbubbles and control (PEG:DSPC 1:9) without nanoparticles. Ultrasound driving frequency is 3.5 MHz with a pulse of 5 cycles.

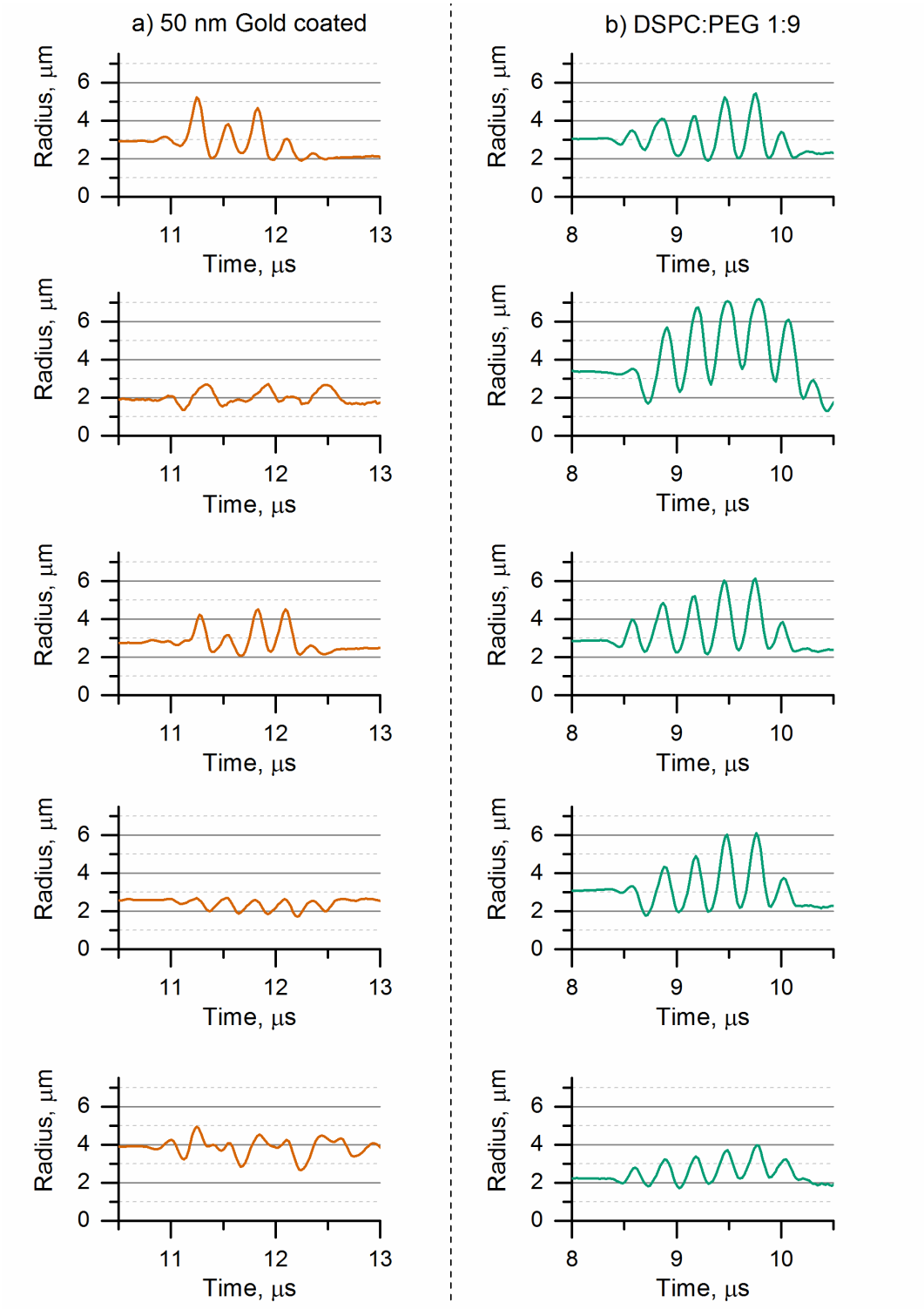

Figure 5.13: Example radial responses when driven at a peak negative pressure between 125 kPa – 130 kPa of a) 50 nm gold coated and b) PEG:DSPC 1:9 microbubbles. Ultrasound driving frequency of 3.5 MHz and pulse length of 5 cycles.

4.3.1.3. Nonlinear and linear scattered power

Interestingly, gold nanoparticle coated microbubbles were observed to show comparable ratios between the estimated nonlinear and linear scattered power for peak negative pressures up to 150 kPa, Figure 5.14. Above this pressure it can be seen that the ratio for the control increases by over 3 times, whereas less than 1.5 times for the gold coated microbubbles. This could be explained by the apparent increase in the 'inertial' cavitation threshold and compression dominated behaviour seen for both the 2 nm and 50 nm gold coated microbubbles previously. As discussed in Section 1.2.2, it is desirable to maximise this ratio to increase the nonlinear residual, exploited by CEUS imaging techniques.

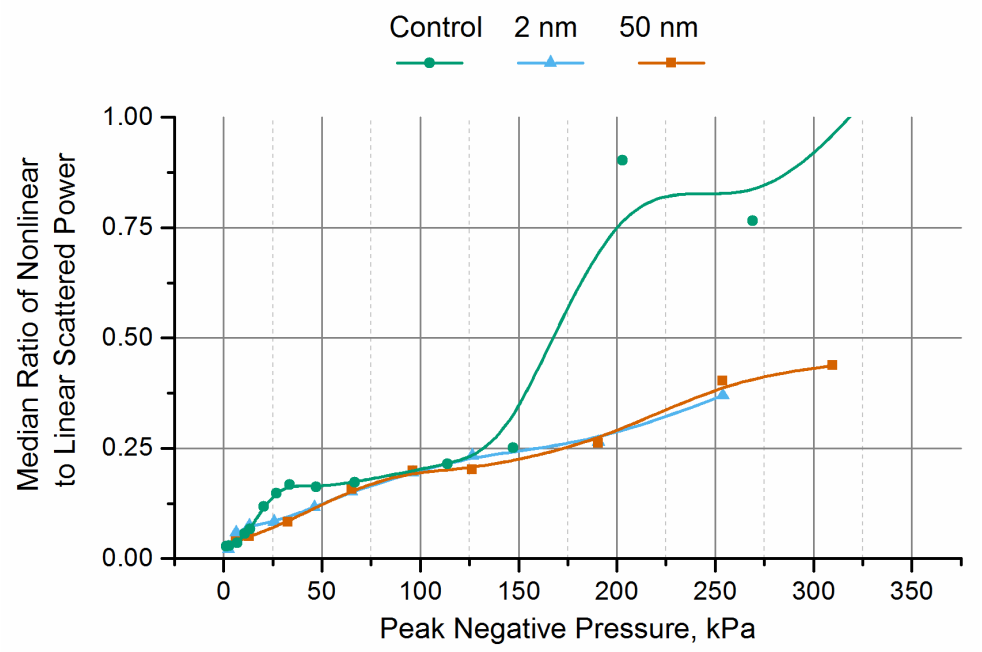

Figure 5.14: Median ratio of the estimated nonlinear and linear scattered power components as a function of peak negative pressure, plotted for gold nanoparticle coated microbubbles (2 nm and 50 nm) and the control (PEG:DSPC 1:9) microbubbles. Ultrasound driving frequency of 3.5 MHz and pulse length of 5 cycles.

4.3.1.4. Increased stability

The implications of these findings are that gold nanoparticle coated microbubbles show a significant decrease in radial amplitude of oscillation, and thus radiated pressure. This decrease in response also appears to correlate with a smaller change in equilibrium radius after ultrasound excitation, Figure 5.15. Here it can be seen that the gold nanoparticle microbubbles show a smaller decrease in the median change in size after ultrasound excitation. The implication for CEUS imaging is that the addition of gold particles may help the microbubble to survive longer over multiple ultrasound exposures. However a more interesting implication is for drug delivery is that the addition of nanoparticles may provide some control of the amount of drug released during ultrasound excitation, albeit at the cost of lower echogenicity.

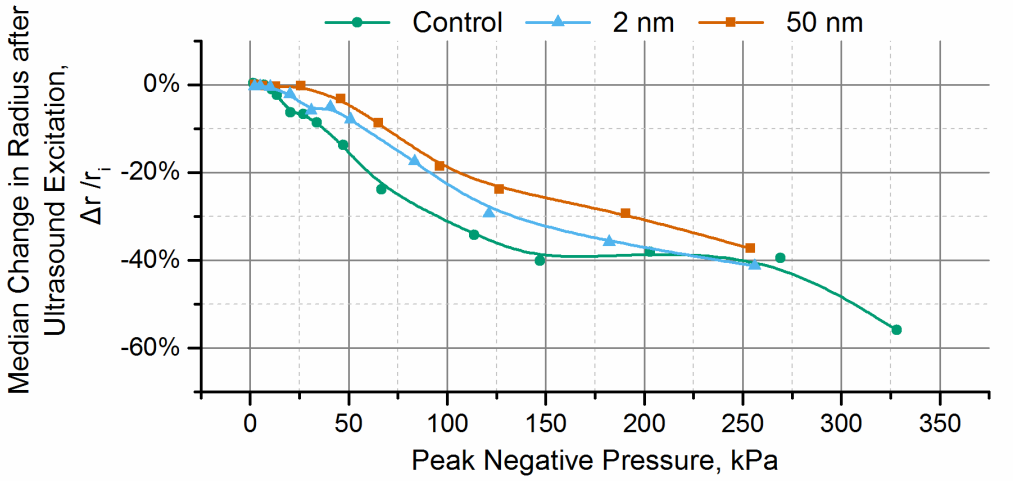

Figure 5.15: Change in microbubble radius after ultrasound excitation for control and gold nanoparticle coated microbubbles (2 nm and 50 nm)

5.3.2. Magnetic nanoparticles

It has been shown previously that super-paramagnetic nanoparticles can be embedded with the microbubble coating to enable localisation using an externally applied magnetic field [165]. The preparation of the magnetic microbubbles is described in Section 5.1.2. Although the intended applications of the gold and magnetic particles are different, the physical properties are expected to be comparable in terms of their influence on the coating properties and hence a microbubble's response to ultrasound excitation. The magnetic particles have a measured hydrodynamic diameter of 50 nm, and it has been confirmed using TEM that they are embedded in the surface of the microbubbles, Figure 5.16.

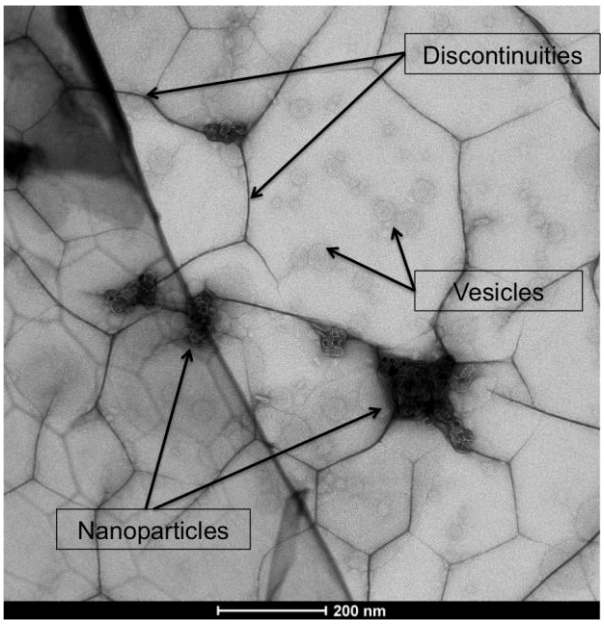

Figure 5.16: Close up TEM image of magnetic particle coated microbubble. Boundaries of microbubble cannot be seen. Image taken by Dr Joshua Owen using his technique [164]

Figure 5.17 shows the median expansion ratio as a function of the peak negative driving pressure for the magnetic microbubbles and gold coated microbubbles. However, it can be seen in Figure 5.17b that the size distribution of the magnetic microbubbles is significantly larger than that of the gold microbubbles. Despite this, it is clear that the addition of the magnetic nanoparticles during fabrication is able to significantly reduce the microbubble expansions, in a similar fashion to the gold nanoparticles. On closer inspection of the expansion ratio as a function of the initial microbubble radius, Figure 5.18, it can be seen that the response of the magnetic microbubbles appears to continue the trends as expected from the smaller 2 nm and 50 nm gold coated microbubbles. From these results it is difficult to say if there is more correlation with either the 2 nm or 50 nm gold particles, the magnetic particles have a mean diameter of 50 nm and it would therefore be assumed to be more similar to the 50 nm gold microbubble responses. However, given the large variability in the results it is not possible to draw any conclusions.

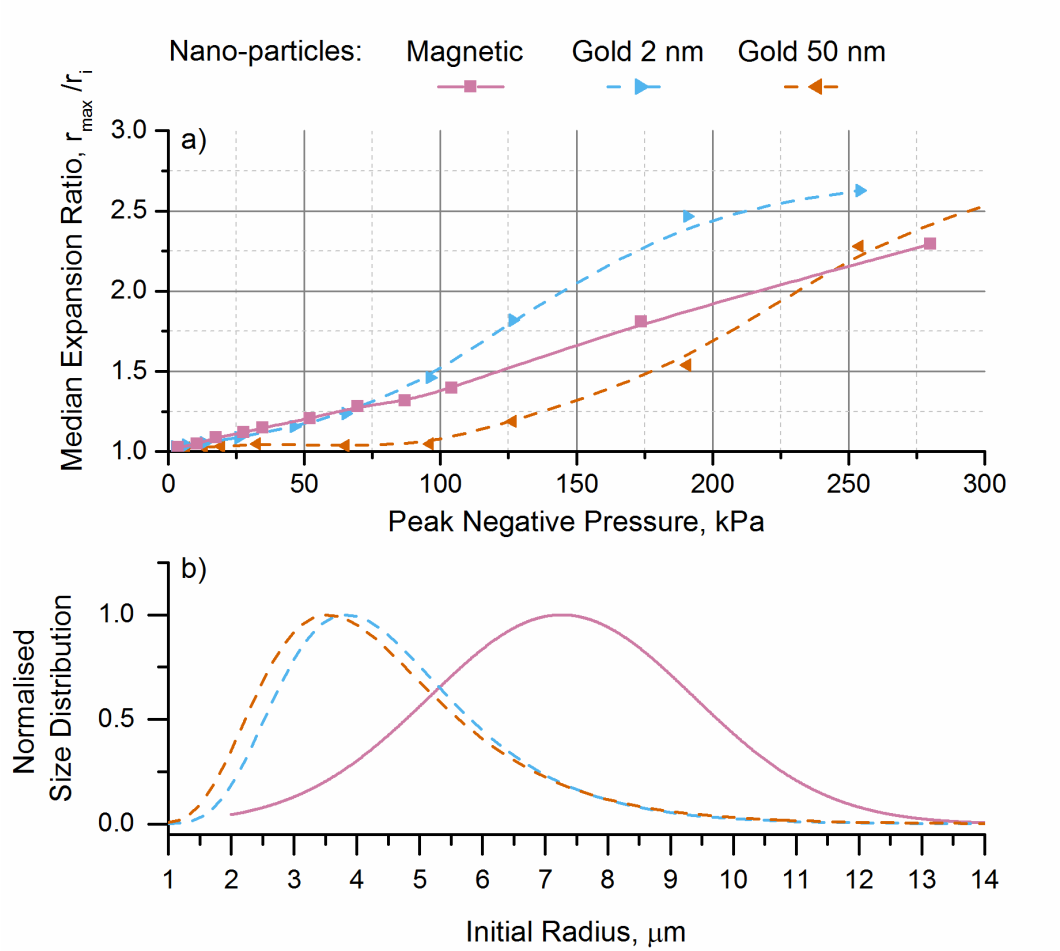

Figure 5.17: Median expansion ratio as a function of peak negative pressure, comparison of the response from magnetic particle coated microbubbles and gold nanoparticles of 2 nm and 50 nm. Ultrasound driving frequency of 3.5 MHz and pulse length of 5 cycles.

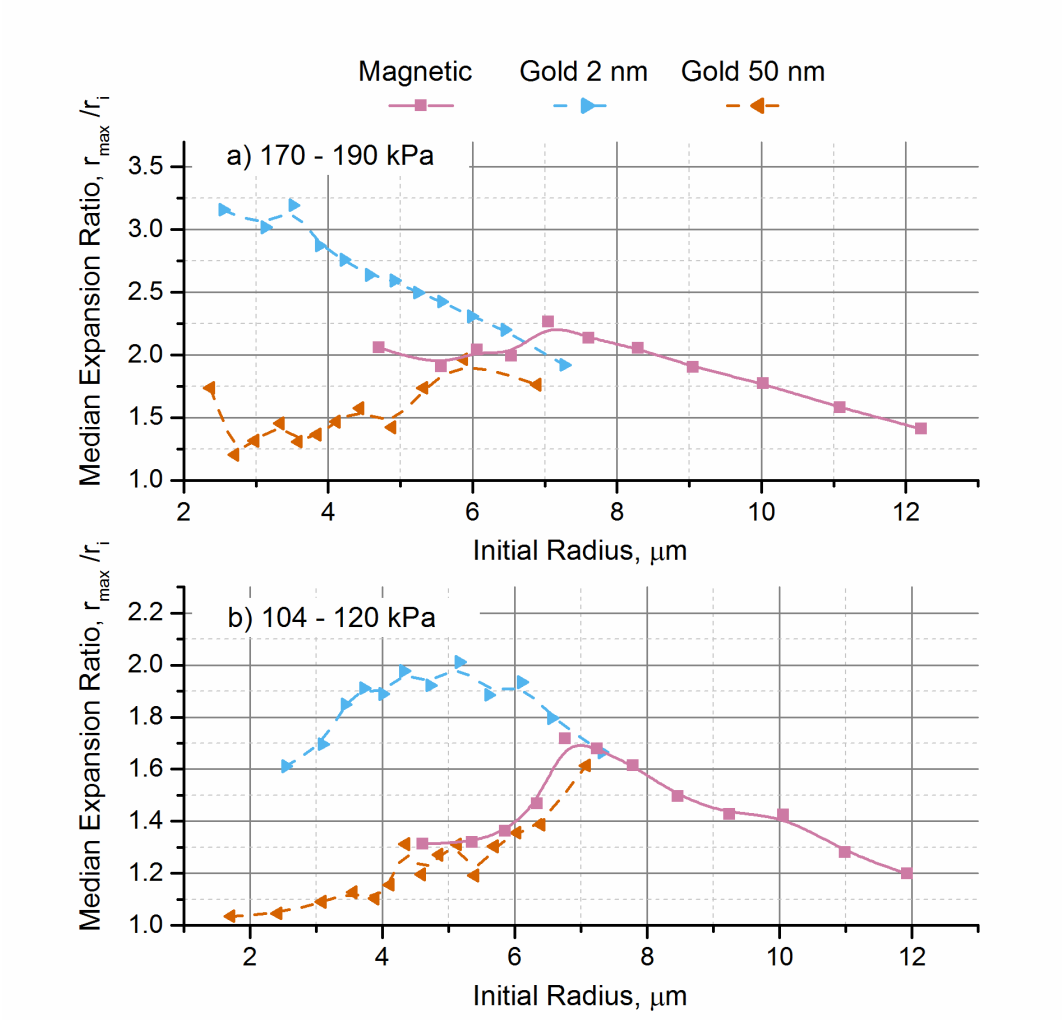

Figure 5.18: Median expansion ratio of Magnetic microbubbles as a function of initial radius, compared to gold 2 nm and 50 nm coated microbubbles. Ultrasound driving frequency of 3.5 MHz, 5 cycles and peak negative pressures of a) 170 – 190 kPa and b) 104 – 120 kPa. Each point represents the median response of at least 100 individual microbubbles.

5.4. Fabrication Technique - Microfluidic Microbubbles

The fabrication technique was investigated by comparing microbubbles of the same PEG:DSPC ratio (1:9) made using sonication and a recently developed

microfluidic device (method as described in Section 5.1.4). It has been suggested that the microfluidic fabrication process is more controllable than sonication and therefore may lead to more homogeneous microbubble samples, i.e. mono-disperse in terms of size and coating properties [166], [167]. The advantage of which is more predictable responses that could be exploited for CEQUS or optimisation of CEUS. Initial experiments, however found that the microbubbles prepared using a conventional microfluidic device were not stable enough to survive loading into a syringe and the journey from the syringe to the characterisation system (~20 cm of tubing, travel time of ~75 seconds at a backpressure of 3 – 4 Pa). However, by connecting the outlet of the new microfluidic device directly into the co-axial flow device, the microbubbles were able to reach the laser and their responses measured. For example, Figure 5.19 shows typical radial responses observed of the microfluidic microbubbles at a driving frequency of 3.5 MHz, pulse length of 5 cycles and driving peak negative pressures of 11 kPa and 115 kPa. The expected compression and expansion dominated behaviour is observed as well as sudden reductions in size at the higher pressure. Despite their relative instability during loading into a syringe, they show typical radial responses seen before for sonicated microbubbles, such as expansion and compression dominated response, as well as changes in size after ultrasound excitation. Despite, in theory, a more controllable fabrication technique, there was a large variability in their radial response and no indications that could suggest homogenous properties. The technique is still being developed and improvements are required to increase the stability for *in vivo*

applications, which may lead to better control of size distributions and composition homogeneity.

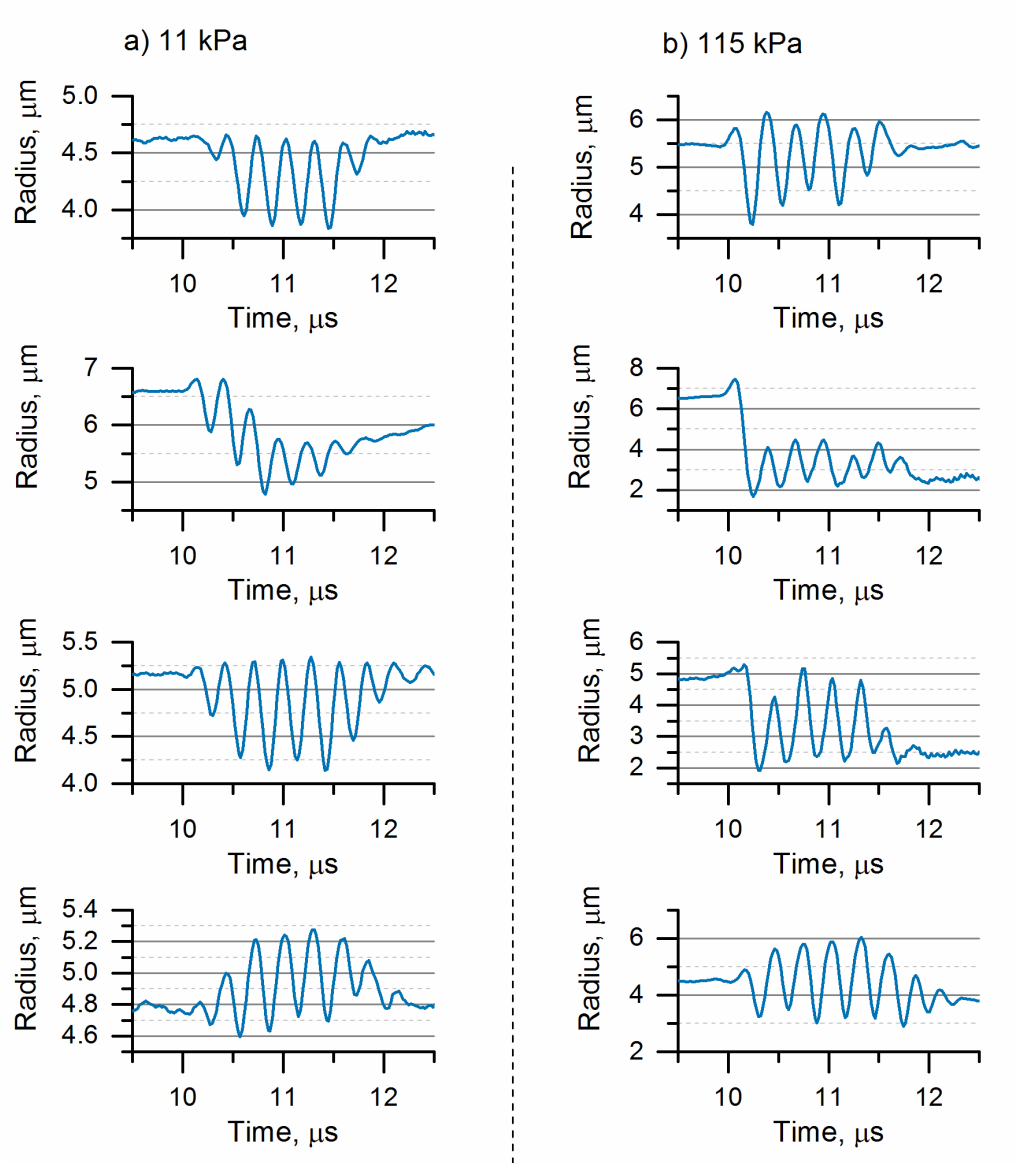

Figure 5.19: Examples of microfluidic microbubble radial responses when driven at 3.5 MHz, pulse length of 5 cycles and peak negative pressures of a) 11 kPa and b) 115 kPa.

In comparison to sonicated microbubbles of the same composition (PEG:DSPC 1:9), it can be seen that the median expansion ratio of the microfluidic microbubbles is much lower in magnitude, Figure 5.20a. Although the microfluidic microbubbles were overall larger in size, this would not account

for the large reduction in the expansion ratio, comparable to that observed with the addition of nanoparticles. Also, similar to the nanoparticle coated microbubbles, the microfluidic microbubbles showed a similar change in the radial response asymmetry with increase compression behaviour at peak negative pressures above 100 kPa, Figure 5.20b. The change in microbubble radius after ultrasound excitation, Figure 5.21, also shows the same trend as before, a smaller change in size albeit much smaller radial oscillations. It is interesting to observe a correlation between the behaviour of the microfluidic microbubbles and the nanoparticle coated microbubbles prepared by sonication. As far as the author is aware, this is the first observation of the radial response of microfluidic fabricated microbubbles.

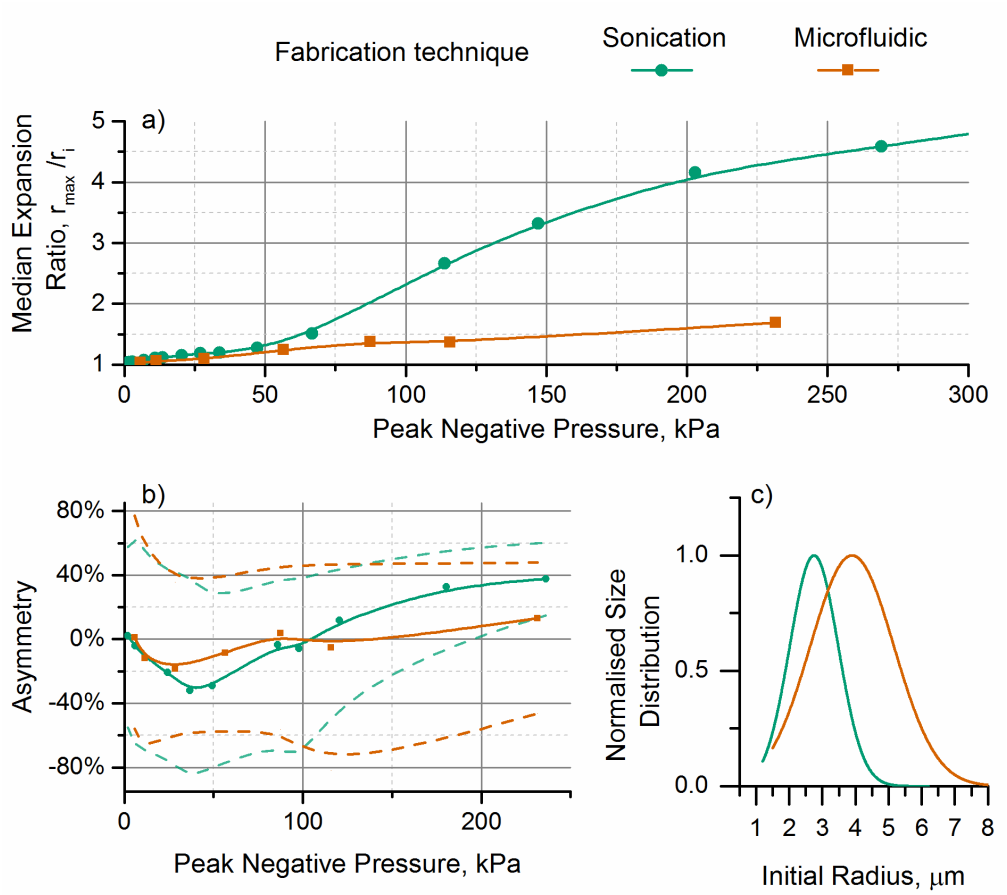

Figure 5.20: Comparison of response of PEG:DSPC 1:9 microbubbles prepared by sonication (green) and microfluidic (orange). a) median expansion ratio as a function of peak negative driving pressure, b) asymmetry of response showing median response (solid lines) and 5th and 95th percentiles (dashed lines) and c) the respective size distributions.

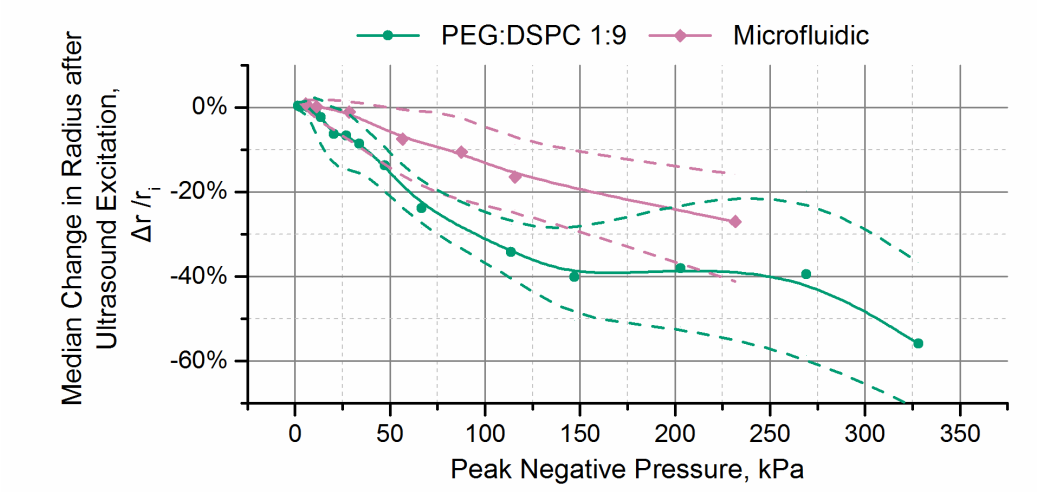

Figure 5.21: Change in microbubble radius after ultrasound excitation as a function of peak negative pressure, plotted for Sonicated microbubbles and microfluidic of the same composition (PEG:DSPC 1: 9). Solid lines represent the median and dash lines represent the 25th and 75th percentiles.

5.5. Summary of Findings

For the ultrasound parameters considered (driving frequency of 3.5MHz, pulse length of 5 cycles and peak negative pressures from 6 kPa up to 300 kPa) it has been observed that:

i) Coating lipid composition of chain lengths of 18 (DSPC) and 16 (DPPC), and charged (DPPC_DESPC) showed no significant effect on microbubble radial response.

ii) Varying the ratio of emulsifier:lipid (PEG:DSPC) within the range of 1:1 to 1:9 had no significant effect upon the median radial responses when compared to each other and to SonoVue® microbubbles.

This was in agreement with previous studies and the findings from the lipid packing measurements

Significantly, it was observed that the addition of surface nanoparticles has a considerable effect on microbubble populations median radial response, despite large variability observed in the distribution of particles on the microbubbles. The findings are:

iii) Nanoparticles added during the fabrication of sonicated microbubbles are observed to significantly reduce the median microbubble expansion ratio.

iv) 50 nm gold particles were observed to reduce the median expansion ratio consistently more than 2 nm gold particles.

v) The addition of gold nanoparticles increased the 'inertial cavitation' pressure threshold, observed at median radial expansions ratios greater than 2 times

vi) Magnetic iron-oxide coated microbubbles showed a similar response to the 2 nm and 50 nm gold coated microbubbles, although had a larger size distribution

Lastly, a method was devised to measure the radial response of the more unstable microbubbles produced in a microfluidic device rather than sonication, it was found that:

vii) Microfluidic microbubbles demonstrated typical radial responses with large variability, despite, in theory, being a more consistent fabrication process.

viii) Although the microfluidic microbubbles were unstable during handling (i.e. loading into syringe destroyed majority of population), they decreased less in size after ultrasound excitation when compared to sonicated microbubbles. Albeit smaller radial expansions.

ix) The overall response of microfluidic microbubbles appears to be similar to that of the nanoparticle coated microbubbles.

5.6. Implications to the Development of Microbubble Contrast Agents

Microbubble contrast agents have been through several generations in their development; from uncoated microbubbles that dissolve in milliseconds to iron-oxide nanoparticle coated microbubbles that have shown potential for targeted imaging *in vivo.* An example of microbubble contrast agent enhancement is the use of higher molecular weight gases such as perfluorocarbon that improve stability and lifetime of microbubbles *in* vivo by reducing the gas core's solubility. As discussed, a limiting factor in the optimisation of composition and fabrication has been a lack of suitable characterisation techniques. This thesis has demonstrated that the device developed in Chapter 2 has significant potential for the efficient assessment of new microbubble fabrication techniques and compositions.

As to whether the findings from this chapter provided any insights into the development of lipid coated contrast agents:

As far as the ultrasound parameters considered, this work found no advantages in varying the lipid composition or ratio of emulsifier to lipid (from 1:1 to 1:9). To better understand this finding further studies are required into the actual composition of the microbubble samples. For example it is clear, from the large variability observed in this and other works, that it cannot be assumed the initial composition during fabrication is the actual composition of the resulting microbubbles, i.e. microbubbles made with an initial composition of PEG:DSPC of ratio 1:9 may produce a sample of microbubbles with every possible ratio of PEG:DSPC.

It is possible that the addition of nanoparticles can be used to engineer the response of microbubbles. However, with current fabrication techniques the overall observed effect was a decrease in radial response which is not a desirable effect in the development of contrast agents. Interestingly, it was observed that this effect was proportional to nanoparticle size. Again, however, to understand this effect more studies are required into the distribution of the particles within a sample of microbubbles.

This work has shown that there is potential for the development of microfluidic microbubbles, typical radial responses were observed despite a lower stability observed during loading into a syringe. The technology should be continued to be improved with the goal of producing homogenous microbubble populations.

“Progress is man's ability to complicate simplicity“

— Thor Heyerdahl

CHAPTER 6

Conclusions and Future Work

The objectives of this thesis were twofold: to i) develop an experimental rig that could accurately capture the radial response of single microbubbles during ultrasound excitation and ii) use the rig to characterise and compare various types of microbubbles with respect to their use as Ultrasound Contrast Agents. The limitations of current characterisation techniques for single microbubbles were identified in Chapter 1 as:

- large experimental uncertainties
- physical restrictions on microbubble response
- failure to provide large data sets suitable for statistical analysis;

An experimental rig to overcome these limitations was developed based on the scattering of plane wave light from hydrodynamically isolated microbubbles (Chapter 2) building on previous works by Roy [81], Roy and Apfel [83] and Matula *et al.* [38]. The theory of light scattering from a microbubble during ultrasound excitation is presented and an analysis protocol developed using a custom written MATLAB® script (Chapter 3).

The new experimental rig was used to investigate the response of a clinical contrast agent, SonoVue®, (Chapter 4) to a range of ultrasound excitation conditions: Driving frequency from 2 MHz to 4.5 MHz, peak negative pressures from 6 kPa to 400 kPa and pulse lengths of 3, 5 and 8 cycles. Lastly, the effect of microbubble composition and fabrication technique on their radial response to similar ultrasound exposure conditions was investigated (Chapter 5).

It was observed, for all microbubble types considered, that there is large variation in individual responses that is independent of initial radius. This is supported by a similar variation observed in measurements of coating properties and by results from previous studies. Thus it would appear that current fabrication techniques and varied compositions produce inhomogeneous microbubble populations with an unknown distribution of properties, including the commercial contrast agent SonoVue®. Due to this large variability the application of current theoretical models to predict a microbubble's response is limited. However, in agreement with previous works and model predictions, microbubbles were observed to display highly nonlinear responses characterised by i) expansion and compression dominated radial expansions, ii) change in size

after ultrasound excitation suggesting rearrangement or loss of lipid from coating and iii) size dependent expansion that occurs at a threshold of twice a microbubble's initial radius.

Despite a large variability in individual responses, there are trends that are of interest to the use of SonoVue® microbubbles for CEUS imaging: i) As would be expected microbubble stability is proportional to driving pressure, however, can be improved by reducing the ultrasound pulse length, ii) The influence of a sample's size distribution on the median back scattered pressure decreases with driving pressure and iii) there was no evidence for a threshold of nonlinear behaviour, nonlinear responses were observed at driving pressures as low as 6 kPa.

The investigation into the effect of microbubble composition and fabrication demonstrated the utility of the characterisation technique, in particular the ability to efficiently obtain large sample numbers. It was found that varying the initial lipid composition (DSPC, DPPC, DSPC-DSEPC) or emulsifier to lipid ratio (1:9, 1:4, 1:1) had no observable effect on microbubble response. However, the addition of gold or magnetic nanoparticles was observed to decrease the magnitude of radial expansion and alter the response asymmetry. Microbubbles fabricated using a microfluidic device rather than sonication, demonstrated comparable responses despite the former exhibiting significant instability during handling.

6.1. Limitations

Importantly, the observations in this work are subject to the uncertainties in the empirical measurements and analysis of the data. Improvements to overcome some of these uncertainties are suggested at the end of this chapter.

6.1.1. Measurement uncertainty

As discussed in Section 2.5, there is uncertainty due to equipment limitations and ADC quantisation of the measurements. There is an inherent 10 – 20% error when measuring an ultrasound driving pressure due the calibration uncertainty of typical hydrophones. For this work the same hydrophone was used throughout experiments and was found to be within 20% error of a reference hydrophone (Figure 2.12). ADC quantisation was found to have an insignificant effect on the uncertainty, accounting for errors in precision of less than 0.78% when measuring the light scattered intensity. However, as discussed, the limited dynamic range resulted in clipping during large expansions, excluding up to 30% of samples (Appendix A3).

6.1.2. Data processing

Importantly there is potential for significant uncertainty when estimating the radius of single microbubbles due to: i) variation in laser intensity due to finite confinement of particles passing through the focussed laser beam and ii) the assumptions of Mie Scattering theory used to convert scattered light intensity to radius. Using the microfluidic device described in Chapter 2,

microbubbles could be confined to within 20 µm along the z axis (across Gaussian profile of laser beam). Given the estimated laser beam diameter at the focus, it was estimated that this variation in laser intensity would produce random errors of 5 – 15% when estimating microbubble radius (Figure 2.11). The same problem arises when calibrating the light – radius transfer function which requires the measurement of light scattered from size standard particles. However, due to the high throughput of the system it is possible to reduce the calibration error by averaging over, typically, 1000 measurements. This technique produced good agreement with theory (Figure 2.9) and would be expected to produce a bias error of no more than 5% when estimating microbubble radius. It was shown that the effects of acoustic radiation force, dipole response and confinement in the y-axis (along the path of the laser beam) would contribute to errors in the light scattering intensity of around 1%.

Another limitation is that this work has not taken into account the effect of the ultrasound pulse bandwidth when comparing sample responses at different driving frequencies. The significance of the bandwidths (demonstrated in Figure 4.4) are not known and should be investigated further as part of a comparison to theoretical models, discussed further at the end of this chapter.

This work is, however, most limited by the assumptions of Mie Scattering when converting the scattered light to particle radius, most significantly that the particle remains spherical. Unfortunately, due to the complexity of Mie Scattering, the sensitivity to non-spherical oscillations is difficult to assess. In a high speed imaging study by Dollet *et. al.* [48] optical tweezers were used to

isolate single microbubbles from any physical boundaries and observe non-symmetrical radial responses. They were able to directly observe non-symmetrical radial oscillations at peak negative pressures in the range of 50 kPa – 100 kPa and above at a driving frequency of 1.7 MHz at 12 cycles. With respect to the use of light scattering, Holt and Crum [92] speculated on non-spherical oscillations based on the complicated nature of observed power spectrums from light scattering measurements of bubbles around 100 µm in diameter. More recently, Matula [168] observed discontinuities in light scattering measurements from inertially collapsing microbubbles that coincided with the occurrence of non-spherical oscillations. The author has not observed any similar discontinuities in the light scattering measurements obtained in this thesis. The use of a 0.8 NA microscope objective with an effective aperture of 80 degrees helps to reduce any error caused by non-spherical oscillations. It is, however, a limitation of this study that such phenomena cannot be studied or accounted for with the current set up.

6.1.3. Supporting methods

The comparisons made in this work to other measurement techniques are not able to take into account the effect of different handling procedures. In particular, for the spectral lambda imaging measurements, microbubbles are centrifuged and left to incubate for up to 30 mins with the fluorescent dye. Although this is likely to favour the most stable microbubbles, the comparison made in this work is to the difference in properties within a sample. The variation

in properties observed could be assumed to be representative of the variation in the same sample before preparation.

6.2. Recommendations and Outlook

The results from this thesis have further demonstrated the complexity of lipid coated microbubble behaviour under ultrasound excitation. Contrary to previous works and current theoretical models, commercial and in-house lipid coated microbubbles show significant variability in their radial response independent of initial radius. This suggests that size alone is not able to accurately describe the state of a microbubble and how it will behave. This was found to be true for all of the microbubble compositions investigated as well as those prepared by microfluidics rather than sonication. Importantly, however, with large sample numbers this work has been able to give an indication of the probability of a microbubble's radial response, based on the percentiles, given its initial radius and the ultrasound conditions investigated.

The high throughput technique developed for this thesis has been shown to be suitable for comparing microbubble composition and fabrication methods. No significant differences were observed for DSPC, DPPC or DSPC-DSEPC lipid coated microbubbles, or for the variation of lipid to PEG from ratios of 1:1 up to 1:9. It is recommended that further investigation is required into the distribution of microbubble composition within individual batches.

6.3. Future Work

The work and findings of this thesis have perhaps most significantly shown the feasibility of accurately comparing microbubble composition and fabrication techniques. However, there are several improvements for the experiment rig described in Chapter 2 that would improve the measurement accuracy and the ability to investigate phenomenon such as microbubble collapse.

6.3.1. Experimental design improvements

There are several modifications that could be implemented to improve the experimental set up described in Chapter 2: i) Increase the bandwidth of the PMT's amplifier, ii) increase the power of the laser and/or refine the optical components and iii) include a second PMT to observe light scatter at separate angles to detect the presence of non-spherical oscillations.

An advantage of light scattering over acoustic measurements is the (theoretically) flat bandwidth of measurements compared to the significant frequency sensitivity of ultrasound transducers that must be corrected for. Full advantage was not taken of this fact since there is a trade-off between bandwidth and noise when choosing an amplifier to increase the signal output from the PMT. In the design described in Chapter 2 bandwidth was sacrificed to minimise noise and the upper limit for the amplifier used in the experiments was 8 MHz. However, after refinement of the optical system (focussed 5 mW laser and 40x microscope objective to capture the scattered light) the SNR was more

than suitable for the analysis required. It would therefore be recommended that for the same optical components given in Chapter 2, that a higher bandwidth amplifier can be used without significantly reducing the accuracy of the light scattering measurements. This would be particularly useful for further investigating inertial cavitation and to be able to measure the characteristic high frequency ringing caused by microbubble collapse. Moreover, if a higher bandwidth amplifier, or other light measurement device, is used that has a higher level of noise, then the SNR could be improved by optimisation of the optical system. Firstly, the laser power can be increased, for this work a 5mW laser was used to reduce safety requirements but it could be easily replaced with a higher power provided care is taken not to saturate the PMT, which can cause permanent damage and decrease its linearity. More significantly, however, it was found that the laser's beam profile had a larger impact on the SNR. The ideal beam profile would be a top hat with uniform intensity across its face.

Further, the width of the laser beam is of interest. The larger the width then the more time there is to interrogate a microbubble and multiple pulse analysis could be done. Unfortunately there is a trade-off between laser beam width and SNR due to scattering of light from impurities in the water. Therefore if either of the above adjustments are able to significantly improve the SNR it should be possible to have a wider laser beam. This would make it possible to investigate multiple pulses to further explore microbubble stability or to investigate amplitude/ phase modulation imaging. Therefore, further consideration should be given to the laser optical components to enable higher SNR, higher bandwidth

and the ability to excite the microbubbles multiple times before they leave the laser beam.

6.3.2. Data analysis

The analysis protocol presented in Section 3.2 was developed as the experiments increased in volume and complexity, such that there are many improvements that could be made to improve the efficiency of the analysis, in particular by replacing loops with matrices. Currently the processing of a typical experiment (> 100,000 samples) takes around 6 -7 hours.

6.3.3. Experiments / Analysis

There were several experiments that would have been of interest had there been more time:

i) Investigation into the response of non-lipid coated microbubbles, such as polymer or protein coated

ii) Comparison of other clinically approved contrast agents

iii) A systematic study into the effect of surface nanoparticles on a microbubbles response. This was the only microbubble composition that showed any significant difference, the reason for it may be better informed from further TEM imaging and fluorescent microscopy technique.

Importantly, it is suggested for the continuation of this work to investigate the:

i) Physical processes behind observations in this thesis, in particular the effects observed for the nano-particle coated microbubbles

ii) Comparison of these observations to current theoretical models and

iii) Appropriate use of statistics, given the large number of variables involved, to better analyse the data.

All of which would hopefully lead to improved and better informed models to predict the response of ultrasound contrast agents.

References

[1] D. Kane, W. Grassi, R. Sturrock, and P. V. Balint, "A brief history of musculoskeletal ultrasound: 'From bats and ships to babies and hips,'" *Rheumatology*, vol. 43, no. 7, pp. 931–933, 2004.

[2] S. Katzir, "Who knew piezoelectricity? Rutherford and Langevin on submarine detection and the invention of sonar," *Notes and Records of the Royal Society*, vol. 66, no. 2. pp. 141–157, 2012.

[3] K. T. Dussik, "On the possibility of using ultrasound waves as a diagnostic aid," *Neurol Psychiat*, vol. 174, pp. 153–168, 1942.

[4] Department of Health, "NHS Imaging and Radiodiagnostic activity in England: 2012/13 Release," 2013.

[5] H.-D. Liang, J. A. Noble, and P. N. T. Wells, "Recent advances in biomedical ultrasonic imaging techniques," *Interface Focus*, vol. 1, no. 4, pp. 475–476, Jun. 2011.

[6] W. L. Curati, A. Halevy, R. N. Gibson, D. H. Carr, L. H. Blumgart, and R. E. Steiner, "Ultrasound, CT, and MRI Comparison in Primary and Secondary Tumors of the Liver," *Gastrointest Radiol*, vol. 13, pp. 123–128, 1988.

[7] R. Gramiak and P. M. Shah, "Echocardiography of the aortic root," *Invest. Radiol.*, vol. 3, pp. 356 – 366, 1968.

[8] S. B. Feinstein, F. J. Ten Cate, W. Zwehl, K. Ong, G. Maurer, C. Tei, P. M. Shah, S. Meerbaum, and E. Corday, "Two-dimensional contrast echocardiography. I. In vitro development and quantitative analysis of echo contrast agents," *J. Am. Coll. Cardiol.*, vol. 3, no. 1, pp. 14–20, Jan. 1984.

[9] L. S. Ferreira and J. O. Trierweiler, "Formation of Monodisperse Microbubbles in a Microfluidic Device," *IFAC Proc. Vol.*, vol. 7, no. PART 1, pp. 405–410, 2009.

[10] E. Stride and M. Edirisinghe, "Novel preparation techniques for controlling microbubble uniformity: a comparison.," *Med. Biol. Eng. Comput.*, vol. 47, no. 8, pp. 883–92, Aug. 2009.

[11] C. Church, "The effects of an elastic solid surface layer on the radial pulsations of gas bubbles," *J. Acoust. Soc. Am.*, vol. 97, no. 3, pp. 1510–1521, 1995.

[12] S. Sirsi and M. Borden, "Microbubble Compositions, Properties and Biomedical Applications," *Bubble Sci Eng Technol.*, vol. 1, pp. 3–17, 2010.

[13] M. Borden, D. Kruse, C. F. Caskey, S. Zhao, P. A. Dayton, and K. W. Ferrara, "Influence of lipid shell physicochemical properties on ultrasound-induced microbubble destruction," *IEEE Trans. Ultrason. Ferroelectr. Freq. Control*, vol. 52, no. 11, pp. 1992 – 2002, 2005.

[14] S. H. Bloch, R. E. Short, K. W. Ferrara, and E. R. Wisner, "The effect of size on the acoustic response of polymer-shelled contrast agents.," *Ultrasound Med. Biol.*, vol. 31, no. 3, pp. 439–44, Mar. 2005.

[15] K. Soetanto and H. Watarai, "Development of magnetic microbubbles for drug delivery system (DDS)," *Japanese J. Appl. Physics, Part 1 Regul. Pap. Short Notes Rev. Pap.*, vol. 39, no. 5 B, pp. 3230–3232, 2000.

[16] P. A. Grayburn, "Current and future contrast agents.," *Echocardiography*, vol. 19, no. 3, pp. 259–265, 2002.

[17] N. De Jong, R. Cornet, and C. T. Lancee, "Higher harmonics of vibrating gas-filled microspheres. Part two: measurements," *Ultrasonics*, vol. 32, no. 6, pp. 455–459, 1994.

[18] N. de Jong, P. J. Frinking, A. Bouakaz, and F. J. Ten Cate, "Detection procedures of ultrasound contrast agents," *Ultrasonics*, vol. 38, no. 1–8, pp. 87–92, Mar. 2000.

[19] J. Borsboom, C. T. Chin, A. Bouakaz, and N. De Jong, "Nonlinear coded excitation method for contrast imaging," *2001 IEEE Ultrason. Symp. Proceedings. An Int. Symp. (Cat. No.01CH37263)*, vol. 2, no. 2, pp. 277–284, 2001.

[20] M. McCulloch, C. Gresser, S. Moos, J. Odabashian, S. Jasper, J. Bednarz, P. Burgess, D. Carney, V. Moore, E. Sisk, A. Waggoner, S. Witt, and D. Adams, "Ultrasound contrast physics: A series on contrast echocardiography, article 3," *J. Am. Soc. Echocardiogr.*, vol. 13, no. 10, pp. 959–967, 2000.

[21] P. Tortoli, L. Bassi, E. Boni, A. Dallai, F. Guidi, and S. Ricci, "ULA-OP: An advanced open platform for ultrasound research," *IEEE Trans. Ultrason. Ferroelectr. Freq. Control*, vol. 56, no. 10, pp. 2207–2216, 2009.

[22] R. Cobbold, *Foundations of Biomedical Ultrasound*. Engineering University of Toronto: Oxford University Press, 2007.

[23] V. Mor-Avi, E. Caiani, K. Collins, C. Korcarz, and R. Lang, "Quantitative analysis of myocardial perfusion and regional left ventricular function from contrast-enhanced power modulation images," *Comput. Cardiol.*, vol. Vol. 28, pp. 97–100, 2001.

[24] P. N. Burns, S. Wilson, and D. H. Simpson, "Pulse Inversion Imaging of Liver Blood Flow: Improved Method for Characterizing Focal Masses with Microbubble Contrast," *Invest. Radiol.*, vol. 35, no. 1, p. 58, 2000.

[25] T. X. Misaridis, K. Gammelmark, C. H. Jørgensen, N. Lindberg, A. H. Thomsen, M. H. Pedersen, and J. a. Jensen, "Potential of coded excitation in medical ultrasound imaging," *Ultrasonics*, vol. 38, pp. 183–189, 2000.

[26] M. Kitano, M. Kudo, K. Markawa, Y. Suetomi, H. Sakamoto, N. Fukuta, R. Nakaoka, and T. Kawasaki, "Dynamic imaging of pancreatic diseases by contrast enhanced coded phase inversion harmonic ultrasonography," *Gut*, vol. 53, no. 6, pp. 854–859, 2004.

[27] M.-X. Tang, H. Mulvana, T. Gauthier, A. K. P. Lim, D. O. Cosgrove, R. J. Eckersley, and E. Stride, "Quantitative contrast-enhanced ultrasound imaging: a review of sources of variability," *Interface Focus*, vol. 1, no. 4, pp. 520–39, Aug. 2011.

[28] P. Frinking, A. Bouakaz, J. Kirkhorn, F. Ten Cate, and N. de Jong, "Ultrasound contrast imaging: current and new potential methods," *Ultrasound Med. Biol.*, vol. 26, no. 6, pp. 965–975, 2000.

[29] K. Wei, A. R. Jayaweera, S. Firoozan, A. Linka, D. M. Skyba, and S. Kaul, "Quantification of myocardial blood flow with ultrasound-induced destruction of microbubbles administered as a constant venous infusion," *Circulation*, vol. 97, no. 5, pp. 473–83, Feb. 1998.

[30] D. Cosgrove, R. Eckersley, M. Blomley, and C. Harvey, "Quantification of blood flow," *Eur. Radiol.*, vol. 11, no. 8, pp. 1338–1344, Aug. 2001.

[31] T. Albrecht, M. Blomley, D. O. Cosgrove, S. Taylor-Robinson, V. Jayaram, R. J. Eckersley, A. Urbank, J. Butler-Barnes, and N. Patel, "Non-invasive diagnosis of hepatic cirrhosis by transit-time analysis of an ultrasound contrast agent," *Lancet*, vol. 353, pp. 1579–1583, 1999.

[32] M. Arditi, P. J. a Frinking, X. Zhou, and N. G. Rognin, "A new formalism for the quantification of tissue perfusion by the destruction-replenishment method in contrast ultrasound imaging," *IEEE Trans. Ultrason. Ferroelectr. Freq. Control*, vol. 53, no. 6, pp. 1118–29, Jun. 2006.

[33] E. Quaia, B. Cabibbo, L. De Paoli, W. Toscano, G. Poillucci, and M. A. Cova, "The value of time-intensity curves obtained after microbubble contrast agent injection to discriminate responders from non-responders to anti-inflammatory medication among patients with Crohn's disease," *Eur. Radiol.*, vol. 23, no. 6, pp. 1650–9, Jun. 2013.

[34] F. Forsberg, W. Shi, and M. Shimizu, "In vivo pressure estimation using subharmonic contrast microbubble signals: proof of concept," *Ultrasonics*, vol. 52, no. 4, pp. 581–583, 2005.

[35] V. G. Halldorsdottir, J. K. Dave, L. M. Leodore, J. R. Eisenbrey, S. Park, a. L. Hall, K. Thomenius, and F. Forsberg, "Subharmonic Contrast Microbubble Signals for Noninvasive Pressure Estimation under Static and Dynamic Flow Conditions," *Ultrason. Imaging*, vol. 33, no. 3, pp. 153–164, Jul. 2011.

[36] M. Schneider, "Characteristics of SonoVue™," *Echocardiography*, vol. 16, no. 7, pp. 743–746, 1999.

[37] C. Sennoga, J. S. M. Yeh, J. Alter, E. Stride, P. Nihoyannopoulos, J. M. Seddon, D. O. Haskard, J. V Hajnal, M.-X. Tang, and R. J. Eckersley, "Evaluation of methods for sizing and counting of ultrasound contrast agents.," *Ultrasound Med. Biol.*, vol. 38, no. 5, pp. 834–45, May 2012.

[38] T. J. Matula, J. Swalwell, J. Tu, W. Cui, and W. Chen, "Flow cytometry to characterize microbubbles," in *2011 IEEE International Ultrasonics Symposium*, 2011, pp. 156–159.

[39] E. Pelssers, M. Stuart, and G. J. Fleer, "Single Particle Optical Sizing (SPOS) I . Design of an Improved SPOS Instrument and Application to Stable Dispersions," *J. Colloid Interface Sci.*, vol. 137, no. 2, pp. 350 – 361, 1990.

[40] D. Maresca, M. Muller, M. Emmer, H. J. Vos, N. de Jong, and A. F. W. van der Steen, "Acoustic size distribution analyzer for microbubbles," *2009 IEEE Int. Ultrason. Symp.*, vol. 1, no. 2, pp. 1809–1812, Sep. 2009.

[41] N. de Jong, M. Emmer, A. van Wamel, and M. Versluis, "Ultrasonic characterization of ultrasound contrast agents.," *Med. Biol. Eng. Comput.*, vol. 47, no. 8, pp. 861–73, Aug. 2009.

[42] N. A. Hosny, G. Mohamedi, P. Rademeyer, J. Owen, Y. Wu, M.-X. Tang, R. J. Eckersley, E. Stride, and M. K. Kuimova, "Mapping microbubble viscosity using fluorescence lifetime imaging of molecular rotors," *Proc. Natl. Acad. Sci.*, vol. 110, no. 23, pp. 9225–30, May 2013.

[43] E. Sezgin, T. Sadowski, and K. Simons, "Measuring Lipid Packing of Model and Cellular Membranes with Environment Sensitive Probes," *Langmuir*, vol. 30, pp. 8160– 66, 2014.

[44] E. D. Salmon and G. W. Ellis, "A new miniature hydrostatic pressure chamber for microscopy," *J. Cell Biol.*, vol. 65, pp. 587–602, 1975.

[45] A. Zhushma, N. Lebedeva, P. Sen, M. Rubinstein, S. S. Sheiko, and P. A. Dayton, "A system for acoustical and optical analysis of encapsulated microbubbles at ultrahigh hydrostatic pressures," *Rev. Sci. Instrum.*, vol. 84, no. 5, p. 84, May 2013.

[46] J. Tu, J. Guan, Y. Qiu, and T. J. Matula, "Estimating the shell parameters of SonoVue microbubbles using light scattering," *J. Acoust. Soc. Am.*, vol. 126, no. 6, pp. 2954–62, Dec. 2009.

[47] V. Sboros, C. Moran, T. Anderson, and W. McDicken, "An in vitro comparison of ultrasonic contrast agents in solutions with varying air levels," *Ultrasound Med. Biol.*, vol. 26, no. 5, pp. 807–818, 2000.

[48] B. Dollet, S. M. van der Meer, V. Garbin, N. de Jong, D. Lohse, and M. Versluis, "Nonspherical oscillations of ultrasound contrast agent microbubbles," *Ultrasound Med. Biol.*, vol. 34, no. 9, pp. 1465–73, Sep. 2008.

[49] T. Faez, M. Emmer, M. Docter, J. Sijl, M. Versluis, and N. de Jong, "Characterizing the subharmonic response of phospholipid-coated microbubbles for carotid imaging," *Ultrasound Med. Biol.*, vol. 37, no. 6, pp. 958–70, Jun. 2011.

[50] M. Sprague, D. Goertz, E. Cherin, R. Karshafian, and F. S. Foster, "Acoustic characterisation of individual targeted microbubbles with high-frequency ultrasound," *IEEE Int. Ultrason. Symp.*, pp. 1092–1095, 2008.

[51] M. Postema, A. Bouakaz, and C. T. Chin, "Simulations and measurements of optical images of insonified ultrasound contrast microbubbles," *IEEE Trans. Ultrason. Ferroelectr. Freq. Control*, vol. 50, no. 5, pp. 523 – 535, 2003.

[52] F. Guidi, H. Vos, and R. Mori, "Microbubble characterization through acoustically induced deflation," *IEEE Trans. Ultrason. Ferroelectr. Freq. Control*, vol. 57, no. 1, pp. 193 – 202, 2010.

[53] J. Sijl, H. J. Vos, T. Rozendal, N. de Jong, D. Lohse, and M. Versluis, "Combined optical and acoustical detection of single microbubble dynamics," *J. Acoust. Soc. Am.*, vol. 130, no. 5, pp. 3271–81, Nov. 2011.

[54] V. Sboros, S. Pye, T. Anderson, C. M. Moran, M. Averkiou, C. A. Macdonald, J. Gomatam, and W. N. McDicken, "The measurement of backscatter from individual contrast agent microbubbles," *IEEE Int. Ultrason. Symp.*, pp. 1945–1947, 2002.

[55] E. Biagi, L. Breschi, E. Vannacci, and L. Masotti, "Stable and transient subharmonic emissions from isolated contrast agent microbubbles," *IEEE Trans. Ultrason. Ferroelectr. Freq. Control*, vol. 54, no. 3, pp. 480–97, Mar. 2007.

[56] L. Hoff, *Acoustic Characterization of Contrast Agents for Medical Ultrasound Imaging*. Dordrecht, The Netherlands: Klumwer Academic, 2001.

[57] J. Sijl, E. Gaud, P. J. Frinking, M. Arditi, N. de Jong, D. Lohse, and M. Versluis, "Acoustic characterization of single ultrasound contrast agent microbubbles," *J. Acoust. Soc. Am.*, vol. 124, no. 6, pp. 4091–7, Dec. 2008.

[58] T. Faez, D. Goertz, and N. de Jong, "Characterization of Definity™ ultrasound contrast agent at frequency range of 5-15 MHz," *Ultrasound Med. Biol.*, vol. 37, no. 2, pp. 338–42, Feb. 2011.

[59] D. E. Goertz, N. de Jong, and A. F. W. van der Steen, "Attenuation and size distribution measurements of Definity and manipulated Definity populations," *Ultrasound Med. Biol.*, vol. 33, no. 9, pp. 1376–88, Sep. 2007.

[60] B. L. Helfield, E. Cherin, F. S. Foster, and D. E. Goertz, "The effect of binding on the subharmonic emissions from individual lipid-encapsulated microbubbles at transmit frequencies of 11 and 25 MHz," *Ultrasound Med. Biol.*, vol. 39, no. 2, pp. 345–59, Feb. 2013.

[61] N. Olympus, "Ultrasonic transducers technical notes," *Tech. Broch. Olympus NDT, Waltham, MA*, 2006.

[62] Y. A. Ilinskii and E. A. Zabolotskaya, "Cooperative radiation and scattering of acoustic waves by gas bubbles in liquids," *J. Acoust. Soc. Am.*, vol. 92, no. 5, pp. 2837 – 41, 1992.

[63] K. E. Morgan, J. S. Allen, P. A. Dayton, J. E. Chomas, L. Klibaov, and K. W. Ferrara, "Experimental and theoretical evaluation of microbubble behavior: effect of transmitted phase and bubble size," *IEEE Trans. Ultrason. Ferroelectr. Freq. Control*, vol. 47, no. 6, pp. 1494–509, Jan. 2000.

[64] J. Sijl, M. Overvelde, B. Dollet, V. Garbin, N. de Jong, D. Lohse, and M. Versluis, "'Compression-only' behavior: a second-order nonlinear response of ultrasound contrast agent microbubbles," *J. Acoust. Soc. Am.*, vol. 129, no. 4, pp. 1729–39, Apr. 2011.

[65] Y. Luan, G. Lajoinie, E. Gelderblom, I. Skachkov, A. F. W. van der Steen, H. J. Vos, M. Versluis, and N. de Jong, "Lipid shedding from single oscillating microbubbles," *Ultrasound Med. Biol.*, vol. 40, no. 8, pp. 1834–1846, 2014.

[66] A. Brayman and T. J. Matula, "Microbubble dynamics in microvessels: Observations of microvessel dilation, invagination and rupture," *2008 IEEE Ultrason. Symp.*, pp. 1163–1166, Nov. 2008.

[67] K. Chetty, E. Stride, C. a Sennoga, J. V Hajnal, and R. J. Eckersley, "High-speed optical observations and simulation results of SonoVue microbubbles at low-pressure insonation," *IEEE Trans. Ultrason. Ferroelectr. Freq. Control*, vol. 55, no. 6, pp. 1333–42, Jan. 2008.

[68] C. F. Caskey, S. M. Stieger, S. Qin, P. a Dayton, and K. W. Ferrara, "Direct observations of ultrasound microbubble contrast agent interaction with the microvessel wall," *J. Acoust. Soc. Am.*, vol. 122, no. 2, pp. 1191–200, Aug. 2007.

[69] C. T. Chin, C. Lancée, J. Borsboom, F. Mastik, M. E. Frijlink, N. de Jong, M. Versluis, and D. Lohse, "Brandaris 128: A digital 25 million frames per second camera with 128 highly sensitive frames," *Rev. Sci. Instrum.*, vol. 74, no. 12, p. 5026, 2003.

[70] E. C. Gelderblom, H. J. Vos, F. Mastik, T. Faez, Y. Luan, T. J. A. Kokhuis, A. F. W. van der Steen, D. Lohse, N. de Jong, and M. Versluis, "Brandaris 128 ultra-high-speed imaging facility: 10 years of operation, updates, and enhanced features," *Rev. Sci. Instrum.*, vol. 83, no. 10, p. 103706, Oct. 2012.

[71] S. M. van der Meer, B. Dollet, M. M. Voormolen, C. T. Chin, A. Bouakaz, N. de Jong, M. Versluis, and D. Lohse, "Microbubble spectroscopy of ultrasound contrast agents," *J. Acoust. Soc. Am.*, vol. 121, no. 1, p. 648, 2007.

[72] J. Guan and T. J. Matula, "Using light scattering to measure the response of individual ultrasound contrast microbubbles subjected to pulsed ultrasound in vitro," *J. Acoust. Soc. Am.*, vol. 116, no. 5, p. 2832, 2004.

[73] P. L. Marston, S. C. Billette, and C. E. Dean, "Scattering Of Light By A Coated Bubble In Water Near The Critical And Brewster Scattering Angles," in *Proc. SPIE*, 1988, vol. 0925, pp. 308–316.

[74] P. Dayton, K. Morgan, A. Klibanov, G. Brandenburger, and K. Ferrara, "Optical and acoustical observations of the effects of ultrasound on contrast agents," *IEEE Trans. Ultrason. Ferroelectr. Freq. Control*, vol. 46, no. 1, pp. 220–232, 1999.

[75] P. Rademeyer, D. Carugo, J. Y. Lee, and E. Stride, "Microfluidic system for high throughput characterisation of echogenic particles," *Lab Chip*, vol. 15, no. 2, pp. 417–428, 2015.

[76] C. F. Caskey, D. E. Kruse, P. A. Dayton, T. K. Kitano, and K. W. Ferrara, "Microbubble oscillation in tubes with diameters of 12, 25, and 195 microns," *Appl. Phys. Lett.*, vol. 88, p. 033902, 2006.

[77] D. Thomas, V. Sboros, M. Emmer, H. J. Vos, and N. de Jong, "Optical observations of microbubble oscillation in small tubes," in *IEEE International Ultrasonics Symposium*, 2009, pp. 2782–2784.

[78] V. Garbin, D. Cojoc, E. Ferrari, E. Di Fabrizio, M. L. J. Overvelde, S. M. van der Meer, N. de Jong, D. Lohse, and M. Versluis, "Changes in microbubble dynamics near a boundary revealed by combined optical micromanipulation and high-speed imaging," *Appl. Phys. Lett.*, vol. 90, no. 11, p. 114103, 2007.

[79] V. Garbin, "Optical tweezers for the study of microbubble dynamics in ultrasound," Ph.D. Thesis, University of Trieste, 2006.

[80] V. Sboros, S. D. Pye, C. A. Macdonald, J. Gomatam, C. M. Moran, and W. N. McDicken, "Absolute measurement of ultrasonic backscatter from single microbubbles," *Ultrasound Med. Biol.*, vol. 31, no. 8, pp. 1063–72, Aug. 2005.

[81] R. Roy, "Quantitative particle characterization by scattered ultrasound," Ph.D. Thesis, Yale University, 1987.

[82] M. Roos, "A technique for the study of acoustic scattering from microparticles," *J. Acoust. Soc. Am.*, vol. 83, no. 2, pp. 770–776, 1988.

[83] R. Roy and R. Apfel, "Mechanical characterization of microparticles by scattered ultrasound," *J. Acoust. Soc. Am.*, vol. 87, no. 6, pp. 2332– 41, 1990.

[84] E. C. Everbach, D. B. Khismatuliin, J. T. Flaherty, and R. A. Roy, "Characterization Of Individual Submicron Perfluorocarbon Gas Bubbles By Ultrasonic Backscatter," *Acoust. Soc. Am.*, vol. 6, no. 3, pp. 175– 181, 2005.

[85] X. Xuan, J. Zhu, and C. Church, "Particle focusing in microfluidic devices," *Microfluid. Nanofluidics*, vol. 9, no. 1, pp. 1–16, Mar. 2010.

[86] P. Paiè, F. Bragheri, R. M. Vazquez, and R. Osellame, "Straightforward 3D hydrodynamic focusing in femtosecond laser fabricated microfluidic channels," *Lab Chip*, vol. 14, no. 11, pp. 1826–33, Jun. 2014.

[87] S. C. Hur, S.-E. Choi, S. Kwon, and D. Di Carlo, "Inertial focusing of non-spherical microparticles," *Appl. Phys. Lett.*, vol. 99, no. 4, p. 044101, 2011.

[88] J. Oakey, R. W. Applegate, E. Arellano, D. Di Carlo, S. W. Graves, and M. Toner, "Particle focusing in staged inertial microfluidic devices for flow cytometry," *Anal. Chem.*, vol. 82, no. 9, pp. 3862–7, May 2010.

[89] J. P. Golden, J. S. Kim, J. S. Erickson, L. R. Hilliard, P. B. Howell, G. P. Anderson, M. Nasir, and F. S. Ligler, "Multi-wavelength microflow cytometer using groove-generated sheath flow," *Lab Chip*, vol. 9, no. 13, pp. 1942–50, Jul. 2009.

[90] D. Maresca, M. Emmer, P. L. M. J. van Neer, H. J. Vos, M. Versluis, M. Muller, N. de Jong, and A. F. W. van der Steen, "Acoustic sizing of an ultrasound contrast agent," *Ultrasound Med. Biol.*, vol. 36, no. 10, pp. 1713–21, Oct. 2010.

[91] S. J. Satinover, J. D. Dove, and M. A. Borden, "Single-Particle Optical Sizing of Microbubbles," *Ultrasound Med. Biol.*, vol. 40, no. 1, pp. 138–147, Oct. 2014.

[92] R. G. Holt and L. a Crum, "Mie scattering used to determine spherical bubble oscillations.," *Appl. Opt.*, vol. 29, no. 28, pp. 4182–91, Oct. 1990.

[93] D. Elger, B. Williams, C. Crowe, and J. Roberson, *Engineering Fluid Mechanics, 10th Edition SI Version*. Jefferson City: Wiley, 2012.

[94] J. E. Hall, *Guyton and Hall Textbook of Medical Physiology*, 12th edn. Elsevier Saunders, Philadelphia, 2010.

[95] *ANSYS® Academic Research, Release 14.5, Help System, Modeling Discrete Phase, ANSYS, Inc.* .

[96] C. a Schneider, W. S. Rasband, and K. W. Eliceiri, "NIH Image to ImageJ: 25 years of image analysis," *Nat. Methods*, vol. 9, no. 7, pp. 671–675, 2012.

[97] C. A. Dimarzio, *Optics for Engineers*. Taylor & Francis Inc , CRC Press Inc, 2011.

[98] J. S. Allen, D. E. Kruse, and K. W. Ferrara, "Shell Waves and Acoustic Scattering from Ultrasound Contrast Agents," *IEEE Trans. Ultrason. Ferroelectr. Freq. Control*, vol. 48, no. 2, pp. 409–418, 2001.

[99] P. A. Dayton, K. E. Morgan, A. L. Klibanov, G. Brandenburger, K. R. Nightingale, and K. W. Ferrara, "A preliminary evaluation of the effects of primary and secondary radiation forces on acoustic contrast agents," *IEEE Trans. Ultrason. Ferroelectr. Freq. Control*, vol. 44, no. 6, pp. 1264–1277, Nov. 1997.

[100] Lord Rayleigh, "VIII. On the pressure developed in a liquid during the collapse of a spherical cavity," *Philos. Mag. Ser. 6*, vol. 34, no. 200, pp. 94–98, 1917.

[101] W. Lauterborn, "Numerical investigation of nonlinear oscillations of gas bubbles in liquids," *J. Acoust. Soc. Am.*, vol. 59, no. 2, pp. 283–293, 1976.

[102] T. Faez, M. Emmer, K. Kooiman, M. Versluis, A. van der Steen, and N. de Jong, "20 Years of Ultrasound Contrast Agent Modeling," *IEEE Trans. Ultrason. Ferroelectr. Freq. Control*, vol. 60, no. 1, pp. 7–20, Jan. 2013.

[103] L. Trilling, "The collapse and rebound of a gas bubble," *J. Appl. Phys.*, vol. 23, no. 1, pp. 14–17, 1952.

[104] J. B. Keller and M. Miksis, "Bubble oscillations of large amplitude," *J. Acoust. Soc. Am.*, vol. 68, no. 2, pp. 628 – 633, 1980.

[105] M. A. Borden, G. V Martinez, J. Ricker, N. Tsvetkova, M. Longo, R. J. Gillies, P. a Dayton, and K. W. Ferrara, "Lateral phase separation in lipid-coated microbubbles," *Langmuir*, vol. 22, no. 9, pp. 4291–7, Apr. 2006.

[106] G. Pu, M. a Borden, and M. L. Longo, "Collapse and shedding transitions in binary lipid monolayers coating microbubbles," *Langmuir*, vol. 22, no. 7, pp. 2993–9, Mar. 2006.

[107] N. De Jong, R. Cornet, and C. T. Lancée, "Higher harmonics of vibrating gas-filled microspheres. Part one: simulations," *Ultrasonics*, vol. 32, pp. 447–453, 1994.

[108] K. Sarkar, W. T. Shi, D. Chatterjee, and F. Forsberg, "Characterization of ultrasound contrast microbubbles using in vitro experiments and viscous and viscoelastic interface models for encapsulation," *J. Acoust. Soc. Am.*, vol. 118, pp. 539–550, 2005.

[109] P. Marmottant, S. Van Der Meer, M. Emmer, M. Versluis, N. De Jong, S. Hilgenfeldt, and D. Lohse, "A model for large amplitude oscillations of coated bubbles accounting for buckling and rupture," *J. Acoust. Soc. Am.*, vol. 118, no. 8, pp. 3499 – 3505, 2005.

[110] R. E. Glazman, "Damping of bubble oscillations induced by transport of surfactants between the absorbed film and the bulk solution," *J. Acoust. Soc. Am.*, vol. 76, no. 3, pp. 890 – 6, 1984.

[111] E. Stride, "The influence of surface adsorption on microbubble dynamics," *hilosophical Trans. R. Soc. - Ser. A Math. Phys. Eng. Sci.*, vol. 366, pp. 2103–2115, 2008.

[112] S. Hilgenfeldt, D. Lohse, and M. Zomack, "Response of bubbles to diagnostic ultrasound: a unifying theoretical approach," *Eur. Phys. J. B*, vol. 4, pp. 247 – 255, 1998.

[113] M. Kerker, *The scattering of light and other electromagnetic radiation*. New York: Academic Press, 1969.

[114] P. Laven, "MiePlot." version 4.3.05, 2014, 2014.

[115] S. Zhu, S. Wang, L. Yang, T. Huang, and X. Yan, "Progress in the development of techniques based on light scattering for single nanoparticle detection," *Sci. China Chem.*, vol. 54, no. 8, pp. 1244–1253, Aug. 2011.

[116] M. W. Davidson, "Concepts and Formulas in Microscopy: Resolution," *Nikon*, 2015. [Online]. Available: http://www.microscopyu.com/articles/formulas/formulasresolution.html. [Accessed: 13-Apr-2016].

[117] S. Koyama, T. Miwa, T. Sato, and M. Aizawa, "Optical chamber system designed for microscopic observation of living cells under extremely high hydrostatic pressure," *Extremophiles*, vol. 5, no. 6, pp. 409–15, Dec. 2001.

[118] B. Frey, M. Hartmann, M. Herrmann, R. Meyer-Pittroff, K. Sommer, and G. Bluemelhuber, "Microscopy under pressure--an optical chamber system for fluorescence microscopic analysis of living cells under high hydrostatic pressure," *Microsc. Res. Tech.*, vol. 69, no. 2, pp. 65–72, Feb. 2006.

[119] S. Timoshenko, S. Woinowsky-Krieger, and S. Woinowsky, *Theory of plates and shells*. McGraw-Hill, 1959.

[120] N. Hosny, G. Mohamedi, P. Rademeyer, J. Owen, Y. Wu, M.-X. Tang, R. J. Eckersley, E. Stride, and M. K. Kuimova, "Mapping microbubble viscosity using fluorescence lifetime imaging of molecular rotors," *Proc. Natl. Acad. Sci. U. S. A.*, vol. 110, no. 23, pp. 9225–30, Jun. 2013.

[121] Y. Luan, T. Faez, I. Skachkov, E. Gelderblom, B. Geers, I. Lentacker, T. Van Der Steen, and N. De Jong, "Optical Characterization of Individual Liposome- loaded Microbubbles," *IEEE Int. Ultrason. Symp.*, pp. 1890–1893, 2011.

[122] J. L. Raymond, Y. Luan, T. van Rooij, K. Kooiman, S.-L. Huang, D. D. McPherson, M. Versluis, N. de Jong, and C. K. Holland, "Impulse response method for characterization of echogenic liposomes," *J. Acoust. Soc. Am.*, vol. 137, no. 4, pp. 1693–1703, 2015.

[123] D. H. Thomas, V. Sboros, M. Emmer, H. Vos, and N. de Jong, "Microbubble oscillations in capillary tubes," *IEEE Trans. Ultrason. Ferroelectr. Freq. Control*, vol. 60, no. 1, pp. 105–14, Jan. 2013.

[124] Y. Luan, G. Lajoinie, E. Gelderblom, I. Skachkov, A. F. W. van der Steen, H. J. Vos, M. Versluis, and N. De Jong, "Lipid shedding from single oscillating microbubbles," *Ultrasound Med. Biol.*, vol. 40, no. 8, pp. 1834–1846, 2014.

[125] S. M. Van Der Meer, M. Versluis, D. Lohse, C. T. Chin, A. Bouakaz, and N. De Jong, "The resonance frequency of SonoVue™ as observed by high-speed optical imaging," *2004 IEEE Ultrason. Symp.*, vol. 00, no. c, pp. 343–345, 2004.

[126] M. Emmer, A. van Wamel, D. E. Goertz, and N. de Jong, "The Onset of Microbubble Vibration," *Ultrasound Med. Biol.*, vol. 33, no. 6, pp. 941–949, 2007.

[127] J. Sijl, B. Dollet, M. Overvelde, V. Garbin, T. Rozendal, N. de Jong, D. Lohse, and M. Versluis, "Subharmonic behavior of phospholipid-coated ultrasound contrast agent microbubbles," *J. Acoust. Soc. Am.*, vol. 128, no. 5, pp. 3239–52, Nov. 2010.

[128] B. L. Helfield and D. E. Goertz, "Nonlinear resonance behavior and linear shell estimates for Definity™ and MicroMarker™ assessed with acoustic microbubble spectroscopy," *J. Acoust. Soc. Am.*, vol. 133, no. 2, pp. 1158–68, Feb. 2013.

[129] M. Overvelde, V. Garbin, J. Sijl, B. Dollet, N. de Jong, D. Lohse, and M. Versluis, "Nonlinear shell behavior of phospholipid-coated microbubbles," *Ultrasound Med. Biol.*, vol. 36, no. 12, pp. 2080–2092, 2010.

[130] H. G. Flynn, "Cavitation dynamics. I. A mathematical formulation," *J. Acoust. Soc. Am.*, vol. 57, no. 6, p. 1379, 1975.

[131] H. G. Flynn, "Cavitation dynamics: II. Free pulsations and models for cavitation bubbles," *J. Acoust. Soc. Am.*, vol. 58, no. 6, p. 1160, 1975.

[132] R. E. Apfel and C. K. Holland, "Gauging the likelihood of cavitation from short-pulse, low-duty cycle diagnostic ultrasound," *Ultrasound Med. Biol.*, vol. 17, no. 2, pp. 179–185, 1991.

[133] C. C. Church, "Frequency, pulse length, and the mechanical index," *Acoust. Res. Lett. Online*, vol. 6, no. 3, p. 162, 2005.

[134] Y. S. Tung, J. J. Choi, B. Baseri, and E. E. Konofagou, "Identifying the inertial cavitation threshold and skull effects in a vessel phantom using focused ultrasound and microbubbles," *Ultrasound Med. Biol.*, vol. 36, no. 5, pp. 840–852, 2010.

[135] E. C. Unger, T. O. Matsunaga, T. McCreery, P. Schumann, R. Sweitzer, and R. Quigley, "Therapeutic applications of microbubbles," *Eur. J. Radiol.*, vol. 42, pp. 160–168, 2002.

[136] E. Talu, R. L. Powell, M. L. Longo, and P. A. Dayton, "Needle Size and Injection Rate Impact Microbubble Contrast Agent Population," *Ultrasound Med. Biol.*, vol. 34, no. 7, pp. 1182–1185, 2008.

[137] J. N. Marsh, C. Hall, M. Hughes, J. Mobley, J. Miller, and G. Brandenburger, "Broadband through-transmission signal loss measurements of Albunex® suspensions at concentrations approaching in vivo doses," *J. Acoust. Soc. Am.*, vol. 101, no. 2, p. 1155, 1997.

[138] E. Stride and N. Saffari, "Investigating the Significance of Multiple Scattering in Ultrasound Contrast Agent Particle Populations," *IEEE Trans. Ultrason. Ferroelectr. Freq. Control*, vol. 52, no. 12, pp. 2332–2345, 2005.

[139] M. Lampaskis and M. Averkiou, "Investigation of the Relationship of Nonlinear Backscattered Ultrasound Intensity with Microbubble Concentration at Low MI," *Ultrasound Med. Biol.*, vol. 36, no. 2, pp. 306–312, 2010.

[140] M. Overvelde, "Dynamics of Coated Microbubbles: Chapter 6 : Bubble-wall interactions," University of Twente, 2010.

[141] W. Wiedemair, Z. Tukovic, H. Jasak, D. Poulikakos, and V. Kurtcuoglu, "Modeling the interaction of microbubbles: Effects of proximity, confinement, and excitation amplitude," *Phys. Fluids*, vol. 26, no. 6, p. 062106, 2014.

[142] E. Stride and N. Saffari, "Theoretical and experimental investigation of the behaviour of ultrasound contrast agent particles in whole blood," *Ultrasound Med. Biol.*, vol. 30, no. 11, pp. 1495–1509, 2004.

[143] C. X. Deng, Q. Xu, R. E. Apfel, and C. K. Holland, "In Vitro Measurements of Inertial Cavitation Thresholds in Human Blood," *Ultrasound Med. Biol.*, vol. 22, no. 7, pp. 939–948, 1996.

[144] J. Owen, P. Grove, P. Rademeyer, and E. Stride, "The influence of blood on targeted microbubbles," *J. R. Soc. Interface*, vol. 11, no. 100, p. 20140622, 2014.

[145] C. Guiot, G. Pastore, M. Napoleone, P. Gabriele, M. Trotta, and R. Cavalli, "Thermal response of contrast agent microbubbles: Preliminary results from physico-chemical and US-imaging characterization," *Ultrasonics*, vol. 44, no. SUPPL., pp. 127–130, 2006.

[146] H. Mulvana, E. Stride, J. V Hajnal, and R. J. Eckersley, "Temperature dependent behavior of ultrasound contrast agents," *Ultrasound Med. Biol.*, vol. 36, no. 6, pp. 925–34, Jun. 2010.

[147] G. N. Stewart, "The pulmonary circulation time, the quantity of blood in the lungs and the output of the heart," *Am J Physiol*, vol. 58, no. 1, pp. 20–44, 1921.

[148] A. Brayman, M. Azadniv, M. W. Miller, and R. S. Meltzer, "Effect of static pressure on acoustic transmittance of Albunex microbubble suspensions.," *J. Acoust. Soc. Am.*, vol. 99, no. 4 Pt 1, pp. 2403–2408, 1996.

[149] J. K. Dave, V. G. Halldorsdottir, J. R. Eisenbrey, D. Merton, J.-B. Liu, J.-H. Zhou, H.-K. Wang, S. Park, S. Dianis, C. L. Chalek, F. Lin, K. E. Thomenius, D. B. Brown, and F. Forsberg, "Investigating the efficacy of subharmonic aided pressure estimation for portal vein pressures and portal hypertension monitoring," *Ultrasound Med. Biol.*, vol. 38, no. 10, pp. 1784–98, Oct. 2012.

[150] J. Owen, P. Rademeyer, D. Chung, Q. Cheng, D. Holroyd, C. Coussios, P. Friend, Q. A. Pankhurst, and E. Stride, "Magnetic targeting of microbubbles against physiologically relevant flow conditions," *Interface Focus*, vol. 5, 2015.

[151] M. Emmer, "The Onset of Microbubble Vibration: Chapter 10 - Influence of phospholipid-coating composition on bubble vibration," Erasmus Medical Center, Rotterdam, 2009.

[152] C.-H. Wang and C.-K. Yeh, "Controlling the Size Distribution of Lipid-Coated Bubbles via Fluidity Regulation," *Ultrasound Med. Biol.*, vol. 39, no. 5, pp. 882–892, Feb. 2013.

[153] Cen Zhang, "Characterisation of Microbubbles for Ultrasound Mediated Drug Delivery," 2014.

[154] Ý. Mørch, R. Hansen, S. Berg, A. K. O. Åslund, W. R. Glomm, S. Eggen, R. Schmid, H. Johnsen, S. Kubowicz, S. Snipstad, E. Sulheim, S. Hak, G. Singh, B. H. McDonagh, H. Blom, C. de Lange Davies, and P. M. Stenstad, "Nanoparticle-stabilized microbubbles for multimodal imaging and drug delivery," *Contrast Media Mol. Imaging*, 2015.

[155] C. Sciallero, D. Grishenkov, S. V. V. N. Kothapalli, L. Oddo, and A. Trucco, "Acoustic characterization and contrast imaging of microbubbles encapsulated by polymeric shells coated or filled with magnetic nanoparticles," *J. Acoust. Soc. Am.*, vol. 134, no. 5, pp. 3918–30, Nov. 2013.

[156] X. Cai, F. Yang, and N. Gu, "Applications of magnetic microbubbles for Theranostics," *Theranostics*, vol. 2, no. 1, pp. 103–112, 2012.

[157] E. Stride, K. Pancholi, M. J. Edirisinghe, and S. Samarasinghe, "Increasing the nonlinear character of microbubble oscillations at low acoustic pressures," *J. R. Soc. Interface*, vol. 5, no. 24, pp. 807–811, 2008.

[158] J. Il Park, D. Jagadeesan, R. Williams, W. Oakden, S. Chung, G. J. Stanisz, and E. Kumacheva, "Microbubbles loaded with nanoparticles: A route to multiple imaging modalities," *ACS Nano*, vol. 4, no. 11, pp. 6579–6586, 2010.

[159] A. Feis, C. Gellini, P. R. Salvi, and M. Becucci, "Photoacoustic excitation profiles of gold nanoparticles," *Photoacoustics*, vol. 2, no. 1, pp. 47–53, 2014.

[160] J. R. McLaughlan, R. A. Roy, H. Ju, and T. W. Murray, "Ultrasonic enhancement of photoacoustic emissions by nanoparticle-targeted cavitation," *Opt. Lett.*, vol. 35, no. 13, pp. 2127–2129, Jul. 2010.

[161] X. Yang, E. W. Stein, S. Ashkenazi, and L. V. Wang, "Nanoparticles for photoacoustic imaging," *Wiley Interdiscip. Rev. Nanomedicine Nanobiotechnology*, vol. 1, no. 4, pp. 360–368, 2009.

[162] C. H. Farny, T. Wu, R. G. Holt, T. W. Murray, and R. A. Roy, "Nucleating cavitation from laser-illuminated nano-particles," *Acoust. Res. Lett. Online*, vol. 6, no. 3, pp. 138–143, 2005.

[163] R. R. Letfullin, C. Joenathan, T. F. George, and V. P. Zharov, "Laser-induced explosion of gold nanoparticles: potential role for nanophotothermolysis of cancer," *Nanomedicine (Lond).*, vol. 1, no. 4, pp. 473–480, 2006.

[164] J. Owen and E. Stride, "Technique for the Characterization of Phospholipid Microbubbles Coatings by Transmission Electron Microscopy," *Ultrasound Med. Biol.*, vol. 41, no. 12, pp. 3253–3258, 2015.

[165] J. Owen, B. Zhou, P. Rademeyer, M.-X. Tang, Q. Pankhurst, R. Eckersley, and E. Stride, "Understanding the structure and mechanism of formation of a new magnetic microbubble formulation," *Theranostics*, vol. 2, no. 12, pp. 1127–39, Jan. 2012.

[166] K. Hettiarachchi, E. Talu, M. L. Longo, P. A. Dayton, and A. P. Lee, "On-chip generation of microbubbles as a practical technology for manufacturing contrast agents for ultrasonic imaging," *Lab Chip*, vol. 7, no. 4, pp. 463–468, 2007.

[167] M. Parhizkar, E. Stride, and M. Edirisinghe, "Preparation of monodisperse microbubbles using an integrated embedded capillary T-junction with electrohydrodynamic focusing," *Lab Chip*, vol. 14, pp. 2437–2446, 2014.

[168] T. J. Matula, "Inertial cavitation and single-bubble sonoluminescence," *Philos. Trans. R. Soc. A Math. Phys. Eng. Sci.*, vol. 357, no. 1751, pp. 225–249, 1999.

Appendix

A1. Construction of 3D model geometry

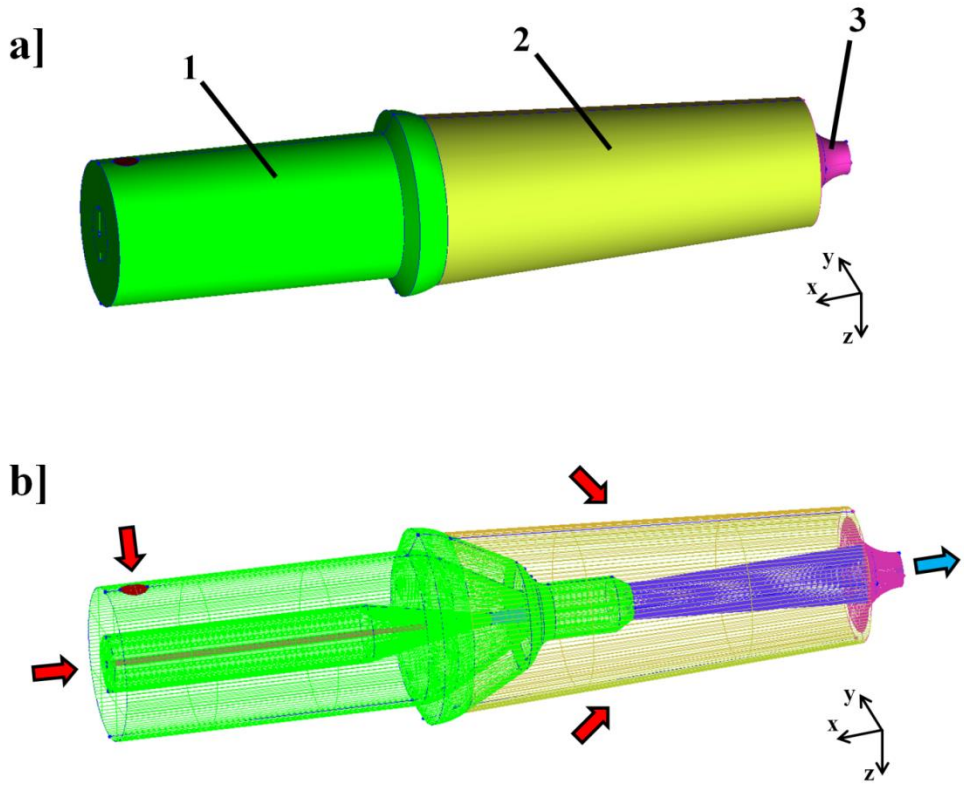

Figure A1.1: (a) Schematic representation of the computational model geometry (with surface rendering). The three main components of the model can be appreciated, including (1) the microfluidic flow focussing device (green), (2) the truncated cone joining the microfluidic device with the suction element (yellow), and (3) the suction element (violet). The inner surfaces generated for meshing purposes can be appreciated in (b). Red and blue arrows in (b) correspond to mass flow inlet and outflow boundary conditions, respectively.

A2. MATLAB scripts for processing light scattering measurements

Main program – this script runs the analysis of light scattering data captured using the device presented in Chapter 2. The script contains the main analysis method, as well as sub-functions to perform necessary calibrations and file handling routines. Subroutines highlighted in bold are shown following.

```
clear all
debug = 0; % 0 = no debug
s = 'n'; % 'y' to use previously processed data, 'n' overwrite previous data

% 2) Load samples and their details ------------------------------------------------
% Find filenames
disp('Checking Files....')
path = uigetdir(start_path);
[sampleInfo sizeParam] = loadExperimentalData(path,debug);

% Select sample(s) to analyise
for i = 1:length(sampleInfo.uniqueNames);
 disp([sampleInfo.uniqueNames{i}, ' = ' num2str(i)]);
end

if length(sampleInfo.uniqueNames) > 1;
 sampleN = input('Enter number(s) for analysis ');
else
 sampleN = 1;
end

load([path,'\FittingBounds.mat'])

for j = 1:length(sampleN) % Start looping through selected samples
 % Clear variables
 clearvars -except j sampleInfo path sampleN Metrics sizeParam bounds

 % load sample parameters
 freq(j) = sampleInfo.frequency(sampleN(j));
 voltage(j) = sampleInfo.voltage(sampleN(j));
 cycles(j) = sampleInfo.cycles(sampleN(j));

 % load file names
 [sampleNames, ~] = SearchFileNames(path,['C4',sampleInfo.uniqueNames{sampleN(j)}]);

 % load pressure field
 pressureFields =
PressureCalibration(path,sampleInfo.uniqueNames,freq(j),voltage(j),debug);
```

```
 % load ultrasound timing and signal window
 eventTimings = usGateTime(path, sampleNames,cycles(j),freq(j));

% Remove Outliers ------------------------------------------------
 debug =0;
 s ='y';
 [Samples] = SampleDoctor(path,
sampleNames(),sampleInfo.uniqueNames{sampleN(j)},eventTimings.usStart,eventTimings.usE
nd, debug,s);

% Data Analysis ----------------------
 k = 0; s= 'y';
 % Categories; no response, increase in size, decrease in size, expansion,
 % compression, other
 tempMetrics.Category = [0 0 0 0 0 0 0];

 % Check for previously saved data
 if exist([path,'\',sampleInfo.uniqueNames{sampleN(j)},'_ProcessedData.mat']) && debug
== 0 && s == 'y'
 file = dir([path,'\',sampleInfo.uniqueNames{sampleN(j)},'_ProcessedData.mat']);
 warning(['Using previously processed data from ', file.date]);
 index.G = 1;
 else
 index.G = 0;
 end

 if index.G == 0;
 for i = 1:length(Samples) % Loop through filtered traces from each sample

 % Display progress
 dispstat([num2str(100*(i/length(Samples))),'%'])

 % Load signal
 trace = load([path,'\',Samples{i}]);
 % find index of Ultrasound excitation
 index.I = find(trace(:,1) > eventTimings.gate(1),1,'first');
 index.IUS = find(trace(:,1) > eventTimings.usStart,1,'first');
 index.IUSend = find(trace(:,1) > eventTimings.usEnd,1,'first');
 index.I2 = find(trace(:,1) > eventTimings.gate(2),1,'first');

 % Measure Sampling Frequency
 Fs(i) = 1/(trace(2,1) - trace(1,1));

 % Selection portion of trace of response to ultrasound
 ScatterTrace = trace(index.I:index.I2,2);
 TimeScatter = trace(index.I:index.I2,1);%[0:1:length(ScatterTrace)-1]./Fs(i);

 % Define new indicies of the windowed traces
 index.IUSs = find(TimeScatter > eventTimings.usStart,1,'first');
 index.IUSends = find(TimeScatter > eventTimings.usEnd,1,'first');

 % --- Estimate gradient for light scatter correction
 ft = fittype( 'gauss2' );
 opts = fitoptions( ft );
 % bounds are estimated from fitting to the size standard particles
 % ( separate script and bounds are saved as FittingBounds.mat)
```

```
 opts.Lower = [-Inf bounds.b1(1)*0.5 bounds.c1(1)*0.5 -Inf bounds.b2(1)*0.1
bounds.c2(1)*0.1];
 opts.StartPoint = [bounds.a1(2) bounds.b1(2) bounds.c1(2) bounds.a2(2) bounds.b2(2)
bounds.c2(2)];
 opts.Upper = [Inf bounds.b1(3)*2 bounds.c1(3)*2 bounds.a2(3)*5 bounds.b2(3)*4
bounds.c2(3)*4];

 % Estimate Guassian fit to entire trace except for the portion that
 % is responding to ultrasound excitation
 [functions.f,gof] = fit([trace(1:index.IUS,1);
trace(index.IUSend+40:end,1)],[(trace(1:index.IUS,2));
trace(index.IUSend+40:end,2)],ft,opts);

 sizeTrace = feval(functions.f,trace(:,1));
 functions.c = feval(functions.f,TimeScatter);


 %-- Mie Scattering Convert voltage to radius
 % 1) Convert voltage to max. ie. Point of scatter needs to be
 % equivalent voltage to max of scatter

 functions.kF = max(sizeTrace(1:index.I))./functions.c;



 ScatterTraceR =
interp1(sizeParam.tFunction(:,2),sizeParam.tFunction(:,1),(ScatterTrace).*functions.kF
,'linear','extrap');
 ScatterTraceR(ScatterTraceR < 0) = 0;
 ScatterTraceR = smooth(ScatterTraceR,5);
 % Measure size properties
 tempMetrics.initialSize = mean(ScatterTraceR(1:index.IUSs));
 tempMetrics.endSize = mean(ScatterTraceR(index.IUSends:index.IUSends+40));
 tempMetrics.deltaSize = (tempMetrics.initialSize-
tempMetrics.endSize)/tempMetrics.initialSize; %microns!

 tempMetrics.baseScatter = mean(ScatterTraceR(index.IUSs:index.IUSends));

 % Peak detection for response categorisation
 [tempMetrics.peakLocC, tempMetrics.peakMagC]=
peakfinder(ScatterTraceR(index.IUSs:index.IUSends)-tempMetrics.baseScatter,[],0,-1,0);
 [tempMetrics.peakLocE, tempMetrics.peakMagE]=
peakfinder(ScatterTraceR(index.IUSs:index.IUSends)-tempMetrics.baseScatter,[],0,1,0);

 if debug == 1
 figure(142)
 plot(TimeScatter(tempMetrics.peakLocC+index.IUSs-1),tempMetrics.peakMagC +
tempMetrics.baseScatter,'ro'); hold on
 plot(TimeScatter(tempMetrics.peakLocE+index.IUSs-1),tempMetrics.peakMagE +
tempMetrics.baseScatter,'ro'); hold on
 plot(TimeScatter,ScatterTraceR)
 end

 tempMetrics.peakMean = mean(tempMetrics.peakMagE) + mean(tempMetrics.peakMagC);
 tempMetrics.MaxMean = mean(tempMetrics.peakMagE)+ tempMetrics.baseScatter;
 tempMetrics.MinMean = mean(tempMetrics.peakMagC)+ tempMetrics.baseScatter;
```

```
 tempMetrics.Perc_Class = ((tempMetrics.initialSize -
tempMetrics.MinMean)/(tempMetrics.MaxMean - tempMetrics.MinMean)) * 100;

 k = k + 1;
 tempMetrics.maxExpansionsStore(k) = max((ScatterTraceR(index.IUSs:index.IUSends)));
 tempMetrics.minCompressionStore(k) = min((ScatterTraceR(index.IUSs:index.IUSends)));


 % Noise stats:
 tempMetrics.NoiseLimit = std(ScatterTraceR(1:index.IUSs));
 tempMetrics.stdScatter = std(ScatterTraceR(index.IUSs:index.IUSs+80));
 tempMetrics.STest = tempMetrics.maxExpansionsStore(k)/tempMetrics.initialSize;
 tempMetrics.STest2 = tempMetrics.minCompressionStore(k)/tempMetrics.initialSize;
 % Categories!
 % 0) first check for suitable response above noise level


 if tempMetrics.STest < 1.1 && tempMetrics.STest2 > 0.9
 titleStr = 'No response';
 tempMetrics.Category(1) = tempMetrics.Category(1) + 1;
 tempMetrics.cat_store(k) = 0;
 else

 % 1) Significant change in radius
 if tempMetrics.deltaSize > 0.25
 titleStr = 'Change in size greater than 25 %';
 tempMetrics.Category(2) = tempMetrics.Category(2) + 1;

 elseif tempMetrics.deltaSize < - 0.25
 tempMetrics.Category(3) = tempMetrics.Category(3) + 1;

 end


 % 2) Expansion only behaviour
 if tempMetrics.Perc_Class < 30
 titleStr = 'Expansion Dominated';
 tempMetrics.Category(4) = tempMetrics.Category(4) + 1;
 tempMetrics.cat_store(k) = 2;
 % 3) Compression-only behaviour
 elseif tempMetrics.Perc_Class > 70
 titleStr = 'Compression Dominated';
 tempMetrics.Category(5) = tempMetrics.Category(5) + 1;
 tempMetrics.cat_store(k) = 3;
 else
 titleStr = 'Symmetrical Response';
 tempMetrics.Category(6) = tempMetrics.Category(6) + 1;
 tempMetrics.cat_store(k) = 1;
 end
 end

 % Estimate Scattered Pressure
 ScatterR = smooth(ScatterTraceR(index.IUSs-30:index.IUSends+30),10)*10^-6;

 dt = 1/Fs(i); % seconds
 PScatter = (1000*(ScatterR./(75*10^-3)) .*...
 (2*(derivative(ScatterR)/dt).^2 + ...
```

```
 ScatterR .* derivative(derivative(ScatterR)/dt)/dt)) /1000; % kPa
 PScatter = tukeywin(length(PScatter),0.5) .* PScatter;
 [tempFFT.FTrace,tempFFT.freq]=powerFFT([zeros(10,1); PScatter; Zeros(10,1)],Fs(i));
       [tempFFT.PFTrace,tempFFT.Pfreq]=powerFFT(pressureFields.pressureTrace,Fs(i));

 index.a = find(tempFFT.freq/10^6 > freq(j)/2, 1,'first');
 tempMetrics.subPower(k) = max(abs(tempFFT.FTrace(index.a)));
 index.a = find(tempFFT.freq/10^6 > freq(j), 1,'first');
 tempMetrics.FundPower(k) = max(abs(tempFFT.FTrace(index.a)));
 index.a = find(tempFFT.freq/10^6 > freq(j)*2, 1,'first');
 tempMetrics.HarmPower(k) = max(abs(tempFFT.FTrace(index.a)));
 tempMetrics.TotalPower(k) = sum(abs(tempFFT.FTrace));
 tempMetrics.minPScatter(k) = min(PScatter);
 tempMetrics.maxPScatter(k) = max(PScatter);
 index.a1 = find(tempFFT.freq/10^6 > freq(j)*0.75, 1,'first');
 index.a2 = find(tempFFT.freq/10^6 > freq(j)*1.5, 1,'first');
 index.a3 = find(tempFFT.freq/10^6 > 8, 1,'first');
 tempMetrics.FundPower2(k) = max(abs(tempFFT.FTrace(index.a1:index.a2)));
 tempMetrics.HarmPower2(k) = max(abs(tempFFT.FTrace([index.a2+1:end])));
 tempMetrics.SubPower2(k) = max(abs(tempFFT.FTrace([1:index.a1-1])));
 tempMetrics.FundPower2Area(k) = ((tempFFT.freq(index.a2)-tempFFT.freq(index.a1)));
 tempMetrics.HarPower2Area(k) = ((tempFFT.freq(index.a1-1)))+(tempFFT.freq(index.a3)-
tempFFT.freq(index.a2+1));


 % Store temp metrics
 tempMetrics.maxWallV(k) = max(abs((derivative(ScatterR)/dt)));
 tempMetrics.maxWallA(k) =max(abs(derivative(derivative(ScatterR)/dt)/dt));
 tempMetrics.initialsizeStore(k) = tempMetrics.initialSize;
 tempMetrics.deltaSizeStore(k) = tempMetrics.deltaSize;
 tempMetrics.deltaExpSizeStore(k) =
tempMetrics.maxExpansionsStore(k)/tempMetrics.initialsizeStore(k);
 tempMetrics.deltaVolumeStore(k) =
tempMetrics.maxExpansionsStore(k)^3/tempMetrics.initialSize^3;

 tempMetrics.Perc_Class_store(k) = tempMetrics.Perc_Class;
```

```
 % Is expansion greater than 2 x r?
 if tempMetrics.deltaExpSizeStore(k) > 2
 tempMetrics.Category(7) = tempMetrics.Category(7) + 1;
 end
 % Debugging
 if debug == 1
 num2clip([TimeScatter,ScatterTraceR]);
 figure(29)

 subplot(2,1,1); plot(trace(:,1),trace(:,2)); hold on
 title(titleStr)
 plot(trace(:,1),sizeTrace,'r');
 hold off
 xlabel('Time, s');ylabel('Uncalibrated Light Scattering Intensity, Voltage');

 subplot(2,1,2); plot(TimeScatter,ScatterTraceR); hold on
 xlabel('Time, s');ylabel('Calibrated Radius, \mum');
 hold off
```

```
 pause()

 end
 end

 save([path,'\',sampleInfo.uniqueNames{sampleN(j)},'_ProcessedData.mat'],
'tempMetrics');
 % Save all variables for quick analysis later
else % (if processed data already exists)

load([path,'\',sampleInfo.uniqueNames{sampleN(j)},'_ProcessedData.mat'],'tempMetrics')
 dispstat('Using previously processed data...','keepthis')
end

% Store results for analysis

 Metrics.maxRadius{j} = tempMetrics.maxExpansionsStore';
 Metrics.minRadius{j} = tempMetrics.minCompressionStore';
 Metrics.initialRadius{j} = tempMetrics.initialsizeStore';
 Metrics.filename{j} = sampleInfo.uniqueNames{sampleN(j)};
 Metrics.deltaRadius{j} = tempMetrics.deltaSizeStore';
 Metrics.deltaExpRadius{j} = tempMetrics.deltaExpSizeStore';
 Metrics.deltaVolume{j} = tempMetrics.deltaVolumeStore';
 Metrics.Categories(j,:) = tempMetrics.Category;
 Metrics.catIndex{j} = tempMetrics.cat_store';
 Metrics.peakNegative(j) = pressureFields.peakNegative;
 Metrics.frequency(j) = freq(j);
 Metrics.cycles(j) = cycles(j);
 Metrics.Class{j} = tempMetrics.Perc_Class_store';
 Metrics.SubPower{j} = tempMetrics.subPower;
 Metrics.FundPower{j} = tempMetrics.FundPower;
 Metrics.HarPower{j} = tempMetrics.HarmPower;
 Metrics.TotalPower{j} = tempMetrics.TotalPower;
 Metrics.minPScatter{j} = tempMetrics.minPScatter;
 Metrics.maxPScatter{j}= tempMetrics.maxPScatter;
 Metrics.HarPower2{j} = tempMetrics.HarmPower2;
 Metrics.FundPower2{j} = tempMetrics.FundPower2;
 Metrics.SubPower2{j} = tempMetrics.SubPower2;
 Metrics.maxWallV{j} = tempMetrics.maxWallV;
 Metrics.maxWallA{j} = tempMetrics.maxWallA;
 Metrics.FundPower2Area{j} = tempMetrics.FundPower2Area;
 Metrics.HarPower2Area{j} = tempMetrics.HarPower2Area;

end
```

Function Sample Doctor – This script removes samples based on criteria discussed in Section 3.2.1 that are not suitable for analysis.

```
function [Samples] = SampleDoctor(path, SampleNames,UniqueName,USstartTime,USendTime,
debug , s)

% check if outlier detection has been already performed
Samples = [];

if exist([path,'\',UniqueName,'_SampleDoctor.mat']) && debug == 0 && s == 'y'
 load([path,'\',UniqueName,'_SampleDoctor.mat'])
 disp('Loading previously performed outlier processing')
else
dispstat('','init')
disp('Removing Outliers.....')

i = 0; k = 0; % Start indexing

for k = 1:length(SampleNames) % Loop through samples

 dispstat([num2str(k),'\',num2str(length(SampleNames))])
 trace = [];

 try % Catch in case of bad file

 trace = load([path,'\',SampleNames{k}]); % Load file
 IUS = find(trace(:,1) > USstartTime,1,'first'); % Find index of US scatter
 IUSend = find(trace(:,1) > USendTime,1,'first');

 % fix clipped data
 [aa ClipBeforeScatter] = ClipDetect(trace(1:IUS,2),debug);
 [aa index] = ClipDetect(trace(IUS:IUSend,2),debug);

 % Evaluate index of clipped points for entire trace, clipped
 % points only fixed for scatter event, not for size trace

 index = [false(IUS-1,1) ; index ; false(length(trace) - IUSend,1)];
 index = index & (trace(:,2)) == max(trace(:,2));
 ClipBeforeScatter = ClipBeforeScatter & (trace(1:IUS,2)) == max(trace(1:IUS,2));

 % If there are clips in region of interest and max signal is
 % significantly high: then fix clips
 if sum(index > 0)
 [trace SampleNames{k}] = ClippingFix(path,trace, index, SampleNames{k});

 end
 % Measuring Guassian fit and width properties
 [widths(k) rSquared(k) sTime(k)] = GuassianProperties(trace,IUS,IUSend,debug); %
Width of scatter event % width = 0 is for nan


 % Remove unwanted samples

 if max(trace(IUS:end,2)) < 2*max(trace(1:IUS,2))
 if widths(k) == 10 || sTime(k) > 1.2 || sTime(k) <0.01 || rSquared(k) < 0.94 ||
sum(ClipBeforeScatter) > 10
 if debug == 1
 figure(12); plot(trace(:,1),trace(:,2))
```

```
 title(['Width =',num2str(widths(k)),' sTime = ',num2str(sTime(k)),' r^2 =
',num2str(rSquared(k))])
 end
 pass(k) = false;
 else
  if debug == 1
 figure(13); plot(trace(:,1),trace(:,2),'r')
 title(['Width =',num2str(widths(k)),' sTime = ',num2str(sTime(k)),' sse =
',num2str(rSquared(k))])
 end
 pass(k) = true;
 end

  else
 if widths(k) == 10 || sTime(k) > 1.6 || sTime(k) <0.01
 if debug == 1
 figure(12); plot(trace(:,1),trace(:,2))
 title(['Width =',num2str(widths(k)),' sTime = ',num2str(sTime(k)),' r^2 =
',num2str(rSquared(k))])
 end
 pass(k) = false;
 else
  if debug == 1
 figure(13); plot(trace(:,1),trace(:,2),'r')
 title(['Width =',num2str(widths(k)),' sTime = ',num2str(sTime(k)),' sse =
',num2str(rSquared(k))])
 end
   pass(k) = true;
 end
  end



 catch
 dispstat('Error, Sample failed to load','keepthis')
 end
end % repeat to next sample


% Now remove outliers ------------------------------------------------------
disp('Removing outliers 1 SD from mean')
mW = mean(widths(pass)); % Get mean width of those greater than 0
SDW = std(widths(pass)) ; % Find Standard deviation of widths

% Plot results for interest
if debug == 1
 figure(27); hist(widths(widths<10),50,'b'); hold on; plot([mW - SDW, mW + SDW],[100
100],'r')
 xlabel('Time of travel through laser beam, s');ylabel('Occurances')
end
widths_ = widths(pass);
% Index the samples within 1 Standard deviation of the mean and those that
% have not clipped (ie. gone off the dynamic range of oscilloscope
sampleIndex = ((widths_ > mW - SDW & widths_ < mW + SDW));

% Return Samples to be used
```

```
SampleNames_ = SampleNames(pass);

Samples = SampleNames_(sampleIndex==1);

dispstat(['There are ',num2str(length(Samples)),' suitable samples.'])

% Save Sample as variable to for later analysis
save([path,'\',UniqueName,'_SampleDoctor.mat'],'Samples','widths','rSquared')
end
dispstat(['There are ',num2str(length(Samples)),' suitable samples.'])
end
```

A3. Interpolation of clipped light scattering data

Due to the dynamic range limitation of digital oscilloscopes (8 bit = 256 possible levels), especially during large radial expansions, there is occasionally clipping in the light scattering data. Figure A3.1 shows the percentage of such events for a typical experiment. Since the data are obtained at sampling rates of at least 50 MHz it is possible to 'repair' the clipped data by using a cubic spline interpolator based on the valid points before and after the clipping. Unfortunately it was found that the interpolation could not account for the nonlinear behaviour of microbubble expansion and the interpolation in general underestimates the amplitude of expansion, Figure A3.2. Therefore, these samples were excluded from quantitative measurements.

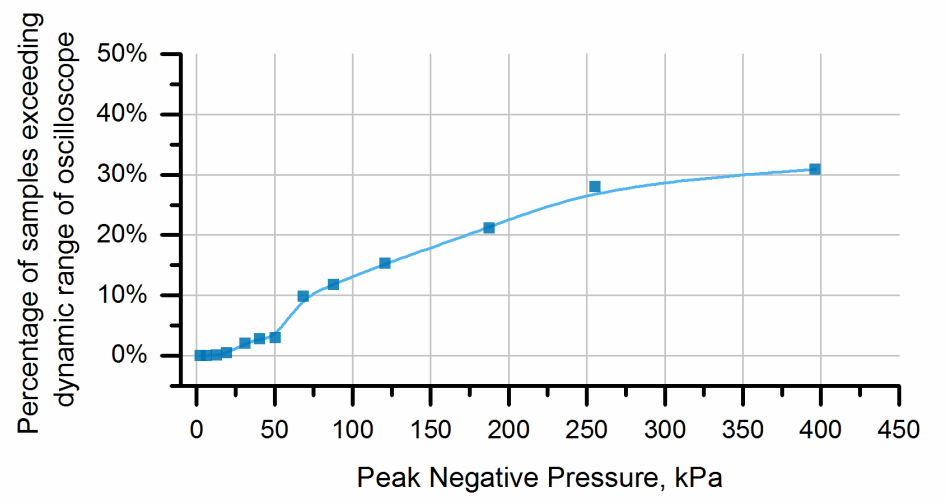

Figure A3.1: Percentage of samples during a typical experiment that exceeded the dynamic range of the oscilloscope as a function of the peak negative driving pressure.

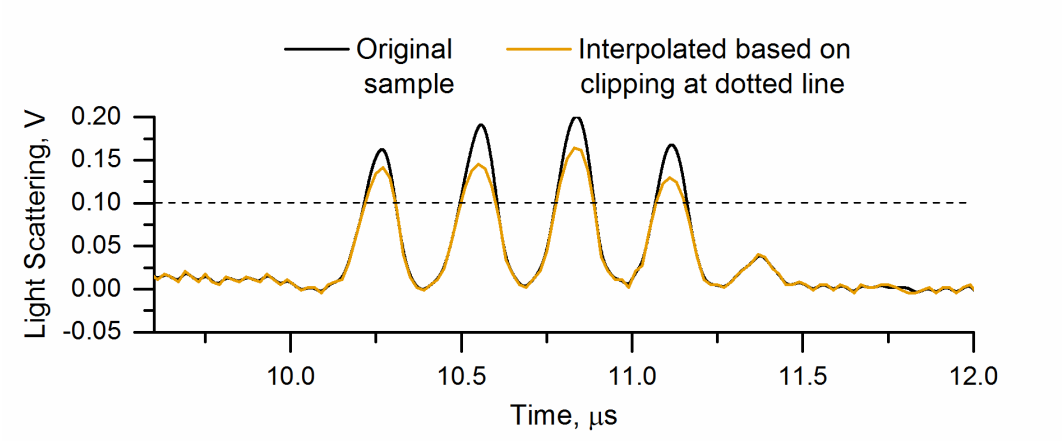

Figure A3.2: Light scattering data is artificially clipped along dotted line to demonstrate under estimation of expansion when interpolating the clipped peaks (orange line).

A4. Ultrasound Excitation Pulse Harmonic Content

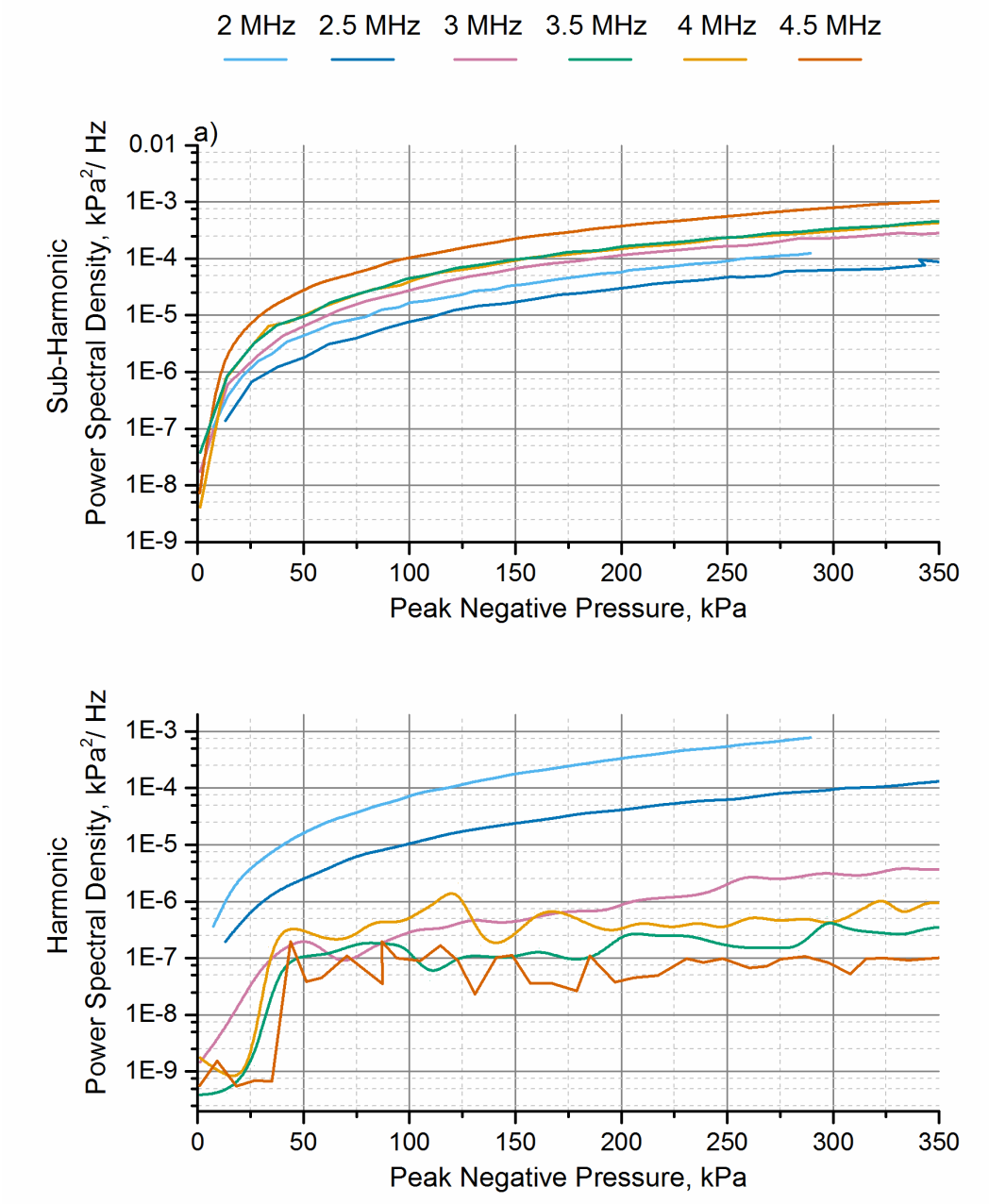

Figure A4.1: Sub-harmonic and harmonic pressure magnitude for ultrasound excitation pulses of 5 cycles as a function of peak negative driving pressure.